

**SYNTHESIS, CHARACTERIZATION AND
CATALYTIC EVALUATION OF MODIFIED
NANOCRYSTALLINE ZEOLITES**

*Thesis submitted to
the University of Calicut
for the award of*

DOCTOR OF PHILOSOPHY IN CHEMISTRY

By

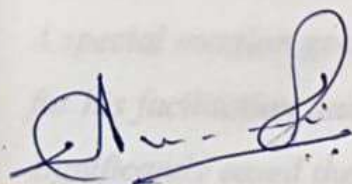
FARSANA O. P.



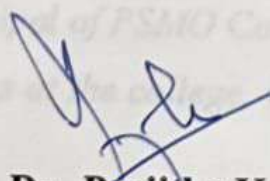
**DEPARTMENT OF CHEMISTRY
POCKER SAHIB MEMORIAL ORPHANAGE COLLEGE
TIRURANGADI
KERALA-676 306
APRIL 2024**

DECLARATION

I hereby declare that the work presented in the thesis entitled **"Synthesis, Characterization and Catalytic Evaluation of Modified Nanocrystalline Zeolites"** is based on the original work done by me under the guidance of Dr. Prajitha Kumari, Assistant Professor, Department of Chemistry, PSMO College Tirurangadi and Dr. Aneesh. P, Assistant Professor, Department of Chemistry, St. Joseph's College (Autonomous), Devagiri, Calicut and has not been included in any other thesis submitted previously for the award of any degree. The contents of the thesis have undergone a plagiarism check using iThenticate software at C.H.M.K. Library, University of Calicut, and the similarity index found within the permissible limit. I also declare that the thesis is free from AI generated contents.



Dr. Aneesh. P
(Co-Guide)



Dr. Prajitha Kumari
(Guide)


Farsana. O. P.

Tirurangadi
25th April 2024



POCKER SAHIB MEMORIAL ORPHANAGE COLLEGE

(Aided College | Affiliated to University of Calicut | Re-accredited At A' Grade by the NAAC)
SAUDABAD, TIRURANGADI, MALAPPURAM, KERALA-676 306
T: 9961460335, 0494 2460335; Email: mail@psmocollege.ac.in; Web: www.psmocollege.ac.in

Dr. K. Azeez, Principal
Mobile: +91 7510782005
Email: drkazeez@gmail.com
principal@psmocollege.ac.in

Date..17.12.2024..

CERTIFICATE

This is to certify that the thesis entitled "Synthesis, Characterization and Catalytic Evaluation of Modified Nanocrystalline Zeolites" is an authentic record of precise research work carried out by Farsana. O. P. at the Department of Chemistry, PSMO College Tirurangadi, under our joint guidance and supervision for the award of the degree of Doctor of Philosophy in Chemistry. The contents of the thesis have been checked for plagiarism using the software "iThenticate" and the similarity index falls under permissible limit, and I further certify that the thesis or part has not previously formed the basis for the award of any degree, diploma or associate ship of any other University or Institute. I also certify that the adjudicators have not suggested any changes or corrections in the scientific content, results and interpretations of the thesis.

Dr. Aneesh. P
(Co-Guide)
Assistant Professor
Department of Chemistry
St. Joseph's College (Autonomous)
Devagiri, Kozhikkode

Dr. Prajitha Kumari
(Guide)
Assistant Professor
Department of Chemistry
PSMO College Tirurangadi
Malappuram

DECLARATION

*I hereby declare that the work presented in the thesis entitled “**Synthesis, Characterization and Catalytic Evaluation of Modified Nanocrystalline Zeolites**” is based on the original work done by me under the guidance of Dr. Prajitha Kumari, Assistant Professor, Department of Chemistry, PSMO College Tirurangadi and Dr. Aneesh. P, Assistant Professor, Department of Chemistry, St. Joseph’s College (Autonomous), Devagiri, Calicut and has not been included in any other thesis submitted previously for the award of any degree. The contents of the thesis have undergone a plagiarism check using iThenticate software at C.H.M.K. Library, University of Calicut, and the similarity index found within the permissible limit. I also declare that the thesis is free from AI generated contents.*

Farsana. O. P.

Dr. Aneesh. P
(Co-Guide)

Dr. Prajitha Kumari
(Guide)

Tirurangadi
25th April 2024

ACKNOWLEDGMENT

First and foremost, I extend my heartfelt gratitude to God, the Almighty, for granting me strength, guidance, and perseverance throughout this transformative journey.

I wish to express my sincere appreciation to my research supervisor, Dr. Prajitha Kumari, for her unwavering support, invaluable guidance, and persistent encouragement, which have been instrumental in shaping this research endeavour.

I am also deeply thankful to my Co-Guide, Dr. Aneesh. P from Devagiri College for his pivotal role in initiating the experimental work at Devagiri College and his constant support.

Furthermore, I extend my gratitude to Dr. Aneesh M. H, Head, Department of Chemistry, PSMO College, whose consistent support and proactive measures have been crucial in establishing the necessary research facilities to complete this work successfully.

A special mention goes to Dr. Azeez K, principal of PSMO College, for his facilitation and provision of resources at the college, which significantly eased the research process.

Additionally, I am indebted to Dr. Shafeekh K M for his instrumental and chemical support through the SERB TARE project.

My heartfelt appreciation extends to all the teachers and non-teaching staff of the Department of Chemistry, especially Mr. Ansar Parakkal and Mr. Mohamed Favish. P, for their consistent support and encouragement.

I am grateful to UGC-India for providing JRF and SRF fellowships, which have been pivotal in completing my Ph. D work. I am also thankful to CSIF University of Calicut, STIC CUSAT, CIF PSMO College Tirurangadi., St Thomas College Thrissur, CeNS Bangalore, and Pondicherry University for the necessary characterization facilities for my research.

I must acknowledge the invaluable contribution of my project students, Ms Faseeba Banu, Ms. Afnan KM, Ms. Shamna Mirfath, Ms. Murshida Shirin, Ms Razeena, and Ms. Haneena Choottan, whose dedication and assistance have been indispensable in my research endeavors.

Special mention goes to my co-research scholars, Ms Thasleena Panakkal, and Ms Resha Kasim V.C, for their stable support, insightful discussions, and encouragement throughout my Ph.D journey.

To my beloved family, words cannot express my gratitude. To my mother, Ms. Subaida KM, and father, Mr. Alikutty O. P, along with my siblings, Muhammed Ali Azhar O. P and Thahseena O. P, their support has been my greatest strength.

I extend my heartfelt gratitude to my parents-in-law, Mr. Aboobacker and Ms. Pathumma, for their unwavering support and affection. Likewise, I sincerely appreciate the encouragement and care my sister-in-law, Ms. Asmabi S, provided.

To my dear husband, Mr. Abdul Saleem, his determined support and understanding have been my pillar of strength.

I extend my heartfelt thanks to my dear daughter, Raeda T, whose patience and understanding throughout my Ph.D journey have been a source of immense strength and motivation. Despite her challenges as a young child, her support and love have been a guiding light, reminding me the importance to balance family life and my academic pursuits.

Lastly, I sincerely appreciate all whose names may not be mentioned but have contributed in any form to this work. This accomplishment would not have been possible without the collective support and encouragement.

With profound gratitude,

25th April 2024

Farsana. O. P.

PREFACE

Zeolites are extensively employed in industries ranging from petroleum refining to environmental remediation due to their exceptional adsorption capacity and catalytic properties. These crystalline porous aluminosilicates, better known as ‘Molecular Sieves’ are invaluable in various industrial, environmental, and agricultural applications. From purifying water to catalyzing chemical reactions, zeolites play a pivotal role in addressing global challenges and advancing technological innovations. Earlier studies based on bulk commercial zeolite catalysts have revealed limitations during its use for industrial purposes, such as the need for large quantities, requirement of harsh reaction conditions, and low selectivity towards desired products, diffusion resistance in micropores etc. Inception of nanocrystalline and hierarchical zeolites address these limitations as they possess high surface area, more number of active sites and enhanced accessibility of inner active sites through uniform mesopores, potentially enabling catalysis of reactions involving bulky substrates. These benefits prompted this investigation into metal-modified nanocrystalline and hierarchical zeolites as novel materials for catalyzing aromatic acetylation under milder experimental conditions.

For applicability of zeolites in fine chemical synthesis, there has to be perfect control over the size of crystals within aggregates during the synthesis of zeolites so that it can address the pressure drop issue

during reactor loading. This study has fine-tuned the hydrothermal method to tailor crystal size and its aggregation. Hierarchical zeolites were synthesized by introducing the exo-template after initiating the crystallization process, aiming to customize hierarchical porosity efficiently. This study adopts a greener route with minimum experimental conditions for the industrially important acetylation reaction using modified and hierarchical zeolites. Furthermore, the dielectric response of metal-modified zeolites were also investigated.

The whole thesis is divided into seven chapters. A brief outline of these chapters is given below:

Chapter 1 overviews metal-modified and hierarchical zeolites. This chapter also provides a comprehensive account of the dielectric study of metal-modified zeolites. It highlights the gap in research on the comparative analysis of rare earth and transition elements incorporated zeolites. The objectives of the present work are also furnished at the end of the chapter.

Chapter 2 details the materials and methods employed for the preparation, characterization, and catalytic evaluation of these metal-modified and hierarchical nanocrystalline zeolites.

Chapter 3 consists of three sections. The first two sections describe the synthesis and characterization of metal-modified ZSM-5 and zeolite beta, and the third section is the catalytic evaluation of these zeolites by testing the efficiency for acetylation of toluene.

Section A describes the acidic properties, textural properties, and structural parameters of metal-modified nanocrystalline ZSM-5. UV-Visible spectra revealed the presence of several metal-oxide species in the samples in addition to respective cations. The modification changes both the texture characteristics and acidic properties, as indicated by the analysis of TPD and nitrogen adsorption studies. XRD measurements confirm that the modification does not alter the lattice stability and crystallinity.

Section B provides a detailed study of metal-modified nanocrystalline zeolite beta. According to XRD data, metal loading raises the lattice strain but does not change the zeolite structure. UV-Visible spectra show that metal ions are found in zeolite beta structures as metal oxides and cations. Skeletal vibration patterns in FTIR spectra are comparable to typical zeolite adsorption peaks. The TPD and surface area analysis proves that modification alters the acidic and textural characteristics.

Section C describes the testing of metal-exchanged zeolite beta and ZSM-5 for acetylation of toluene by optimizing experimental settings to the bare minimum, emphasizing lower temperatures and lower catalyst concentrations. Among all the modified samples, the ZSM-5 and zeolite beta samples treated with Ce showed a catalytic conversion of above 90% for AC₂O.

Chapter 4 consists of three sections: the first two sections describe the synthesis and characterization of hierarchical ZSM-5 and zeolite

beta, and the third section is the catalytic evaluation using these zeolites.

Section A describes the development of hierarchical porosity in nanocrystalline ZSM-5 by using PMMA powder in the aged precursor solution. This novel synthesis method lowers the occurrence of internal defective silanols which is confirmed by infrared and Raman spectroscopy. The thermogravimetric analysis also confirms the interaction of PMMA and TPAOH for providing hierarchical porosity via reducing internal defective silanols.

Section B describes the synthesis of hierarchical zeolite beta by hydrothermal approach, utilizing PMMA as an additional structure-directing agent. The resultant zeolite beta displays XRD patterns and FTIR spectra similar to those obtained from nanocrystalline zeolite beta. The zeolite beta synthesized with the inclusion of PMMA showcases a distinctly narrow distribution of mesopores with augmentation of the mesoporous surface area and mesopore volume.

Section C describes the evaluation of the catalytic efficiency of hierarchical ZSM-5 and zeolite beta in catalyzing the acetylation of 2-MON. Hierarchical ZSM-5 and zeolite beta possessing uniform mesopores displayed significant conversions of AC₂O with exclusive selectivity towards the kinetic product 1AC-2MON isomer. This observation is attributed to the fact that increase in regularity of mesopore surface facilitates interactions between reactant molecules and active sites occur.

Chapter 5 describes the dielectric properties of cerium-doped zeolite beta. At room temperature, synthesized cerium-doped zeolite beta and zeolite beta exhibit significant ultrahigh dielectric constants, 26k and 7k, respectively. The chapter discusses the dependence of AC conductivity, impedance, and modulus properties of these materials on temperature and frequency.

Chapter 6 accounts for the significant findings of the research work.

Chapter 7 discusses the scope of further work on metal-modified nanocrystalline zeolite catalysts in fine chemical synthesis. The enhanced properties of the metal-modified and hierarchical zeolites can be a green alternative for synthesizing chemicals. The very high dielectric constant values of the metal-modified zeolites indicate that they can be used to develop high-quality dielectric materials.

A comprehensive bibliography is provided at the end of each chapter.

LIST OF ABBREVIATIONS

1AC-2MON	:	1-acetyl-2-methoxynaphthalene
2-MON	:	2-methoxynaphthalene
6AC-2MON	:	6-acetyl-2-methoxynaphthalene
AC	:	Alternating Current
AC ₂ O	:	Acetic anhydride
AFI	:	Aluminophosphate-five
AIP	:	Aluminium isopropoxide
Al-HMS	:	Aluminium-rich mesoporous aluminosilicate
BDS	:	Broadband Dielectric Spectroscopy
BET	:	Brunauer-Emmett-Teller
BJH	:	Barrett-Joyner-Halenda
BPO	:	Benzoyl Peroxide
CAS	:	Chemical Abstracts Service Registry
CCD	:	Cooled Charge Coupled Device
DC	:	Direct Current
DENOX	:	de-Nitrogen Oxides
DPSS	:	Diode-Pumped Solid-State
EDS; EDX; EDXA	:	Energy Dispersive X-Ray Analysis
FER	:	Ferrierite

FID	:	Flame Ionisation Detector
FTIR	:	Fourier Transform Infrared spectroscopy
FWHM	:	Full Width Half Maximum
GC-MS	:	Gas Chromatography-Mass Spectrometry
H-USY	:	High-Silica Ultra Stable Y
IUPAC	:	International Union of Pure and Applied Chemistry
IZA	:	International Zeolite Association
JCPDS	:	Joint Committee on Powder Diffraction Standards
MAS NMR	:	Magic Angle Spinning Nuclear Magnetic Resonance
MFI	:	Mobil Five
MMA	:	Methylmethacrylate
MOR	:	Mordenite
NBZ	:	Nano crystalline zeolite beta
NZSM-5	:	Nanocrystalline Zeolite Socony Mobil-5
PMMA	:	Polymethyl methacrylate
PVA	:	Polyvinyl alcohol
SAD /SAED	:	Selected Area Electron Diffraction
SCO	:	Selective Catalytic Oxidation
SCR	:	Selective Catalytic Reduction
SEM	:	Scanning Electron Microscopy
TCD	:	Thermal Conductivity Detector

TEA	:	Tetraethyl ammonium
TEAOH	:	Tetraethyl ammonium hydroxide
TEM	:	Transmission Electron Microscopy
TEOS	:	Tetraethyl orthosilicate
TGA	:	Thermogravimetric analysis
TOF	:	Turnover frequency
TON	:	Turnover number
TOS	:	Time on stream
TPAOH	:	Tetrapropyl ammonium hydroxide
TPD	:	Temperature Programmed Desorption
UV	:	Ultra Violet
XRD	:	X-Ray Diffraction
ZSM-5	:	Zeolite Socony Mobil- 5

Abstract

Nano dimensions unveil a canvas of limitless possibilities. Decreasing the size of zeolite crystals to nanometer dimensions improves their characteristics by boosting surface area and minimizing diffusion path length. Research is focused on preparing zeolites with dispersed metal ions, especially high-silica zeolites, which are applauded for their effectiveness as catalysts in various chemical reactions. The development of hierarchical zeolites with secondary pore structures has been notable over the last decade. Additionally, zeolites doped with extra framework cations are found to exhibit excellent dielectric properties. This study investigates the fundamental aspects of metals in zeolites and hierarchical zeolite structures, discussing their applications for catalyzing reactions. The synthesized zeolites undergo a thorough characterization by FTIR, XRD, FESEM, UV-Visible spectroscopy, surface area, and surface acidity measurement. Furthermore, a comprehensive investigation into the sustainable catalytic reactions facilitated by these metal-modified zeolites, analyzing how metals in zeolites impact the selective acetylation of toluene under minimal experimental conditions. The study showcases innovative strategies for enhancing the catalytic activity through developing hierarchical porosity in nanocrystalline ZSM-5 and beta. Adding PMMA during nucleation minimizes internal defective silanols and successfully creates hierarchically porous ZSM-5 zeolite. However, the zeolite beta

synthesized with PMMA addition features narrowly distributed mesopores and microporous structure. This study also evaluates the effectiveness of hierarchical ZSM-5 and zeolite beta in the selective acetylation of 2-MON. Improved homogeneity of mesopore features and active site environments enhances selective catalytic behavior, highlighting the significance of heteroporous structures in zeolite catalysis. The study delves into the dielectric characteristics of cerium-doped zeolite beta employing broadband spectroscopic methods. The introduction of cerium induces significant variations in dielectric readings, leading to remarkably high dielectric constants compared to unmodified zeolite beta. Insights gained from impedance and modulus analyses contribute to the progression of zeolite-based charge storage device technologies. The study suggests that the research could lead to improvements in fixing defects in zeolites and in making specific organic compounds for medicines using zeolite catalysts. It also hints at potential uses for zeolites as dielectric materials. Understanding the dielectric properties of zeolites provides crucial insights for researchers and engineers to design applications beyond catalysis.

Key words: Zeolites, Nanocrystalline, Catalysis, Acetylation, Hierarchical zeolites

നാനോ അളവുകളിലൂടെ ശാസ്ത്രരംഗത്ത് അനന്തസാധ്യതകളാണ് തെളിഞ്ഞുവരുന്നത്. സിയോലൈറ്റ് ക്രിസ്റ്റലുകളുടെ വലുപ്പം നാനോമീറ്റർ അളവുകളിലേക്ക് കുറയ്ക്കുന്നത്, ഉപരിതല വിസ്തീർണ്ണം വർദ്ധിപ്പിച്ച്, ഡിഫ്യൂഷൻ പാത്ത് ദൈർഘ്യം കുറയ്ക്കുന്നതിലൂടെ അവയുടെ സവിശേഷതകൾ ഏറെ മെച്ചപ്പെടുത്താൻ സാധിക്കുന്നു. ചിതറിക്കിടക്കുന്ന ലോഹ അയോണുകൾ ഉള്ളതും, രാസപ്രവർത്തനങ്ങളിൽ രാസത്വരകമായി വർത്തിക്കുന്നതുമായ സിയോലൈറ്റുകളെ തയ്യാറാക്കുക എന്നതാണ് ഈ ഗവേഷണത്തിന്റെ ലക്ഷ്യം. കഴിഞ്ഞ ദശകത്തിൽ ദ്വിതീയ സൂഷിര ഘടനകളുള്ള ഹൈറാർക്കിക്കൽ സിയോലൈറ്റുകൾ തയ്യാറാക്കാൻ സാധിച്ചിട്ടുണ്ട്. കൂടാതെ, അധികമായ ഹൈഡ്രജൻ കാറ്റയോണുകൾ ഉപയോഗിച്ച് ഡോപ്പ് ചെയ്ത സിയോലൈറ്റുകൾ മികച്ച ഡൈ ഇലക്ട്രിക് ഗുണങ്ങൾ പ്രകടിപ്പിക്കുന്നതായും കണ്ടെത്തി. ഈ പഠനം സിയോലൈറ്റുകളിലെയും ഹൈറാർക്കിക്കൽ സിയോലൈറ്റ് ഘടനകളിലെയും ലോഹങ്ങളുടെ അടിസ്ഥാന വശങ്ങൾ അന്വേഷിക്കുന്നതിനും, ഉൽപ്രേരകമെന്നനിലയിൽ ഉത്തേജിപ്പിക്കുന്നതിനുള്ള അവയുടെ പ്രയോഗങ്ങളെക്കുറിച്ചുള്ള ചർച്ചകളിലേക്കും നയിച്ചു. എഫ്ഐആർ, എക്സ്ആർഡി, എഫ്ഇഎസ്ഇഎം, യുവി വിസിബിൾ സ്പെക്ട്രോസ്കോപ്പി, ഉപരിതല വിസ്തീർണ്ണം, ഉപരിതല അസിഡിറ്റി അളക്കൽ എന്നിവയിലൂടെ കൃത്രിമമായി നിർമ്മിച്ച സിയോലൈറ്റുകൾ സമഗ്രമായ വിശകലനത്തിന് വിധേയമാക്കി. കൂടാതെ ലോഹങ്ങളുപയോഗിച്ച് പരിഷ്കരിച്ച സിയോലൈറ്റുകൾ വഴി സുസ്ഥിരമായ കാറ്റലിക് പ്രതിപ്രവർത്തനങ്ങളെക്കുറിച്ചുള്ള വിശദമായ അന്വേഷണം കുറഞ്ഞ പരീക്ഷണാത്മക സാഹചര്യങ്ങളിൽ സിയോലൈറ്റുകളിലെ ലോഹങ്ങൾ ടൊളൂവീനിന്റെ തിരഞ്ഞെടുത്ത അസറ്റൈലേഷനെ എങ്ങനെ സ്വാധീനിക്കുന്നുവെന്ന് വിശകലനവും നടത്തി. നാനോക്രിസ്റ്റലിൻ ZSM-5, ബീറ്റ എന്ന് വിളിക്കാൻ പറ്റാത്ത പോരോസിറ്റി വികസിപ്പിക്കുന്നതിലൂടെ കാറ്റലിക് പ്രവർത്തനം വർദ്ധിപ്പിക്കുന്നതിനുള്ള നൂതന തന്ത്രങ്ങൾ പഠനത്തിൽ ഉൾപ്പെടുത്തിയിട്ടുണ്ട്. ന്യൂക്ലിയേഷൻ സമയത്ത് പിഎംഎംഎ ചേർക്കുന്നത് ഉള്ളിലുള്ള വികലമായ സിലനോളുകളെ കുറയ്ക്കുകയും ശ്രേണീപരമായി പോറസ് ZSM-5 സിയോലൈറ്റ് വിജയകരമായി സൃഷ്ടിക്കുകയും ചെയ്യുന്നു.

എന്നിരുന്നാലും, പിഎംഎംഎ കൂട്ടിച്ചേർക്കലുമായി സമന്വയിപ്പിച്ച സിയോലൈറ്റ് ബീറ്റയും ഇടുങ്ങിയ വിതരണ മെസോപോറുകളും മൈക്രോപോറസ് ഘടനയും സവിശേഷതകളായുണ്ട്. ഈ പഠനം 2-MON-ന്റെ സെലക്ടീവ് അസറ്റിലേഷനിൽ ഹൈറാർക്കിക്കൽ ZSM-5, സിയോലൈറ്റ് ബീറ്റ എന്നിവയുടെ ഫലപ്രാപ്തിയും വിലയിരുത്തുന്നു. കൂടാതെ മെസോപോർ ഫീച്ചറുകളുടെയും സജീവമായ സെറ്റിന്റെ പരിതസ്ഥിതികളുടെയും മെച്ചപ്പെടുത്തിയ ഹോമോജെനിറ്റി സെലക്ടീവ് കാറ്റലിക് സ്വഭാവം വർദ്ധിപ്പിക്കുന്നതുമായ സിയോലൈറ്റ് കാറ്റലിസിസിലെ ഹെറ്ററോപോറസ് ഘടനകളുടെ പ്രാധാന്യത്തേയും എടുത്തുകാണിക്കുന്നു. ബ്രോഡ്ബാൻഡ് സ്പെക്ട്രോസ്കോപ്പിക് രീതികൾ ഉപയോഗിക്കുന്ന സെറിയം-ഡോപ്പഡ് സിയോലൈറ്റ് ബീറ്റയുടെ വൈദ്യുത സ്വഭാവസവിശേഷതകൾ പഠനം പരിശോധിക്കുന്നു. സീറിയംവഴി ഡൈഇലക്ട്രിക് സ്വഭാവത്തിൽ കാര്യമായ വ്യതിയാനങ്ങൾ ഉണ്ടാക്കുന്നതായും ഇത് പരിഷ്കരിക്കാത്ത സിയോലൈറ്റ് ബീറ്റയുമായി താരതമ്യപ്പെടുത്തുമ്പോൾ ശ്രദ്ധേയമായ ഉയർന്ന വൈദ്യുത സ്ഥിരതകളിലേക്ക് നയിക്കുന്നതായും കണ്ടെത്തി. ഉയർന്ന ആവൃത്തിയിലുള്ള വൈദ്യുതിക്ക് അനുഭവപ്പെടുന്ന പ്രതിരോധത്തിൽ (ഇംപിഡൻസ്) നിന്നും മോഡ്യൂലസ് വിശകലനങ്ങളിൽ നിന്നും ലഭിച്ച സ്ഥിതിവിവരക്കണക്കുകൾ സിയോലൈറ്റ് അടിസ്ഥാനമാക്കിയുള്ള ചാർജ് സ്റ്റോറേജ് ഉപകരണ സാങ്കേതികവിദ്യകളുടെ പുരോഗതിക്ക് നിദാനമാകുന്നു. സിയോലൈറ്റുകളിലെ തകരാറുകൾ പരിഹരിക്കുന്നതിലും സിയോലൈറ്റ് കാറ്റലിസ്റ്റുകൾ ഉപയോഗിച്ച് മരുന്നുകൾക്കായി പ്രത്യേക ഓർഗാനിക് സംയുക്തങ്ങൾ നിർമ്മിക്കുന്നതിലും ഈ ഗവേഷണത്തിൽ പ്രാധാന്യം നൽകിയിട്ടുണ്ട്. വൈദ്യുത പദാർത്ഥങ്ങളായി സിയോലൈറ്റുകളുടെ ഉപയോഗ സാധ്യതയെക്കുറിച്ചും ഇത് സൂചന നൽകുന്നു. സിയോലൈറ്റുകളുടെ ഡൈ ഇലക്ട്രിക് ഗുണങ്ങൾ മനസ്സിലാക്കുന്നത്, ഗവേഷകർക്കും എഞ്ചിനീയർമാർക്കും കാറ്റലിസിസിനുള്ള വ്യാപകമായ ഉപയോഗങ്ങൾ രൂപകൽപ്പന ചെയ്യുന്നതിനുമുള്ള നിർണായക കണ്ടെത്തലുകളുമായി പരിണമിക്കുന്നു.

സൂചകപദങ്ങൾ: സിയോലൈറ്റുകൾ, നാനോക്രിസ്റ്റലൈൻ, കാറ്റലിസിസ്, അസറ്റിലേഷൻ, ഹൈറാർക്കിക്കൽ സിയോലൈറ്റുകൾ

Contents

	<i>Page No.</i>
Chapter 1	1-69
A Profound Exploration into Metal-Loaded and Hierarchical Zeolites	
1.1 Zeolite: A Comprehensive Journey through History	1
1.2 Synthesis of Zeolites	5
1.2.1 Ionothermal Synthesis	6
1.2.2 Alkali Fusion Method	6
1.2.3 Ultrasound Energy Method	6
1.2.4 Microwave-Assisted Synthesis	7
1.2.5 Sol-Gel Method	7
1.2.6 Hydrothermal Synthesis	8
1.3 Properties of Zeolites	9
1.3.1 Shape Selectivity (Molecular Sieving)	9
1.3.2 Ion Exchange Capacity	11
1.3.3 Surface Area	12
1.3.4 Lewis and Bronsted acidity	13
1.3.5 Chemical and Thermal Stability	14
1.4 Applications of Zeolites	14
1.5 High Silica Zeolite	16
1.5.1. ZSM-5	16
1.5.2 Zeolite Beta	18
1.6 Metal Ions in Zeolite	20
1.6.1. Modification on Zeolite Beta and ZSM-5 for Refinery Applications	21

1.6.2 Modification of Zeolite Beta and ZSM-5 or Pharmaceutical and Chemical Application	25
1.6.3 Modification of Zeolite Beta and ZSM-5 for Pollution Abatement	28
1.7 Nanocrystalline Zeolites	29
1.7.1 Synthesis of Nanocrystalline Zeolite	30
1.7.2. Modification of Nanocrystalline BETA and ZSM-5	31
1.8 Hierarchical Zeolites	34
1.9 Defects	37
1.10 Friedel- Crafts Acylation	41
1.10.1 Acylation of Toluene	42
1.10.2 Acylation of 2-methoxynaphthalene (2-MON)	43
1.11 Dielectric Study of Zeolite	44
1.12 Existing Gaps	49
1.13 Objectives	51
References	53
Chapter 2	71-91
Materials and Methods	
2.1 Introduction	73
2.2 Chemicals	73
2.3 Instrumentation and Analytical Techniques	74
2.3.1 X-ray Diffraction (XRD)	74
2.3.2 Fourier Transform Infrared Spectroscopy (FTIR)	75
2.3.3 Ultra Violet- Visible spectroscopy (UV- Visible spectroscopy)	76
2.3.4 Scanning Electron Microscopy (SEM)	77
2.3.5 Energy Dispersive X-ray Analysis (EDX)	77

2.3.6 Nitrogen Adsorption/Desorption Isotherm Analysis	77
2.3.7 Surface Acidity Determination of Solid Catalysts	78
2.3.7.1. FTIR of pyridine sorbed samples	78
2.3.7.2. Ammonia-temperature programmed desorption (TPD)	79
2.3.8 Al Magic Angle Spinning Nuclear Magnetic Resonance (Al MAS NMR)	81
2.3.9 Transmission Electron Microscopy (TEM)	81
2.3.10 Thermogravimetric Analysis (TGA)	82
2.3.11 Raman Spectroscopy	82
2.3.12 Gas Chromatography-Mass Spectrometry(GC-MS)	83
2.3.13 Broadband Dielectric Spectroscopy (BDS)	83
2.4 Synthesis of Zeolite Samples	83
2.4.1 Synthesis of Nanocrystalline ZSM-5	83
2.4.2 Modification of Synthesized ZSM-5	85
2.4.2.1 Ion exchange with NH ₄ Cl solution	85
2.4.2.2 Modification by ion exchange with metal ions	85
2.4.3 Synthesis of Nanocrystalline Zeolite Beta	86
2.4.4. Modification of Beta with Metal Ions	87
2.5 Catalytic Activity of Metal-Modified Nanocrystalline ZSM-5 and Zeolite Beta for Acetylation of Toluene	88
2.6 Synthesis of Nanocrystalline Hierarchical Zeolites by Dual Template Method	88
2.6.1. Synthesis of PMMA	88

2.6.2 Synthesis of Defect-Free Nanocrystalline Hierarchical ZSM-5	89
2.6.3 Synthesis of Nanocrystalline Hierarchical Zeolite Beta	90
2.7 Catalytic Activity of Nanocrystalline Hierarchical ZSM-5 and Zeolite Beta	91
2.8 Conclusions	91
Chapter 3	93-174
Investigations Into Metal-Modified Nanocrystalline Zeolites	
Section A: Studies on Metal-Modified Nanocrystalline ZSM-5	95
3A.1 Introduction	95
3A.2 Results and Discussion	96
3A.3 Conclusions	118
Section B: Studies on Metal-Modified Nanocrystalline Zeolite Beta	120
3B.1 Introduction	120
3B.2 Results and Discussion	122
3B.3 Conclusions	141
Section C: Evaluation of Catalytic Activity of Metal-Modified Zeolites	142
3C.1 Introduction	142
3C.2 Results and Discussion	144
3C.2.1 Effect of Molar Ratio of Reactants on Acetylation of Toluene	147
3C.2.2 Effect of Quantity of Catalyst on Acetylation of Toluene	149
3C.2.3 Effect of Temperature on Acetylation of Toluene	151

3C.2.4 Effect of Metal Modification of Nanocrystalline Zeolite on Acetylation of Toluene	152
3C.3 Conclusions	161
References	162
Chapter 4	175-240
Development of Nanocrystalline Hierarchical ZSM-5 and Zeolite Beta: Investigating Structural Properties and Catalytic Activity	
Section A: Tailoring of Hierarchical Porosity in Nanocrystalline ZSM-5 and Curing of Silanol Defects	177
4A.1 Introduction	177
4A.2 Results and Discussion	180
4A.3 Conclusions	200
Section B : Designing and Structural Assessment of Nanocrystalline Hierarchical Zeolite Beta	202
4B.1 Introduction	202
4B.2 Results and Discussion	203
4B.3 Conclusions	215
Section C: Evaluation of Catalytic Activity of Nanocrystalline Hierarchical Zeolites ZSM-5 and Beta	216
4C.1 Introduction	216
4C.2 Results and Discussion	218
4C.2.1 Effect of Molar Ratio of Reactants on Acetylation of 2-MON	221
4C.2.2 Effect of Temperature on Acetylation of 2-MON	222
4C.2.3 Effect of Quantity of Catalyst on Acetylation of 2-MON	223

4C.2.4 Effect of Hierarchical Porosity on Acetylation of 2-MON	225
4C.3 Conclusions	229
References	230
Chapter 5	241-261
Exploring the Dielectric and Electrical Properties of Cerium-Doped Zeolite Beta: Temperature-Dependent Analysis	
5.1 Introduction	243
5.2 Experimental	244
5.3 Results and Discussion	244
5.3.1 Analysis of Dielectric Parameters	244
5.3.2 Analysis of AC Conductivity	249
5.3.3 Analysis of Impedance Spectra	251
5.3.4 Analysis of Electric Modulus Spectra	255
5.4 Conclusions	257
References	259
Chapter 6	263-270
Conclusions	263
Chapter 7	271-274
Recommendations	271
List of Publications	275
List of Conference Presentations	275

List of Figures

<i>Figure No.</i>	<i>Title</i>	<i>Page No.</i>
1.1.	Primary building units of zeolite	3
1.2.	Development of zeolite framework (a) Faujasite (b) Sodalite (c) Zeolite A	3
1.3.	Classification of zeolites	5
1.4.	Properties of zeolites	9
1.5.	Shape-selective reactions and Molecular traffic control	11
1.6.	Representation of acidity of zeolites	13
1.7.	Pentasil building unit of ZSM-5	17
1.8.	(a) Secondary building unit of ZSM-5 (b) Pentasil units (c) Tertiary units: chain type arrangement of pentasil groups (d) layers of pentasil units	18
1.9.	Secondary building unit (a) top view (b) and side view (c) of centrosymmetric layer of zeolite beta	19
1.10.	Schematic representations of the zeolite beta structure	20
1.11.	The different methods for the synthesis of hierarchical zeolites	35
3A.1.	FTIR spectra of NZSM-5 and NZSM-5/M samples	97
3A.2.	UV-Visible spectra of NZSM-5 and NZSM-5/M samples with deconvoluted bands of NZSM -5/Fe (inset)	98
3A.3.	Nitrogen adsorption-desorption isotherm of NZSM-5 and NZSM-5/M samples	101

3A.4.	t-plot of NZSM-5 and NZSM-5/M samples	103
3A.5.	TPD profile of NZSM-5 and NZSM-5/M samples	106
3A.6.	SEM images of zeolite samples (a) NZSM-5 (b) NZSM-5/La (c) NZSM-5/Ce (d) NZSM-5/Nd (e) NZSM-5/Fe (f) NZSM-5/Cu and (g) NZSM-5/Zn	108
3A.7.	²⁷ Al MAS NMR of NZSM-5 and NZSM-5/M samples	110
3A.8.	XRD patterns of NZSM-5 and NZSM-5/M samples	113
3A.9.	Variation of dislocation density with crystallite size of NZSM-5 and NZSM-5/M samples	116
3A.10.	Variation in crystallinity and lattice strain by the elemental composition	117
3B.1.	XRD patterns of NBZ and NBZ/M samples with simulated pattern	122
3B.2.	FTIR patterns of NBZ and NBZ/M samples	126
3B.3.	UV Visible spectra of NBZ/M samples with spectra of NBZ (inset)	127
3B.4.	Nitrogen adsorption-desorption isotherm of NBZ and NBZ/M samples	129
3B.5.	Pore size distribution of NBZ and NBZ/M samples	132
3B.6.	TPD profile of NBZ and NBZ/M samples	133
3B.7.	FTIR of Pyridine sorbed zeolite beta samples: B for Bronsted acid sites, L for Lewis acid sites, H for hydrogen-bonded sites	135
3B.8.	SEM images of zeolite samples (a) NBZ (b) NBZ/Fe (c) NBZ/Cu (d) NBZ/Zn (e) NBZ/La (f) NBZ/Ce (g) NBZ/Nd	138

3C.1	Conversion of AC ₂ O against time at different molar ratios of reactants on a) NZSM-5 and b) NBZ	148
3C.2.	Conversion of AC ₂ O against time at different amounts of a) NZSM-5 and b) NBZ	150
3C.3.	Conversion of AC ₂ O against time at different temperatures on a) NZSM-5 and b) NBZ	152
3C.4.	Conversion of AC ₂ O against time on different zeolite samples a) NZSM-5/M and b) NBZ/M at optimized conditions.	153
4A.1.	XRD patterns of NZ and NZ xP with simulated IZA pattern	182
4A.2.	FTIR spectra of NZ and NZ xP samples a) 4000-500 cm ⁻¹ b) 1400-500 cm ⁻¹	183
4A.3.	FTIR Spectra of prepared PMMA	184
4A.4.	(a) FTIR spectra of NZ and NZ xP samples from 3750 cm ⁻¹ to 3700 cm ⁻¹ (b) Schematic representation of the formation of internal silanols in NZ (I) & (II) and disappearance of internal silanols in NZ xP by PMMA (III) & (IV)	184
4A.5.	Suggested mechanism for the creation of mesoporosity and the removal of silanol defects in zeolites using PMMA	186
4A.6.	Raman spectra of NZ and NZ 2.0P; the inset highlights the spectral region between 960-1020 cm ⁻¹	187
4A.7.	FTIR of pyridine sorbed NZ and NZ xP samples	189
4A.8.	Nitrogen adsorption-desorption isotherm of NZ and NZ xP samples	190
4A.9.	Pore size distribution of NZ and NZ xP samples	192
4A.10.	TGA curves of NZ and NZ xP samples; AC and BC indicate after and before calcination respectively	194

4A.11.	Low and High magnification SEM images of NZ (a) and (b) and NZ 2.0 P (c) and (d)	197
4A.12.	Typical TEM images and SAED pattern of NZ (a, c, e) and NZ 2.0P (b, d, f)	199
4B.1.	XRD patterns of NBZ and NBZ xP samples and simulated IZA pattern	204
4B.2.	FTIR spectra of NBZ and NBZ xP samples a) 4000-500 cm^{-1} b) 1400-500 cm^{-1}	206
4B.3.	a) Nitrogen adsorption-desorption isotherm and b) Pore size distribution (right) of NBZ and NBZ xP samples	206
4B.4.	FTIR of pyridine sorbed NBZ and NBZ xP	209
4B.5.	TGA profile of NBZ and NBZ xP; BC and AC indicate before and after calcination, respectively	210
4B.6.	SEM images of a) NBZ and b) NBZ 2.0P	212
4B.7.	TEM images of NBZ (a, c, e) and NBZ 2.0P (b, d, f)	214
4C.1.	Variation of conversion of AC_2O at different molar ratios of 2MON: AC_2O	222
4C.2.	Variation of conversion of AC_2O at different temperatures	223
4C.3.	Variation of conversion of AC_2O over different amounts of catalyst samples	225
4C.4.	Variation of conversion of AC_2O over different zeolite samples	226
5.1.	Variation of the dielectric constant of NBZ and NBZ/Ce with frequency at different temperatures	247
5.2.	Variation of dielectric Loss factor ($\tan \delta$) of NBZ and NBZ/Ce with frequency at different temperatures	248

5.3.	Variation of AC conductivity of NBZ and NBZ/Ce with frequency at different temperatures	250
5.4.	Variation of the real impedance of NBZ and NBZ/Ce with frequency at different temperatures	252
5.5.	Variation of the imaginary impedance of NBZ and NBZ/Ce with frequency at different temperatures	253
5.6.	Cole-Cole plot of NBZ and NBZ/Ce at different temperatures	256

List of Tables

<i>Table No.</i>	<i>Title</i>	<i>Page No.</i>
2.1.	List of chemicals used for the present study	73
3A.1.	The mode and frequency of each vibration for NZSM-5 and NZSM-5/M	98
3A.2.	Textural and acidic properties of NZSM-5 and NZSM-5/M	102
3A.3.	The elemental composition of NZSM-5 and NZSM-5/M	111
3A.4.	Structural parameters of the NZSM-5 and NZSM-5/M samples	115
3B.1.	Structural parameters of NBZ and NBZ/M	124
3B.2.	Textural and acidic characteristics of NBZ and NBZ/M	130
3B.3.	Elemental composition of NBZ and NBZ/M	139
3C.1.	Effect of molar ratio of reactants on the conversion of AC ₂ O	147
3C.2.	Effect of quantity of catalyst on the conversion of AC ₂ O	149
3C.3.	Effect of temperature on conversion of AC ₂ O	151
3C.4.	Effect of metal modification of NZSM-5 on the conversion of AC ₂ O	154
3C.5.	Effect of metal modification of NBZ on the conversion of AC ₂ O	154

3C.6.	Properties of metal-modified zeolite samples	156
3C.7.	Comparative analysis of various zeolite samples used in acetylation of toluene	160
4A.1.	Crystallinity of NZ and NZ xP	181
4A.2.	Textural properties of NZ and NZ xP	193
4A.3.	Summary of TGA results NZ and NZ xP	194
4B.1.	Crystallinity and crystallite size of NBZ and NBZ xP	205
4B.2.	Textural properties of NBZ and NBZ xP	207
4B.3.	Summary of TGA results of NBZ and NBZ xP	211
4C.1.	Comparative study of acetylation of 2-MON over NZ and NBZ at different ratios of 2-MON: AC ₂ O.	221
4C.2.	Comparative study of acetylation of 2-MON over NZ and NBZ at different temperatures	222
4C.3.	Comparative study of acetylation of 2-MON over NZ and NBZ for different amounts of catalyst samples	224
4C.4.	Comparative study of acetylation of 2-MON over different zeolite samples	226
4C.5.	Comparative analysis of different zeolite samples from literature for the acetylation of 2-MON	228

List of Schemes

<i>Scheme No.</i>	<i>Title</i>	<i>Page No.</i>
2.1.	Flow chart showing the synthesis of nanocrystalline ZSM-5	84
2.2.	Flow chart for the modification of NZSM-5	86
2.3.	Steps involved in the hydrothermal synthesis of NBZ	87
2.4.	Steps involved in the metal modification of NBZ	88
2.5.	Method of preparation of PMMA	89
3C.1.	Mechanism of the catalysis of acetylation at the Bronsted acid sites of zeolites	145
3C.2.	Mechanism of the catalysis of acetylation at the Lewis acid sites of zeolites	157
4C.1.	Acetylation of 2-MON	218
4C.2.	Mechanism of acetylation of 2-MON on zeolite	219

Chapter 1

A Profound Exploration into Metal-Loaded and Hierarchical Zeolites

Abstract

Nano dimensions unveil the limitless possibilities of ordinary matter exposing its extraordinary appeal. Reducing zeolite crystals to nanometer dimensions immensely enhances their properties by increasing the surface area and shortening of diffusion paths. Research is focused on preparing nano crystalline zeolites with dispersed metal ions, especially high-silica zeolites, which are highly regarded for their effectiveness as catalysts in various chemical reactions. The development of hierarchically porous zeolites with secondary pore structures have been much sought after research work by chemists over the last decade. Additionally, an exploration into the dielectric properties of zeolites with extra framework cations unravelled the capabilities of it as a capacitor which can lead to an umpteen number of applications in near future.

This chapter gives an introduction to the fascinating world of zeolites, fundamental aspects of incorporation of metals in zeolites and the importance of hierarchically porous zeolites, discussing their applications in catalyzing reactions. Furthermore, it explores the dielectric and electric properties of zeolites. This chapter also highlights existing research gaps and outlines the objectives of the current study.

1.1 Zeolites: A Comprehensive Journey Through History

Zeolites are naturally occurring crystalline aluminosilicates with three-dimensional microporous structures consisting of tetrahedrons of alumina and silica. The first systematic report on the discovery of zeolite was in 1765 by Axel Fredrik Cronstedt (Swedish mineralogist); he discovered crystals of the mineral stilbite and described them as “boiling stones” because of their ability to retain water within their structures even at high temperatures for a considerable period. They are highly porous and can capture water in tiny holes, releasing significant steam when heated. Therefore, ‘zeolite’ originates from the Greek words *zeo* (to boil) and *lithos* (stone).(1) Analcime, erionite, clinoptilolite, mordenite, laumontite, and heulandite are the other universally plentiful zeolites found in alkaline environments of volcanic areas. Although these materials exhibit exciting properties as catalysts and adsorbents, they have some limitations because of their structural irregularities.(2) For better activity, scientists have tried to synthesize zeolites since 1950. The absence of analytical instruments, like X-ray diffraction (XRD), led to a large gap between its discovery and synthesis. However, Robert Milton from Union Carbide discovered a facile method for synthesizing zeolites using alkaline aluminosilicate gel. Simultaneously, Richard Barrer found another effective synthesis strategy at a temperature range between 60 - 450 °C by using different hydroxides. In 1961, Barrer and Denny (3) tried the synthesis using organic bases instead of

inorganic ones. This led to the usage of quaternary ammonium salts for the synthesis.

As indicated in Figure 1.1, the primary structure has Si or Al occupying the center of the tetrahedron and oxygen atoms occupying the corners. A precise structural hierarchy exists in the framework of zeolites. The tetrahedra of aluminium and silicon oxides are the primary building units. They are linked through bridging oxygen atoms leading to the secondary building units. The interconnection of these secondary building units produces three-dimensional structures such as cube, hexagonal prism, truncated octahedron, etc.(4) These tertiary units are interconnected, resulting in the final hollow quaternary structure encompassing different pores depending on its constitution. Figure 1.2 illustrates the evolution of the zeolite framework. Faujasite structures result from connecting three-dimensional units of truncated octahedra with hexagonal prisms. Similarly, sodalite is generated by exclusive fusion of tertiary truncated octahedron units. Zeolite A takes shape through the arrangement of truncated octahedra with cubic units. The diverse zeolite structures are distinguished by the varying interconnections and the different sizes of pores formed.(3,5)

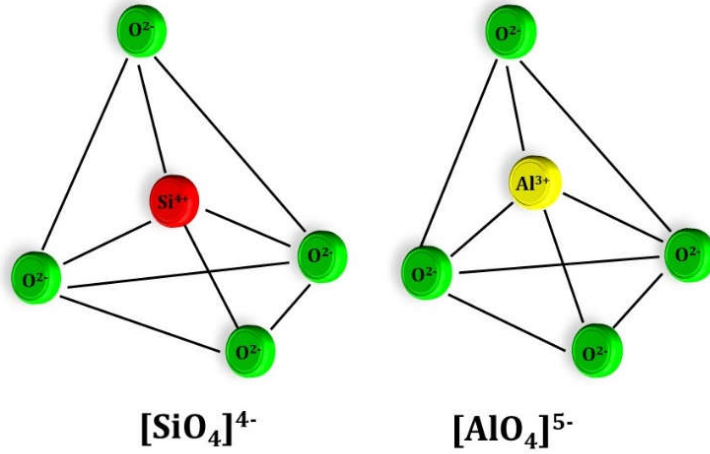


Figure 1.1. Primary building units of zeolites

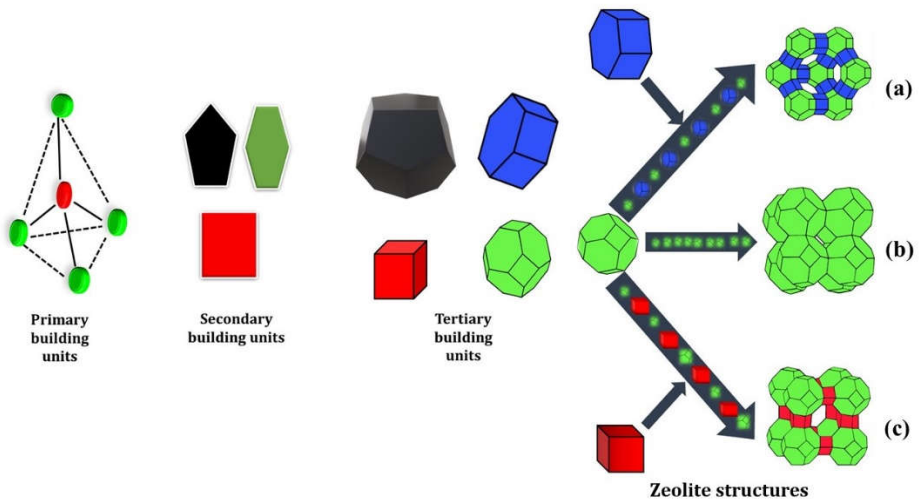


Figure 1.2. Development of zeolite framework (a) Faujasite (b) Sodalite (c) Zeolite A

The Structure Commission of the International Zeolite Association has allotted different codes for each framework type. A three-letter code is recognized by the International Union for Pure and Applied Chemistry (IUPAC).⁽⁶⁾ Now, almost 230 frameworks are known. The exciting properties exhibited by zeolites are due to the replacement of tetravalent silicon with trivalent aluminium. The charges on the aluminium tetrahedra are stabilized by incorporating cations into the structure. Open porous systems with cages, voids, and channels are created by interconnecting the silica and alumina tetrahedra. These pores are probably of nano dimension and can trap different cations and molecules such as carbon dioxide, ammonia, and water.

The zeolites are classified in different ways based on factors such as silica/alumina ratio (Si/Al), pore size, channel system, etc. They are categorized as low silica zeolites (Si/Al < 5), medium silica zeolites (Si/Al varies from 5 to 10), and high silica zeolites (Si/Al > 10) based on the Si/Al ratio. One-dimensional (such as AFI type), two-dimensional (such as MOR), and three-dimensional (such as MFI) zeolites are the classifications of zeolites based on the channel systems. They can also be categorized into extra-large pore zeolites (formed by more than 12 membered rings with pore diameter 0.8-1.0 nm), large pore zeolites (formed by 12 membered rings with pore diameter 0.6-0.8 nm), medium pore zeolites (formed by ten membered rings with pore diameter 0.45-0.60 nm) and small pore

zeolites (formed by eight-membered rings with pore diameter 0.30-0.45 nm).(7) The pictorial representation is given in Figure 1.3.

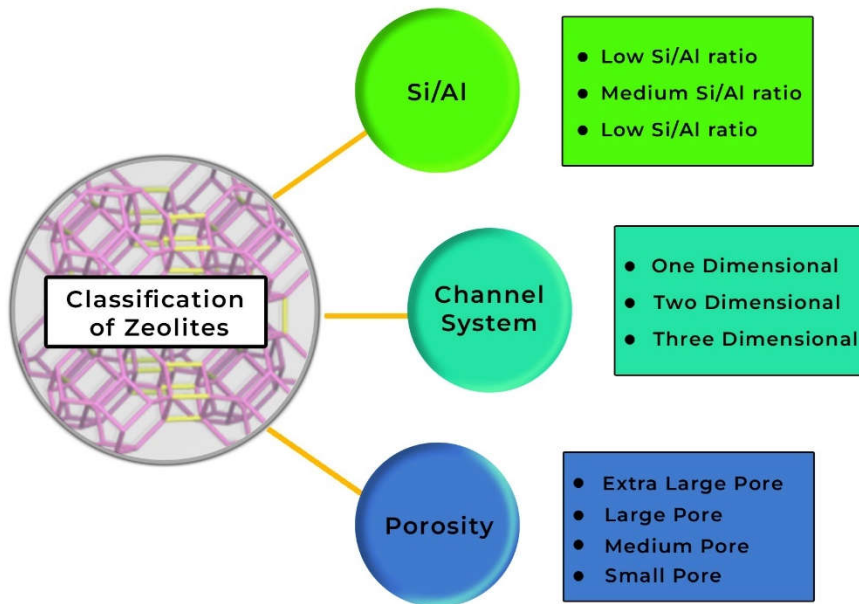


Figure 1.3. Classification of zeolites

1.2 Synthesis of Zeolites

Synthesis of zeolites is a new era of enduring research since their applicability is growing enormously. The creation of natural zeolites takes decades, whereas synthetic zeolites can be prepared within days. The synthesis process has a history since the 1950s. Scientists synthesized a wide variety of zeolite frameworks through arduous effort. Different synthesis routes used for the same are listed below.

1.2.1 Ionothermal Synthesis

The synthesis of zeolites using ionic liquids is referred to as ionothermal. The procedure utilizes ionic liquids as both the solvent and the structure-directing template. The most challenging task after the synthesis is to remove solvents and templates from the products. Although the ionothermal method produces good quality crystals with better control of composition, it has disadvantages such as severe operating conditions and the creation of toxic chemical species.(8)

1.2.2 Alkali Fusion Method

In this method, silica and alumina-rich materials from the earth's crust or industrial byproducts are decomposed using alkali, resulting in soluble aluminate and silicate salts. The fused products were mixed with water at an appropriate temperature for effective crystallization. Here, the alkali acts as an activator for the synthesis.(9) Although this method consumes more energy, it gives birth to high-purity anhydrous zeolites. Moreover, the raw materials are available cheaply and do not require any purification procedure before synthesis.(10)

1.2.3 Ultrasound Energy Method

Zeolite with tunable properties can be synthesized using ultrasound waves with 20 kHz to 2 MHz frequencies. The plan shows a higher rate of crystal growth and proper distribution of particle size, and it

does not need any complex facilities. Moreover, the method is simple, quick, and keeps nucleation under control. Ultrasound energy permits the quick crystallization of zeolites by generating active radicals.(11,12) Ultrasonic irradiation of the reacting mixture imparts the growth and collapse of bubbles, termed cavitation. Cavitation promotes the purity of crystals and the secondary nucleation rate.(13)

1.2.4 Microwave-Assisted Synthesis

Applying microwave radiation in the synthesis results in the formation of zeolite crystals characterized by particle sizes smaller than 10 nm and exhibiting high purity. The high-frequency electric field generated by microwaves provides a high temperature for efficient synthesis.(14) Resonance or relaxation of microwaves leads to quick heating.(15) Usually, microwave-assisted synthesis is used with other synthesis methods to reduce the particle size and increase the nucleation rate. Although different factors affect microwave methods, such as Si/Al ratio, alkalinity, and temperature, the advantage of the microwave method is its relatively short time for synthesis. A patent was claimed in 1988 by Mobil for the successful synthesis of zeolites using microwave irradiation by considering its ability to produce tiny crystals with high efficiency.(16)

1.2.5 Sol-Gel Method

It is a process of formation of three-dimensional network structures from inorganic colloidal suspension. The gelation of this colloidal suspension is a crucial factor in the synthesis. This method provides

better control of the pore characteristics and particle size. The lower equipment cost and convenient operating system make this synthesis procedure more suitable for zeolites. Several researchers have adopted this method in conjunction with the hydrothermal or microwave-assisted method for increasing the crystallinity.(17)

1.2.6 Hydrothermal Synthesis

Hydrothermal synthesis is a well-accepted primary route for zeolite synthesis. Water is used as the solvent, and a base acts as a mineralizer.(18) The environmentally benign nature, enhanced reactivity, low energy consumption, and formation of unique condensed and metastable phases make this method superior to others. Moreover, this method produces high-quality zeolite crystals with proper control over their composition.

Cundy CS and Cox PA (19) delineate the attributes of hydrothermal synthesis as follows: a mixture of amorphous materials containing alumina and silica along with a structure-directing species is the primary medium. When the mixture is heated to a temperature exceeding 100 °C in a sealed autoclave, the amorphous material transforms into a crystalline product, passing through a stage referred to as the "induction period," during which only a minimal proportion of crystalline products is observed. Subsequently, crystalline zeolites are generated from an equal mass of amorphous reactants. The Si-O and Al-O bonds in the amorphous precursors convert into Si-O-Al linkages in the crystallized zeolite.

1.3 Properties of Zeolites

The huge success of this fine-tunable novel class of catalysts in academe and industry is explained by a deep inquiry into its exceptional properties. The most striking properties that can be listed are their microporous crystalline structure, high ion exchange capacity, internal acidity, high thermal stability, high inner surface area, and tall shape selectivity with uniform pore dimensions, etc., which make these zeolites unique among inorganic oxides in their applications. The properties are depicted in Figure 1.4.

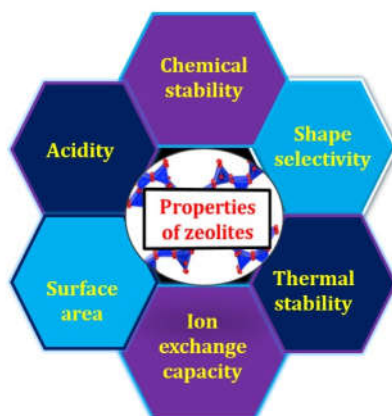


Figure 1.4. Properties of zeolites

1.3.1 Shape Selectivity (Molecular Sieving)

Alumina and silica-alumina combinations had been used widely as heterogeneous acid catalysts before the induction of zeolites. They have wide pore diameters ranging from 10 Å to 100 Å. Since zeolites have pore diameters of less than 10 Å with different-sized pores, they

have good molecular sieving properties. The sieving efficiency depends on the number of tetrahedra in a ring. The permeability of molecules through the pores is subjected to geometric or steric limitations. Molecules with dimensions smaller than a particular size can enter and react with the internal catalytic sites that usually reside within the pores. Moreover, only those molecules that can leave the pores appear as final products. Shape selectivity can be categorized based on the interaction of reactants, products, and reaction transition states with the pore system.⁽²⁰⁾ Examples of shape-selective reactions are represented in Figure 1.5.

➤ **Reactant selectivity**

Only those reactant molecules that can diffuse through the internal catalyst sites proceed to product formation.

➤ **Product selectivity**

Only molecules of a specific size and shape that can leave the pore system appear as products. When some of the molecules formed within the pore are too bulky to exit from the pore, they deactivate the catalyst by pore blocking or are converted into less bulky molecules.

➤ **Restricted transition-state selectivity**

This type of selectivity is observed in those reactions where the reactants and products do not face any accessibility restrictions in the pores, but the formation of the transition state is restricted. The reaction proceeds through the pathway that has a transition state that

fits in the pore system. The products obtained from transition states bigger than the pore system are not obtained as such transition states are restricted by the pore system.

➤ Molecular traffic control

Molecular traffic control occurs in zeolites having more than one type of pore system in different directions. Here, starting materials can enter the catalytic sites through a pore system, while products can diffuse through another type of pore system in another direction. The deployment of different pore systems in different directions thus minimizes counter diffusion.

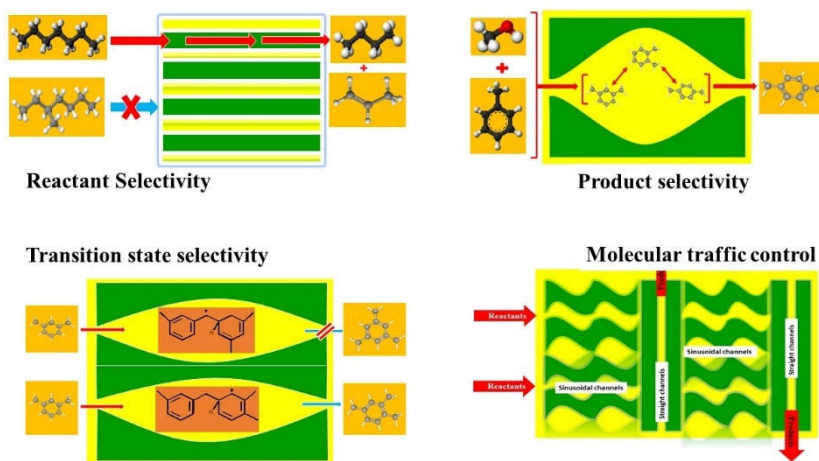


Figure 1.5. Shape-selective reactions and molecular traffic control

1.3.2 Ion Exchange Capacity

Negative charges are developed on the zeolitic framework by substituting silicon with aluminium atoms. They are neutralized by acidic protons bonded to the oxygen or by other cations. Moreover,

these protons or cations can be exchanged by other cationic species. When the cationic species are transition or rare-earth elements, the zeolites become catalytically superior.(21) The higher cation exchange capacity and excellent environmental adaptability make zeolites the most critical inorganic cation exchangers and effective adsorbents in water treatment. They can challenge other industrial cation exchange resins in the treatment of wastewater. The cations on the zeolite drop out of their sites and are replaced by other cations from the electrolytic solution when it comes into contact with it.(22)

1.3.3 Surface Area

One of the most striking properties of zeolites is their high surface area and pore characteristics. Different synthesis procedures generate zeolites with peculiar arrangements of fundamental building units, leading to various pore systems and varying surface areas.(23) Pores of molecular dimensions are responsible for the adsorbing of molecules. The presence of inherent micropores produces some diffusion constraints when applied to specific reactions. Introducing heteroporosity fixes the problems posed by diffusion constraints in micropores. Furthermore, different functional groups, acid sites, and active ions are incorporated at the zeolite surface, permitting catalytic conversion of bulkier guest molecules.(24)

1.3.4 Lewis and Bronsted Acidity

Another versatile property of zeolites is their resourceful acidity. The acidity makes it very attractive in various genres of reactions. The neutralization of negative charges in the zeolite framework is affected by protons produced by the dissociation of water molecules and the hydroxyl groups subsequently get attached to the aluminium atoms. Such protons bring about proton donor acidity or Bronsted acidity. The electron-accepting acidity or Lewis acidity is created by removing occupied water molecules via high-temperature treatment. Now the tetravalent aluminium converts into trivalent. The vacant orbital made in the aluminium can act as a Lewis acid center.(25) The schematic representation of Lewis and Bronsted acidity is depicted in Figure 1.6.

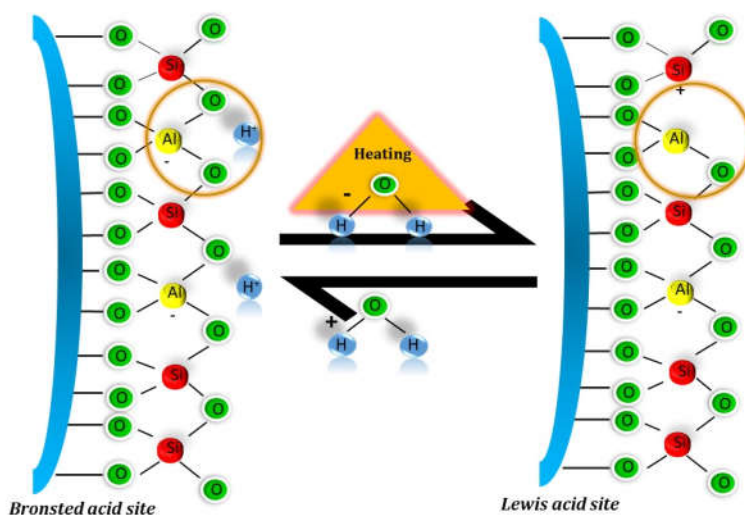


Figure 1.6. Representation of acidity of zeolites

1.3.5 Chemical and Thermal Stability

The excellent thermal stability of zeolites is, undoubtedly, one of the main factors in their selection as catalysts for high-temperature processes. Temperatures as high as 650 °C have no impact on most zeolites. The thermal stability of zeolites with a high Si/Al ratio is as high as 1000 °C.(26) Zeolites may be thermally regenerated by burning carbon deposits at 600 °C.(4) When zeolites are heated past the point of dehydration, the degree of structural order is not substantially affected; their thermal stability may be assessed by examining the stability of the geometry of the crystal lattice.(27) Zeolites are assumed to remain stable when exposed to water or water vapor in a natural setting. However, high water vapor pressure, acidic surroundings, or basic environments can entirely or partially destroy their crystalline structure.(28)

1.4 Applications of Zeolites

Zeolites exhibit distinctive features like high selectivity, efficient adsorption, and ion exchange capabilities, excellent hydrothermal stability, adjustable acidity and polarity, and low manufacturing costs, making them the most applicable materials for various industrial applications. Zeolites offer a green route for the synthesis of many materials as they are an excellent replacement for corrosive mineral acids. Such sustainable technologies are used for different applications such as removing radionuclides, producing hydrogen, post-treatment of exhaust from vehicles, converting and capturing

carbon dioxide, converting biomass, separating oil and water etc.(29) Demand for zeolites is rapidly growing in the petrochemical industries and refineries. Zeolites have efficiently replaced traditional thermal cracking methods as they result in better yields and better product quality at a smaller cost. Zeolites act as bifunctional catalysts, i.e., combining the functions of a cracking catalyst and playing the role of a hydrogenation component, leading to 100% conversion of heavy crude oil fractions. The efficiency of zeolites has also been proven for the conversion of methanol using a two-bed process into high-quality, aromatics-rich gasoline and olefins.

Large-scale acid-catalyzed organic syntheses like selective alkylation of aromatics are done in the gas phase. Compared to the conventional homogeneous catalysis approach in which AlCl_3 is used as the Friedel-Crafts catalyst, this procedure has several economic and environmental advantages like 95% heat recovery at a reaction temperature of 400 °C, little difficulty in separating and recovering the catalyst, ease of renewability, absence of corrosion-related issues, and no waste disposal concerns.(4)

Numerous forms of zeolites have been used as catalysts in reactions like hydrocracking, hydrodimerization, catalytic dewaxing, etc. The wide variety of specific catalytic applications becomes possible due to the combination of acid sites and pore size in favorable amounts. Zeolites are utilized in automobile catalytic converters to reduce nitrogen oxide (NO_x) emissions and thus it has become an

indispensable part of the DENOX process. The pharmaceutical industry also evaluates zeolite catalysts for fine chemical synthesis.(30) Zeolites are efficient substitutes for phosphates in laundry detergents, making them crucial in the detergents sector. They act as excellent soil conditioners to retain water in the soil and are also added to fertilizers to enable nutrient availability. To sum it up, zeolites play a vital role in broad areas such as catalysis, adsorption, ion exchange, environmental remediation, detergent and cleaning products, and food and agriculture sectors.

1.5 High Silica Zeolites

High silica zeolites have a Si/Al ratio of more than 3:1. The high silica concentration makes them more robust and resistant to chemical deterioration at high temperatures and in acidic environments, making them suitable for a wide range of industrial applications. They are frequently employed as catalysts in the petroleum sector for processes such as hydrocracking, isomerization, and alkylation, as well as in chemical manufacturing sectors. They can also be used for gas/liquid separation and adsorbents in air purification. High silica zeolites are adsorbent materials with high thermal stability and low hydrophilicity. FER, MFI, TUN, MWW, and BEA are examples of high silica zeolites.

1.5.1 ZSM-5

Argauer and Landolt synthesized a beneficial variety of zeolites called the ZSM-5 (Zeolite Socony Mobil-5), which Mobil Oil

Corporation patented in 1972. These zeolites were originally made available as petrochemical catalysts by Mobil Group. Its chemical formula is $\text{Na}_n\text{Al}_n\text{Si}_{96-n}\text{O}_{192.16}\text{H}_2\text{O}$ ($0 < n < 27$). The framework structure of ZSM-5 is built up of pentasil blocks (Figure 1.7).(31)

The structure is defined by the arrangement of six smaller building units (Figure 1.8 a), which then combine to form larger pentasil-like structural units (Figure 1.8 b). The configuration of these chain groups (Figure 1.8 c) results in the development of layers of tetrahedrons (Figure 1.8 d), resulting in the typical porous nature of ZSM-5 zeolites. The organization of the secondary building units produces a microporous framework consisting of straight channels interconnected by sinusoidal channels within the MFI zeolites. The straight [010] channels have elliptical apertures with 10-membered rings with 0.51 x 0.55 nm in internal diameter. The sinusoidal [100] channels have an inner dimension of 0.54 x 0.56 nm and are surrounded by a circular 10-member ring.(6,32)

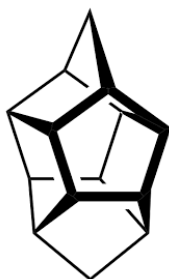


Figure 1.7. Pentasil building unit of ZSM-5

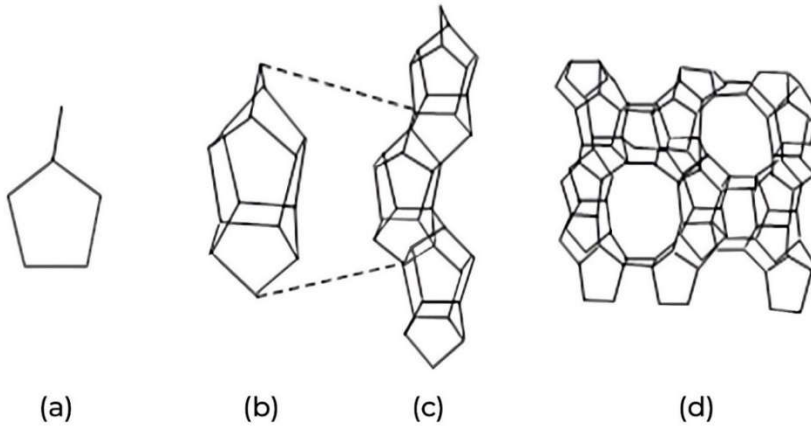


Figure 1.8. (a) Secondary building unit of ZSM-5 (b) Pentasil units (c) Tertiary units: chain type arrangement of pentasil groups (d) layers of pentasil units

1.5.2 Zeolite Beta

Wadlinger et al. were the first to synthesize zeolite beta (1967). Zeolite beta is the first high silica zeolite ($\text{Si}/\text{Al} = 10$ to 100) and the framework type in it is referred to as BEA structure. BEA structure generally refers to uniform large pored high silica zeolite with a unique interconnected network of channels and cages. The structure is synthesized using tetraethyl ammonium cations as an organic template in a gel containing alkali metals. The typical formula for zeolite beta is $\text{Na}_n [\text{Al}_n \text{Si}_{64-n} \text{O}_{128}]$, where $n = 7$.

Lohse U et al.(33) synthesized zeolite beta using tetraethyl ammonium ion (TEA^+) cation. The ion-exchange process on zeolite beta at 25°C demonstrated the ability to exchange cations into the pore system that are large enough up to the size of TEA^+ . This result

suggests that the channels in zeolite beta have at least 12 fused rings surrounding them.

An intergrowth structure of different but distinct closely related polymorphs i.e. polymorph A and polymorph B are commonly found in zeolite beta. Several stacking sequences from a single centrosymmetric layer are used to produce these polymorphs. The centrosymmetric 2-dimensional layer is formed by expanding 16 T-atoms in the plane in two directions via a 12-membered ring structure in a secondary construction unit. The top and side views are schematically represented in Figure 1.9.(34)

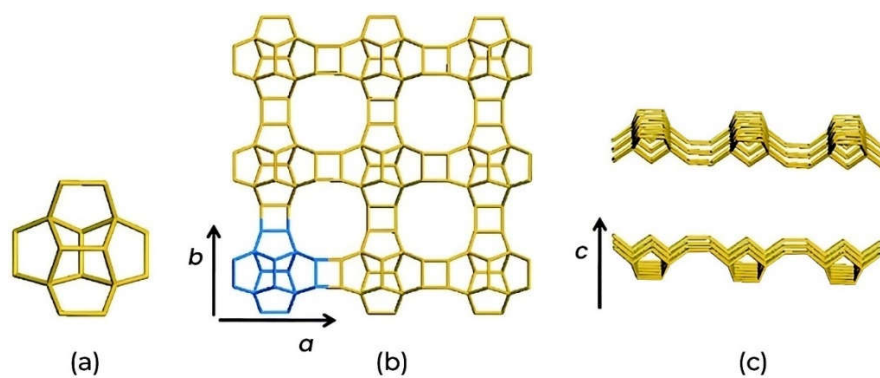


Figure 1.9. Secondary building unit (a) top view (b) and side view (c) of centrosymmetric layer of zeolite beta

The straight channels have elliptical apertures, while the sinusoidal channels have circular openings. The pore size of the consecutive channels is the only distinction between polymorphs (a) and (b). The openings of the straight channels are 6.0 x 7.3 nm in the tetragonal

system and 6.8 x 7.3 nm in the monoclinic system. The view of the zeolite beta framework along [100] is depicted in Figure 1.10.(35,36)

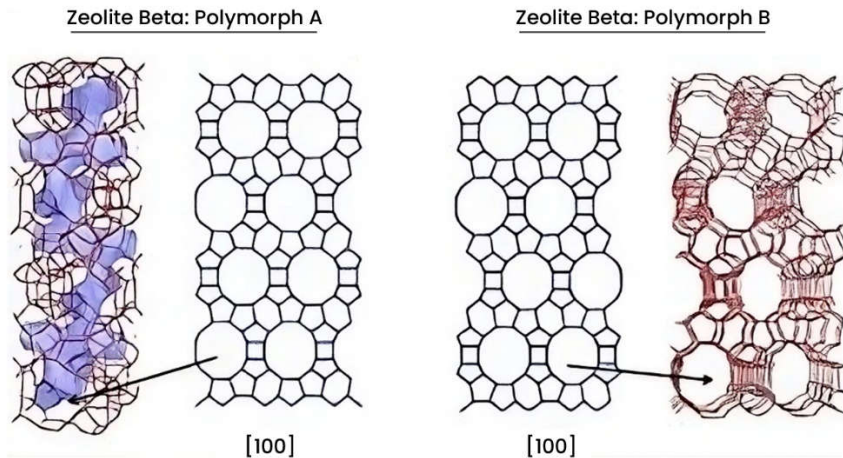


Figure 1.10. Schematic representations of the zeolite beta structure

1.6 Metal Ions in Zeolites

The capacity of zeolites to take part in ion-exchange processes is one of their key characteristics. As previously indicated, the isomorphous replacement of silicon with aluminium atoms produces negative charges on the zeolite lattice, which are typically balanced by Bronsted acidic protons as well as other exchangeable cations (Na^+ , K^+ , Mg^{2+} , and others) in the zeolite matrix channels or cages. Replacing them with transition metal ions can significantly alter the chemical characteristics of zeolites, making them energetic and effective.(37)

It is a common practice to modify zeolites with various metals to

create materials with multiple applications. Ion exchange and wet impregnation are the approaches most frequently employed to incorporate metals into zeolites. Wet impregnation is used for high silica zeolites with lower cation exchange sites. It is employed to obtain the desired metal concentrations. Small amounts of solutions containing the desired quantity of metal are typically used for the wet impregnation of zeolites. The slurry is equilibrated for even distribution of cations across the zeolite surface and subsequent solvent removal by rotary evaporation is done. Controlling the amount of metal in the zeolite is simple because no washing process is involved. Despite being widely used, according to reports, most impregnation causes more significant agglomeration of metal particles.

The cation substitution by ion exchange process is usually done by immersing zeolites in a solution that contains the target metal ions. Then the process is repeated to attain a significant degree of substitution. Then it is thoroughly washed to eliminate the excess metal salt trapped inside the pores of zeolites. The cations occupy the charge-compensating sites by coordinating with the surface oxygen as a result of high-temperature treatment. The cations are uniformly distributed through channels using this technique.(38)

1.6.1 Modification of Zeolite Beta and ZSM-5 for Refinery Applications

Zeolite beta and ZSM-5 have been modified with alkali, alkaline

earth metals, transition elements, noble metals, and their compounds to enhance the catalytic properties for petrochemical applications. The most common reactions are fluid catalytic cracking, hydrocracking, dewaxing, aliphatic alkylation, reforming, hydrogenation, aromatization, oxidation, biomass-transformation, isomerization, oligomerization, transformation of aromatics and conversion of methanol to hydrocarbons, etc.

Due to their unique chemical characteristics, such as their capacity to store and release oxygen in molecular sieves, skeletal, thermal, and hydrothermal stability, etc., metal-exchanged zeolites are also very effective catalysts or catalytic promoters. Zeolite beta was modified by Gnanapragasam S et al.(39) using La, Ce, Ga, and Zn. Transition metals in trace quantities affect the characteristics of zeolitic frameworks and trigger redox activity. However, the extreme acidity produced by the modification catalyzes side reactions. Hexane isomerization and cracking on zeolite beta modified with La_2O_3 and CeO_2 have excellent potential for isomerizing linear alkanes to branched alkanes. The prevention of coke deposition is also observed by modifying zeolites with rare earth oxides, which leads to novel, long-lasting solid catalysts.(40) Dalla Costa BO et al. (41) converted glycerol to acrolein using zeolite beta-containing lanthanum. The production of acrolein was found to be higher at lower temperatures and so was the selectivity of the catalyst. The enhanced activity of zeolite beta-containing lanthanum is attributed to the creation of new acid sites.

The incorporated cation plays a vital role in catalyzing distinct reactions. Pt and Pd on zeolite beta efficiently catalyze the hydrogenation of toluene. Here the zeolite acts as a bifunctional catalyst, i.e., the catalytic support aids in the adsorption of toluene on the acid surface and the metallic component serves as a sites for hydrogen adsorption.(42) The ring-opening of bicyclic molecules is an essential reaction in industry. Zeolite beta modification with Ru increases its Bronsted acidity and encourages isomerization and ring opening of decalin.(43) The Ru and Pt doping of zeolite beta significantly enhances the yield of diethyl ether during the catalytic dehydration of ethanol and here the catalyst acts as a chemical promoter. The presence of ideal weak acid sites leads to the higher intrinsic activity of the catalysts, resulting in increased diethyl ether yields.(44) Pd nanoparticles supported by zeolite beta showed 100% oxidation of naphthalene to carbon dioxide. In this case, the porosity of the catalyst is related to the increased activity of beta catalysts. They discovered that the capacity of the catalyst to oxidize naphthalene is correlated with its apparent surface area. It is generally known that zeolite beta has an exceptionally high exterior surface area because of the intergrowth of two polymorphs in its structure. As a result, achieving complete oxidation of naphthalene to CO₂ is possible at lower temperatures using Pd-based nanoparticles supported by zeolite beta.(45)

Copper and magnesium were incorporated into zeolite beta to enable the etherification of fluidized catalytic cracking of gasoline and it

promotes the reduction of olefin and improves ethanol conversion.(46) Aho A et al. (47) tried the upgradation of pine wood oil using iron-modified zeolite beta. Compared to non-catalytic pyrolysis, the deoxygenation processes over the modified zeolites were more pronounced. High-silica zeolite beta treated with Zn was found to be a good catalyst for the aromatization of light alkanes. The mechanism of the enhanced aromatization depends on the presence of metal sites and Bronsted acid sites available for C-H activation. The presence of metal species has a significant impact on the activation of the C-H bond by Bronsted acid sites, as shown by H/D exchange experiments of alkanes with Zn-modified zeolite beta.(48) Transformation of acetone into hydrocarbons was done by Cruz-Cabeza AJ and coworkers (49) using zeolite beta with different metal cations such as Cr, Mn, Fe, Co, Cu, Ni, Zn, Al, and Pb. New Lewis acid sites were produced while the Bronsted acidity was reduced by the ion exchange process, especially for medium- and high-strength sites. The samples that were exchanged with Co^{2+} , Ni^{2+} , and Cu^{2+} had the largest populations of Lewis sites.

Many processes have benefited from the active catalytic properties of transition metals supported on zeolite ZSM-5. The characteristics of the metals and the acidic zeolite sites affect the efficiency and selectivity of the catalyzed reactions. Platinum on zeolite is a very effective and stable catalyst for hydrocracking, hydroisomerization, and hydrocarbon reforming. Treesukol P et al. (50) explored the interaction between platinum atoms and H-ZSM-5 highlighting the

crucial function of the acid site of zeolite in the catalytic process. They identified two distinct interactions. Firstly, platinum bonds with zeolitic oxygen, prompting electron transfer from H-ZSM-5 to the platinum atom. Secondly, electron transfer from the platinum atom to the acidic proton of H-ZSM-5 resulting in electron redistribution within the platinum atom. HZSM-5, modified with cerium oxide and tungsten hydride, exhibits enhanced activity in converting methanol to hydrocarbons. Additionally, it enhances the transformation of residual fluid catalytic cracking gas into propylene and paraxylene.(51) Catalytic cracking of naphtha was attempted using Ce and Zr-loaded HZSM-5. The number of weak acid sites was shown to rise in the Zr-loaded HZSM-5, whereas the number of strong acid sites remained the same. On the other hand, in the Ce-loaded sample, the number of both strong and weak acid sites increased. The increase in acid sites was found to be prominent by the separate loading of Ce and Zr than by the simultaneous loading of both metals.(52) The adsorptive removal of thiophene from benzene is achieved using ZSM-5 zeolite loaded with Ce, La, Ag, and Ni.(53)

1.6.2 Modification of Zeolite Beta and ZSM-5 for Pharmaceutical and Chemical Applications

Zeolite beta and ZSM-5 have been altered to catalyze diverse organic processes in the chemical and pharmaceutical sectors. Adding specific elements or groups leads to notable enhancements in qualities such as reactivity, selectivity, and acidity.

Zeolite beta is employed as catalysts for the Fries rearrangement of phenyl acetate. This reaction yields hydroxyl acetophenones, a crucial pharmaceutical and fine chemical intermediary. The bivalent cations like calcium and zinc occupy the charge-compensating sites in zeolite beta, which requires only one positive charge. The resulting excess charge is indirectly compensated through electrostatic interaction with the surrounding bivalent cations leading to the formation of bridged cation-oxygen species.(54) Yadav MK et al. (55) used rare earth and transition metal ions, including lanthanum, silver, cerium, cobalt, iron, manganese, copper, nickel, strontium and zinc-modified zeolite beta to study the hydration and acetylation of limonene and α -pinene. This study demonstrates that the increased Bronsted acidity catalyzed the hydration and acetylation reactions. Thakur R et al.(56) investigated the feasibility of transalkylation of toluene over cerium-modified zeolite beta kinetically. The exchange of monovalent cations for polyvalent cations results in the creation of concentrated acidic sites rather than distributed acidic sites, which enhances the activity of modified zeolite.

Kareem M et al. (57) used ion-exchanged HZSM-5 in the disproportionation reaction of toluene to produce benzene and p-xylene. H^+ ions of ZSM-5 are exchanged with Ni, Cr, Mg, Bi, and Zn ions during the ion exchange process. The Ni-exchanged catalyst exhibited maximum conversion and selectivity to p-xylene when compared to Mg and Cr-exchanged ZSM-5. The poor performance of chromium-exchanged zeolite is ascribed to the superior oxidizing

ability of Cr, which oxidized the coke built up on the surface of the catalyst and reduced the size of the pore mouth responsible for selective diffusion. However, the utilization of Cr-ZSM-5 as a catalyst can facilitate the oxidation of alcohols and benzylic methylene groups using t-butyl hydroperoxide. Several secondary benzylic alcohols may be converted using extremely little Cr-ZSM-5 and aqueous t-butyl hydroperoxide in toluene. Chromium partially leaches out while heating Cr-ZSM-5 in toluene with t-butyl hydroperoxide. The leached chromium is re-adsorbed onto the zeolite when the system is cooled to room temperature.(58) Co^{2+} exchanged beta and ZSM-5 zeolites have been used to epoxidate styrene and α -pinene in air.(59) Formylation of amines is a valuable process in synthetic organic chemistry because formamides are helpful intermediates in synthesizing several pharmaceutically essential molecules. According to Tajbakhsh M et al., (60) copper oxide nanoparticles supported on HZSM-5 zeolite effectively synthesize formamides by increasing its Lewis acidity.

The Strecker synthesis is a method for producing amino nitriles, which are adaptable intermediates for the hydrolysis of nitriles to produce amino acids. The strong and weak acid sites decrease in quantity and increase in strength by ion exchanging with tin. Tin ions by their polarising and inductive effects weaken the OH bonds of bridging hydroxyl groups and hence increase the acidity.(61) Niobium oxide-modified zeolite beta samples improve the alkylating capacity of resorcinol.(62)

Zeolite beta and ZSM-5 treated with Cu (I) or Sc (III) are effective

catalysts for cycloadditions, multicomponent processes, and Mukaiyama-type aldolization. The incorporation of scandium initiates intense Lewis acidity that can stimulate various organic processes.(63)

1.6.3 Modification of Zeolite Beta and ZSM-5 for Pollution Abatement

Selective Catalytic Reduction (SCR) and breakdown of NO_x (DENOX) are the two inevitable processes taking place in an automobile to protect the environment. Several attempts have been made for the removal of NO_x and SO_x using many metals modified by ZSM-5 and zeolite beta. Iron-modified ZSM-5 and beta are well-known efficient catalysts for N₂O breakdown and the SCR of NO_x by ammonia. Only a tiny portion of cationic sites in beta-zeolite are occupied by active Fe³⁺. Hosting Cu²⁺ in the vacant cationic sites enhances the reducibility of iron in the Cu-Fe/ZSM-5 catalyst.(64,65) Additionally, Fe-ZSM-5, modified by noble metals (Pt, Rh, Co, and Pd), are found to be effective catalysts for Selective Catalytic Oxidation (SCO) of ammonia with O₂ to generate NO, N₂O, and N₂, and the oxides are subsequently reduced to N₂.(66–68)

Zeolite beta, supported by copper, iron, and cerium, is one of the most effective catalysts for the urea/NH₃-(SCR) process. The type of copper species in the catalyst is responsible for this superior activity. Copper can be found in the matrix as CuO clusters or as Cu (II) species. The Cu (II) ions support strong NO_x conversion to NO at

high temperatures and CuO clusters are responsible for the reduction of NO at low temperatures.(69)

Gao F et al. (70) studied the catalytic activity of aged zeolite Fe-beta for fast NH₃-SCR and oxidation of NO. Another study on Ag/Cu modified ZSM-5 revealed that NO_x decomposition by the Ag(I)/ZSM-5 catalyst happens more quickly than that by the Cu(I)/ZSM-5 catalyst. The remarkable chemical stability of silver ions and their efficient interaction with NO in its excited electronic state are responsible for this observation.(71) Another comparison of the activities of Cu/La exchanged ZSM-5 shows that Cu/ZSM-5 matrix exhibits more activity for SCR of NO than La/ZSM-5 and HZSM-5.(72,73)

Odorous emissions may significantly impact the quality of life. As a result, treating gaseous emissions is a crucial step in safeguarding the environment and the general population. Szyrkowska and colleagues (74) investigated the oxidation of the pungent nitrogen-containing chemical, trimethylamine, using the zeolites ZSM-5 and beta, modified with Cu. It was demonstrated that Cu/ZSM-5 has excellent oxidizing power.

1.7 Nanocrystalline Zeolites

Nanocrystalline zeolites are materials characterized by crystal dimensions smaller than 100 nm. Reducing the crystal size diminishes the diffusion path lengths and increases the ratio of the external surface area to the total surface area of the zeolite. This

makes the active sites on the external surface more accessible compared to those inside the zeolite pore network.(75) Particle size reduction shortens diffusion paths, increases catalyst activity, and prolongs catalyst life.

1.7.1 Synthesis of Nanocrystalline Zeolites

Nanoscale zeolites are synthesized by a hydrothermal method similar to conventional micron-sized crystals. Synthesis occurs within sealed containers without the introduction of additional reactants. The final crystal size is regulated by the number of nuclei in the system, emphasizing the critical role of nucleation. Abundant nucleation results in tiny crystals, whereas a scarcity of viable nuclei leads to the formation of larger crystals.(76) The process of nucleation has been thoroughly investigated by the scientific community. According to Larsen SC (75), the lower synthesis temperatures promote nucleation over crystal growth. Apart from hydrothermal synthesis, supercritical fluid-assisted crystallization can also be used for synthesizing nanocrystalline zeolite beta, which has several technological benefits for chemical engineering and separation technology.(77) To synthesize nanocrystalline zeolites, various techniques involving the use of different structure directing agents, different sources of silica viz. silica gel, cellulose, dextrose, rice husk, etc. may be used.(46,78–85)

1.7.2 Modification of Nanocrystalline Beta and ZSM-5

If the crystal size is decreased to nanoscale, it may drastically change the physicochemical properties of zeolites. Exchanging the acidic protons within the channels of nanocrystalline ZSM-5 zeolites with diverse metal cations has the potential to redistribute the relative count of Bronsted and Lewis acid sites on the catalyst. Additionally, this process can lead to modifications in the effective pore characteristics.⁽⁸⁶⁾ Several factors such as textural characteristics, acid strength, and metal concentration determine the efficiency of the metal-modified nanocrystalline catalysts. It is crucial to locate the active site and understand the reaction mechanism in the metal-containing catalysts since doing so might hasten the development of more effective heterogeneous catalysts for this procedure. The catalytic qualities of the metal-modified catalysts will rely on some of these parameters, including the type of metal ion, coordination number, oxidation state, location on the support, and method of production. Metal-modified nanocrystalline zeolites can take up the dual role of a catalyst and also of an additive. One of the advantages of using nano-sized zeolite catalysts is the selectivity imparted. Nanocrystalline zeolite beta with Mo-Ni and W-Ni were employed in the hydrodesulfurization and hydrodearomatization processes in the petroleum refinery. These catalyzed processes yielded greater amounts of the desirable liquids while considerably reducing the undesirable gaseous products. This can be partly explained through the short diffusion route and the higher concentration of active sites

on the outside, which serve to inhibit secondary cracking of the product molecules. Similarly, the superior external surface area of the nanocrystalline HZSM-5 zeolite containing Mo and Ni resulted in better activity in the catalytic conversion of rapeseed oil.(87,88)

Rather than employing metal as extraframework cations in zeolite beta, researchers have dealuminated zeolites to incorporate tetrahedrally coordinated metal as Lewis acid catalysts for various redox reactions. Chang CC and colleagues (89) introduced a facile seeding technique to produce beta nanocrystals containing tin by effectively reducing the crystallization time. The resultant zeolite beta, infused with tin, demonstrates significant catalytic activity in facilitating the isomerization reactions of pentose, triose, and hexose sugars.

The addition of rare earth elements and transition metals into nanocrystalline ZSM-5 introduces supplementary functionalities, which has garnered growing interest in research.

The incorporation of cerium into ZSM-5 could improve thermal stability, potentially at the expense of reducing the strength of acid sites. The decrease might be due to dealumination in the ZSM-5 structure and the dehydroxylation of Bronsted sites caused by elevated calcination temperatures. Additionally, the leaching of strong acidic sites could reduce coke formation and enhance the overall stability of the catalyst.(90) Another study shows that CeO₂ nanoparticles applied onto high surface area nanocrystalline ZSM-5

are effective for the electrochemical oxidation of methanol. The electrocatalytic activity is attributed to the interconversion of the oxidation state of cerium induced by the application of low potential.(91) Incorporation of iron into nanocrystalline ZSM-5 results in the coexistence of various Fe species within the zeolite structure, including isolated Fe^{3+} , small oligomeric Fe_xO_y clusters, and large Fe_2O_3 particles. This leads to zeolites with smaller crystallites, wider pore sizes, and shorter diffusion path lengths. Moreover, the acid strength is enhanced through the formation of new acid sites. These factors collectively contribute to the improved catalytic activity observed in the conversion of methanol to gasoline.(92) Ion exchange of silver with nanocrystalline ZSM-5 is used as a bio-implant material by coating with hydroxyapatite. The augmented external surface area of silver exchanged nanocrystalline ZSM-5, along with its abundance of surface silanol groups, contributes to improved interaction with hydroxyapatite. Moreover, the heterogeneous distribution of silver ions promotes the heterogeneous growth of hydroxyapatite within the nanocrystalline ZSM-5 matrix.(93)

By employing wetness impregnation, metallic species are introduced into nanocrystalline ZSM-5, ensuring a favorable dispersion of metals. This dispersion is facilitated by the ample external surface area provided by the nanocrystalline zeolitic support. The introduction of zinc into nanocrystalline ZSM-5 induces notable alterations in its textural and acidic characteristics. These changes in

acidity result from the emergence of new acid sites.(94) Heteroatomic nanocrystalline ZSM-5 has been synthesized by integrating metals like Ce and La into the framework sites of zeolites, specifically to the tetrahedrally coordinated Si or Al sites. The multiple pH-adjusting synthesis yields hydrothermally incorporated Ce/La ZSM-5. These metals can exist in the form of hydroxides under basic conditions, thus facilitating their incorporation into the zeolite framework. The synthesized Ce/La-ZSM-5, according to observations, have an unusual microsphere morphology made up of several cubic prism-shaped nanocrystallites.(95)

1.8 Hierarchical Zeolites

Once zeolites were limited to the concept of microporous aluminosilicates, but over time they have evolved significantly through extensive modifications. Zeolites with at least one additional level of porosity, in addition to the intrinsic micropore system that characterizes zeolites, are referred to as "hierarchical zeolites." Different strategies for adjusting heteroporosity have been conceptualized as a result of the great demand for hierarchically porous zeolites in a variety of applications.(96) The techniques for synthesizing hierarchical zeolites are broadly classified as destructive and constructive methods (Figure 1.11).

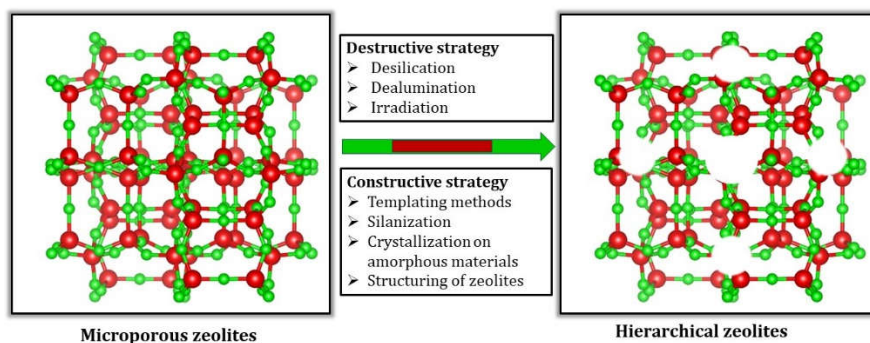


Figure 1.11. The different methods for the synthesis of hierarchical zeolites

The destructive method is a widely used top-down approach, involving the dissolution of framework atoms and the creation of mesopores by breaking down pre-existing microporous zeolites. The primary techniques employed are desilication and dealumination. Desilication typically involves the use of sodium hydroxide in the presence of quaternary ammonium cations and ammonium fluoride to remove silicon atoms. Dealumination, on the other hand, utilizes compounds like ammonium hexafluorosilicate, oxalic acid, and silicon tetrachloride for the removal of aluminum atoms. Despite their ease of use in industry, both dealumination and desilication methods have certain drawbacks, such as the formation of irregular mesopores through partial dissolution of the framework and entails substantial loss of zeolite material. Another destructive method is through irradiation, employing high-energy heavy ^{238}U ion beams, followed by treatment with HF to induce amorphization in zeolites, resulting in the formation of a secondary porous structure.

Constructive methods focused on synthesizing hierarchical zeolites are some of the most innovative techniques in this field. Researchers have investigated templating methods aimed at generating secondary porous structures. The term templating is described as the use of macro or meso pore-generating substances to direct the formation of the additional porosity desired. Such exo templates are mixed with micropore directing template and silica-alumina precursor during the crystallization of zeolites. Hard templates such as caramel, beach wood, starch, carbon materials, and various polymers have been employed to introduce secondary porosity. Additionally, soft templates like cationic polymers and ionic liquids have proven to be effective in producing hierarchical zeolites.(97–100)

The investigation into the development of hierarchical porosity in nanocrystalline zeolites is of significant importance. Templating methods have been effectively integrated, with particular emphasis on the design of nanocrystalline hierarchical zeolites. In the presence of a surfactant such as cetyltrimethylammonium bromide (CTAB), microporous zeolites are subjected to acid and basic treatments, which enable the controlled introduction of intracrystalline mesoporosity in zeolite beta. However, this approach initiates desilication and dealumination on the external surface and grain boundaries of ZSM-5 and zeolite beta.(101) Zeolite beta with a hierarchical structure was synthesized using silanized protozeolitic nanounits through the application of phenylaminopropyl-trimethoxysilane and CTAB. Examination of this material unveiled

a reduction of zeolitic crystallinity, yet it exhibited a significant degree of mesoporosity.(102) The facile approach for synthesizing nanocrystalline hierarchical silicalite-1 and beta, utilizing styrene butadiene rubber without the need for an aging process, yielded a high-quality long-range macropore arrangement. The existence of macropores within the hierarchical zeolite results in enhanced conversion rates during the acylation process of anisole.(103,104) Hydrothermal synthesis of nanocrystalline hierarchical ZSM-5 in the presence of polydiallyldimethylammonium chloride resulted in pores of larger dimensions while preserving the crystal size and crystallinity to a considerable extent. The synthesized material demonstrated effectiveness in the selective alkylation of phenol with cyclohexene.(105) The utilization of Triton X-100 as a mesopore template in the synthesis of hierarchical ZSM-5 yields disc-like zeolite nanostructures with added mesoporosity while preserving the microporosity. The resulting ZSM-5 showed excellent activity in the selective oxidation of benzyl alcohol.(106)

1.9 Defects

Defects that are prevalent in solid materials can be classified into four types: point defects, linear defects, two-dimensional defects, and volume defects. Point defects such as vacancies and impurities, enhance internal energy while decreasing structural stability. Linear defects, such as dislocations, weaken crystals and disrupt bonds. Volume defects, such as precipitates, inclusions, fractures, voids, and pores, impact solid characteristics during production, whereas

two-dimensional defects affect mechanical strength and chemical reactivity.

Defect sites have an essential role in determining the stability and performance of high silica zeolites. A defect is a change in the crystalline structure that disrupts the ideal symmetry expected from the periodic arrangement of TO_4 building units. Networks containing only SiO_4 units are neutral networks whereas, the presence of Al^{3+} in a Si^{4+} oxide (O^{2-}) network provides a negative charge on the framework that has to be neutralized by an extra-framework positive charge. When the extra-framework positive charge, i.e. a proton connected to oxygen in the Si-O-Al bond, becoming Si-O(H)-Al, leads to the production of Bronsted acid sites, also referred to as bridging hydroxyls. such defects initiate the origin of remarkable properties.(107,108)

Silanols (Si-OH) are defects in the internal or exterior structure of zeolites. While external silanols are necessary to satisfy the valency of oxygen atoms after crystal formation ceases, internal silanols are often the result of unbalanced charges in the zeolitic framework. These silanols have a lower acid strength than the Bronsted acid sites.

Isolated silanols are frequently found near crystal terminations. Other defects caused by the absence of one or more T-O-T bonds include geminal, vicinal, bridging silanols, and clusters. Their configurations can also change somewhat due to clustering, as

shown in silanol nests generated by a vacancy caused by a missing T atom. Defects provide an alternate method for compensating for a charge imbalance in the zeolite structure. They are produced by (i) a variety of synthetic processes, the kind and quality of the reagents, and (ii) post-synthesis treatments applied to the zeolite.

Typically, zeolites are synthesized at high pH utilizing hydroxide ions as mineralizing agents. However, it is widely known that this causes defects in the zeolites. Conversely, the production of zeolites may be performed at near-neutral pH utilizing fluoride ions as mineralizing agents. Defects are not observed in this situation. Defects also result from the dissolution of zeolite crystals. The Si/Al ratio, temperature, and leaching period play essential roles in crystal dissolution in zeolites. The presence of aluminium in the framework reduces crystal dissolution by providing a negative charge. This charge can shield aluminium-rich materials from hydroxide ion attack. As a result, zeolites with low Si/Al ratios are generally well protected from defects due to dissolution. The production of soluble ionic species also increases leaching at high pH levels. Furthermore, defects in catalysts can occur during catalytic processes. It is well known that zeolite framework defect locations are prone to retaining coke precursors. As a result, defects are frequently seen as degrading the fundamental zeolite qualities. This results in the destruction of active sites and the cessation of activity.

The research works associated with the generation and healing of defects are reviewed below.

Prodinger S et al. (109) investigated the effects of treating a silylating chemical, trimethylchlorosilane, with BEA zeolites containing well-defined silanol nest concentrations to selectively eliminate silanol defects. The defect sites in the Ga/ZSM-5 were annealed by ammonium hexafluorosilicate treatment, indicating that mesopore formation and reducing defects in zeolites are highly beneficial for delaying catalyst deactivation.(110) Qin Z et al. (111) used oxalic acid and ammonium fluoride to create point defects in mordenite zeolite crystals. It is discovered that inherent defects cause the extraction of misoriented nanodomains, but oxalic acid-induced defects create tiny irregular mesopores. The resulting hierarchical zeolite has significantly increased mesopore volume, the spatial distribution of mesopores, and excellent accessibility to micropore acid sites. Grosskreuz I et al.(112) extensively studied defect formation and curing by changing the synthesis parameters and starting materials. Starting materials containing fluoride do not produce any defects in MFI zeolites, whereas, those containing boron produce MFI zeolites with incurable silanol defects since the deboronation creates silanol defects by removing tetrahedral atoms. Since high silica zeolites are being increasingly used in membranes for separation processes, silanol defects inside MFI channels significantly impact the permeability and diffusion of water. This is because adsorbed water and silanol defects interact strongly. Consequently, catalytic processes and separation techniques are affected by the research on silanol defects.(113)

1.10 Friedel-Crafts Acylation

Friedel-Crafts acylation is a much acclaimed and frequently employed technique for synthesizing aromatic ketones which are used as essential building blocks in flavor, pharmaceutical, paint, and agrochemical industries. This method involves introducing acyl groups into aromatic compounds, leading to the production of aromatic ketones. Lewis acids (such as iron trichloride, zinc chloride, titanium tetrachloride, tin tetrachloride, and aluminium trichloride) or powerful protic acids such as sulfuric acid and hydrofluoric acid are typically used to catalyze electrophilic acylation. While using metal halides, the hydrolysis of the complex generated between the ketone produced and the metal halide demands more catalysts than stoichiometric amounts, leading to catalyst loss and the creation of large quantities of corrosive waste. The advantage of using heterogeneous catalysts lies in the fact that they can be easily retrieved and reused, causing no corrosion or unwanted by-products. Materials like zeolites, metal oxides, and heteropolyacids are effective catalysts for Friedel–Crafts acylation. Zeolite catalysts offer advantages over traditional ones in acylation processes.(114) Here is a list of a few of these benefits:

- Zeolites possess a wide range of clearly defined crystalline structures that vary in dimensions, shape, and channel diameter. This offers high shape selectivity at various levels such as reactant, product, and transition state selectivity.

- The enhanced surface area facilitates easy access for more number of reactant molecules to the active sites.
- Presence of Lewis and Bronsted acidity.
- Ability to tailor the strength and concentration of acid sites (Lewis and Bronsted).
- Maneuvering the catalytic activity by cation exchange with suitable metals.

1.10.1 Acylation of Toluene

Acylation of toluene is a significant chemical reaction that includes adding an acyl group to the benzene ring of toluene. One of the most common applications of acylation of toluene is the synthesis of benzyl acetate, a common industrial solvent. Benzyl acetate is widely used in the food and beverage industries as a flavoring agent and as a fragrance in the perfume industry. 4-methyl acetophenone holds significant importance in the flavor and fragrance sector. It contributes to creating the lilac scent in acacia soap and is crucial in numerous food flavorings, enhancing the taste sensation. Furthermore, it reacts with morpholine in the presence of sulfur to yield 4-(p-tolyl-thioacetyl)-morpholine, an important initiator used in polymer manufacturing.

Zeolites have demonstrated their unique catalyzing property for acylating less-activated aromatic rings like toluene.(115–117) The Friedel-Crafts acylation reaction mechanism involves either free

acylium ions or an adduct of the catalyst and acylating agent, depending on the reaction conditions.(118) Das D and Cheng S(119) described the use of heterogeneous zeolite-catalyzed acylation, in which an adduct is formed when an acylating agent interacts with the surface acid sites. The first acylation of an aromatic substrate, toluene, over CeNaY zeolite with straight-chain carboxylic acids was reported by Chiche et al. (120). The conditions were extremely harsh, like heating in an autoclave at 150 °C for two days. However, using carboxylic acid as an acylating agent is not beneficial for acylation since it would leach out the metal atom in the framework of the catalyst.(121) Similar to this, while having a high potential acylating agent activity, acetyl chloride is rarely used due to the catalytic activity being reduced by hydrogen chloride emission during the acylation reaction.(122) When less reactive acylating agents, are utilized, the efficiency of the reaction is lowered, especially for low-activated aromatic rings, like toluene. However, the quick catalyst deterioration caused by "coke" deposition within the micropores severely restricts the application of these materials in industrial operations.

1.10.2 Acylation of 2-methoxynaphthalene (2-MON)

Acetylation of 2-MON is particularly interesting since it is used in the pharmaceutical industry. It occurs mainly in 1-position and 6-position, resulting in 1AC-2MON and 6AC-2MON. The effort to selectively acylate 2-MON holds promise in producing 1-acetyl-2-methoxynaphthalene (1AC-2MON) a crucial intermediate with

particular relevance in phenylation reactions. Beyond its involvement in phenylation, this intermediate holds potential for diverse applications in organic compound synthesis, emphasizing its significance in organic chemistry. Additionally, research shed light on the formation of 6-acetyl-2-methoxynaphthalene (6AC-2MON), highlighting its critical role as a precursor in the synthesis pathway of naproxen, a well-established anti-inflammatory medication.

Due to environmental concerns, substituting traditional homogeneous catalysts with solid acid catalysts is imperative in the industrial sector. Zeolites have been proven to be viable alternatives to liquid acids in various cases due to their shape-selective characteristics and strong renewability. However, distinct product distributions were achieved over acidic zeolites depending on the type of framework. The shape-selective properties of zeolites were used to explain these differences. Researchers continuously have been focusing on the usage of zeolites for the Friedel–Crafts acylation of 2-MON over zeolite catalysts.(119,123–126) Many researchers have faced severe pore size constraints while using zeolites as a catalyst for acylation. It has been discovered that industrially significant processes like acylation over hierarchical zeolites result in excellent catalytic activity and less catalyst degradation.

1.11 Dielectric Study of Zeolites

A dielectric substance is an electrical insulator that can get polarized in an applied electric field. The dielectric material prevents the flow

of electric charges when an electric field is applied to it. Instead, it aligns its internal electric dipoles (pairs of opposite charges) in the direction of the field. This alignment decreases the overall electric field within the dielectric material while increasing the electrical capacitance.

The complex permittivity (ϵ_r^*) is the primary factor influencing dielectric properties, which characterizes how a material responds to an electromagnetic field. The complex permittivity, also known as complex relative permittivity, is mathematically represented in equation 1.1.

$$\epsilon_r^* = \epsilon_r' - j \times \epsilon_r'' \quad (1.1)$$

In the above equation, $j = -1$. Here ϵ_r' denotes the fundamental part referred to as the dielectric constant or dielectric permittivity. This parameter signifies the ability of a material to store an electric field. On the other hand, ϵ_r'' represents the imaginary part, known as the loss factor. The loss factor is a measure of the energy dissipated when exposed to an external electric field.(127)

The permittivity (ϵ_r') is the primary parameter for dielectric studies (Equation 1.2) and it specifies the behavior of materials when subjected to an electromagnetic field.

$$\epsilon_r' = \frac{C_p d}{\epsilon_0 A} \quad (1.2)$$

ϵ_0 is vacuum permittivity, d represents the thickness of the sample material, A is the electrode area, and C_p represents the capacitance.(128,129)

Equation 1.3 can be used to obtain the static conductivity (DC) at low frequencies from the AC conductivity measurements.

$$\sigma_{AC}(\omega) = \omega\epsilon_0\epsilon''(\omega) = \sigma_{DC} + K\omega^n \quad (1.3)$$

Conductivity (σ) measures the ability of a material to conduct electric current. ω indicates the angular frequency. The parameter K represents an empirical value, while n represents the high-frequency slope of the AC conductivity, which ranges from 0 to 1.

An essential property of a dielectric substance is its ability to be polarized in an electrostatic field while dissipating minimum energy in the form of heat. The lower the dielectric loss of a material, the more influential the dielectric material is. The energy dissipated can be quantified as $\tan \delta$, the ratio between the loss factor (imaginary part) and the dielectric constant (real part) and it is given by equation 1.4:

$$\tan \delta = \frac{\epsilon_r''}{\epsilon_r'} = \frac{1}{RCp\omega} \quad (1.4)$$

R represents the resistance.

Impedance is the resistance offered by the matrix to the electric flow, which considers the phase variations between the input voltage and the output current. Impedance, represented by the symbol Z^* , which

accounts for the frequency-dependent electrical resistance of the system, containing Z' and Z'' as in equation 1.5.(130,131)

$$Z^*(\omega) = Z'(\omega) + jZ''(\omega) \quad (1.5)$$

Impedance spectroscopy is an efficient tool to investigate the electrical properties of materials that are influenced by dopant, composition, distribution of dopant, and its texture.

The complex electric modulus is a useful and crucial quantity for examining the relaxation mechanism and the electric transport phenomenon in materials. Complex electric modulus M^* is defined as the inverse of the complex relative permittivity ϵ_r^* given in equation 1.6.

$$M^* = \frac{1}{\epsilon_r^*} = M' + jM'' = j\omega C_0 Z^* \quad (1.6)$$

where M' represents real part and M'' represents imaginary part. C_0 is the vacuum capacitance. Examining the imaginary component of the electric modulus often yields clearer insights into charge transport within the material. Analyzing its frequency and temperature dependence facilitates a more precise and straightforward inference of polarization processes.(132)

Broadband dielectric spectroscopy methods can provide fresh and essential knowledge on the translation and reorientation motion of molecules in various amorphous, crystalline, and liquid crystal

systems, which ultimately explains the behavior of zeolite as a dielectric. Here is a review of some of the earlier works.

Deshpande and Bhaskar (133) investigated the dielectric characteristics of ZSM-5 and found that these characteristics are crucial in defining the nature of zeolite. Dielectric spectra of Heulandite zeolite reveal two loss peaks (two relaxations), which shifted to a higher frequency as the temperature increased, showing that the two relaxations are thermally stimulated processes. The studies revealed that the presence of different molecular and ionic species significantly impacts their ionic conductivity and several dielectric relaxation events.(134) Dielectric studies can be used to study the interaction of the adsorbed gas molecules with the cations that are non-covalently bonded to the zeolite lattice. Low-frequency and high-frequency impedance studies in H-form zeolites examine protons' translational and local mobility. Adsorbed gas molecules can bring about changes in the results of electrical conductivity thereby it can be used as probes for sensors.(135) Zhou W (136) examined the response of NaA zeolite to various thermal pretreatments by observing its dielectric response. The crystal structure transition and the acceptable structural evolution of zeolite are identified by fitting and calculating the dielectric characteristics of zeolite with an appropriate model. Dielectric studies can be used for sensing the change in thermal aging resistance of nanocomposites. The dielectric strength test discovered that nano doping of zeolites with low-density polyethylene could dramatically

improve the breakdown field strength and stability of both DC and AC indicating higher resistance to thermal aging.(137) The dielectric behaviour of zeolite clinoptilolite is significantly altered by adding silver iodide to it, and the capacity value of the silver-modified zeolite is abnormally high with increased sample conductivity.(138,139) Lowered charge compensating cations are responsible for the decreased dielectric constant for high silica zeolite at room temperature. When the temperature is high, intensifying cationic motions will improve the dielectric behaviour.(140) The dielectric behavior of zeolite such as Na-Y, Na-X, and Ca-A with frequency for a variety of humidity levels and at a variety of temperatures was reported by Haidar AR and Jonscher AK.(141) Some ions are liberated to participate in the conduction process when water molecules interact with the cations of the zeolite structure.

1.12 Existing Gaps

According to the literature review presented in the preceding sections, research on the synthesis and catalytic activity of metal-modified zeolites and hierarchical zeolites is of great interest in both the academic and industrial sectors. The reason for extensive research in this field is due to the huge demand for environment-friendly and highly active catalysts for organic reactions such as Friedel-Crafts acylation. The purpose of the synthesis and characterization of hierarchical zeolites is to increase pore characteristics while preserving crystallinity and other intrinsic

qualities as such. The current thesis focuses on the synthesis, characterization, and evaluation of metal-modified nanocrystalline and hierarchical zeolites ZSM-5 and beta, with specific objectives to overcome the following existing gaps:

- No comparative study has been reported on the characterization of nanocrystalline ZSM-5 and zeolite beta modified with transition and rare earth elements.
- Studies have not yet been done till date to heal the defects in hierarchical zeolite ZSM-5 by utilizing Polymethylmethacrylate (PMMA) as a template for imparting mesoporosity.
- Till date, hierarchical zeolites have not been synthesized by introducing the exotemplate PMMA after the initiation of the crystallization process, aiming to efficiently customize hierarchical porosity.
- Friedel-Crafts acylation in the presence of zeolites has been extensively researched. However, there have been only a few publications on the catalytic activity of metal-modified nanocrystalline ZSM-5 and zeolite beta.
- To date, no research has been published on the acetylation of toluene in the presence of metal-modified nanocrystalline zeolites without the use of a solvent and requiring the least experimental conditions.

- To date, no research has been published on the selective acetylation of 2-MON in the presence of hierarchical zeolites at low temperatures without using a solvent.
- An extensive literature survey about zeolites revealed that no detailed studies have been conducted on the dielectric, impedance, and modulus properties of zeolites doped with cerium ions at different temperatures.

1.13 Objectives

The following are the primary goals of the current work

- To synthesize Ce, La, Nd, Fe, Cu, and Zn-modified nanocrystalline ZSM-5 and zeolite beta
- To determine the crystallinity, morphology, composition, surface area, pore size distribution, and acidity of these catalysts.
- To adopt a novel synthetic pathway to hierarchical ZSM-5 with fewer defects.
- To fabricate hierarchical zeolites through a novel route by introducing PMMA (secondary template) into the reaction mixture after the initiation of crystallization.
- To determine the crystallinity, morphology, composition, surface area, and pore size distribution of these hierarchical zeolites.

- To assess the catalytic activity of metal-modified nanocrystalline zeolites for acetylation of toluene.
- To determine the catalytic activity of nanocrystalline hierarchical zeolites in the acetylation of 2-MON.
- To study the dielectric properties of zeolite beta incorporated with cerium ions.

References

1. Zimmermann NER, Haranczyk M. History and Utility of Zeolite Framework-Type Discovery from a Data-Science Perspective. *Cryst Growth Des.* 2016;16(6):3043–8. Available from: <https://doi.org/10.1021/acs.cgd.6b00272>
2. Chester Arthur W, Derouane EG. Zeolite Characterization and Catalysis: a tutorial. Dordrecht : Springer;Vol. 2010, Available from: <http://dx.doi.org/10.1007/978-1-4020-9678-5>
3. Weitkamp J, Puppe L. (Eds.). *Catalysis and Zeolites*. Springer-Verlag Berlin. 1999.
4. Hagen. J. *Industrial catalysis: a practical approach*. Vol. 21, WILEY-VCH, Germany. 2007. 520 p.
5. Moshoeshe M, Silas Nadiye-Tabbiruka M, Obuseng V. A Review of the Chemistry, Structure, Properties and Applications of Zeolites. *Am J Mater Sci [Internet]*. 2017;2017(5):196–221. Available from: <http://journal.sapub.org/materials>
6. Baerlocher C, Lynne B, McCusker, Olson DH. *Atlas of Zeolite Framework Types* (2007, Elsevier Science). Available from <https://doi.org/10.1016/B978-0-444-53064-6.X5186-X>
7. Vinaches P, Bernardo-Gusmão K, Pergher SBC. An introduction to zeolite synthesis using imidazolium-based cations as organic structure-directing agents. *Molecules*. 2017;22(8). Available from: <https://doi.org/10.3390/molecules22081307>
8. Cooper ER, Andrews CD, Wheatley PS, Webb PB, Wormald P, Morris RE. Ionic liquids and eutectic mixtures as solvent and template in synthesis of zeolite analogues. *Nature*. 2004;430(7003):1012–6. Available from: <https://doi.org/10.1038/nature02860>
9. Belviso C, Cavalcante F, Niceforo G, Lettino A. Sodalite, faujasite and A-type zeolite from 2:1dioctahedral and 2:1:1 trioctahedral clay minerals. A singular review of synthesis methods through laboratory trials at a low incubation temperature. *Powder Technol [Internet]*. 2017;320:483–97. Available from: <http://dx.doi.org/10.1016/j.powtec.2017.07.039>

10. Yoldi M, Korili SA, Gil A. Zeolite synthesis from industrial wastes. *Microporous Mesoporous Mater.* 2019;287:183-191. Available from: <https://doi.org/10.1016/j.micromeso.2019.06.009>
11. Andac O, Tatlier M, Sirkecioğlu A, Ece I, Erdem-Şenatalar A. Effects of ultrasound on zeolite A synthesis. *Microporous Mesoporous Mater.* 2005;79(1-3):225-33.
12. Pal P, Das JK, Das N, Bandyopadhyay S. Synthesis of NaP zeolite at room temperature and short crystallization time by sonochemical method. *Ultrason Sonochem* [Internet]. 2013;20(1):314-21. Available from: <http://dx.doi.org/10.1016/j.ultsonch.2012.07.012>
13. Boels L, Wagterveld RM, Mayer MJ, Witkamp GJ. Seeded calcite sonocrystallization. *J Cryst Growth* [Internet]. 2010;312(7):961-6. Available from: <http://dx.doi.org/10.1016/j.jcrysgro.2010.01.016>
14. Li Y, Yang W. Microwave synthesis of zeolite membranes: A review. *J Memb Sci.* 2008;316(1-2):3-17.
15. Rao KJ, B. V. MG, Ramakrishnan PA. Synthesis of Inorganic Solids Using Microwaves. *Chem. Mater.* 1999;11:882-95. Available from: <http://dx.doi.org/10.1021/cm9803859>
16. Conner WC, Tompsett G, Lee KH, Yngvesson KS. Microwave synthesis of zeolites: 1. Reactor engineering. *J Phys Chem B.* 2004;108(37):13913-20. Available from: <http://dx.doi.org/10.1021/jp037358c>
17. Khaleque A, Alam M, Hoque M, Mondal S, Bin J, Xu B, et al. Zeolite synthesis from low-cost materials and environmental applications : A review. *Environ Sci* 2020;2(December). Available from: <http://dx.doi.org/10.1016/j.envadv.2020.100019>
18. Rabenau A. The Role of Hydrothermal Synthesis in Preparative Chemistry. *Angew Chemie Int Ed English.* 1985;24(12):1026-40. Available from: <https://doi.org/10.1002/anie.198510261>
19. Cundy CS, Cox PA. The hydrothermal synthesis of zeolites: Precursors, intermediates and reaction mechanism. *Microporous Mesoporous Mater.* 2005;82(1-2):1-78. Available from: <https://doi.org/10.1016/j.micromeso.2005.02.016>

-
20. Csicsery SM. Shape-selective catalysis in zeolites. *Zeolites*. 1984;4(2):116–26. Available from: [https://doi.org/10.1016/0144-2449\(84\)90024-1](https://doi.org/10.1016/0144-2449(84)90024-1)
 21. Guanna Li. Structure and reactivity of iron and copper-containing high-silica zeolites. PhD[dissertation] Eindhoven: Chemical Engineering and Chemistry, Technische Universiteit Eindhoven;2013. Available from:<https://doi.org/10.6100/IR750184>
 22. Rashed MN, Palanisamy PN. Adsorption and Ion Exchange Properties of Zeolites for Treatment of Polluted Water. In: *Zeolites and Their Applications*. 2018. p. 3–10. Available from: <http://dx.doi.org/10.5772/intechopen.77190>
 23. Leofanti G, Padovan M, Tozzola G, Venturelli B. Surface area and pore texture of catalysts. *Catal today*. 1998;41:207–19. Available from: [http://dx.doi.org/10.1016/S0920-5861\(98\)00050-9](http://dx.doi.org/10.1016/S0920-5861(98)00050-9)
 24. Na K, Choi M, Ryoo R. Recent advances in the synthesis of hierarchically nanoporous zeolites. *Microporous Mesoporous Mater* [Internet]. 2013;166:3–19. Available from: <http://dx.doi.org/10.1016/j.micromeso.2012.03.054>
 25. Deka RC. Acidity in zeolites and their characterization by different spectroscopic methods. *Indian J Chem Technol*. 1998;5(3):109–23.
 26. Sousa-Aguiar EF. Y Zeolites as a Major Component of FCC Catalysts: Main Challenges in the Modification Thereof. In: *Zeolites and zeolite-like materials*. 2016. p. 265–80. Available from : <http://dx.doi.org/10.1016/B978-0-444-63506-8.00007-0>
 27. Castroa PRS, Maia AÁB, Angélica RS. Study of the thermal stability of faujasite zeolite synthesized from kaolin waste from the Amazon. *Mater Res*. 2019;22(5). Available from: <https://doi.org/10.1590/1980-5373-MR-2019-0321>
 28. Heard CJ, Grajciar L, Uhlík F, Shamzhy M, Opanasenko M, Čejka J, et al. Zeolite (In)Stability under Aqueous or Steaming Conditions. *Adv Mater*. 2020;32(44):1–29. Available from: <http://dx.doi.org/10.1002/adma.202003264>
 29. Li Y, Li L, Yu J. Applications of Zeolites in Sustainable
-

-
- Chemistry. *chem.* 2017;928–49. Available from: <https://doi.org/10.1016/j.chempr.2017.10.009>
30. Petushkov A, Yoon S, Larsen SC. Synthesis of hierarchical nanocrystalline ZSM-5 with controlled particle size and mesoporosity. *Microporous Mesoporous Mater* [Internet]. 2011;137(1–3):92–100. Available from: <http://dx.doi.org/10.1016/j.micromeso.2010.09.001>
 31. Zoubida L, Hichem B. The Nanostructure Zeolites MFI-Type ZSM5. In: Simonescu C M, editor. *Nanocrystals and Nanostructures*[e-book]. London: IntechOpen Limited;2018. Available from: <http://dx.doi.org/10.5772/intechopen.77020>
 32. D. H. Olson, G. T. Kokotailo, SLL, W. M. Meier. Crystal Structure and Structure-Related Properties of ZSM-5. *J Phys Chem.* 1981;85(3):2238–43. Available from: <https://doi.org/10.1021/j150615a020>
 33. Lohse, U, Altrichter B, Donath R, Fricke R, Jancke K, Parltitz B, Shreier E. Synthesis of zeolite beta. Part 1. *J Chem Soc Faraday Trans* [Internet]. 1996;92(1):159–65. Available from: <https://doi.org/10.1039/FT9969200159>
 34. Lu T, Yan W, Xu R. Chiral zeolite beta: Structure, synthesis, and application. *Inorg Chem Front.* 2019;6(8):1938–51. Available from: <http://dx.doi.org/10.1039/C9QI00574A>
 35. Davis ME. A Thirty-Year Journey to the Creation of the First Enantiomerically Enriched Molecular Sieve. *ACS Catal.* 2018;8(11):10082–8. Available from: <https://doi.org/10.1021/acscatal.8b03080>
 36. Jansen JC, Creyghton EJ, Njo SL, Van Koningsveld H, Van Bekkum H. On the remarkable behaviour of zeolite Beta in acid catalysis. *Catal Today.* 1997;38(2):205–12. Available from: [https://doi.org/10.1016/S0920-5861\(97\)00070-9](https://doi.org/10.1016/S0920-5861(97)00070-9)
 37. Hartmann M, Kevan L. Transition-Metal Ions in Aluminophosphate and Silicoaluminophosphate Molecular Sieves: Location, Interaction with Adsorbates and Catalytic Properties. *Chem Rev.* 1999;99(3). Available from: <https://doi.org/10.1021/cr9600971>
-

-
38. Smeets PJ, Woertink JS, Sels BF, Solomon EI, Schoonheydt RA. Transition-metal ions in zeolites: Coordination and activation of oxygen. *Inorg Chem.* 2010;49(8):3573–83. Available from: <https://doi.org/10.1021/ic901814f>
 39. Gnanapragasam S, Krishnasamy V, Mohan V. Isopropylation of benzene in the vapour phase over zeolite beta modified by lanthanum, cerium, gallium and zinc. *Indian J Chem.* 2001;40:947–52.
 40. Haga Y, Pusparatu, Aoyama K, Komura K, Nishimura Y, Sugi Y, et al. Beta Zeolites Modified with Lanthanum and Cerium Oxides for the Isomerization of Hexane. *Mater Sci Forum.* 2007;539–543:2323–8. Available from: <http://dx.doi.org/10.4028/www.scientific.net/MSF.539-543.2323>
 41. Dalla Costa BO, Peralta MA, Querini CA. Gas phase dehydration of glycerol over, lanthanum-modified beta-zeolite. *Appl Catal A Gen* [Internet]. 2014;472:53–63. Available from: <http://dx.doi.org/10.1016/j.apcata.2013.12.011>
 42. Loiha, S. Synthesis of zeolite beta as a support of metal supported catalysts for toluene hydrogenation and application of in situ XAS on catalysts characterization. PhD [dissertation]. Thailand: School of Chemistry, Institute of Science, Suranaree University of Technology;2008.
 43. Kumar N, Kubicka D, Garay AL, Mäki-Arvela P, Heikkilä T, Salmi T, et al. Synthesis of Ru-modified MCM-41 mesoporous material, Y and Beta zeolite catalysts for ring opening of decalin. *Top Catal.* 2009;52(4):380–6. Available from: <https://doi.org/10.1007/s11244-008-9170-4>
 44. Kamsuwan T, Praserttham P, Jongsomjit B. Diethyl ether production during catalytic dehydration of ethanol over Ru- and Pt- modified H-beta zeolite catalysts. *J Oleo Sci.* 2017;66(2):199–207. Available from: <https://doi.org/10.5650/jos.ess16108>
 45. Varela-Gandía FJ, Berenguer-Murcia ángel, Lozano-Castelló D, Cazorla-Amorós D, Sellick DR, Taylor SH. Total oxidation of naphthalene using palladium nanoparticles supported on BETA, ZSM-5, SAPO-5 and alumina powders. *Appl Catal B Environ.* 2013;129:98–105. Available from:
-

<https://doi.org/10.1016/j.apcatb.2012.08.041>

46. Kiatkittipong W, Wongsakulphasatch S, Tintan N, Laosiripojana N, Praserttham P, Assabumrungrat S. Gasoline upgrading by self-etherification with ethanol on modified beta-zeolite. *Fuel Process Technol.* 2011;92(10):1999–2004. Available from: <https://doi.org/10.1016/j.fuproc.2011.05.024>
47. Aho A, Kumar N, Lashkul A V, Eränen K, Ziolek M, Decyk P, et al. Catalytic upgrading of woody biomass derived pyrolysis vapours over iron modified zeolites in a dual-fluidized bed reactor. *Fuel* [Internet]. 2010;89(8):1992–2000. Available from: <http://dx.doi.org/10.1016/j.fuel.2010.02.009>
48. Anton A, Gabrienko, Sergei S, Arzumanov, Alexander V, Toktarev, Irina G, Danilova, DF, AGS. H/D exchange of molecular hydrogen with Brønsted acid sites of Zn- and Ga-modified zeolite BEA. *Phys Chem Chem Phys.* 2010;12:5149–55. Available from: <http://dx.doi.org/10.1039/b918648d>
49. Cruz-Cabeza AJ, Esquivel D, Jiménez-Sanchidrián C, Romero-Salguero FJ. Metal-Exchanged β Zeolites as Catalysts for the Conversion of Acetone to Hydrocarbons. Vol. 5, *Materials*. 2012. p. 121–34. Available from: <https://doi.org/10.3390/ma5010121>
50. Treesukol P, Srisuk K, Limtrakul J, Truong TN. Nature of the metal-support interaction in bifunctional catalytic Pt/H-ZSM-5 zeolite. *J Phys Chem B.* 2005;109(24):11940–5. Available from: <https://doi.org/10.1021/jp0511348>
51. Li S, Cui P, Wang Z, Momuinou N, Liu L, Wang L. Highly Effective Transformation of Methanol and RFCC Gas to Propylene and Paraxylene with Tungsten Hydride and Cerium Oxide Comodified HZSM-5 Zeolite. *Ind Eng Chem Res.* 2015;54(47):11929–36. Available from: <http://dx.doi.org/10.1021/acs.iecr.5b03311>
52. Momayez F, Towfighi Darian J, Teimouri Sendesi SM. Synthesis of zirconium and cerium over HZSM-5 catalysts for light olefins production from naphtha. *J Anal Appl Pyrolysis* [Internet]. 2015;112:135–40. Available from: <http://dx.doi.org/10.1016/j.jaap.2015.02.006>
53. Liao J, Bao W, Chen Y, Zhang Y, Chang L. The Adsorptive

-
- Removal of Thiophene from Benzene over ZSM-5 Zeolite. *Energy Sources, Part A Recover Util Environ Eff.* 2012;34(7):618–25. Available from: <http://dx.doi.org/10.1080/15567036.2010.549916>
54. Ismail R, Adryan P, Roessner F. Activity of H-Beta Zeolites Re-Exchanged with Alkaline and Earth-Alkaline Cations in the Fries Rearrangement of Phenyl Acetate. *Jordan Journal of Chemistry.* 2007;2(3):235–45.
 55. Yadav MK, Patil M V, Jasra R V. Acetoxylation and hydration of limonene and α -pinene using cation-exchanged zeolite beta. *J Mol Catal A Chem* 2009;297:101–9. Available from: <http://dx.doi.org/10.1016/j.molcata.2008.09.017>
 56. Thakur R, Barman S, Gupta RK. Synthesis of xylene over cerium modified large pore zeolite: A kinetic study. *Indian J Chem Technol.* 2014;21(5–6):379–85.
 57. Kareem MAA, Chand S, Mishra IM. Ion-exchanged ZSM-5 Zeolites As Catalysts for Toluene Disproportionation Reaction. *JSIR.* 2000;59(7):591–5.
 58. Lounis Z, Riahi A, Djafri F, Muzart J. Chromium-exchanged zeolite (CrE-ZSM-5) as catalyst for alcohol oxidation and benzylic oxidation with *t*-BuOOH. *Appl Catal A Gen.* 2006;309(2):270–2. Available from: <http://dx.doi.org/10.1016/j.apcata.2006.05.015>
 59. Tang B, Lu XH, Zhou D, Lei J, Niu ZH, Fan J, et al. Highly efficient epoxidation of styrene and α -pinene with air over Co^{2+} -exchanged ZSM-5 and Beta zeolites. *Catal Commun.* 2012;21:68–71.
 60. Tajbakhsh M, Alinezhad H, Nasrollahzadeh M, Kamali TA. Preparation, characterization, and application of nanosized CuO / HZSM-5 as an efficient and heterogeneous catalyst for the *N*-formylation of amines at room temperature. *J Colloid Interface Sci* [Internet]. 2016;471:37–47. Available from: <http://dx.doi.org/10.1016/j.jcis.2016.02.062>
 61. Shah AK, Khan NUH, Sethia G, Saravanan S, Kureshy RI, Abdi SHR, et al. Tin exchanged zeolite as catalyst for direct synthesis of α -amino nitriles under solvent-free conditions. *Appl Catal A Gen* [Internet]. 2012;419–420:22–30. Available from: <http://dx.doi.org/10.1016/j.apcata.2012.01.001>
-

-
62. Mazak MA. Modified zeolite beta as catalysts in friedel-crafts alkylation of resorcinol. marzita bt abd mazak universiti teknologi malaysia.
 63. Chassaing S, Alix A, Olmos A, Keller M, Sommer J, Pale P. Metal-doped zeolites as Green catalysts for organic synthesis. *Zeitschrift fur Naturforsch - Sect B J Chem Sci.* 2010;65(7):783–90. Available from: <http://dx.doi.org/10.1515/znb-2010-0703>
 64. Kuchеров A V., Doronkin DE, Stakheev AY, Kustov AL, Grill M. ESR study of competition between Fe³⁺ and Cu²⁺ active sites for NOx selective catalytic reduction by NH₃ in Cu-Fe-Beta catalyst. *J Mol Catal A Chem* [Internet]. 2010;325(1–2):73–8. Available from: <http://dx.doi.org/10.1016/j.molcata.2010.03.035>
 65. Sultana A, Sasaki M, Suzuki K, Hamada H. Tuning the NOx conversion of Cu-Fe / ZSM-5 catalyst in NH₃ -SCR. *Catal Commun* [Internet]. 2013;41:21–5. Available from: <http://dx.doi.org/10.1016/j.catcom.2013.06.028>
 66. Long RQ, Yang RT. Noble metal (Pt, Rh, Pd) promoted Fe-ZSM-5 for selective catalytic oxidation of ammonia to N₂ at low temperatures. *Catal Letters.* 2002;78(1–4):353–7. Available from: <http://dx.doi.org/10.1023/A:1014929222854>
 67. Broeke P Van Den. Removal of SOx and NOx Gases From Stationary Sources Using Copper Zeolite Based Catalysts. Qatar University College of Engineering Environmental. 2014
 68. Martins L, Peguin RPS, Urquieta-González EA. Cu and co exchanged ZSM-5 zeolites: activity towards NO reduction and hydrocarbon oxidation. *Quim Nov.* 2006;29(2):223–9. Available from: <https://doi.org/10.1590/S0100-40422006000200009>
 69. Pereda-Ayo B, De La Torre U, Illán-Gómez MJ, Bueno-López A, González-Velasco JR. Role of the different copper species on the activity of Cu/zeolite catalysts for SCR of NOx with NH₃. *Appl Catal B Environ* [Internet]. 2014;147(May):420–8. Available from: <http://dx.doi.org/10.1016/j.apcatb.2013.09.010>
 70. Gao F, Szanyi J, Wang Y, Schwenzer B, Kollár M, Peden CHF. Hydrothermal Aging Effects on Fe/SSZ-13 and Fe/Beta NH₃-SCR Catalysts. *Top Catal.* 2016;59(10–12):882–6. Available from: <http://link.springer.com/article/10.1007/s11244-016-0563-5>
-

-
71. Kanan SM, Omary MA, Patterson HH, Matsuoka M, Anpo M. Characterization of the excited states responsible for the action of silver(I)-doped ZSM-5 zeolites as photocatalysts for nitric oxide decomposition. *J Phys Chem B*. 2000;104(15):3507–17. Available from: <http://dx.doi.org/10.1021/jp992703c>
 72. Broclawik E, Datka J, Gil B, Piskorz W, Kozyra P. The interaction of CO, N₂ and NO with Cu cations in ZSM-5: Quantum chemical description and IR study. *Top Catal*. 2000;11–12(1–4):335–41. Available from: <http://dx.doi.org/10.1023/A:1027235511555>
 73. Li L, Guan N. HC-SCR reaction pathways on ion exchanged ZSM-5 catalysts. *Microporous Mesoporous Mater* [Internet]. 2009;117(1–2):450–7. Available from: <http://dx.doi.org/10.1016/j.micromeso.2008.07.021>
 74. Szyrkowska I, El M. Oxidation of odorous nitrogen-containing compounds: ammonia and trimethylamine over Cu/zeolite catalysts. *Reac Kinet Mech Cat*. 2014;111:763–73. Available from: <http://dx.doi.org/10.1007/s11144-013-0666-y>
 75. Larsen SC. Nanocrystalline zeolites and zeolite structures: Synthesis, characterization, and applications. *J Phys Chem C*. 2007;111(50):18464–74.
 76. Mintova S, Grand J, Valtchev V. Nanosized zeolites: Quo Vadis? *C R Chim*. 2016;19(1–2):183–91. Available from: <http://dx.doi.org/10.1016/j.crci.2015.11.005>
 77. Kantam ML, Rao BPC, Choudary BM, Rao KK, Sreedhar B, Iwasawa Y, et al. Synthesis of nanocrystalline zeolite beta in supercritical fluids, characterization and catalytic activity. *J Mol Catal A Chem*. 2006;252(1–2):76–84. Available from: <http://dx.doi.org/10.1016%2Fj.molcata.2006.02.044>
 78. Bok TO, Onuchin ED, Zabil'skaya A V., Konnov S V., Knyazeva EE, Panov A V., et al. Nanocrystalline zeolites beta: Features of synthesis and properties. *Pet Chem*. 2016;56(12):1160–7. Available from: <http://dx.doi.org/10.1134/S0965544116120021>
 79. Martínez-Franco R, Paris C, Martínez-Armero ME, Martínez C, Moliner M, Corma A. High-silica nanocrystalline Beta zeolites: Efficient synthesis and catalytic application. *Chem Sci*. 2016;7(1):102–8.
-

-
80. Viswanadham N, Kamble R, Singh M, Kumar M, Murali Dhar G. Catalytic properties of nano-sized ZSM-5 aggregates. *Catal Today*. 2009;141(1–2):182–6. Available from: <http://dx.doi.org/10.1016/j.cattod.2008.03.026>
 81. Bajaj HC, Parikh PA. Synthesis of hierarchical nano-crystalline zeolite beta using biomass-derived hard templates. *Int J Mater Eng Innov*. 2015;6(1):49–58. Available from: <http://dx.doi.org/10.1504/IJMATEI.2015.069800>
 82. Serrano DP, van Grieken R, Melero JA, García A, Vargas C. Nanocrystalline ZSM-5: A catalyst with high activity and selectivity for epoxide rearrangement reactions. *J Mol Catal A Chem*. 2010;318(1–2):68–74. Available from: <http://dx.doi.org/10.1016/j.molcata.2009.11.009>
 83. Younesi H, Vajheh Sari Z G L, Kazemian H. Synthesis of nanosized ZSM-5 zeolite using extracted silica from rice husk without adding any alumina source. *Appl Nanosci*. 2015;737–45. Available from: <http://dx.doi.org/10.1007/s13204-014-0370-x>
 84. Figueiredo AL, Araujo AS, Linares M, Peral Á, García RA, Serrano DP, et al. Catalytic cracking of LDPE over nanocrystalline HZSM-5 zeolite prepared by seed-assisted synthesis from an organic-template-free system. *J Anal Appl Pyrolysis*. 2016;117:132–40. Available from: <http://dx.doi.org/10.1016/j.jaap.2015.12.005>
 85. Ni Y, Sun A, Wu X, Hai G, Hu J, Li T, et al. Facile synthesis of hierarchical nanocrystalline ZSM-5 zeolite under mild conditions and its catalytic performance. *J Colloid Interface Sci [Internet]*. 2011;361(2):521–6. Available from: <http://dx.doi.org/10.1016/j.jcis.2011.06.020>
 86. Roohi H, Jahantab M. Adsorption sensitivity of nanocrystalline B-substituted H-ZSM-5 and alkali metal-exchanged M-ZSM-5 zeolites towards parent nitrosamine: A B97D study. *Comput Theor Chem [Internet]*. 2015;1066:76–87. Available from: <http://dx.doi.org/10.1016/j.comptc.2015.05.015>
 87. Ding L, Zheng Y, Yang H, Parviz R. LCO hydrotreating with Mo-Ni and W-Ni supported on nano- and micro-sized zeolite beta. *Appl Catal A Gen*. 2009;353(1):17–23. Available from:
-

<https://doi.org/10.1016/j.apcata.2008.10.023>

88. Botas JA, Serrano DP, García A, De Vicente J, Ramos R. Catalytic conversion of rapeseed oil into raw chemicals and fuels over Ni- and Mo-modified nanocrystalline ZSM-5 zeolite. *Catal Today*. 2012;195(1):59–70. Available from: <https://doi.org/10.1016/j.cattod.2012.04.061>
89. Chang CC, Wang Z, Dornath P, Je Cho H, Fan W. Rapid synthesis of Sn-Beta for the isomerization of cellulosic sugars. *RSC Adv*. 2012;2(28):10475–7. Available from: <http://dx.doi.org/10.1039/C2RA21381H>
90. Bi J, Liu M, Song C, Wang X, Guo X. C₂ – C₄ light olefins from bioethanol catalyzed by Ce-modified nanocrystalline HZSM-5 zeolite catalysts. *Applied Catal B, Environ* [Internet]. 2011;107(1–2):68–76. Available from: <http://dx.doi.org/10.1016/j.apcatb.2011.06.038>
91. Kaur B, Srivastava R, Satpati B. Highly Efficient CeO₂ Decorated Nano-ZSM-5 Catalyst for Electrochemical Oxidation of Methanol. *ACS Catal*. 2016;6(4):2654–63. Available from: <https://doi.org/10.1021/acscatal.6b00525>
92. Li J, Miao P, Li Z, He T, Han D, Wu J, et al. Hydrothermal synthesis of nanocrystalline H[Fe, Al]ZSM-5 zeolites for conversion of methanol to gasoline. *Energy Convers Manag* [Internet]. 2015;93(March):259–66. Available from: <http://dx.doi.org/10.1016/j.enconman.2015.01.031>
93. Kaur B, Srivastava R, Satpati B, Kondepudi KK, Bishnoi M. Biomineralization of hydroxyapatite in silver ion-exchanged nanocrystalline ZSM-5 zeolite using simulated body fluid. *Colloids Surf B Biointerfaces*. 2015;135:201–8. Available from: <https://doi.org/10.1016/j.colsurfb.2015.07.068>
94. Ramos R, García A, Botas JA, Serrano DP. Enhanced Production of Aromatic Hydrocarbons by Rapeseed Oil Conversion over Ga and Zn Modified ZSM-5 Catalysts. *Ind Eng Chem Res*. 2016;55(50):12723–32. Available from: <http://dx.doi.org/10.1021/acs.iecr.6b03050>
95. Gu J, Wu Y, Jin Y, Wang J. Hydrothermal incorporation of Ce(La) ions into the framework of ZSM-5 by a multiple pH-adjusting co-

- hydrolysis. *J Porous Mater.* 2013;20(1):7–13. Available from: <http://dx.doi.org/10.1007/s10934-012-9569-y>
96. Bai R, Song Y, Li Y, Yu J. Creating Hierarchical Pores in Zeolite Catalysts. *Trends Chem.* 2019;1(6):601–11. Available from: <https://doi.org/10.1016/j.trechm.2019.05.010>
97. Valtchev V, Mintova S. Hierarchical zeolites. *MRS Bull.* 2016;689–93. Available from: <http://dx.doi.org/10.1557/mrs.2016.171>
98. Egeblad K, Christensen CH, Kustova M, Christensen CH. Templating Mesoporous Zeolites. *Chem Mater.* 2008;946–60. Available from: <http://dx.doi.org/10.1021/cm702224p>
99. Ozhukka Parambil F, Kumari P. Hierarchical Assembly of Zeolites: A Present Scenario. *Eng Sci [Internet]*. Available from: <http://dx.doi.org/10.30919/es8d781>
100. Ji Y, Yang H, Yan W. Strategies to Enhance the Catalytic Performance of ZSM-5 Zeolite in Hydrocarbon Cracking: A Review. *Catalysts.* 2017; 7(367). Available from: <https://doi.org/10.3390/catal7120367>
101. Al-Ani A, Haslam JJC, Mordvinova NE, Lebedev OI, Vicente A, Fernandez C, et al. Synthesis of nanostructured catalysts by surfactant-templating of large-pore zeolites. *Nanoscale Adv.* 2019;1(5):2029–39. Available from: <https://doi.org/10.1039%2F9na00004f>
102. Caldeira VPS, Peral A, Linares M, Araujo AS, Garcia-Muñoz RA, Serrano DP. Properties of hierarchical Beta zeolites prepared from protozeolitic nanounits for the catalytic cracking of high density polyethylene. *Appl Catal A Gen.* 2017;531:187–96. Available from: <http://dx.doi.org/10.1016/j.apcata.2016.11.003>
103. Padmanabhan A, Selvin R, Unnikrishnan G, Hsiu-Ling H, Bououdina M. A facile method for the fabrication of hierarchical porous nanocrystalline zeolite silicalite-1. *Int J Mater Eng Innov.* 2011;2(1):30–7. Available from: <http://dx.doi.org/10.1504/IJMATEI.2011.037878>
104. Selvin R, Roselin LS, Khayyat SA, Umar A. Hierarchical zeolite Beta: An efficient and eco-friendly nanocatalyst for the Friedel-

-
- Crafts acylation of toluene. *J Nanosci Nanotechnol.* 2013;13(6):4415–20. Available from: <https://doi.org/10.1166/jnn.2013.7153>
105. Radhika NP, Selvin R, Kakkar R, Roselin LS. Nanocrystalline Hierarchical ZSM-5 : An Efficient Catalyst for the Alkylation of Phenol with Cyclohexene. *J Nanosci Nanotechnol.* 2018;18:5404–13. Available from: <http://dx.doi.org/10.1166/jnn.2018.15390>
106. Narayanan S, Judith Vijaya J, Sivasanker S, Yang S, John Kennedy L. Hierarchical ZSM-5 catalyst synthesized by a Triton X-100 assisted hydrothermal method. *Chinese J Catal [Internet].* 2014;35(11):1892–9. Available from: [http://dx.doi.org/10.1016/S1872-2067\(14\)60177-7](http://dx.doi.org/10.1016/S1872-2067(14)60177-7)
107. Costa ICM, Dib E, Nesterenko N, Dath JP, Gilson JP, Mintova S. Silanol defects engineering and healing in zeolites: Opportunities to fine-tune their properties and performances. *Chem Soc Rev.* 2021;50:11156–79. Available from: <https://doi.org/10.1039/D1CS00395J>
108. Nabavi MS. Defects in Zeolite Catalysts and Membranes. Sweden: Lulea University of Technology;2020.
109. Prodinger S, Derewinski MA, Vjunov A, Burton SD, Arslan I, Lercher JA. Improving Stability of Zeolites in Aqueous Phase via Selective Removal of Structural Defects. *J Am Chem Soc.* 2016;138(13):4408–15. Available from: <https://doi.org/10.1021/jacs.5b12785>
110. Lee K, Lee S, Jun Y, Choi M. Cooperative effects of zeolite mesoporosity and defect sites on the amount and location of coke formation and its consequence in deactivation. *J Catal [Internet].* 2017;347:222–30. Available from: <http://dx.doi.org/10.1016/j.jcat.2017.01.018>
111. Qin Z, Hafiz L, Shen Y, Daele S Van, Boullay P, Ruaux V, et al. Defect-engineered zeolite porosity and accessibility. *J Mater Chem A.* 2020;8(7):3621–31. Available from: <https://doi.org/10.1039/C9TA11465C>
112. Grosskreuz I, Gies H, Marler B. Alteration and curing of framework defects by heating different as-made silica zeolites of the MFI framework type. *Microporous Mesoporous Mater*
-

- [Internet]. 2020;291(September 2019):109683. Available from: <https://doi.org/10.1016/j.micromeso.2019.109683>
113. Resasco DE, Crossley SP, Wang B, White JL. Interaction of water with zeolites: a review. *Catal Rev - Sci Eng*. 2021;63(2):302–62. Available from: <http://dx.doi.org/10.1080/01614940.2021.1948301>
 114. Maggi R, Sartori G. *Friedel-Crafts Acylation Reactions: Catalytic and Green Processes*. New York: Taylor and Francis;2010
 115. Pandey AK, Singh AP. A novel catalytic method for the acylation of aromatics to the corresponding ketones over zeolite catalysts. *Catal Letters*. 1997;44(1–2):129–33.
 116. Neves I, Jayat F, Magnoux P, Pérot G, Ribeiro FR, Gubelmann M, et al. Acylation of phenol with acetic acid over a HZSM5 zeolite, reaction scheme. *J Mol Catal*. 1994;93(2):169–79.
 117. Neves I, Jayat F, Magnoux P, Pérot G, Ribeiro FR, Gubelmann M, et al. Phenol acylation: Unexpected improvement of the selectivity to o-hydroxyacetophenone by passivation of the external acid sites of HZSM5. *J Chem Soc Chem Commun*. 1994;(6):717–8. Available from: <https://doi.org/10.1039/C39940000717>
 118. Olah, G.A., Reddy, V.P. and Prakash GKS. FRIEDEL-CRAFTS. In: *Kirk-Othmer Encyclopedia of Chemical Technology*,. 2000. p. 38. Available from: <https://doi.org/10.1002/0471238961.0618090515120108.a01>
 119. Das D, Cheng S. Friedel-Crafts acylation of 2-methoxynaphthalene over zeolite catalysts. *Applied Catal A Gen*. 2000;201:159–68. Available from: [http://dx.doi.org/10.1016/S0926-860X\(00\)00438-5](http://dx.doi.org/10.1016/S0926-860X(00)00438-5)
 120. Chiche B, Finiels A, Gauthier C, Geneste P. Friedel-Crafts Acylation of Toluene and p -Xylene with Carboxylic Acids Catalyzed by Zeolites. *J Org Chem*. 1986;51(11):2128–30. Available from: <https://doi.org/10.1021/jo00361a039>
 121. Vinu A, Krithiga T, Gokulakrishnan N, Srinivasu P, Anandan S, Ariga K, et al. Halogen-free acylation of toluene over FeSBA-1 molecular sieves. *Microporous Mesoporous Mater*. 2007;100(1–3):87–94. Available from: <https://doi.org/10.1016/j.micromeso.>

2006.10.014

122. Sheemol VN, Tyagi B, Jasra R V. Acylation of toluene using rare earth cation exchanged zeolite β as solid acid catalyst. *J Mol Catal A Chem.* 2004;215(1–2):201–8. Available from: <http://dx.doi.org/10.1016/j.molcata.2004.02.002>
123. Fromentin E, Coustard J, Guisnet M. Mechanism of 1-Acetyl-2-methoxynaphthalene Isomerisation over a HBEA Zeolite. *J Catal.* 2000;190:433–8. Available from: <https://doi.org/10.1006/jcat.1999.2762>
124. Cahyono E, Priatmoko S, Haryani S. Acetylation of 2-Methoxynaphthalene with Acetic anhydride over Zr^{4+} -Zeolite beta. *Orient J Chem.* 2015;31:79–83.
125. Guidotti M, Canaff C, Coustard J marie, Magnoux P. Acetylation of aromatic compounds over H-BEA zeolite : the influence of the substituents on the reactivity and on the catalyst stability. *J of Catalysis.* 2005;230:375–83. Available from: <http://dx.doi.org/10.1016/j.jcat.2004.12.021>
126. Yadav GD, Krishnan MS. Solid acid catalysed acylation of 2-methoxy-naphthalene : role of intraparticle diffusional resistance. *Chem Eng Sci.* 1999;54:4189–97. Available from: [http://doi.org/10.1016/S0009-2509\(99\)00092-5](http://doi.org/10.1016/S0009-2509(99)00092-5)
127. Jilani MT, Zaka M, Khan AM, Khan MT, Ali SM. A Brief Review of Measuring Techniques for Characterization of Dielectric Materials. *Int J Inf Technol Electr Eng.* 2012;1(1):1–5
128. Deshmukh K, Sankaran S, Ahamed B, Sadasivuni KK, Pasha KSK, Ponnamma D, et al. Dielectric Spectroscopy [Internet]. In: Thomas S, Thomas R, Zachariah AK, Mishra RK, editors. *Spectroscopic Methods for Nanomaterials Characterization[e-book]*.:ScienceDirect;2017:237-299p. Available from:<https://doi.org/10.1016/B978-0-323-46140-5.00010-8>
129. Ward AA. State of the Art Dielectric Materials for Advanced Applications[e-book].. Egypt: National Research Centre;2015. 1–70 p. Available from: <http://dx.doi.org/10.13140/RG.2.1.3481.5600>

-
130. Woodward WHH. Broadband Dielectric Spectroscopy - A Practical Guide. ACS Symp Ser. 2021;1375:3–59. Available from: [10.1021/bk-2021-1375.ch001](https://doi.org/10.1021/bk-2021-1375.ch001)
 131. Lvovich VF. Impedance spectroscopy: Applications to Electrochemical and Dielectric Phenomena[e-book]. United Kingdom: Wiley;2012.353 p
 132. Ohki Y. Broadband Complex Permittivity and Electric Modulus Spectra for Dielectric Materials Research. IEEJ Trans Electr Electron Eng. 2022;17(7):958–72. <https://doi.org/10.1002/tee.23565>
 133. Deshpande VP, Aurangabad D, Bhoskar PBT. Characterization and Dielectric study of Zeolite ZSM5. Int J Eng Res Technol. 2012;1(7):1–18.
 134. Praveena K, Murthy SR. Dielectric Properties of Dehydrated Zeolites. Int J Emerg Technol Adv Eng. 2013;3(1):363–8.
 135. Chen P, Schönebaum S, Simons T, Rauch D, Dietrich M, Moos R, et al. Correlating the Integral Sensing Properties of Zeolites with Molecular Processes by Combining Broadband Impedance and DRIFT Spectroscopy—A New Approach for Bridging the Scales. Sensors. 2015;15:28915–41. Available from: <https://doi.org/10.3390/s151128915>
 136. Zhou W, Zhao K shuang. Dielectric Response and Analysis of Structural Evolution of NaA Zeolite with High Pretreatment Temperature. J Phys Chem. 2008;112(38):15015–21
 137. Han B, Yin C, Chang J, Pang Y, Lv P, Song W, et al. Study on the structure and dielectric properties of zeolite/LDPE nanocomposite under thermal aging. Polymers. 2020;12(9):1–12. Available from: <https://doi.org/10.3390/polym12092108>
 138. Bunyatova U, Ozturk Koc S, Orbukh VI, Eyvazova GM, Agamaliev ZA, Lebedeva NN, et al. Peculiarities of the dielectric response of the silver-modified-zeolite porous microstructure. Superlattices Microstruct [Internet]. 2016;98:295–305. Available from: <http://dx.doi.org/10.1016/j.spmi.2016.08.040>
 139. Šály V, Kočálka S. Dielectric response of natural clinoptilolite type zeolitic material containing silver iodide. Chem Pap.
-

- 1996;50(6):328–33.
140. Fernández-Gutierrez F, Hernández-Velez M, Roque-Malherbe R. Dielectric relaxation in na-mfi zeolite. In: *Studies in Surface Science and Catalysis*. 1994. p. 883–90. Available from: [http://dx.doi.org/10.1016/S0167-2991\(08\)64094-X](http://dx.doi.org/10.1016/S0167-2991(08)64094-X)
141. Haidar AR, Jonscher AK. The dielectric properties of zeolites in variable temperature and humidity. *J Chem Soc Faraday Trans 1 Phys Chem Condens Phases*. 1986;82(12):3535–51.

Chapter 2

Materials and Methods

Abstract

The specifications of the materials used and the experimental methods followed for the synthesis and modification of ZSM-5 and Zeolite beta are given in this chapter. It also discusses various analytical techniques for characterizing the synthesized zeolites and methods to investigate their catalytic reactions. The code names for various ZSM-5 and zeolite beta samples are also mentioned in this chapter

2.1. Introduction

The previous chapter summarized recent advances in the synthesis and applications of nanocrystalline, metal-modified nanocrystalline, and hierarchical zeolites. This chapter explains the materials and experimental methodologies used in the current investigation to:

- Synthesize nanocrystalline metal-modified ZSM-5 and zeolite beta
- Synthesize nanocrystalline hierarchical ZSM-5 and zeolite beta.
- Characterise the synthesized nanocrystalline and hierarchical ZSM-5 and zeolite beta.
- Assess the catalytic activity of metal-modified nanocrystalline, hierarchical ZSM-5, and zeolite beta as solid heterogeneous catalysts in Friedel-Crafts acetylation reactions.

2.2. Chemicals

Table 2.1. List of chemicals used for the present study

Name of chemical	Molecular formula	Manufacturer and CAS number
Aluminium isopropoxide (AIP)	$\text{Al}[\text{O}(\text{CH}(\text{CH}_3)_2)_3]$	Merck & 555-31-7
Tetrapropylammonium hydroxide (TPAOH)	$\text{C}_{12}\text{H}_{29}\text{NO}$	Merck & 4499-86-9
Tetraethyl orthosilicate (TEOS)	$\text{Si}(\text{OC}_2\text{H}_5)_4$	Merck & 78-10-4
Tetraethylammonium hydroxide (TEAOH)	$\text{C}_8\text{H}_{21}\text{NO}$	Merck & 77-98-5

Ammonium Chloride	NH_4Cl	Fischer Scientific & 12125-02-9
Iron (III) Nitrate	$\text{Fe}(\text{NO}_3)_3 \cdot 9\text{H}_2\text{O}$	Alfa Aesar & 7782-61-8
Zinc (II) Nitrate	$\text{Zn}(\text{NO}_3)_2 \cdot 6\text{H}_2\text{O}$	Fisher Scientific & 10196-18-6
Lanthanum (III) Nitrate	$\text{La}(\text{NO}_3)_3 \cdot 6\text{H}_2\text{O}$	Alfa Aesar & 10277-43-7
Copper (II) Nitrate	$\text{Cu}(\text{NO}_3)_2 \cdot 3\text{H}_2\text{O}$	Sigma-Aldrich & 10031-43-3
Cerium (III) Nitrate	$\text{Ce}(\text{NO}_3)_3 \cdot 6\text{H}_2\text{O}$	Alfa Aesar & 10294-41-4
Neodymium (III) Nitrate	$\text{Nd}(\text{NO}_3)_3 \cdot 6\text{H}_2\text{O}$	Alfa Aesar & 16454-60-7
Toluene	$\text{C}_6\text{H}_5\text{CH}_3$	SRL & 108-88-3
2-methoxynaphthalene (2-MON)	$\text{C}_{11}\text{H}_{10}\text{O}$	Merck & 93-04-9
Acetic anhydride (AC_2O)	$(\text{CH}_3\text{CO})_2\text{O}$	Merck & 108-24-7
Methyl methacrylate (MMA)	$\text{C}_5\text{H}_8\text{O}_2$	Fisher Scientific & 80-62-6
Polyvinylalcohol (PVA)	$[\text{CH}_2\text{CH}(\text{OH})]_n$	Fisher Scientific & 9002-89-5
Disodium hydrogen phosphate (DSP)	Na_2HPO_4	Fisher Scientific & 7558-79-4
Benzoyl Peroxide (BPO)	$(\text{C}_6\text{H}_5\text{CO})_2\text{O}_2$	Fisher Scientific & 94-36-0

2.3 Instrumentation and Analytical Techniques

2.3.1 X-ray Diffraction (XRD)

XRD is a fast, non-invasive technique used to identify crystalline substances and measure the dimensions of unit cells. XRD patterns were obtained on a Rigaku 2000 diffractometer using Cu-K α radiation to confirm and analyze the materials synthesized in this study.

The average crystallite size of zeolite samples was calculated using the Debye Scherrer formula, i.e., equation 2.1.

$$L = \frac{K\lambda}{\beta \cos\theta} \quad (2.1)$$

Where L is the average crystallite size, λ , is the wavelength of the X-ray (1.54 Å), θ the Bragg diffraction angle, and β is the full width at half maximum (FWHM) of the observed peaks.

The percentage crystallinity or crystallinity index can be evaluated using XRD results by utilizing the following equation 2.2.

$$\text{Crystallinity index} = \frac{\text{Total area of crystalline peaks}}{\text{Total area of all amorphous and crystalline peaks}} \quad (2.2)$$

The magnitude of crystal defects, i.e., the dislocation lines per unit volume of samples, is indicated by δ value using equation 2.3.

$$\delta = \frac{1}{L^2} \quad (2.3)$$

The lattice strain, ε , is calculated using equation 2.4.

$$\varepsilon = \frac{\beta}{4 \tan \theta} \quad (2.4)$$

2.3.2 Fourier Transform Infrared Spectroscopy (FTIR)

FTIR is a method for identifying chemicals and detecting the functional groups in molecules. Molecules absorb specific IR frequencies based on the energy required for the vibration of the

particular bond. The FTIR approach allows for the simultaneous collection of absorption and transmission data across the spectral range. Solid samples are analyzed by mixing the zeolite with KBr and pelletizing it under high pressure using a hydraulic press. The current research recorded the FTIR spectrum of the catalyst on a Shimadzu IR Spirit.

2.3.3 Ultra Violet- Visible spectroscopy (UV-Visible Spectroscopy)

Using UV-Visible spectroscopy, one can obtain the absorbance spectra of a solid or in solution. A compound's or substance's ability to absorb light energy or electromagnetic radiation, which drives electrons from their ground state into their first singlet excited state, is known spectroscopically. The UV–Visible energy region in the electromagnetic spectrum corresponds to a wavelength of 800–200 nm. The Beer-Lambert Law (Equation 2.5) is the fundamental principle of absorbance spectroscopy. A is absorbance (unitless, generally expressed as arb. units or arbitrary units) for a single wavelength, ϵ is the molar absorptivity of the substance or molecule in solution ($M^{-1} \text{ cm}^{-1}$), b is the path length of the cuvette or sample holder (usually 1 cm), and c is the concentration of the solution (M).

$$A = \epsilon bc \quad (2.5)$$

UV-visible spectroscopy was carried out on the Shimadzu 1900i spectrophotometer after dispersing zeolite samples in ethanol using a sonicator.

2.3.4 Scanning Electron Microscopy (SEM)

SEM is an indispensable technique to study the morphology of a substance. The technique that images the surface of a material in a raster scan pattern by scanning it with a focused beam of high-energy electrons. Nonconductive samples tend to accumulate charge on being scanned by the electron beam. The build-up of charge can lead to scanning errors and image distortions. The nonconductive samples are prepared for conventional SEM analysis by coating them with an electrically conducting material such as gold, platinum, tungsten, or graphite. Additionally, to be analyzed by conventional SEM, samples must be stable in a vacuum of 10^{-5} - 10^{-6} torr. The SEM instrument used in the present work was SEM (HITACHI SU 6600).

2.3.5 Energy Dispersive X-ray Analysis (EDX)

EDX is a reliable method for determining elemental composition of samples. The fundamental working principle of EDX is the capacity of high-intensity electromagnetic radiation (X-rays) to eject "core" electrons, which are not in the outermost shell from an atom. The EDX instrument used in the present work was Jeol 6390LA/OXFORD XMXN.

2.3.6 Nitrogen Adsorption/Desorption Isotherm Analysis

Nitrogen adsorption/desorption is an essential method for estimating Brunauer-Emmett-Teller (BET) surface area and Barrett-Joyner-

Halenda (BJH) pore size distribution of materials. BET theory is based on the concept that multilayer adsorption occurs infinitely when a non-corrosive gas, such as nitrogen, adsorbs on an adsorbent. The pore size is determined by putting the data from the nitrogen adsorption and desorption branches of the isotherm to BJH analysis. All pores are assumed to be filled with adsorbate liquid before desorption due to capillary condensation. The pores are believed to be cylindrical and non-interacting.

The t-plot method is a well-known approach for measuring the micro- and mesoporous volumes and specific surface area of a sample by comparing it to a reference adsorption isotherm of a nonporous material with the same surface chemistry. It is commonly used to determine the microporous and mesoporous volumes of porous materials such as hierarchical zeolites. In the present work, nitrogen was made to adsorb and desorb at 77.8 K using BELSORB. Before recording the adsorption measurements, the sample was vacuum-degassed at 473 K for 5 hours.

2.3.7 Surface Acidity Determination of Solid Catalysts

2.3.7.1 FTIR of pyridine sorbed samples

Acid sites on a solid surface make it suitable for catalyzing chemical reactions depending on their nature and strength. The different types of acid sites are Lewis acid sites that can accept an electron pair and Bronsted acid sites that can donate a hydrogen ion. In this study, pyridine was used as a probe molecule; as an aromatic base, it can

be co-ordinately bonded to the Lewis acid site, and it can also be converted to the pyridinium ion to detect the Bronsted acidity.

A drop of pyridine is added to a few milligrams of the samples for the differentiation of Lewis and Bronsted acidity, and it is then aged in a hot air oven at 60 °C for around 3 hours. When heated, unadsorbed pyridine evaporates, whereas adsorbed load remains at acid sites. The KBr wafer approach was then used to record FTIR on an IR Spirit spectrometer.

2.3.7.2 Ammonia-temperature programmed desorption (TPD)

The ammonia-TPD method can determine the amount and strength of acid sites. The number of acid sites is calculated by counting the number of base molecules chemisorbed on the acid sites. In addition, the enthalpy change of desorption, or adsorption heat, and the equilibrium constant offer an indicator of intrinsic acid strength. A specific approach of ammonia-TPD is proposed for experimental ease of reproducing findings.

The adsorption and desorption of ammonia molecules are assumed to occur under the following conditions:

- (i) The intercrystalline zeolite surface exhibits homogeneity, and the quantity of ammonia adsorbed during the experiment is lower than what is required for monolayer coverage.

- (ii) No ammonia is readsorption during the desorption phase, and
- (iii) there is no lateral contact among the molecules of adsorbed ammonia.

The quantity of ammonia that is desorbed at progressively higher temperature intervals is seen in the ammonia thermogram profile. This fits the distribution of the total acid strengths of surface acidity. Two peaks may be seen in the thermograms of samples at both high and low temperatures. Ammonia desorption from strong acid sites is represented by the intensity of the high-temperature desorption peak, while base desorption from weak acid sites is represented by the low-temperature peak. The low-temperature acid sites correspond to the physisorbed ammonia. In contrast, the high-temperature acid sites consist of chemically bonded ammonia with the catalysts, also known as chemisorbed ammonia. The acid sites on the zeolite materials were measured using BELCAT-M. The following procedure was used for ammonia TPD: Each TPD experiment utilized 0.1 g of sample. It was performed after the catalyst sample had been dehydrated for 1 hour at 500 °C in helium gas (30 cm³ min⁻¹). The temperature was reduced to 100 °C, and NH₃ was adsorbed by exposing the sample to a stream containing 10% NH₃ in helium for 1 hour at 100 °C. After that, it was flushed with helium for 1 hour to eliminate the physisorbed NH₃. The desorption of NH₃ was performed in a helium gas flow of 30 cm³ min⁻¹ by increasing the temperature to 600 °C at a heating rate of 10 °C min⁻¹ and monitoring NH₃ desorption with a Thermal conductivity detector (TCD).

2.3.8 Al Magic Angle Spinning Nuclear Magnetic Resonance (Al MAS NMR)

The MAS NMR method utilizes the fast rotation of the sample at the "magic" angle in relation to the applied magnetic field to eliminate chemical shift anisotropy and broadening from dipole-dipole interactions. Otherwise, spinning sidebands will be present if the spinning speed is greater than the frequency width of the spectrum.

In this work, the chemical shifts of aluminium are determined by collecting solid-state ^{27}Al MAS NMR spectra obtained using ECX400-Jeol 400-MHz high-resolution FT NMR spectrometer.

2.3.9 Transmission Electron Microscopy (TEM)

TEM is a microscopic technique in which an intense high-energy electron beam is passed through an ultra-thin (200 nm) specimen. These electrons that pass through the sample are viewed through the detector, generating a two-dimensional projection of the sample.

The image captured in bright field imaging mode provides contrast information about the sample, indicating that thicker sections or areas with a more significant atomic number are darker and vice versa. The dark and light fields of TEM images can characterize the particle size, shape, and crystal structure.

Selected Area Electron Diffraction (SAD or SAED) is one of the most prevalent experimental techniques that use electron diffraction for material research and solid-state physics. SAED patterns, especially when combined with proper analytical software, can be

used to determine the crystal structure, orientation, and lattice constants. It is also beneficial in inspecting crystal flaws and in studying material textures. The morphology of the samples was investigated using a TEM Talos F200.

2.3.10 Thermogravimetric Analysis (TGA)

Using a thermo-analytical technique called TGA, one can measure weight change of material quantitatively as a function of temperature (in a scanning mode and at a constant heating rate) or time (isothermally and with a constant mass loss). The technique provides information regarding the thermal stability of the material, its purity, the presence of volatile components, and the kinetic parameters of the reactions taking place in the sample. The method is widely used for material characterization, corrosion studies, and compositional analysis. Temperature resolution of weight loss can be improved by slowing down the heating rate and reducing the sample weight. The sample weight can be varied from 2 to 50 mg. TGA is done by using the STA7200 HITACHI thermal analysis system. The temperature was increased from 100 °C to 700 °C with a rate of 5 °C/min followed by cooling.

2.3.11 Raman Spectroscopy

Raman spectra were collected using a LabRAM HR Evolution Raman microscope equipped with a microscope (objective: 50x) and a thermoelectrically cooled CCD camera. The spectra were acquired three times for 40 seconds each using a 532 nm DPSS laser.

2.3.12 Gas Chromatography-Mass Spectrometry (GC-MS)

GC-MS is a method used to analyze and characterize various substances within a complex mixture. It combines the capabilities of gas chromatography and mass spectrometry. Traditionally, GC employs a flame ionization detector (FID) for detection. In the present work, the progress of the reaction was monitored, and products were identified and confirmed by using a combination of gas chromatographic (GC) analysis (Hewlett Packard 5890), using an OV-101 column (2 m length, 1/8 inch diameter) and FID detector.

2.3.13 Broadband Dielectric Spectroscopy (BDS)

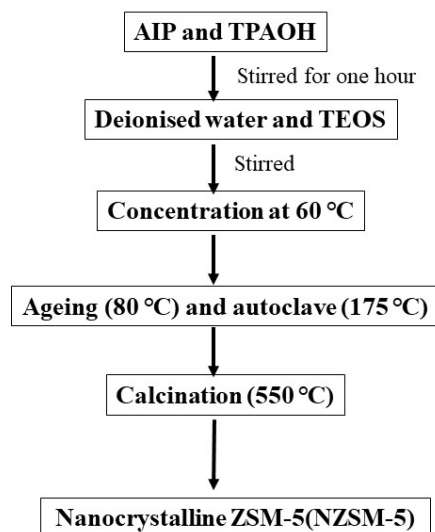
BDS is a powerful analytical technique for studying electronic dipoles within an electric field, such as dipolar molecules. Operating across a broad frequency range, BDS probes the rotation and relaxation dynamics of dipoles, offering insights into material behavior under varying conditions. This analytical instrument requires little supervision and can investigate a broad range of pressures, temperatures, and electric field strengths. BDS uses NOVOCONTROL Technologies GmbH & Co. Germany Model: Concept 80.

2.4 Synthesis of Zeolite samples

2.4.1 Synthesis of nanocrystalline ZSM-5

In this synthesis, 0.1021 g AIP was slowly added to 6.3400 g TPAOH (from Aldrich) and stirred for one hour at 25 °C using a magnetic stirrer. Then, dissolve 10.4 g of TEOS (silica source)

slowly in 15.0 g of deionized water. The components were mixed well with constant vigorous stirring for 24 hours to hydrolyze the TEOS. The above solution was concentrated at 60 °C at a pressure of about 700 mmHg for 30 min. The resulting mixture was aged for 24 hours in an oven, which also caused the hydroxylation to occur. The hydrolysis of TEOS led to the formation of a concentrated gel. The obtained gel was then loaded into a Teflon-lined stainless steel autoclave and crystallized using hydrothermal treatment at 175 °C for 24 hours without stirring. The product was separated by centrifugation, washed several times using double distilled water, dried at 80 °C, and then calcined at 550 °C for 20 hours in the air to remove residues of organic template TPAOH. Scheme 2.1 shows the flow chart for synthesizing the nanocrystalline ZSM-5(NZSM-5).



Scheme 2.1. Flowchart showing the synthesis of nanocrystalline ZSM-5

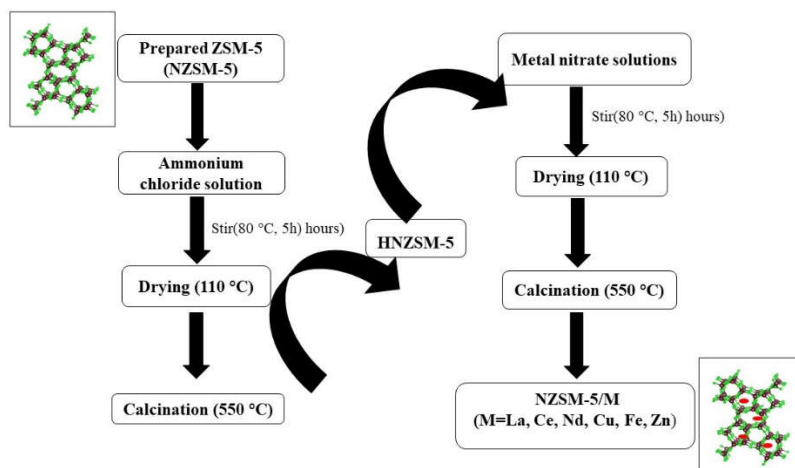
2.4.2 Modification of Synthesized ZSM-5

2.4.2.1 Ion exchange with NH_4Cl solution

The NZSM-5 zeolite was placed in 20 mL of 0.2 M NH_4Cl aqueous solution at 80 °C and stirred for 5 hours in order to convert it into H^+ form. There were three different instances of the exchange procedure. Subsequently, the zeolite experienced a washing process, centrifugation separation, and three hours of drying at 110 °C. The crystals that were obtained at this point were in the NH_4^+ form. After that, the sample was calcined for six hours at 550 °C to remove the ammonia, leaving the H^+ on the catalyst to maintain the ionic charge balance. The calcined sample is named HNZSM-5.

2.4.2.2 Modification by Ion Exchange with metal ions

H-NZSM-5 was mixed with metal nitrate solution (0.2 M) with 20 mL solution per 1.0 g of zeolite; then, it was stirred continuously at 80 °C for 5 hours. The ion exchange treatment was repeated three times. The obtained solid was recovered by centrifugation, washed with deionized water, and dried at 110 °C for 3 hours. Then, the sample was calcined at a temperature of 550 °C for 5 hours. The metal-modified nanocrystalline ZSM-5 samples were named NZSM-5/M, where M=La, Ce, Nd, Fe, Cu, and Zn. Scheme 2.2 shows the flow chart for modification of the synthesized nanocrystalline ZSM-5.

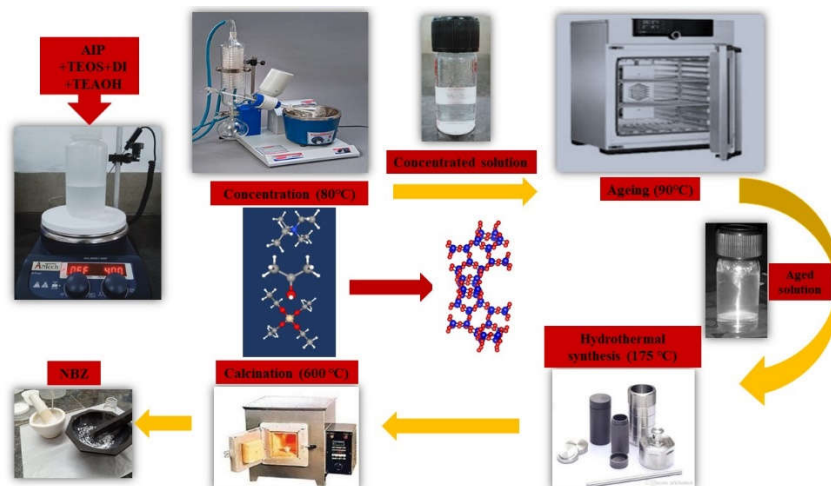


Scheme 2.2. Flow chart for the modification of NZSM-5

2.4.3 Synthesis of Nanocrystalline Zeolite Beta

This synthesis took 11.5014 g of TEAOH solution in a polypropylene bottle, and 0.2033 g AIP was added. After that, the mixture was stirred using a magnetic stirrer for 30 minutes at room temperature. 15.0 g of deionized water was added dropwise, followed by 10.4 g of TEOS. The solution was stirred continuously for approximately two hours at room temperature to obtain a clear, hydrolyzed sol. The aforementioned transparent solution was concentrated for 30 minutes at 80 °C and a high pressure of 700 mm Hg in a rotary evaporator. The resultant concentrated sol was aged in a hot air oven at 90 °C for 72 hours; at this stage, it took on a very faint grey color with turbidity, signifying the beginning of crystallization. After that, the resultant sol is placed in a Teflon-lined stainless steel autoclave and hydrothermally treated at 170 °C for 40

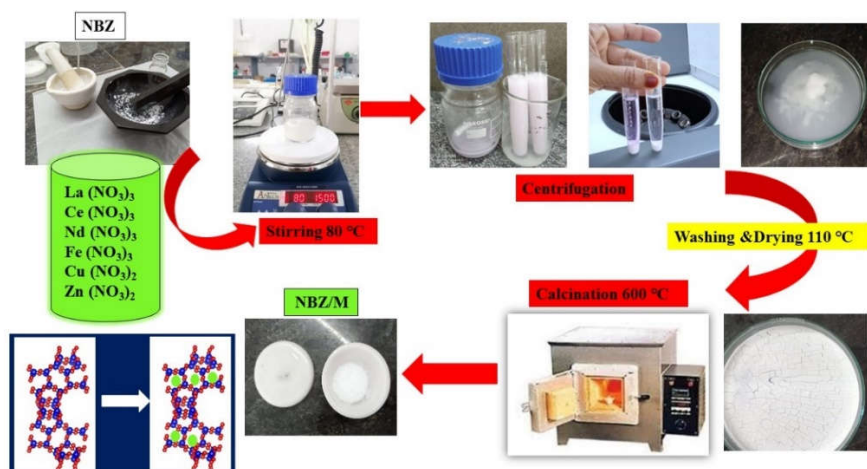
hours in order to crystallize. Centrifuged, the product was dried in a hot oven and calcined in air for 20 hours at 600 °C. The resultant nanocrystalline zeolite beta is named NBZ. The synthesis steps are depicted in scheme 2.3.



Scheme 2.3. Steps involved in the hydrothermal synthesis of NBZ

2.4.4 Modification of Beta with Metal Ions

1.0 g of resulting NBZ was stirred with 20 mL (0.2 M) of metal nitrates (lanthanum, cerium, neodymium, copper, iron, and zinc) and thoroughly stirred at 80 °C for five hours. Centrifuged to obtain the solid. After being cleaned with deionized water, the mixture is put in a petri dish and dried for three hours at 110 °C. Following that, the product was burnt for 6 hours at 600 °C. The entire modification procedure was repeated 3 times. The sample obtained is designated as NBZ/M, where M=La, Ce, Nd, Fe, Cu, and Zn. Scheme 2.4 illustrates the whole process of modification.



Scheme 2.4. Steps involved in the metal modification of NBZ

2.5 Catalytic Activity of Metal-Modified Nanocrystalline ZSM-5 and Zeolite Beta for Acetylation of Toluene

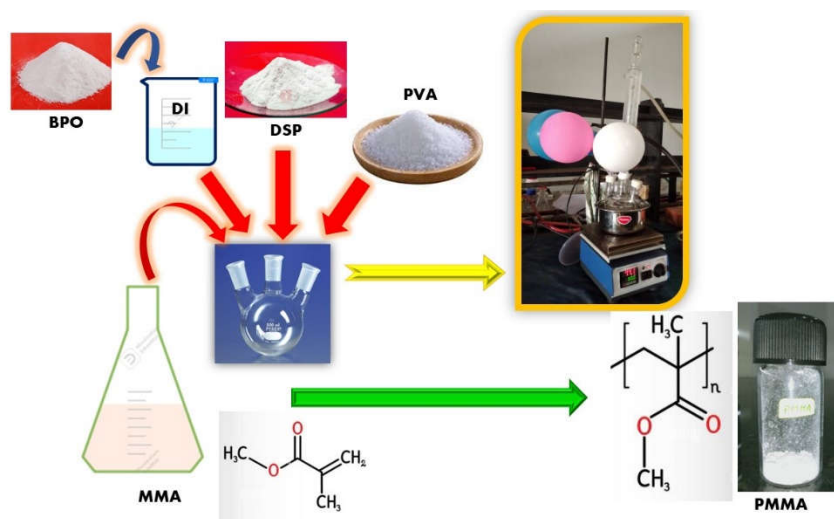
The liquid phase acetylation of toluene catalyzed by the synthesized nanocrystalline zeolites was carried out in a Teflon autoclave under autogenous pressure for three hours. Transfer 8:1 of toluene: AC_2O and the 0.1 g of nanocrystalline zeolites into the autoclave and raise the temperature to 60 °C. Identify the products using gas chromatographic (GC) analysis and an FID detector.

2.6 Synthesis of Nanocrystalline Hierarchical Zeolites by Dual Template Method

2.6.1 Synthesis of PMMA

The polymerization of MMA was carried out in a three-necked flask in a nitrogen atmosphere by free radical polymerization. The method

for PMMA synthesis involves mixing 40 mL of MMA, 0.3 g of BPO, 1.0 g of PVA, and 10.0 g of disodium hydrogen phosphate in 200 mL of water in a 500 mL three-necked round bottom flask. The mixture was agitated at a temperature of 80 °C. Nitrogen was continuously pumped into the flask during the process. The product was filtered, rinsed, and dried to obtain solid PMMA. Scheme 2.5 illustrates the method of preparation.



Scheme 2.5. Method of preparation of PMMA

2.6.2 Synthesis of Defect-Free Nanocrystalline Hierarchical ZSM-5

Nanocrystalline hierarchical ZSM-5 zeolites were prepared using the hydrothermal method. For this, 0.1021 g AIP was added to 6.3400 g TPAOH by stirring using a magnetic stirrer at room temperature. 10.4000 g TEOS was dissolved in water by slow dropwise addition.

The components were mixed well with constant vigorous stirring to hydrolyze the TEOS. The above solution was concentrated and aged in a hot air oven, enabling hydroxylation. The obtained gel was then loaded into a Teflon-lined stainless steel autoclave with x g (x=0.5, 1.0, 1.5, and 2.0) of synthesized PMMA powder and crystallized using hydrothermal treatment at 175 °C for 36 hours without stirring. The product was separated by centrifugation, washed several times using double distilled water, dried at 80 °C, and then calcined at 550 °C for 20 hours in the air to remove residues of TPAOH and PMMA. The hierarchically porous zeolite obtained is named NZ xP. The nanocrystalline ZSM-5 synthesized without incorporating the polymer is named NZ.

2.6.3 Synthesis of Nanocrystalline Hierarchical Zeolite Beta

In this synthesis, 0.2033 g AIP was added to 11.5014 g of TEAOH solution in a polypropylene bottle and then stirred at room temperature using a magnetic stirrer for 30 minutes. 15.0 g of deionized water was added dropwise, followed by 10.4 g of TEOS dropwise. Now, constantly stir it for about 24 hours to hydrolyze it to a transparent solution. The above solution was concentrated at 80 °C at a high pressure of about 700 mmHg for 30 minutes. The resulting mixture was aged 72 hours in a hot air oven at 90 °C, where hydroxylation occurs. The obtained concentrated gel with a slightly grey color is then loaded into a Teflon-lined stainless-steel autoclave with x g of synthesized PMMA as it has to be added at the crystallization step (The synthesis is conducted with x= 2.0 g, 1.5 g,

1.0 g and 0.5 g of PMMA). The zeolite beta is crystallized using hydrothermal treatment at 170 °C for 48 hours without stirring. The product was separated by centrifugation, washed several times using double distilled water, dried at 80 °C, and then calcined at 550 °C for 20 hours in the air to remove residues of TEAOH and PMMA. The obtained samples are NBZ xP, where $x = 2, 1.5, 1.0, 0.5$. The zeolite beta synthesized without adding PMMA is named NBZ.

2.7 Catalytic Activity of Nanocrystalline Hierarchical ZSM-5 and Zeolite Beta

The acetylation of 2-MON catalyzed by the synthesized nanocrystalline zeolites was executed under autogenous pressure. The reaction mixture consists of 2-MON (0.03 mol), acetic anhydride (0.15 mol), and nanocrystalline zeolite as a catalyst. The aliquots of the reaction mixture are occasionally withdrawn. GC analysis identified and confirmed the products.

2.8 Conclusions

The methods outlined in this chapter are powerful for studying zeolites. These have been successfully applied in the present work, as described in the subsequent Chapters. The synthesis methods involved in the preparation of nanocrystalline ZSM-5, metal-modified nanocrystalline ZSM-5, nanocrystalline zeolite beta, metal-modified nanocrystalline zeolite beta, PMMA, nanocrystalline hierarchical ZSM-5 using PMMA, nanocrystalline hierarchical zeolite beta using PMMA are given in detail in this chapter.

Chapter 3

Investigations into Metal-Modified Nanocrystalline Zeolites

Abstract

In this chapter, a thorough examination is conducted on metal-modified nanocrystalline zeolites ZSM-5 and beta. The synthesized zeolites undergo characterization through FTIR, XRD, FESEM, UV-Visible spectroscopy, surface area, and surface acidity measurement. Furthermore, a comprehensive investigation delves into the sustainable catalytic reactions facilitated by these metal-modified zeolites, analyzing how metals in zeolites impact the selective acetylation of toluene under minimal experimental conditions.

Section A

Studies on Metal-Modified Nanocrystalline ZSM-5

3A.1 Introduction

ZSM-5 is an acclaimed microporous aluminosilicate zeolite with extensive use in the catalysis of organic reactions, water and air purification, petroleum refining, etc. Zeolites are also excellent ion exchangers. Aluminium ions in the zeolitic framework instead of silicon ions result in negative charges in the zeolite lattice which are neutralized by alkaline or alkaline earth metals.⁽¹⁾ These additional framework ions can swap with other cations, such as rare-earth elements or transition elements with varying oxidation states. The ZSM-5 crystallographic unit cell contains 96 T sites (comprising Si or Al), 192 O sites, and different quantities of compensating cations, depending upon the Si/Al ratio, which spans from 12 to infinity. The higher Si/Al ratio of ZSM-5 indicates less aluminium content, which in turn suggests that the ion exchanging capacity of ZSM-5 is less. So, this poses a challenge to researchers in improving the properties of ZSM-5, thereby creating a wide window for customizing new materials for different uses. Another significant task assigned to present-day researchers is reducing the zeolite crystal size to less than 100 nm, increasing the total surface area and thereby increasing effective adsorption. A combination of increased surface area and intercrystalline voids makes it ideal for various industrial applications since it permits the use of large reactant molecules.

Over the past ten years, numerous researchers have worked to modify zeolites with various elements. However, most of them have concentrated their research on the catalytic capacity rather than the location and coordination state of additional framework ions within structures.(2–5) After a thorough review of the literature, it was found that there are no systematic studies dealing with extensive modification of nanocrystalline ZSM-5(NZSM-5) using copper, zinc, iron, cerium, lanthanum, and neodymium. The study also exhaustively compares the properties of modified nanocrystalline ZSM-5 with rare earth and transition elements. Examining the impact of these metal ions on textural, spectral, acidic, and structural parameters is the primary goal of this chapter.

3A.2 Results and Discussion

The synthesis of NZSM-5 and the procedure for its metal modification (NZSM-5/M) is explained in detail in Sections 2.4.1 and 2.4.2 of Chapter 2. The formation of the NZSM-5 zeolite phase is confirmed by FTIR analysis. Figure 3A.1 depicts the FTIR spectra of NZSM-5 and NZSM-5/M samples. Table 3A.1 gives different types of vibrations and corresponding frequencies of vibrations (1400 cm^{-1} to 500 cm^{-1}) of synthesized samples.

The FTIR vibration patterns of NZSM-5/M closely resemble those of the NZSM-5, suggesting that modification with metal ions causes minimal structural alterations in NZSM-5. This is attributed to the weak interactions between the cations and the framework. The band

around 550 cm^{-1} , corresponds to the external bonds of double five ring (vibrations of the secondary structural unit, i.e., pentasil). There is a reduction in the intensity of this band for NZSM-5/M compared to NZSM-5 that can be attributed to slight crystallinity loss. The vibrational absorption peak at around 1100 cm^{-1} is attributed to the internal asymmetric stretching of O-Si-O or O-Al-O linkages. The frequency associated with this band is sensitive to the Si and Al content of zeolite and shows some slight displacements in NZSM-5/M. Furthermore, it signifies that the NZSM-5 framework remained largely unaltered following metal modification.(6,7)

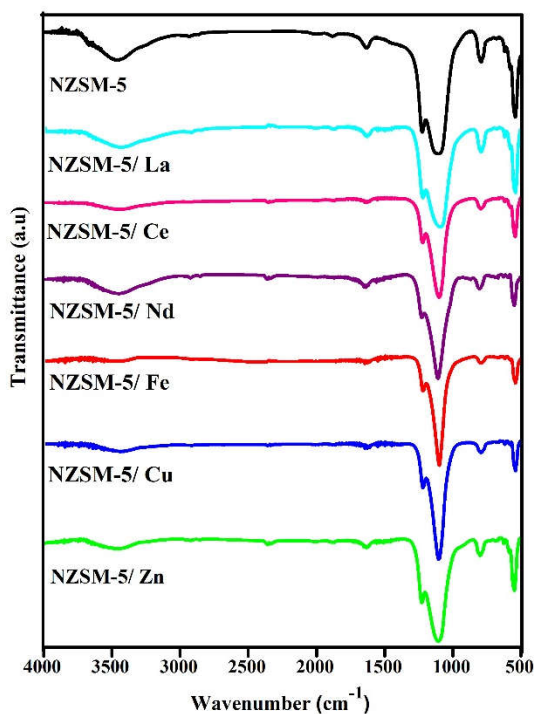
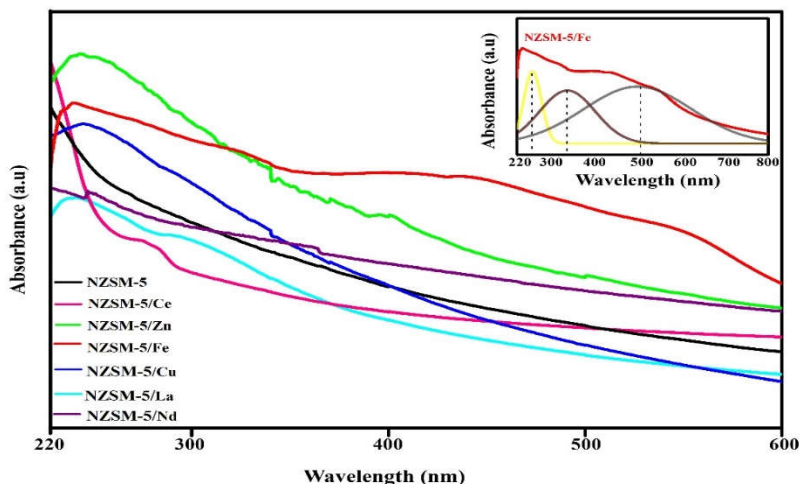


Figure 3A.1. FTIR spectra of NZSM-5 and NZSM-5/M samples

Table 3A.1. The mode and frequency of each vibration for NZSM5 and NZSM-5/M

Sample	Frequencies of vibrations (cm^{-1})			
	External asymmetric stretching	Internal asymmetric stretching	External symmetric stretching	Double five rings of MFI zeolite
NZSM-5	1221	1124	804	555
NZSM-5/Fe	1223	1115	797	545
NZSM-5/Cu	1223	1094	808	544
NZSM-5/Zn	1226	1104	799	547
NZSM-5/La	1224	1103	807	555
NZSM-5/Ce	1221	1113	806	554
NZSM-5/Nd	1223	1114	798	546

**Figure 3A.2.** UV-Visible spectra of NZSM-5 and NZSM-5/M samples with deconvoluted bands of NZSM-5/Fe (inset)

The NZSM-5 exhibits no absorption in the UV-visible band (Figure 3A.2). It indicates the absence of electronic and charge transfer transitions. The spectrum of NZSM-5/M shows peaks at various

wavelengths. The charge transfer transition from O^{2-} to Zn^{2+} sites is indicated by the peak at 250 nm in the NZSM-5/Zn sample. However, a small absorption band of about 380 nm was found, attributed to d-d transition.(8) A band at 250 nm for NZSM-5/Cu shows copper ion interaction with zeolitic oxygen.(9,10) The effective dispersion of copper is proven by the fact that there are no bands at 430-560 nm, which is attributed to dimeric, oligomeric, or aggregated copper oxide.(11–16)

The bands of NZSM-5/Fe were relatively broad, making it difficult to obtain information regarding the distribution of different iron species. The spectrum obtained is similar to those of iron-substituted ZSM-5 in the literature.(17,18) Several characteristic electronic bands can be detected in the 220-800 nm range, which can be attributed to the different iron species, by fitting to deconvoluted Gaussian sub-bands (in the inset of Figure 3A.2). Fe(III) ions that are isolated and in either tetrahedral or octahedral coordination are identified by the band at 250 nm. The oligonuclear $Fe(III)_xO_y$ clusters on the internal and external surfaces of zeolites are attributed to the band ranging from 300 to 400 nm. The peak above 500 nm is attributed to Fe_2O_3 nanoparticles at the surface. The absorption band observed at 275 nm signifies the integration of cerium ions into the NZSM-5 matrix, attributed to the charge transfer from O^{2-} to Ce^{3+} . Additionally, this band serves as confirmation of the effective dispersion of cerium ions within the matrix, revealing a 4f-5d transition occurring at this specific wavelength.(19–22) The UV-Visible spectrum of NZSM-5/La indicates the coordination state of

lanthanum ions. The lanthanum-doped materials have absorption maxima at 250 nm due to the charge transfer transition of O^{2-} to tetrahedrally coordinated La^{3+} in the framework. The octahedrally coordinated La^{3+} in the framework is responsible for the absorption peak at 290 nm.(23) The NZSM-5/Nd spectrum reveals peaks at various wavelengths. The charge transfer transition from O^{2-} to the f orbital of Nd^{3+} is indicated by the peak in the NZSM-5/Nd at 260 nm.(24,25) Furthermore, as the sample contains unpaired f-orbital electrons, an excitonic peak resulting from the transition between different energy levels of the f-sub shell of Nd^{3+} can be observed between 300 to 360 nm. According to the literature, absorbance between 300 and 360 nm corresponds to transitions from $4I_{9/2}$ to $4D_{1/2}+4D_{3/2}$.(26,27)

The nitrogen adsorption isotherms for zeolite samples at 77K are shown in Figure. 3A.3 and Table 3A.2 summarizes their textural characteristics. The NZSM-5 sample exhibits an isotherm, primarily of Type I, typical of only microporous materials. NZSM-5/M, on the other hand, demonstrated a distinct hysteresis loop, a notable slope for intermediate relative pressures, and a dramatic increase for p/p_0 greater than 0.8. This kind of isotherm is typical of mesoporous materials, where intercrystalline porosity plays a significant role in addition to the micropores where adsorption occurs. The presence of micropores is verified by the steep increase in adsorption at low relative pressures. The final calcination step during the synthesis generates mesopores by the creation of intercrystalline voids

between nanosized crystal domains.(28–31) Furthermore, the incorporation of metal ions drives the zeolitic matrix to dissolve smaller nanoparticles leading to redeposition onto larger ones resulting in the merging of pores and the simultaneous formation of mesopores(Ostwald ripening).(32,33) The delayed condensation within these mesopores induces hysteresis in the system.

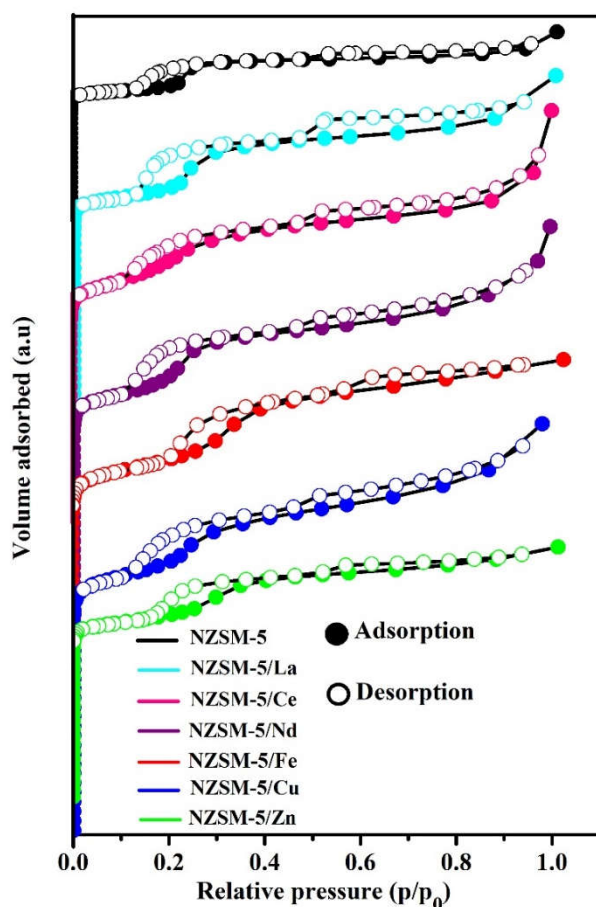


Figure 3A.3. Nitrogen adsorption-desorption isotherm of NZSM-5 and NZSM-5/M samples

Table 3A.2. Textural and acidic properties of NZSM-5 and NZSM-5/M

Sample	Total surface area	Pore volume	External surface area	Total amount of acid sites
	(m ² g ⁻¹)	cm ³ /g	(m ² g ⁻¹)	(mmol/g of ammonia)
NZSM-5	393.89	0.20	64.30	0.17
NZSM-5/La	370.34	0.19	28.32	0.32
NZSM-5/Ce	351.63	0.17	27.71	0.26
NZSM-5/Nd	367.95	0.19	40.17	0.49
NZSM-5/Fe	339.09	0.17	29.45	0.28
NZSM-5/Cu	374.06	0.16	43.41	0.27
NZSM-5/Zn	341.71	0.18	18.26	0.28

In the case of NZSM-5, the initial part of the t-plot (Figure 3A.4), exhibits a sharp increase in pore volume at low thickness (t) values. At high pressure region, a levelling of the plot is observed which corresponds to the filling of the micropore with condensed adsorbate. The metal modification of ZSM-5 is characterized by the presence of both micropores and mesopores, as evidenced by the deviation from linearity at the high-pressure region, which makes the shape of the t-plot more complex. Capillary condensation and micropore filling are responsible for the divergence from linearity.

When metal ions are added, the total surface area and pore volume of NZSM-5/M samples decrease marginally. This decrease is due to the partial blockage of pores by poorly dispersed, extra-crystalline metallic species. It occurs due to the limited access to the internal surfaces of zeolite samples. The form of the t-plot offers more proof

that metal ion inclusion is the source of the pore blockage of zeolite channels. As per literature, when the t-plot passes through the origin, it indicates the lack of microporosity.(34,35) However, in this study, the t-plots for all zeolite samples do not pass through the origin and this proves the existence of micropores within the samples. This observation confirms that introducing metal ions has not entirely obstructed all micropores, indicating that some of them remain accessible.

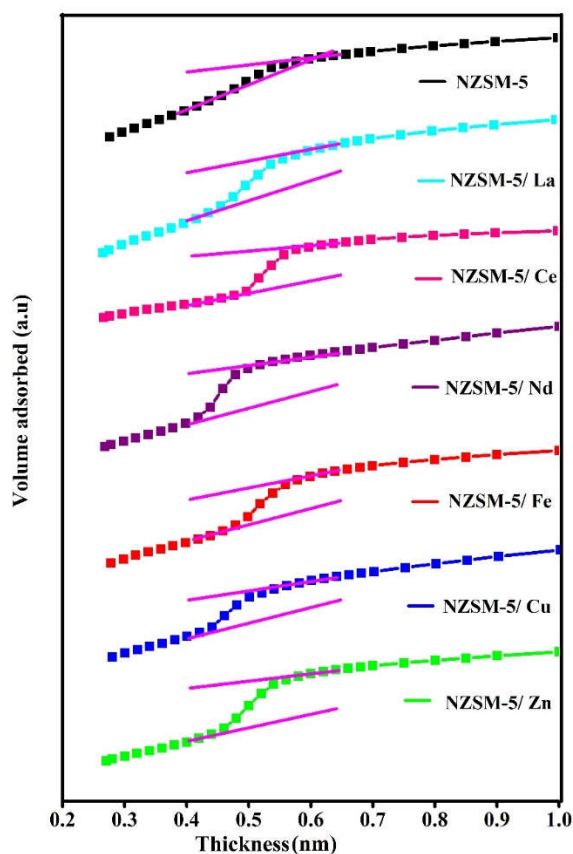


Figure 3A.4. t-plot of NZSM-5 and NZSM-5/M samples

Figure 3A.5 depicts the NH_3 -TPD profiles NZSM-5 and NZSM-5/M samples. Table 3A.2 provides the acidity of zeolite samples. TPD profiles of NZSM-5/M show the presence of peaks at 180 °C, 300-400 °C, and above 500 °C, corresponding to weak, intermediate, and strong acid sites. Low-temperature peaks correspond to acidity imparted by physically adsorbed weak acid sites, whereas high-temperature peaks correspond to chemisorbed strong acid sites. The desorption of ammonia from strong Bronsted and Lewis acid sites is indicated by the high-temperature peaks.(36) Weakly held ammonia, most likely hydrogen bound, is responsible for the low-temperature peak.(37) The intensity of the low-temperature peak decreased as the degree of ion exchange increased, suggesting a reduction in weak acid sites. Conversely, the intensity of the high-temperature peak rose, indicating the further emergence of acid sites due to the ion exchange process.

When metal particles are added, the acidity rises, indicating the interaction of the metal species with the protonic sites in the NZSM-5 zeolite. The peaks of NZSM-5/M exhibit slight widening and shift towards the high-temperature region. It is evident from the TPD profile that new peaks are found at intermediate temperatures, indicating the generation of new acid sites. The TPD profile of NZSM-5/Zn has a high-intensity low-temperature peak that widens towards the intermediate region. Zinc loading increased the intensity of the intermediate region compared to NZSM-5 due to the exchange

of H^+ with Zn^{2+} . This suggests that Zn^{2+} ions interacted with Bronsted acid sites on NZSM-5/Zn to form cationic Zn species that coordinated with the oxygen atoms in the pore channel. Thus, the stronger acidity of the acid center increases the electron cloud density in the zeolite framework.(38) Incorporating copper into the zeolite structure significantly improved the surface acidity of NZSM-5. The desorption profile of NZSM-5/Cu depicts the different types of acidities exhibited. The exceptional nature of the peak of NZSM-5/Cu sample is due to the decomposition of copper ammonia complex, resulting in a significant rise in intensity of the desorption peaks of intermediate acid sites (300-400 °C).(39) On the other hand, a significant increase in the intensity of peaks corresponding to three desorption regions was seen in iron-modified zeolites. NH_3 desorbed from weak silanol (Si-OH) is the cause for the peak at lower temperatures (usually < 200 °C). However, the desorption peaks at higher temperatures (usually between 350 and 550 °C) are attributed to NH_3 , which is highly adsorbed on acidic hydroxyl groups or Bronsted acidic sites.(40)

All three desorption peaks are present in the NH_3 -TPD profile of NZSM-5/Ce, indicating the presence of weak Lewis and Bronsted acid sites. The cerium-modified samples show more prominent peaks corresponding to strong and moderate acid sites. The results suggest that adding neodymium to the zeolite significantly raised the surface acidity. As a result, extra ammonia chemisorption centers are

formed when Nd is present on the surface of ZSM-5. The acidic characteristics of lanthanum oxides are responsible for the increased acidity of NZSM-5/La. The weak Lewis acidic nature of La^{3+} is responsible for the increased acidic nature of NZSM-5/La. The bridging hydroxyl groups in the ZSM-5 channel entrances can interact with La species, reducing the Bronsted acid sites of zeolite.(41,42)

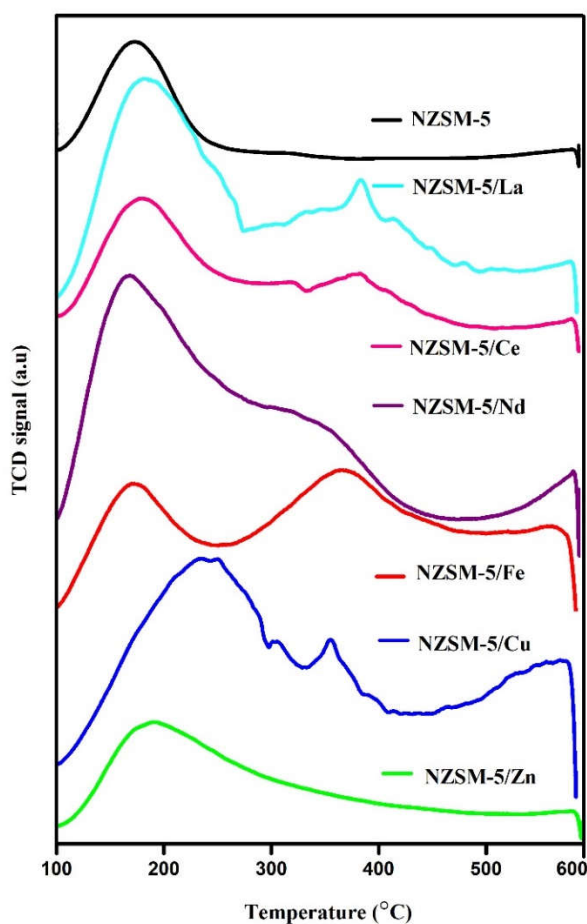


Figure 3A.5. TPD profile of NZSM-5 and NZSM-5/M samples

The SEM images of the nanocrystalline ZSM-5 and metal-modified samples are furnished in Figure 3A.6. A typical spherical-shaped MFI crystal structure made of an assembly of tiny crystallites is obtained for NZSM-5.(43–45) The particle size ranges up to 100 nm for both modified and unmodified samples, the larger aggregates comprise of numerous individual or intergrown zeolite particles. The average crystallite size of the NZSM-5 and NZSM-5/M samples ranges from 10 to 50 nm, which agrees with the result obtained from the Scherrer equation 2.2. This observation confirms the presence of nanometric particles in all samples. The performance of a catalyst betters when more of its reactive sites are exposed by attaining the size of the nano range. The agglomerative morphology of the nanoparticles of all zeolite samples leads to a spherical shape, and some intercrystalline voids were seen both inside and on the surface of the spheres. As zeolites are exposed to both their exterior and interior surfaces due to their channel-like morphology, the metal introduced produces spherical crystal aggregates with a rough surface.(46–49) It is evident that following the ion exchange treatment, the morphology of the ZSM-5 zeolite stayed essentially unaltered. The particles are distributed as aggregate clusters at the surface of NZSM-5, which is the only visible difference.

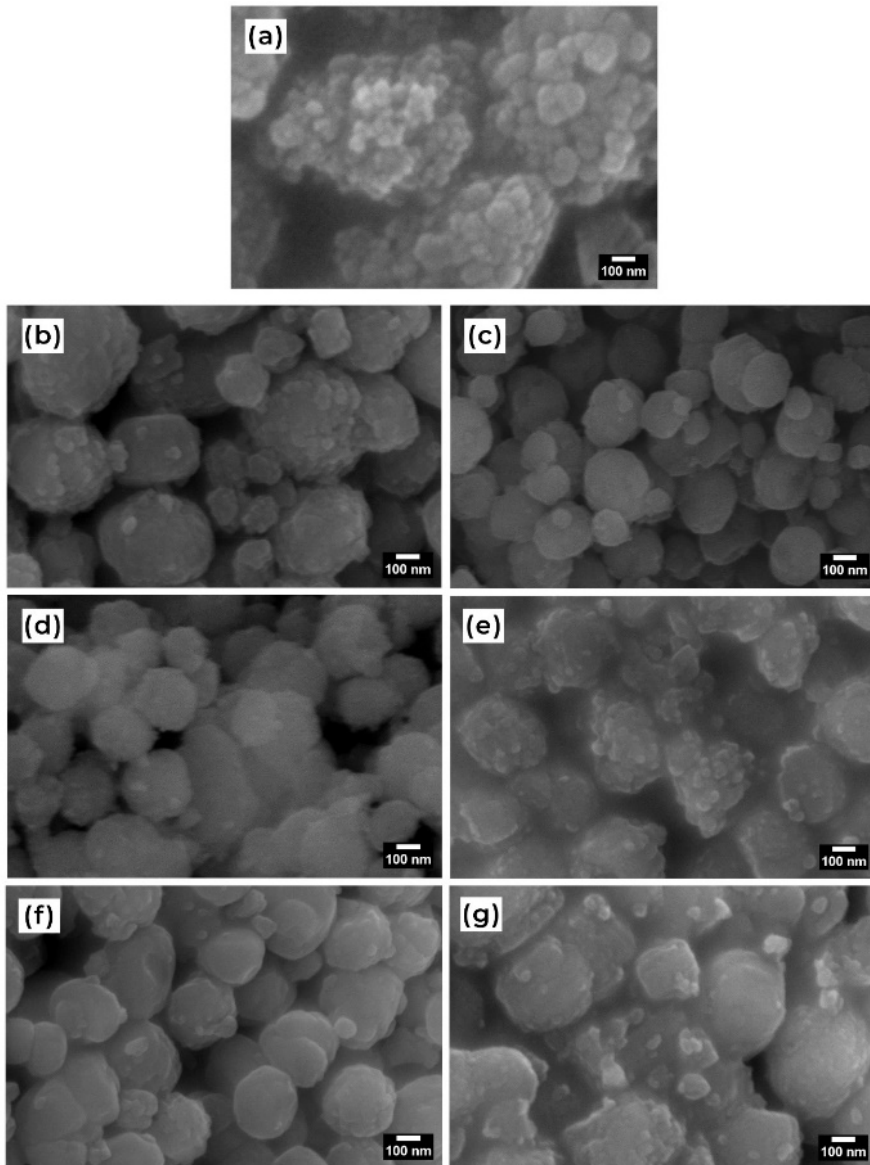


Figure 3A.6. SEM images of zeolite samples (a) NZSM-5 (b) NZSM-5/La (c) NZSM-5/Ce (d) NZSM-5/Nd (e) NZSM-5/Fe (f) NZSM-5/Cu (g) NZSM-5/Zn

²⁷AlMAS NMR spectroscopy was used to obtain information about structure integrity by studying the aluminium distribution (Figure 3A.7). The strong signal at 53 ppm is assigned to a tetrahedrally coordinated aluminium framework, which can be found in all zeolite samples.⁽³⁹⁾ The weak signal at 0 ppm shows the presence of octahedral non-framework or extra-framework aluminium; it can be found in zeolite samples such as NZSM-5 /Ce and NZSM-5 /Cu. The peak positions have slightly moved from their original positions. It indicates that the NZSM-5 are primarily aluminosilicates with tetrahedral framework, and NZSM-5/Ce and NZSM-5 /Cu possess only a relatively minor amount of extra-framework Al species. This confirms dealumination, during the modification process. In the case of other metal-modified samples, the dealumination hardly takes place; however, a tiny shift in the position of tetrahedral aluminium is also visible. Increasing line width and decreasing peak intensity are also observed in the NZSM-5/M; this is attributed to a rise in local heterogeneity of the modified samples compared with the unmodified ones.

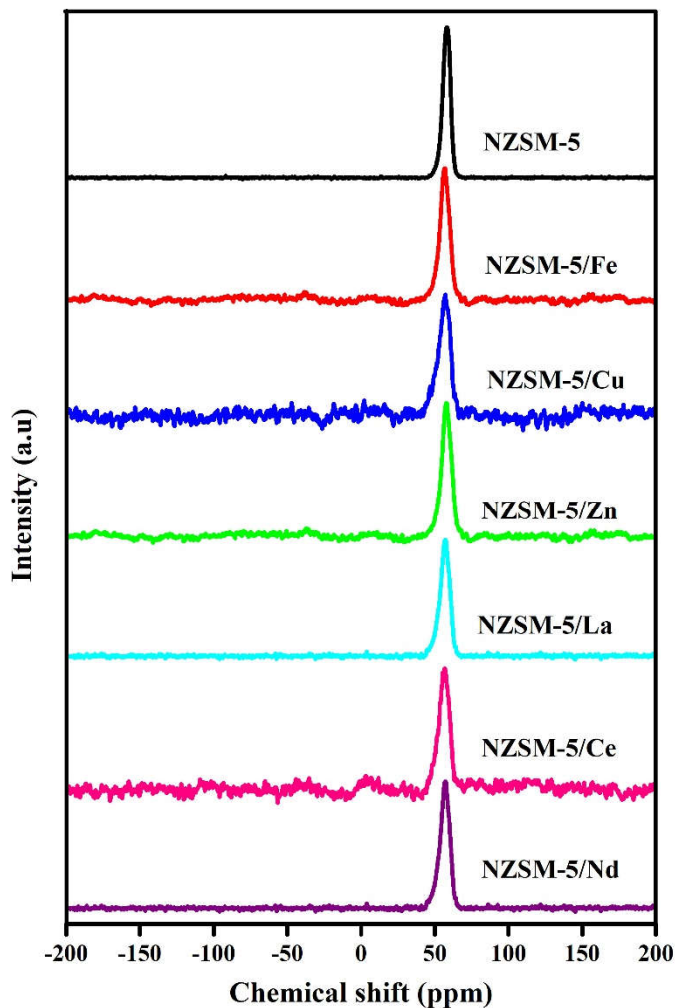


Figure 3A.7. ^{27}Al MAS NMR of NZSM-5 and NZSM-5/M samples

The presence of metal ions significantly alters the general properties of the zeolite. Substantial evidence of modification includes the blockage of pores, the intensification of acidic characteristics, and the difference in absorption maxima in UV-Visible regions. While incorporating these elements, XRD analysis emphasizes the

crystalline characteristics of zeolite. The overall composition of the synthesized samples is studied by the EDX analysis (Table 3A.3). The ionic radius of incorporated ions can be partially linked to the percentage incorporation of each element.(2)

Table 3A.3. The elemental composition of NZSM-5 and NZSM-5/M

Sample	Atomic percentage of elements (%)								
	Si	Al	O	La	Ce	Nd	Fe	Cu	Zn
NZSM-5	39.48	0.74	59.78	---	---	---	---	---	---
NZSM-5/ La	29.22	0.53	69.72	0.53	---	---	---	---	---
NZSM-5/ Ce	31.93	0.48	66.93	---	0.66	---	---	---	---
NZSM-5/ Nd	35.27	0.64	61.04	---	---	2.15	---	---	---
NZSM-5/ Fe	38.39	0.54	57.82	---	---	---	3.24	---	---
NZSM-5/ Cu	31.78	0.5	66.23	---	---	---	---	1.49	---
NZSM-5/ Zn	26.20	0.64	71.19	---	---	---	---	---	1.97

Figure 3A.8 shows the powder XRD patterns of the NZSM-5 and NZSM-5/M zeolites having different metal ions. The planes [313], [303], [051], [031], [020], and [011], are linked to the observed typical diffraction peaks at $2\theta = 24.44^\circ$, 23.96° , 23.14° , 14.82° , 8.82° , and 7.98° respectively. All these values correlate to the

JCPDS card number, 00-037-0359, and the simulated XRD from IZA. They are all indexed to the ZSM-5 structure. All these values are indexed to the ZSM-5 structure and correspond to the JCPDS card no: 00-037-0359 and simulated XRD from IZA. The XRD results indicate the purity of the sample and ensure the MFI structure of all the samples. The sharp peaks suggest that the ZSM-5 samples possess good crystallinity. A slight decrease in peak intensity was observed upon modification with metals compared to NZSM-5. No signals corresponding to the metals or metal oxides were detected in any NZSM-5 samples and this is due to insufficient metal loading or the metal crystallites being too small for detection by XRD. This indicates a high dispersion of the metals within the zeolite structures.

While comparing the XRD patterns of NZSM-5 and NZSM-5/M zeolites, all of them showed similar diffraction peaks, suggesting that the framework structures were not much affected by the loading of metal ion species. XRD profile analysis was used to determine the average crystal size, crystallinity, dislocations, and lattice strain of zeolite nanocrystals using respective equations 2.1, 2.2, 2.3, and 2.4.

The average crystallite size and percentage crystallinity are given in Table 3A.4. Meanwhile, a slight decrease in the percentage crystallinity was observed in NZSM-5/M zeolites, this is ascribed to the intermixing and high dispersion of metal ion species with the zeolite.

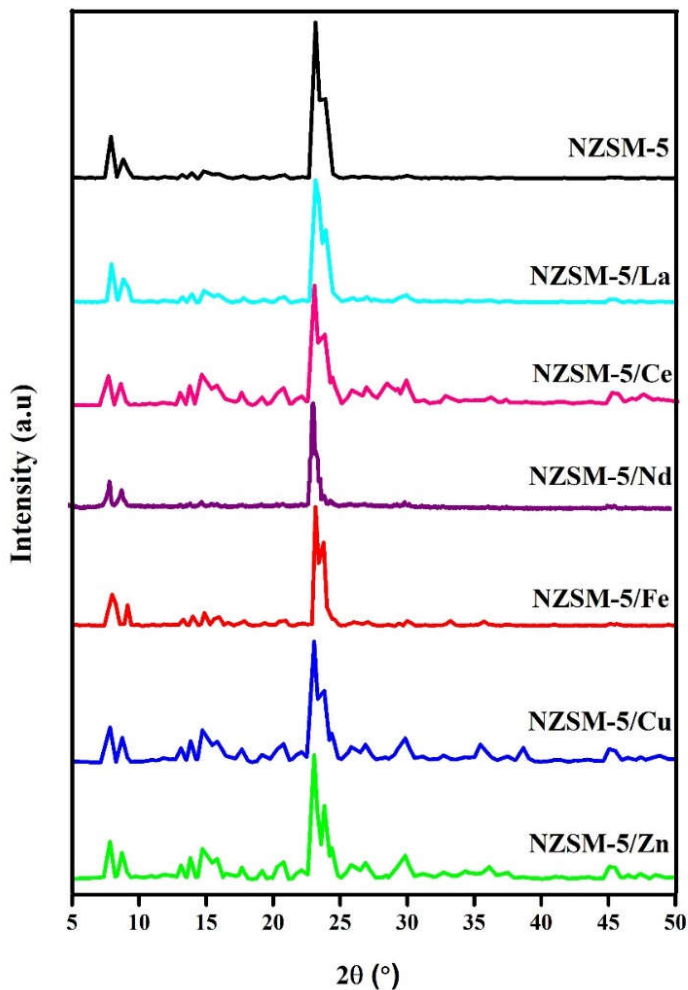


Figure 3A.8. XRD patterns of NZSM-5 and NZSM-5/M samples

The dispersion of the metal species dispersed on the external surface of NZSM-5 are anchored at the cation-exchange sites, potentially leading to distortion of lattice within NZSM-5. Consequently, the metal species interact partially with the NZSM-5 framework,

influencing its lattice structure.(50) Even though the metal modification leads to no substantial change in the crystal structure, the lattice experiences a slight amount of strain.

When zeolite nanocrystals are synthesized, an average crystal size of less than 40 nm is achieved. The acquired results indicate that the hydrothermal synthesis method combined with the ion exchange process, yields nanoparticles with an average size of less than 100 nm. The crystalline nature of the nanoparticle can be further assessed by the dislocation density value (δ) using the equation (2.3). The magnitude of crystal defects, i.e. the dislocation lines per unit volume of crystal, is tabulated in Table 3A.4.

The δ value of NZSM-5 is $0.71 \times 10^{-3} \text{ nm}^{-2}$. As depicted in Figure 3A.9, the δ value of NZSM-5 is relatively tiny compared to the metal-modified ones. The degree of crystallinity is high for NZSM-5. Upon metal modification, the crystallinity decreases, which indicates that metal-modified zeolite samples have more lattice imperfections incorporated due to the deposition of nanometal oxides, thereby causing a rise in the dislocation density.

Table 3A.4. Structural parameters NZSM-5 and NZSM-5/M samples

Sample	Crystallite size(nm)	Dislocation density $\times 10^{-3}$ (nm⁻²)	Lattice strain (%)	Crystallinity (%)
NZSM-5	37.55	0.71	0.88	80.95
NZSM-5/Fe	13.75	5.29	1.73	75.53
NZSM-5/Cu	13.43	5.57	1.56	70.30
NZSM-5/Zn	14.50	4.76	1.33	71.10
NZSM-5/La	13.10	5.82	1.67	73.41
NZSM-5/Ce	11.72	7.28	1.56	68.56
NZSM-5/Nd	12.53	6.36	2.24	62.28

The interconnection between defects and lattice strain is crucial, as they are closely related. When a defect, such as a dislocation, is present, the crystal lattice surrounding it undergoes elastic distortion or strain. Diffraction peaks broaden as a result of these elastic fields, and the degree of strain depends on the non-uniform lattice distortions. There is a progressive decline of the elastic strain field around dislocations from the dislocation core; the total effect of all dislocations plays a major role in X-ray scattering. Strain is produced by the uniform distribution of tension throughout the lattice, and strain shifts the diffraction peaks. For instance, stresses and tiny crystalline domains (size effects) in nanostructured materials cause the diffraction profiles to expand.(51)

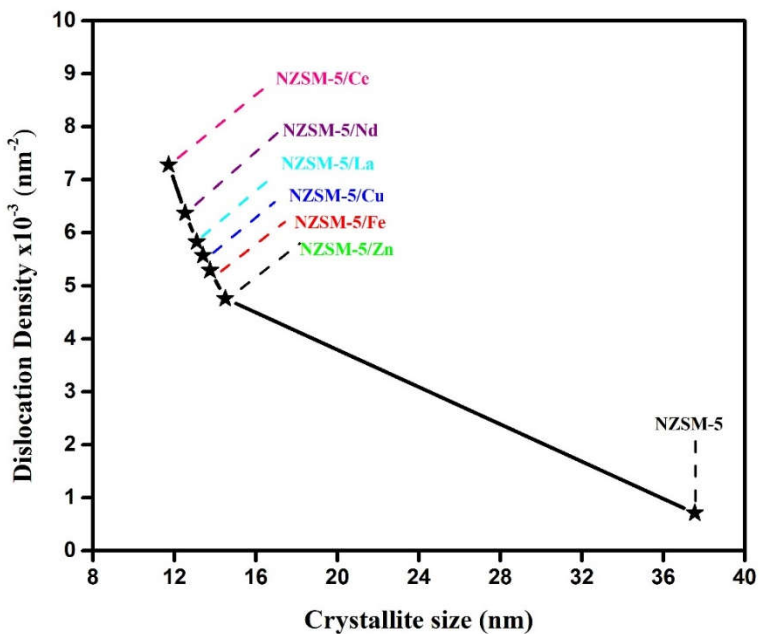


Figure 3A.9. Variation of dislocation density with crystallite size of NZSM-5 and NZSM-5/M samples

Lattice strain increases during modification with metal ions, specifically by decreasing the crystallite size, leading to a lattice shrinkage effect. The reduced crystallinity of the modified nanocrystalline zeolite contributes to the increased lattice strain. Figure 3A.10 illustrates the variation in crystallinity and lattice strain based on data obtained from elemental composition identification.

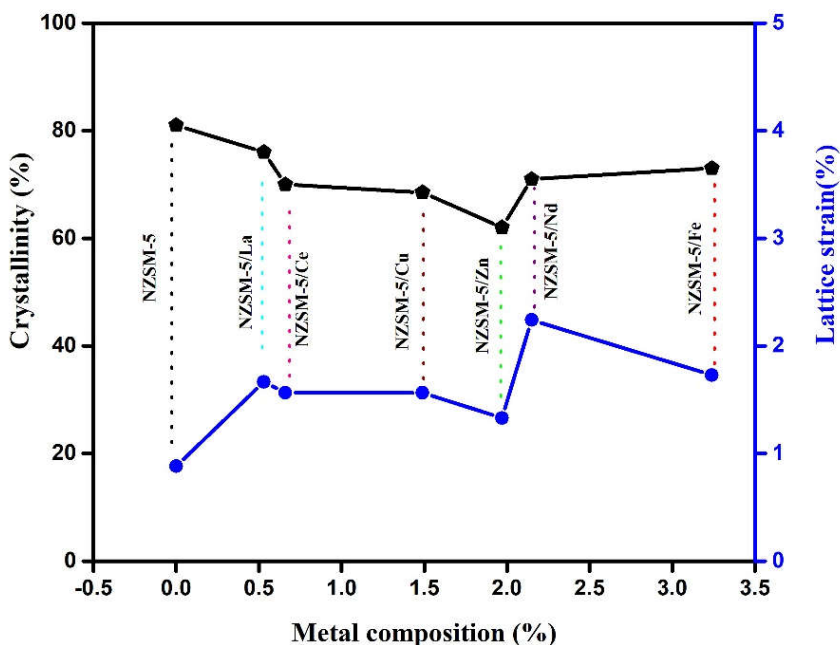


Figure 3A.10. Variation in crystallinity and lattice strain by the elemental composition

Compared to metal-loaded zeolites, the NZSM-5 exhibits a greater crystallite size, higher crystallinity, and lower strain. The loading of metal ions in NZSM-5 increased the lattice strain but did not affect the MFI crystal structure. The shift in crystal strain can be connected to the size of the atoms or ions substituted in the zeolitic matrix, with bigger the size higher the lattice strain. Furthermore, the greater loading capacity of iron and neodymium ions in zeolite caused the increase in the lattice strain seen in Nd^{3+} and Fe^{3+} exchanged NZSM-5 compared to all other metal-exchanged NZSM-5 in this study. The increased loading of Fe^{3+} cations can be attributed to the compact ionic radius and elevated charge density of Fe^{3+} cations compared to

Cu^{2+} and Zn^{2+} within the pores which enable them to form stronger bonds with the zeolite structure. Likewise, the reduced ionic radius and heightened charge density of Nd^{3+} cations, in contrast to La^{3+} and Ce^{3+} within the pores, facilitate stronger binding to the zeolite structure, leading to more significant loading into the framework.

The findings imply that the zeolites can effectively host various ions without significant strain, enhancing their acidic, pore, and overall properties. It suggests that the incorporation of metals into zeolite crystals might cause small cracks to form mesopores. Putting cations into the zeolite structure helps relieve strain, resulting in mesopore formation.

3A.3 Conclusions

A substantial contribution is made by transition and rare earth element-containing nanocrystalline zeolites to the field of catalysis. This chapter depicts the modification of hydrothermally synthesized nanocrystalline ZSM-5 by iron, copper, zinc, lanthanum, cerium, and neodymium using the ion exchange method. A thorough investigation of metal-doped nanocrystalline ZSM-5 sheds light on the modifications made to the acidity, textural characteristics, and structural parameters. According to the SEM results, every zeolite sample has spherical crystals with less than 40 nm crystallite size. The modified samples exhibit absorption in the UV-Visible region, whereas the unmodified ZSM-5 does not. The TPD studies reveal a substantial increase in the acidity of metal-modified nanocrystalline

ZSM-5. XRD analysis confirms that metal modification affects the crystallinity and lattice stability of the zeolite framework. According to the N₂ adsorption isotherm, the total surface area and pore volume of ZSM-5 were slightly reduced with the impregnation of metal ions. It can be said that the formation of hierarchical porosity in metal-modified samples occurs due to the presence of slight lattice strain within the crystallites. Therefore, the crystals attempt to relax this strain, ultimately resulting in the formation of heteroporosity. The results of the characterization suggest that zeolites can efficiently host different metal ions, thereby tuning the nanocrystalline ZSM-5 to be excellent catalysts by improving their acidic properties, bettering the porous nature, and at the same time retaining the crystalline nature.

Section B

Studies on Metal-Modified Nanocrystalline Zeolite Beta

3B.1 Introduction

Zeolite beta is one of the most widely used and first discovered zeolites. It was synthesized even before Mobil patented ZSM-5. It is characterized by the BEA structure and classified among large-pore zeolites. It also possesses a three-dimensional channel structure featuring rings containing 12 oxygen atoms. Its notable attributes, such as excellent thermal stability, hydrophobicity, acid resistance, high catalytic activity, and prolonged service life, render it advantageous in various catalytic reactions. Several studies have indicated that zeolite beta serves as a catalyst for diverse organic reactions and plays a role in purifying water. The alteration of catalytic activity and molecular sieving properties in zeolites is recognized through cation exchange. Introducing transition metals like copper, iron and zinc along with rare earth elements such as lanthanum, cerium and neodymium has been demonstrated as a compelling approach to create effective catalysts for various processes, including acetylation, selective catalytic reduction, dye removal, aromatization, cracking, isomerization, hydration, and decomposition.^(7,4,52–68) Incorporating these elements to modify zeolite beta significantly enhances its stability and activity in these reactions.

Numerous investigations have provided insights into the structures of active sites and reaction mechanisms, shedding light on the connection between physicochemical properties and catalytic

performance. The cation exchange process results in the deposition of various entities within the micropore channels. These include mono- and binuclear metal species and small oligonuclear clusters, which act as active sites for various reactions. Based on the chosen method of preparation, the quantity and nature of the metal species formed differ. The preferred method for ion exchange is solution-based due to its simplicity and ease of control. Nevertheless, a significant challenge with this approach arises from the incomplete exchange, as the pore channels hinder the diffusion of metal ion precursors. The extent of exchange is influenced by variations in diffusion paths, zeolite crystallite size, or changes in pore channel structure, leading to alterations in the acidity and overall performance of zeolite beta.

This chapter depicts the synthesis of metal-modified nanocrystalline zeolite beta by ion exchanging with transition and rare earth elements, focusing on elucidating the internal structure, morphology, and texture. Several research efforts have concentrated on altering the properties by exchanging diverse metal cations. Despite the extensive exploration of metal cation exchange in nanocrystalline zeolite beta, relatively few investigations have been conducted in this domain. To the best of current knowledge, no studies in the open literature directly compare and evaluate the enhancement of properties of zeolite beta using La, Ce, Nd, Cu, Zn, and Fe. The difficulty arises from the limited external surface area and the scarcity of exchangeable positions, making it challenging to achieve highly dispersed metal ions on the surface of zeolite beta. Special attention is given to the effects of modification on acidic

characteristics and textural properties to better understand the presence of metal species within the zeolite structure and their role in contributing to lattice strain and dislocations.

3B.2 Results and Discussion

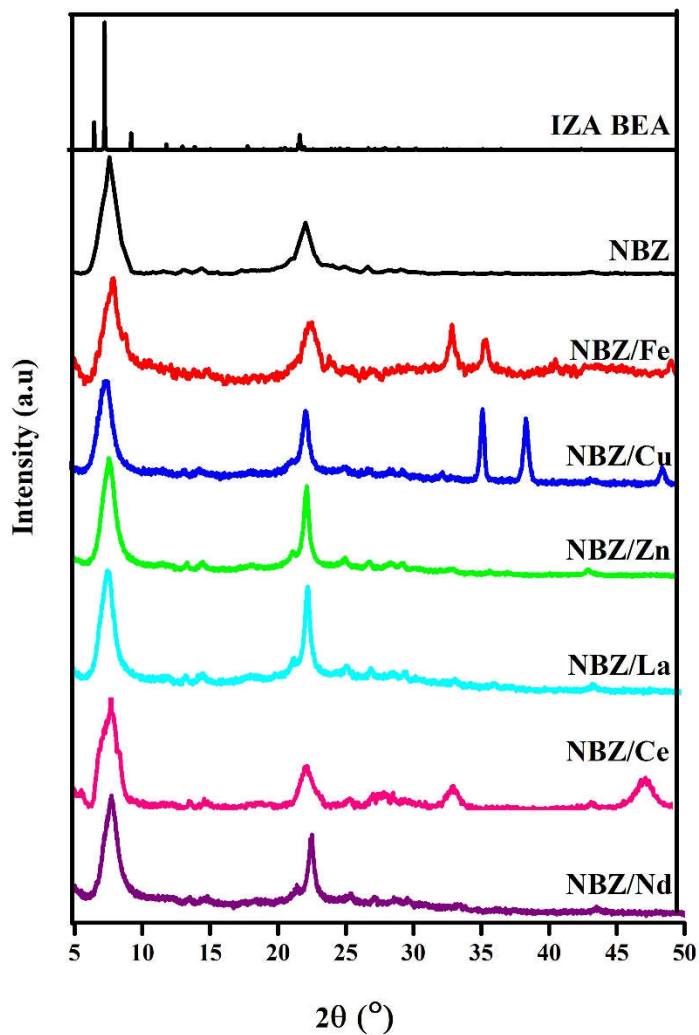


Figure 3B.1. XRD patterns of NBZ and NBZ/M samples with simulated pattern

The synthesis of NBZ and the procedure for its metal modification (NBZ/M) is explained in detail in Sections 2.4.3 and 2.4.4 of Chapter 2. Figure 3B.1 displays the XRD patterns of synthesized samples along with the simulated pattern. The simulated data was obtained from the IZA website. The diffractograms of the NBZ and NBZ/M reveal distinctive peaks at $2\theta = 6.98$ to 8.31 and 22.46 to 23.86 that indicate the zeolite beta of the BEA framework having good crystallinity. The overlap of four peaks at $2\theta = 6.98$ (100) plane, polymorph A; 7.74 (101), polymorph A; 7.34 (110), polymorph B; and 8.31 (111), polymorph B, causes the broad peak in the low angle area ($6.98 - 31$). The overlap of peaks at $2\theta = 22.46$ (311) plane, polymorph A; 22.64 (422) plane, polymorph B; 22.65 (240) plane, polymorph B; 23.03 (222) plane, polymorph B; and 23.86 (113) plane, polymorph B is used to explain the broad peak at 22.46 to 23.86 . Therefore, it proves the fact zeolite beta is an intergrown hybrid of polymorphs A and B.(69)

The analysis of spectra of NBZ/Fe, NBZ/Cu, and NBZ/Ce reveals the presence of additional peaks than those in NBZ in the range $2\theta > 30^\circ$, which serves as an indication of the existence of bulk oxides within the structural composition of these samples. This observation implies that the metal ions and metal oxides in these particular samples are not uniformly distributed or dispersed. There is a lack of homogeneity in the arrangement of these particles, leading to the emergence of distinct peaks in the pattern. Conversely, while examining the pattern of NBZ/Zn, NBZ/La, and NBZ/Nd samples,

the absence of such additional peaks suggests a different scenario. In these cases, there is a notable absence of agglomeration of bulk oxides within the structure, indicating that the metal ions and metal oxides are perfectly dispersed. The lack of distinct peaks in the pattern for these samples points towards a higher degree of uniformity and homogeneity in the distribution of particles, highlighting a more ideal dispersion. The intensity of the peaks is reduced. This is due to the lowering of crystallinity in the ion exchange process. The total crystallinity, crystallite size, and lattice strain of samples are tabulated in Table 3B.1. The average crystallite size and percentage crystallinity of NBZ and NBZ/M were determined by using equations (2.1) and (2.2) respectively.

Table 3B.1. Structural parameters of NBZ and NBZ/M

Sample	Crystallinity (%)	Crystallite size (nm)	Lattice strain (%)
NBZ	77.75	17.20	1.63
NBZ/La	64.91	21.75	2.19
NBZ/Ce	59.74	10.57	2.72
NBZ/Nd	55.80	13.76	2.31
NBZ/Fe	52.22	16.35	2.08
NBZ/Cu	61.09	24.77	2.14
NBZ/Zn	66.45	13.77	2.28

The XRD pattern obtained for nanocrystalline zeolite beta and its metal analogs features an average crystallite size below 30 nm. Lattice strain is found to be increased during modification. The primary sources contributing significantly to lattice strain in metal-

modified nanocrystalline beta samples are identified as dislocations and the excess volume at grain boundaries between metal oxides and zeolites. In general, excessive lattice strain poses the risk of diminishing the stability and structural integrity of zeolites, potentially leading to framework collapse or distortion and impacting their long-term functionality. At the same time, it is clear from Table 3B.1 that incorporating metal ions in this study does not lead to a substantial increase in lattice strain. Furthermore, the positive aspect of the very slight increase in lattice strain is that it induces alterations in the pore size and shape selectivity of zeolites, further increasing their acidic and textural properties.

The formation of the zeolite beta phase is further confirmed by FTIR analysis. The FTIR spectra of modified and unmodified samples are shown in Figure 3B.2. FTIR spectroscopy is used to probe the structure of zeolites. Significant bands are visible in the 500 cm^{-1} to 1700 cm^{-1} of NBZ and NBZ/M, together with additional bands at the 3450 cm^{-1} and 1630 cm^{-1} regions. The broad bands seen for all zeolite beta samples are caused by stretching vibrations of the hydroxyl groups at 3450 cm^{-1} and bending vibrations of the water molecules in the lattice at 1630 cm^{-1} respectively. The 1097 cm^{-1} absorption peak in zeolite beta corresponds to the internal asymmetric stretching vibration of the O-Si-O bonds or O-Al-O bonds and it is susceptible to the aluminium content in the zeolite. The wavenumber rises as the aluminium content decreases within the zeolite structure, thus signifying a shift in the framework of NBZ/M.(70) Consequently, this specific vibration band shifts towards higher wavenumbers during the modification with metals. Additionally, the absorption

peaks at 796 cm^{-1} and 1230 cm^{-1} are associated with the external symmetric stretching and asymmetric stretching of Si–O–Al linkages, respectively. Notably, the double six-ring and double four-ring lattice vibrations of zeolite beta manifest as bands at 524 cm^{-1} and 573 cm^{-1} , respectively. These bands verify the existence of the zeolite beta structure. The decrease in intensity of metal-modified samples typically suggests a loss of crystallinity and that is inferred from XRD.

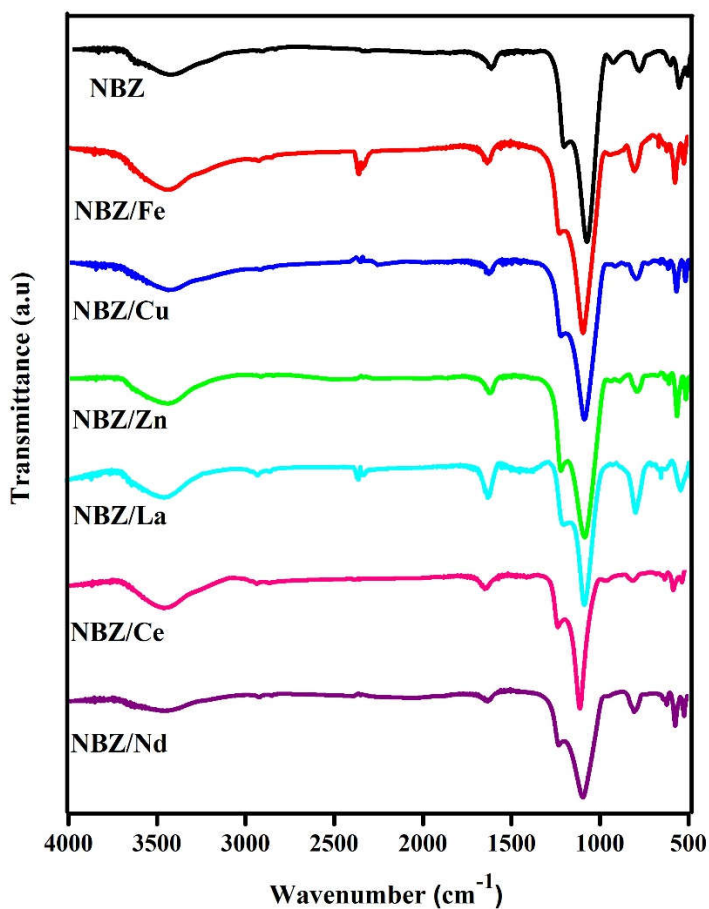


Figure 3B.2. FTIR patterns of NBZ and NBZ/M samples

UV-Visible spectroscopy has been widely employed to describe the nature and coordination centers impacted by the incorporation of metal oxide or metals in zeolite beta structure. The spectra obtained are shown in Figure 3B.3. The UV-Visible range shows no peak for the NBZ sample (inset of Figure 3B.3) signifying that there are no electronic or charge transfer transitions. On the other hand, the metal ion species in the zeolite framework are responsible for the peaks in the NBZ/M spectrum at 220 and 800 nm.

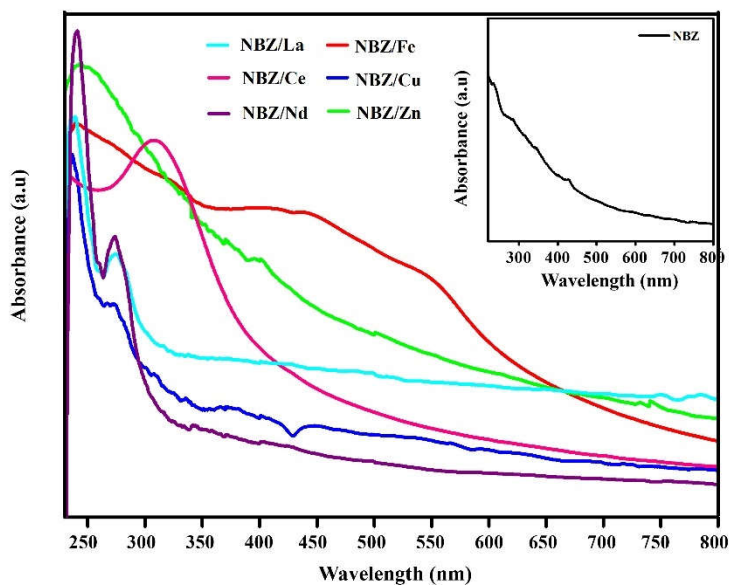


Figure 3B.3. UV-Visible spectra of NBZ/M samples with spectra of NBZ (inset)

The two distinct peaks spotted for the NBZ/Fe sample are at less than 300 nm and in the range 300-400 nm. The peak below 300 nm is associated with the charge transfer transition from oxygen to Fe, and

the broad peak (300-400 nm) suggests the presence of Fe^{3+} octahedra in the Fe_xO_y oligomer clusters.(71) The presence of Fe_2O_3 particles also explains the broad band observed in this sample between 400 and 650 nm.(43,55) A band at 250 nm for NBZ/Cu demonstrates the interaction of copper ions with zeolitic oxygen.(9,10) The bulk CuO exhibits absorption maxima at 380 nm which is absent in the present study but a band at 270 nm is detected which is attributed to blue shift by nano-CuO particles as an effect of nanoparticle size.(72) The literature states that, aggregated, oligomeric, or dimeric copper oxide will result in bands at 430–560 nm.(11,12) The surface of zeolite does not contain these aggregating species, as indicated by the absence of bands in this region. According to UV-Visible patterns of NBZ/Zn, no absorption band is found at 380 nm, indicating that bulk ZnO did not exist in the matrix. The increase in absorbance seen in the NBZ/Zn spectra at about 250 nm is attributed to sub-nanometer ZnO.(8,59)

The peaks observed in the NBZ/La spectra at 240 and 270 nm are ascribed to the extra framework lanthanum species and the La species in the zeolite framework respectively. The absence of peaks at higher than 500 nm indicates the lack of bulk lanthanum oxide species. A strong band was observed at 240 nm due to the charge transfer transition from O^{2-} to tetrahedrally coordinated La^{3+} . Furthermore, the hexa-coordinated La^{3+} species in the extra framework of NBZ/La is responsible for the absorption peak at 270 nm.(23,73)

The peak seen at 325 nm for NBZ/Ce sample is due to the intrinsic absorption of cerium oxide nanoparticles where electron transfer from the valence band to the conduction band occurs. In contrast, peaks at about 300 nm were found in cerium oxide as a result of the absorption due to charge transfer from O^{2-} (2p) to Ce^{3+} (4f).(74)

There are multiple peaks at different wavelength visible in the NBZ/Nd spectrum. Signals arise when the f orbital of Nd^{3+} interacts with nearby O^{2-} ions. The peak in the NBZ/Nd at 260 nm indicates the charge transfer transition from O^{2-} to Nd^{3+} sites.(25)

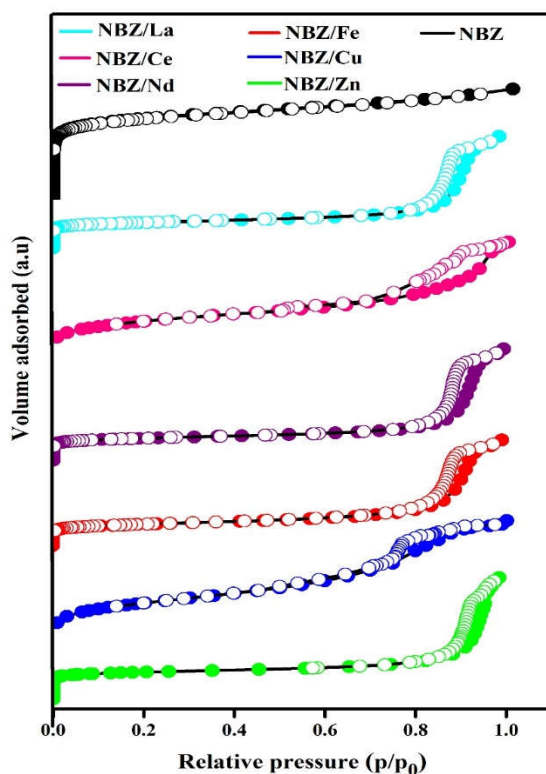


Figure 3B.4. Nitrogen adsorption-desorption isotherm of NBZ and NBZ/M samples

Table 3B.2. Textural and acidic characteristics of NBZ and NBZ/M samples

Sample	Total surface area (m ² /g)	Pore volume (cm ³ /g)	BJH Pore distribution range (nm)	Acidity (mmol/g of ammonia)
NBZ	541.23	0.31	2-3	0.89
NBZ-Fe	396.43	0.20	4-14	1.54
NBZ-Cu	479.65	0.20	5-9	0.95
NBZ-Zn	443.46	0.19	6-10	2.10
NBZ-La	453.54	0.19	6-14	1.93
NBZ-Ce	424.41	0.17	4-16	2.44
NBZ-Nd	466.63	0.18	7-14	2.14

Figure 3B.4 displays the N₂-adsorption isotherms of the NBZ and NBZ/M samples. NBZ sample fully complies with Type I isotherm, suggesting innate microporous structures. According to the IUPAC classification, the metal-modified zeolite beta samples NBZ/M exhibit a combination of Type I and Type IV isotherms. As a result, the presence of mesopores is responsible for the significant increase in adsorption at intermediate relative pressures. At the same time, zeolitic micropores are responsible for the considerable adsorption observed at low relative pressures ($p/p_0 < 0.1$). A hysteresis loop (Figure 3B.4) is formed in the case of NBZ/M due to the variation in adsorption and desorption volumes at the same relative pressure. This variation can be explained by capillary condensation exhibited by mesoporous materials. As per IUPAC guidelines, the Type H2 loop hysteresis demonstrates pore-blocking effects by the accumulation of metal particles.⁽⁷⁵⁾ Consequently, hindering the

diffusion of adsorbate molecules within the zeolite matrix.(76) Furthermore, the incorporation of metal ions drives the zeolitic matrix to dissolve smaller nanoparticles leading to redeposition onto larger ones resulting in the merging of pores and the simultaneous formation of mesopores (Ostwald ripening).(32,33)

The results obtained from applying the BJH pore distribution curve shown in Figure 3B.5, validate the presence of a bimodal pore structure, a characteristic feature of hierarchical zeolites. The BJH plot for NBZ begins at 1.5 nm with a larger volume and continues to decrease to lower pore diameter values. For NBZ/M samples, on the other hand, the pore size distribution curve is broader than that of NBZ samples. It is centered at different pore sizes within the range of 2–20 nm, indicating the presence of a significant mesoporosity in metal-modified zeolite samples.

The impact of adding metal ions on the textural characteristics of the supports is explained in detail in Table 3B.2. Each modified sample under study has different surface area and pore volume values due to metal ion deposition. The size and quantity of cations are thought to be the two primary variables that could have an impact on the surface area. Therefore, it would be reasonable to anticipate that the deposition of metal ions with varying charges, and ionic radii would have an inverse effect on surface area. Multivalent cations, however, have a highly complex influence on surface area. The decrease in textural characteristics imparted by these ions can be attributed to their size, nature, and overall composition within the zeolite structure. Furthermore, the partial blockage of pores by metal species

and the destruction of micropores during metal loading as a result of silica and aluminium leaching is the cause for the decrease in surface area.(55,59,64,66,77) The decrease in surface area seen for NBZ/Fe is significantly greater, which can be attributed to pore blockage caused by the presence of various iron species.

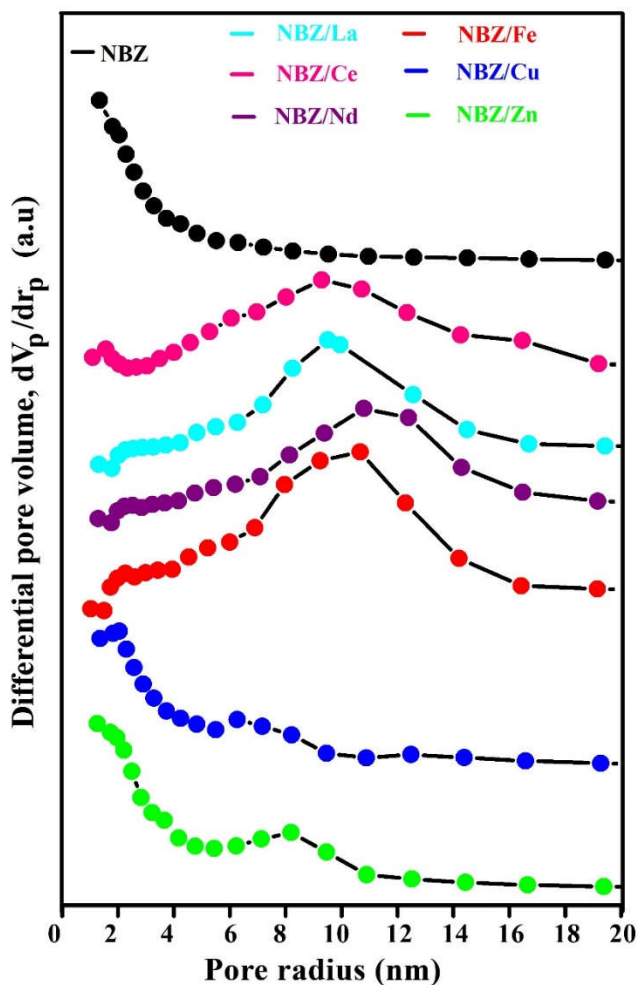


Figure 3B.5. Pore size distribution of NBZ and NBZ/M samples

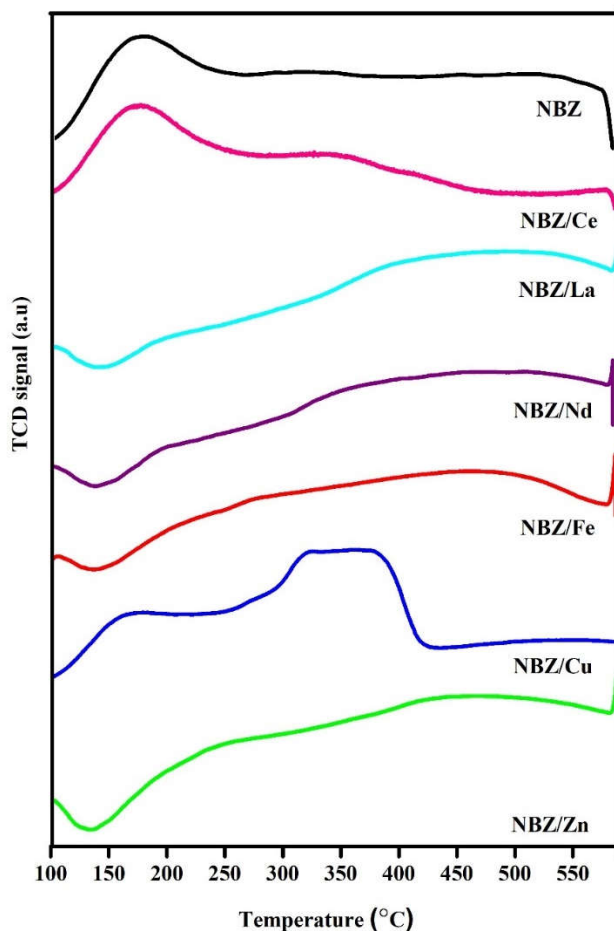


Figure 3B.6. TPD profile of NBZ and NBZ/M samples

The acidic nature of NBZ and NBZ/M were examined using NH_3 /TPD; the findings are displayed in Figure 3B.6. The patterns found for NBZ and NBZ/M show that they have distinct intrinsic acidic properties and display two well-resolved desorption peaks: a high-temperature peak (HTP > 450 °C) and a low-temperature peak (LTP ranging from 100 to 250 °C). In general, weak and strong acid

sites are represented by LTP and HTP, respectively. Medium acid sites are found between weak and strong acid sites in the 250–400 °C temperature range. The quantity of acid sites is correlated with the peak area. The number of estimated acid sites is given in Table 3B.2, and the advantage of metal modification is visible by noting the gradation of acidity values. The total acidity obtained for the NBZ (0.89 mmol NH₃/g) is less than that obtained from the NBZ/M. The surfaces of all zeolites have become noticeably more acidic due to the addition of metal ions to the zeolite. Thus, it can be concluded that more ammonia chemisorption centers are formed due to metal ions or metal oxides on the surface of the catalyst. Furthermore, the notable rise in NH₃ desorption for NBZ/M compared to NBZ can be attributed to the larger pore sizes of the NBZ/M matrix.(23)

A thorough comparison of the modification on TPD profiles shows that the weak acid sites of NBZ are more in number when compared to NBZ/M. There emerge two desorption peaks (intermediate and high temperature) for NBZ/La, NBZ/Fe, NBZ/Nd, and NBZ/Zn, indicating the creation of new types of acid sites. The TPD profiles of NBZ/La, NBZ/Fe, NBZ/Nd, and NBZ/Zn show a steady increase depicting an overall increase in acidity imparted by all three different types of acidities. The TPD profile of NBZ/Cu reveals a higher degree of acid site heterogeneity, with a smaller number of weak acid sites and an increased number of moderate acid sites (peak at 430 °C). Moreover, NBZ/Cu is associated with a lower pore size distribution 5-9 nm as given in Table 3B.2. This decrease in pore

size distribution accounts for the lower acidity of NBZ/Cu. It can be concluded that copper-loaded zeolites have reduced pore size distribution that limits the interaction of NBZ/Cu and ammonia proving the fact that it has lesser acidity compared to other NBZ/M samples.

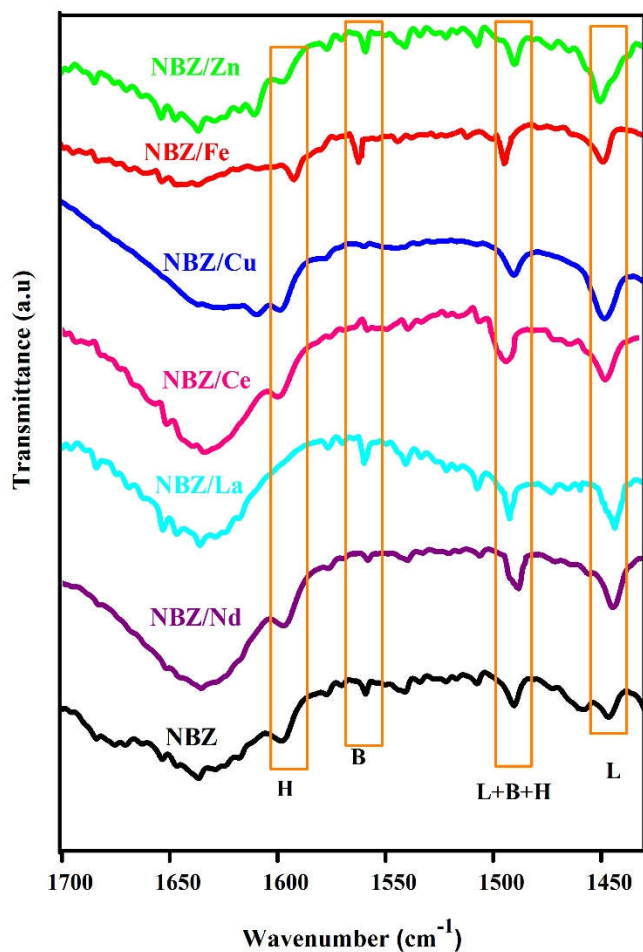
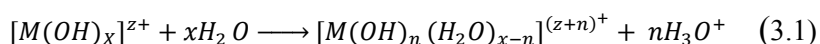


Figure 3B.7. FTIR of pyridine sorbed zeolite beta samples: B for Bronsted acid sites, L for Lewis acid sites, H for hydrogen-bonded sites

Another indispensable tool for investigating the variety of acid sites is to analyze the FTIR of the pyridine-sorbed samples. The infrared spectrum exhibits pyridine vibration bands between 1400 and 1700 cm^{-1} (Figure 3B.7). Pyridine interacts with acid sites on the solid surface, depending on whether they are Bronsted acid sites, Lewis acid sites, or hydrogen-bonded sites. Co-ordinately bound pyridine indicates Lewis acid sites e.g. Al^{3+} or metal cations on the surface of zeolites. The transfer of H^+ ions from the Bronsted acid sites of zeolite to pyridine results in the formation of pyridinium ions. Hydrogen bonds with the OH groups of zeolites and the nitrogen atom of pyridine to form hydrogen-bonded sites. The band at 1540 cm^{-1} , characteristic of Bronsted acid sites, is attributed to the N-H bending of pyridinium ions. The infrared band identifies Lewis acid sites at 1443–1450 cm^{-1} . The bands around 1590 cm^{-1} represent H sites. Pyridine interacts with all the different types of acid sites, i.e., L, B, and H sites are resulting in the band at 1490 cm^{-1} .(4)

There is a notable increase in the intensity of acid sites due to ion exchange evidenced by the increase in intensity exhibited by all NBZ/M samples. Considering the NBZ samples, the decrease in the intensity of Bronsted acid sites validates its inclination to transform into Lewis acid sites because of the presence of aluminium and deposited metal species. This explains the increased intensity of Lewis acid sites in NBZ/M. The formation of Lewis acidic site can occur in positions where the exchanged metals can furnish empty orbitals.(7,64) The partial replacement of framework protons by metal ions reduces the Bronsted acidity within the structure of NBZ/M samples. The Bronsted acid sites are retained because of the

hydrolysis of water of solvation found in the metal cations (Equation 3.1).(62) Furthermore, it is discovered that the location of the L acid sites has shifted to the lower wavenumber region and overlaps with sites of H, corresponding to the hydrogen bonding between the silanol and pyridine groups.(59,60)



$M(OH)_x$ represents the metal hydroxide complex and $M(OH)_n(H_2O)_{x-n}$ represents the hydrated metal hydroxide complex.

The SEM images of the zeolite beta samples reveal a direct correlation between morphological alterations and the modifications brought about by metal incorporation. Zeolite beta was found as agglomerates consisting of indistinct crystal structures containing spheroidal nanocrystals with varying degrees of aggregation. As illustrated in Figure 3B.8, the XRD results indicate that the crystallite size is notably tiny, precisely less than 30 nm. The modified samples exhibit a distinctive spherical morphology with a hierarchical structure composed of aggregates.(55,66) These agglomerates represent clusters of nanosized zeolite crystals characterized by well-defined grain boundaries. Remarkably, the modified zeolites display a morphology reminiscent of the precursors, featuring aggregates of zeolite nanoparticles with sizes smaller than 100 nm. The surfaces of NBZ/M samples appear more rugged and rougher, suggesting the presence of oxide nanoparticles covering these surfaces.

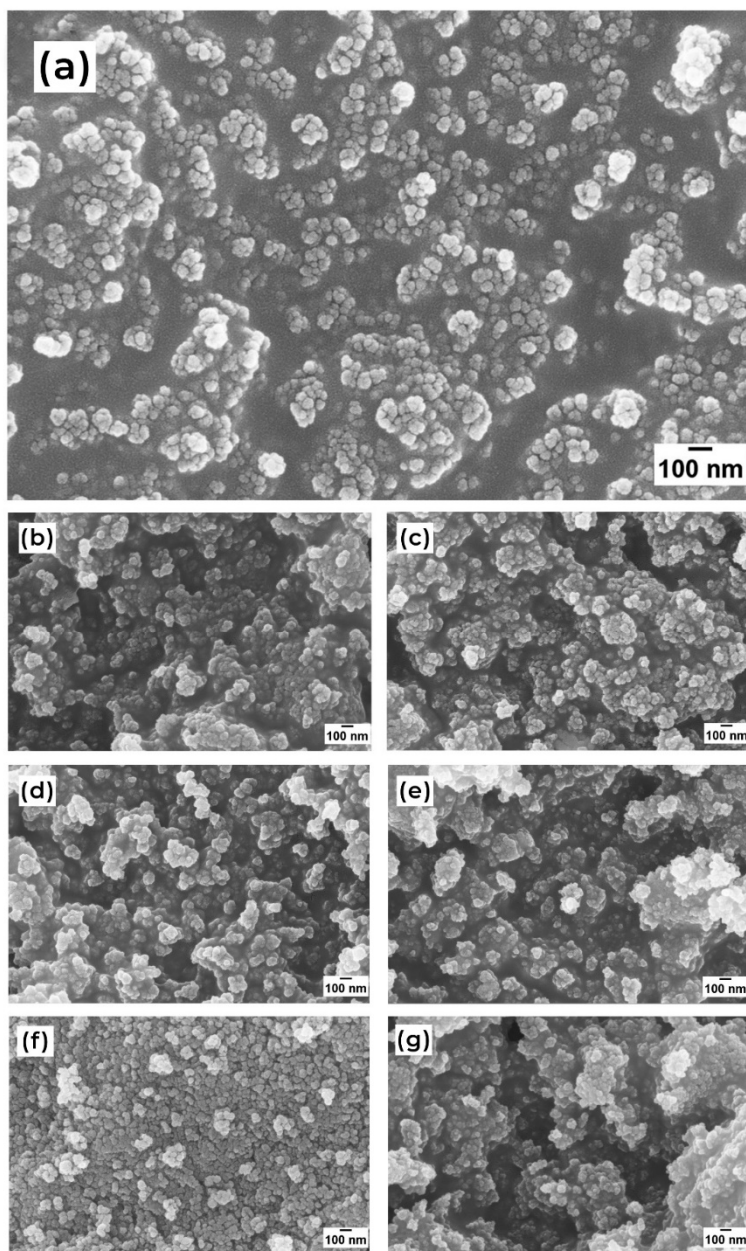


Figure 3B.8. SEM images of zeolite samples (a) NBZ (b) NBZ/Fe (c) NBZ/Cu (d) NBZ/Zn (e) NBZ/La (f) NBZ/Ce (g) NBZ/Nd

Table 3B.3. Elemental composition of NBZ and NBZ/M

Sample	Atomic percentage of elements(%)								
	Si	Al	O	La	Ce	Nd	Fe	Cu	Zn
NBZ	43.57	1.78	54.66	---	---	---	---	---	---
NBZ/La	27.23	1.27	67.70	3.80	---	---	---	---	---
NBZ/Ce	29.50	0.62	63.92	---	5.97	---	---	---	---
NBZ/Nd	35.17	1.28	60.70	---	---	2.84	---	---	---
NBZ/Fe	28.81	0.66	66.33	---	---	---	4.20	---	---
NBZ/Cu	38.35	1.06	59.07	---	---	---	---	1.52	---
NBZ/Zn	32.03	1.56	65.14	---	---	---	---	---	1.3

A detailed elemental analysis of all the samples was conducted, and the composition of each sample is detailed in Table 3B.3. Upon analysis, it becomes apparent that there is a marginal decrease in the weight percentage of the primary constituent elements, namely silicon and aluminium due to metal doping. Notably, the reduction in the concentration of aluminium is more significant. This phenomenon can be attributed to dealumination, a process occurring during the introduction of metal dopants, where aluminium content is diminished.

To further validate the occurrence of oxide deposition, one can observe the percentage of oxygen in the material structure. The analysis of oxygen content indicates the presence of oxides, affirming the transformative effects of the doping process on the elemental composition of the samples. This information contributes to a comprehensive understanding of how metal doping influences

the elemental makeup of the material, shedding light on specific changes such as dealumination and oxide deposition.

The magnitude of the observed changes in the acidity, textural properties, and structural parameters were primarily influenced by the spatial distribution and arrangement of the metal cations. These factors exhibited variability based on the nature of the metal ions and their respective valencies. Specifically, when considering Zn, it was exclusively detected in the form of well-dispersed cationic species.

On the other hand, in the case of copper and iron, the dispersion was notably poorer, and these metal ions were predominantly found in the form of oxides. This implies that the ions of copper and iron were less scattered within the material and tend to aggregate, forming oxide compounds. The presence of oxides can significantly affect the properties and behavior of materials.

In the context of cerium, it shows the presence of oxide and cationic species. Lanthanum and neodymium exhibited an intermediate level of dispersion, suggesting a distribution that was neither as uniform as zinc nor as clustered as copper and iron. The distribution of metal particles has implications for the properties of materials, showcasing a fine relationship between metal ion characteristics and their impact on structural arrangements.

3B.3 Conclusions

Metal ion-incorporated nanocrystalline zeolites with crystal sizes smaller than 100 nm are considered promising alternatives to traditional zeolites due to their beneficial and distinctive characteristics. This study deals with the synthesis of nanocrystalline zeolite beta and its modification with various metal ions, including Cu, Zn, Fe, La, Ce, and Nd. XRD results indicate that metal loading does not alter the zeolite structure but increases lattice strain. The average crystallite size for nanocrystalline zeolite and modified samples is below 30 nm. UV-Visible spectra reveal the presence of metal ions in the form of cations and metal oxides. FTIR spectra show skeletal vibration patterns similar to typical zeolite beta peaks. TPD profiles suggest that the metal modification increases the Lewis acid sites, meanwhile, a decrease in the Bronsted acid sites is also observed. Among the different samples used, NBZ/Ce sample possesses the maximum acidity and this observation can be linked to the uniform dispersion of metal cations in the NBZ framework. The morphology of metal-modified samples resembles that of NBZ, showing a rougher surface, indicative of oxide nanoparticles. This chapter provides detailed insights into the environment of isolated metal atoms and nano oxide clusters within zeolite beta, with the help of the XRD and UV-Visible spectra.

Section C

Evaluation of Catalytic Activity of Metal-Modified Zeolites

3C.1 Introduction

Methyl acetophenone plays a crucial role in the flavor and fragrance industry. It is used in perfumes, colognes, and scented products because of its sweet, fruity, and floral aroma. This resourceful compound is also used in the pharmaceutical industry to synthesize various drugs and medicines. This compound can be synthesized by acetylation of toluene. The acetylation of toluene represents a significant reaction, making use of a wide range of catalysts employed other than the conventional Lewis acid catalysts. These include montmorillonite clay, heteropolyacids with cesium, TiO_2 , SiO_2 and sulfated tin oxide.(78-83) The product distribution, selectivity, and yields are affected by the type of cation incorporated, the chain length of the acylating agent, and the polarity of reactants and solvents. Zeolites have gained a lot of attention in catalysis, particularly in hydrocarbon cracking, isomerization, and alkylation, but their potential for catalyzing the Friedel-Crafts reaction has been underutilized. The reaction requires an acidic zeolite catalyst, producing an electrophile, which attacks the aromatic ring, causing the development of corresponding ketones.(84) The catalytic activity of H-ZSM5 is capable of acetylating toluene with acetic acid, producing ortho and para acetophenone as primary products. The positional selectivity exhibited by ZSM-5 can be attributed to the

shape-selectivity, channel geometry, and cavity space constraints of zeolite. The ortho isomer is not created due to a shortage of space within the channel or cavity.(85) At high temperatures, heavy products are generated due to a series of reactions, such as acylation, disproportionation, decarboxylation, and alkylation.(86,87) The electrophilic substitution involves an intermediate complex, where an acylium ion combines with an aromatic ring. Polar solvents speed up the reaction by stabilizing the acylium ion and the ionic intermediate created by the attack of acylium ion on toluene.(88) Nano-sized zeolites improve the accessibility to the active sites, thereby increasing the catalytic activity. At the same time, the nano-size lowers the deactivation of the catalyst.(89) There is a further increase in the activity when hierarchical porosity is rendered, allowing faster product diffusion and removal of heavy products.(90) Despite all the alterations, the quick deterioration of catalysts severely restricts the application of these materials, making them less economical. However, improved catalyst design is anticipated to increase the likelihood of using zeolites as catalysts for acylation.

As part of such an effort, hierarchical ZSM-5 and zeolite beta are loaded with different metal cations at varying levels and they function as catalysts in the Friedel-Crafts acetylation of toluene with acetic anhydride (AC_2O). The cations used for modification are three transition metals, Fe, Cu, and Zn, and three rare earth metals, La, Ce, and Nd. The synthesis and characterizations of these metal-modified

ZSM-5 and zeolite beta are described in the previous sections (3A & 3B). Furthermore, the performance of these zeolite catalysts is compared with hydrothermally synthesized unmodified nanocrystalline zeolites. The highlight of this process is that no corrosive solvents are used and the reaction is carried out under optimal reaction parameters such as a low amount of catalyst, and optimized temperature thereby ensuring safety and cost-effectiveness in this reaction.

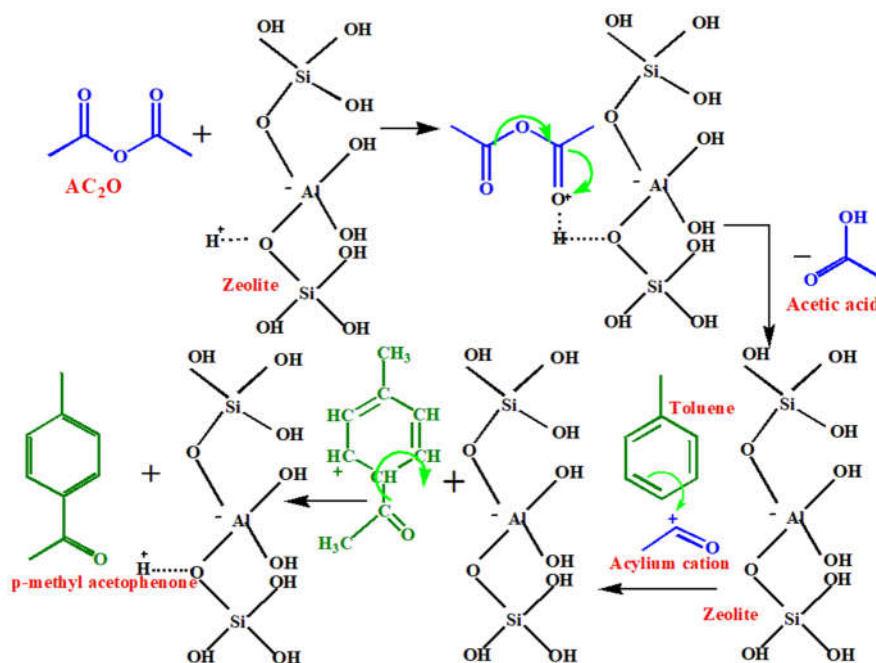
3C.2 Results and Discussion

The effectiveness of the ZSM-5 and zeolite beta samples in catalyzing the acetylation of toluene is investigated. Section 2.5 delves into the specifics of the reaction. The impact of various reaction parameters, including catalyst quantity, the mole ratio of toluene to acetic anhydride, and reaction temperature, is thoroughly examined.

In the acetylation reaction, an acylating reagent, AC_2O , reacts with toluene containing active hydrogen, forming acetylated toluene. The detailed mechanism is depicted in Scheme 3C.1.

Acetylation involving a Bronsted acid site initiates the formation of an acylium cation. The proton attack from the Bronsted acid site of zeolite on the nucleophilic carbonyl group of AC_2O creates an acylium ion and acetic acid. The acylium ion then combines with toluene to generate an arenium ion. In the last stage, the aromaticity of the ring is restored and the proton is released, which causes p-

methyl acetophenone to desorb and the zeolitic acid site to regenerate.



Scheme 3C.1. Mechanism of the catalysis of acetylation at the Bronsted acid sites of zeolites

The degree of conversion of AC₂O plays a pivotal role in determining the efficiency of the acetylation reaction. Monitoring the conversion of AC₂O allows for the optimization of reaction conditions, control over the progress of the reaction, and assurance of maximum yield of the desired product while maintaining selectivity. Furthermore, if toluene is used in excess compared to AC₂O (in molar terms), studying the activity involves measuring the conversion of AC₂O. Monitoring the consumption of AC₂O enables

better control and optimization of these conditions to enhance the conversion and selectivity of the reaction.

The acetylation of toluene with AC_2O was studied systematically using NZSM-5 and NBZ as catalysts. The kinetics of acetylation of toluene over NZSM-5 and NBZ were examined to identify the optimal contact time. The conversion rate rises steadily within the first 120 minutes but subsequently declines, indicating that the optimal reaction time for maximum conversion is 120 minutes under the specified conditions. The decrease in conversion after 120 minutes is attributed to the coke formation on the zeolite surface, potentially affecting the active sites of the catalyst. It was found that the product obtained was exclusively the para isomer, indicating a 100% selectivity for the para isomer. The findings underscored the shape-selective nature of NZSM-5 and NBZ, emphasizing a preference for the para isomer over other isomers due to its smaller molecular size than its ortho or meta counterparts. The choice for the para isomer is explained by its lower energy and minimal steric hindrance between the methyl group and the incoming acetyl group. Therefore, the time for all the subsequent reactions were fixed as 120 minutes. The quantity of catalyst, the toluene/ AC_2O molar ratio, and the reaction temperature were all optimized. The catalytic activity of NZSM-5/M was compared with NZSM-5 and that of NBZ/M was compared with NBZ and all the reactions were carried out under the optimized reaction conditions.

3C.2.1 Effect of Molar Ratio of Reactants on Acetylation of Toluene

The impact of the toluene to AC₂O molar ratio was examined within the range of 6:1 to 10:1 while maintaining a constant total volume. The effect of the molar ratio of reactants is graphically represented in Figure 3C.1. The values are furnished in Table 3C.1. The conversion of AC₂O increased with increase in concentration of toluene. The maximum conversion took place at a ratio of 8:1. Further increase in the molar ratio of toluene did not noticeably affect the conversion of AC₂O. This finding can be explained by the fact that the higher polarity of the acetylated product led to its adsorption onto acid sites, limiting the toluene adsorption on the surface and pores of the zeolite.⁽⁸⁶⁾ Consequently, increasing the concentration of toluene did not significantly boost the conversion. Hence, all reactions were investigated using a toluene:AC₂O molar ratio of 8:1.

Table 3C.1. Effect of molar ratio of reactants on the conversion of AC₂O

Time (min)	Conversion of AC ₂ O (%) on NZSM-5			Conversion of AC ₂ O (%) on NBZ		
	Toluene: AC ₂ O			Toluene: AC ₂ O		
	6:1	8:1	10:1	6:1	8:1	10:1
10	10.5	31.0	40.0	21.8	42.5	48.0
20	21.0	39.5	48.6	32.6	50.8	54.0
30	29.7	48.8	54.8	40.6	59.6	63.7
60	35.8	56.4	61.7	49.7	68.8	70.0
90	42.8	65.5	69.5	55.7	75.8	77.4
120	43.2	66.1	71.0	63.8	77.0	77.7

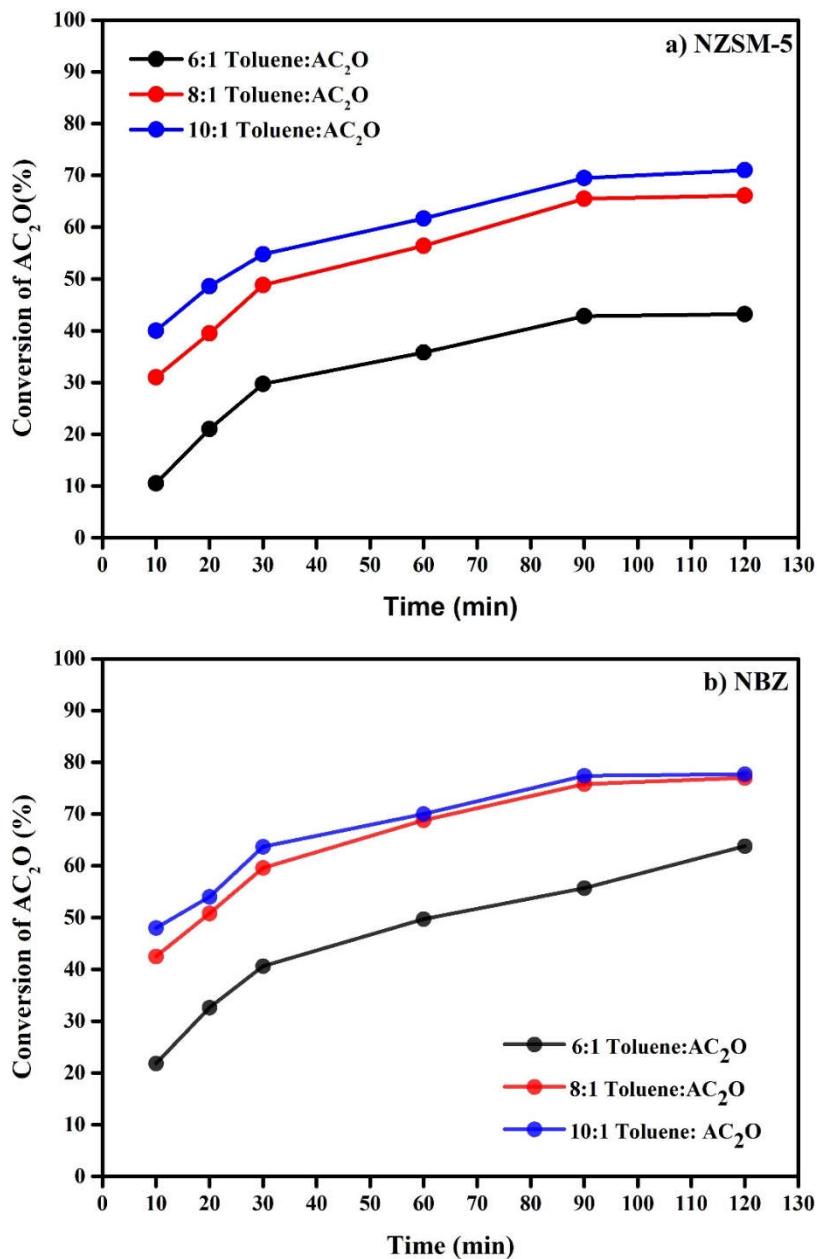


Figure 3C.1. Conversion of AC_2O against time at different molar ratios of reactants on a) NZSM-5 and b) NBZ.

3C.2.2 Effect of Quantity of Catalyst on Acetylation of Toluene

The effect of the quantity of catalyst used was investigated within a range of 0.05–0.20 g for the acetylation of toluene process at 60 °C. Figure 3C.2 illustrates the variation in the conversion of AC₂O with different quantities of catalyst, the values are depicted in Table 3C.2. Due to a corresponding rise in the number of active sites, the conversion of AC₂O increased as catalyst concentration rose. But the impact of this increase was negligible above 0.1 g. This implies that extra active sites above 0.1 g have no discernible effect on reactant adsorption at a particular concentration. As such, there is only a slight improvement in the conversion of AC₂O. As a result, all subsequent experiments were conducted using a fixed amount of 0.1 g catalyst.

Table 3C.2. Effect of quantity of catalyst on the conversion of AC₂O

Time (min)	Conversion of AC ₂ O (%) on NZSM-5			Conversion of AC ₂ O (%) on NBZ		
	0.05 g	0.1 g	0.2 g	0.05 g	0.1 g	0.2 g
10	6.5	31.0	39.6	22.6	42.5	50.6
20	9.1	39.5	47.0	33.0	50.8	61.0
30	15.4	48.8	55.7	41.7	59.6	69.3
60	21.0	56.4	63.8	50.7	68.8	77.0
90	25.8	65.5	68.9	59.0	75.8	79.1
120	27.5	66.1	71.0	60.0	77.0	78.9

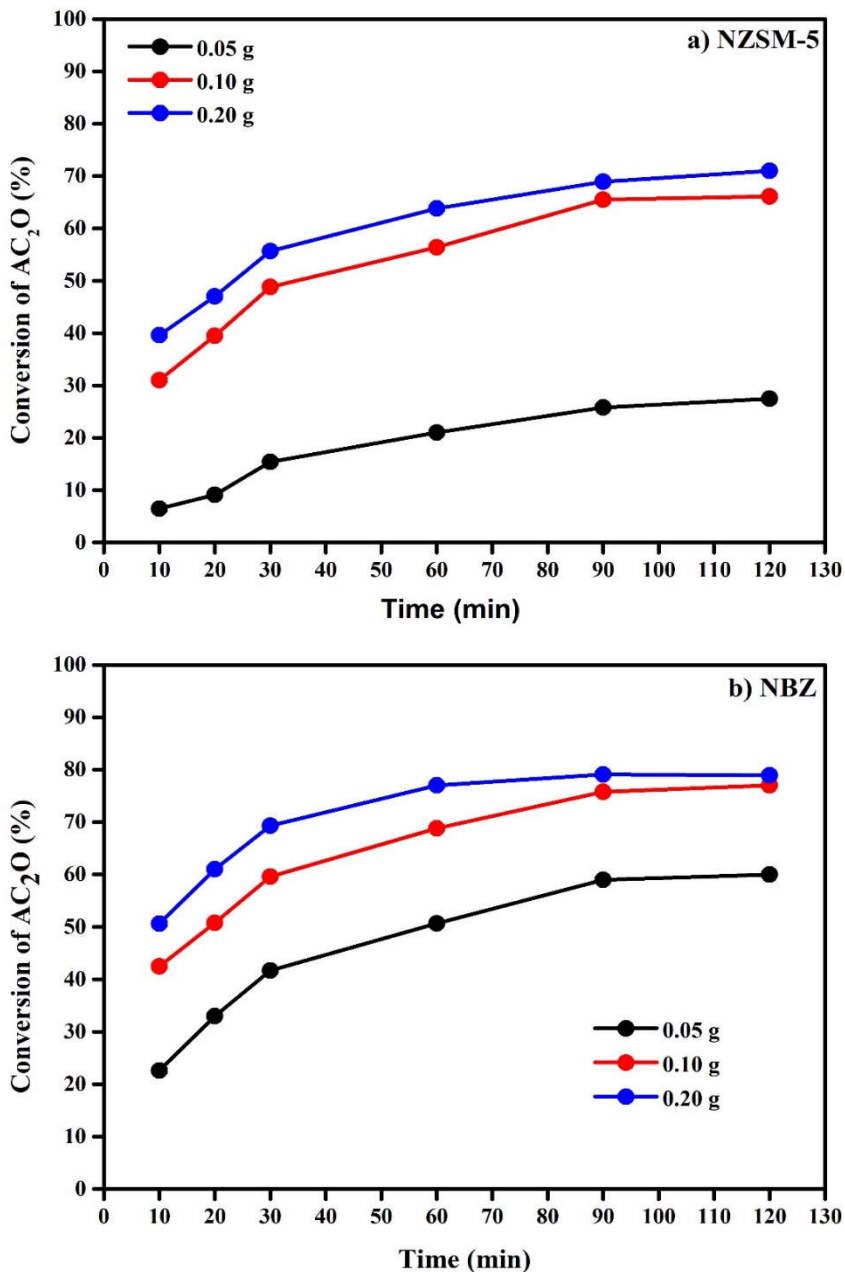


Figure 3C.2. Conversion of AC_2O against time at different amounts of a) NZSM-5 and b) NBZ

3C.2.3 Effect of Temperature on Acetylation of Toluene

Figure 3C.3 and Table 3C.3 depict the changes in conversion of AC₂O across temperatures ranging from 30-80 °C. The conversion was found to increase significantly with increasing temperature up to 60 °C, and after that, an insignificant slight increase was observed at 80 °C. For further studies, the reaction temperature was optimized at 60 °C.

The diminished conversion of AC₂O at elevated temperatures can be attributed to the prevalence of deacetylation over acetylation, combined with a reduced supply of AC₂O as it participates in side reactions like oligomerization or aromatization. Additionally, the high temperatures contribute to the obstruction of the acid sites by unwanted products of side reactions, resulting in lower conversion rates.(80)

Table 3C.3. Effect of temperature on conversion of AC₂O

Time (min)	Conversion of AC ₂ O (%) on NZSM-5			Conversion of AC ₂ O (%) on NBZ		
	30 °C	60 °C	80 °C	30 °C	60 °C	80 °C
10	5.7	31	40.1	12.0	42.5	59.7
20	8.7	39.5	47.9	21.6	50.8	66.5
30	13.7	48.8	54.3	27.8	59.6	72.6
60	17.5	56.4	60.9	33.0	68.8	78.4
90	21.8	65.5	68.9	39.6	75.8	83.7
120	22.1	66.1	70.0	41.0	77.0	85.2

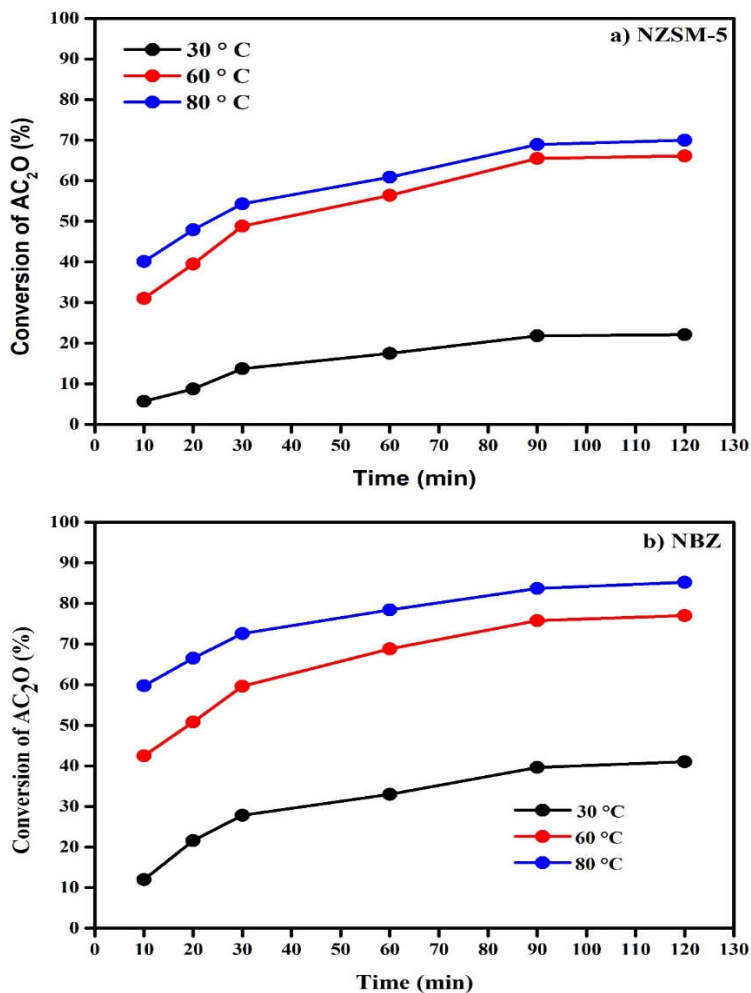


Figure 3C.3. Conversion of AC_2O against time at different temperatures on a) NZSM-5 and b) NBZ

3C.2.4 Effect of Metal Modification of Nanocrystalline Zeolite on Acetylation of Toluene

The effect of metal incorporation on the conversion of AC_2O is studied using the optimized parameters as indicated in Figure 3C.4. The values are tabulated in Table 3C.4 and Table 3C.5.

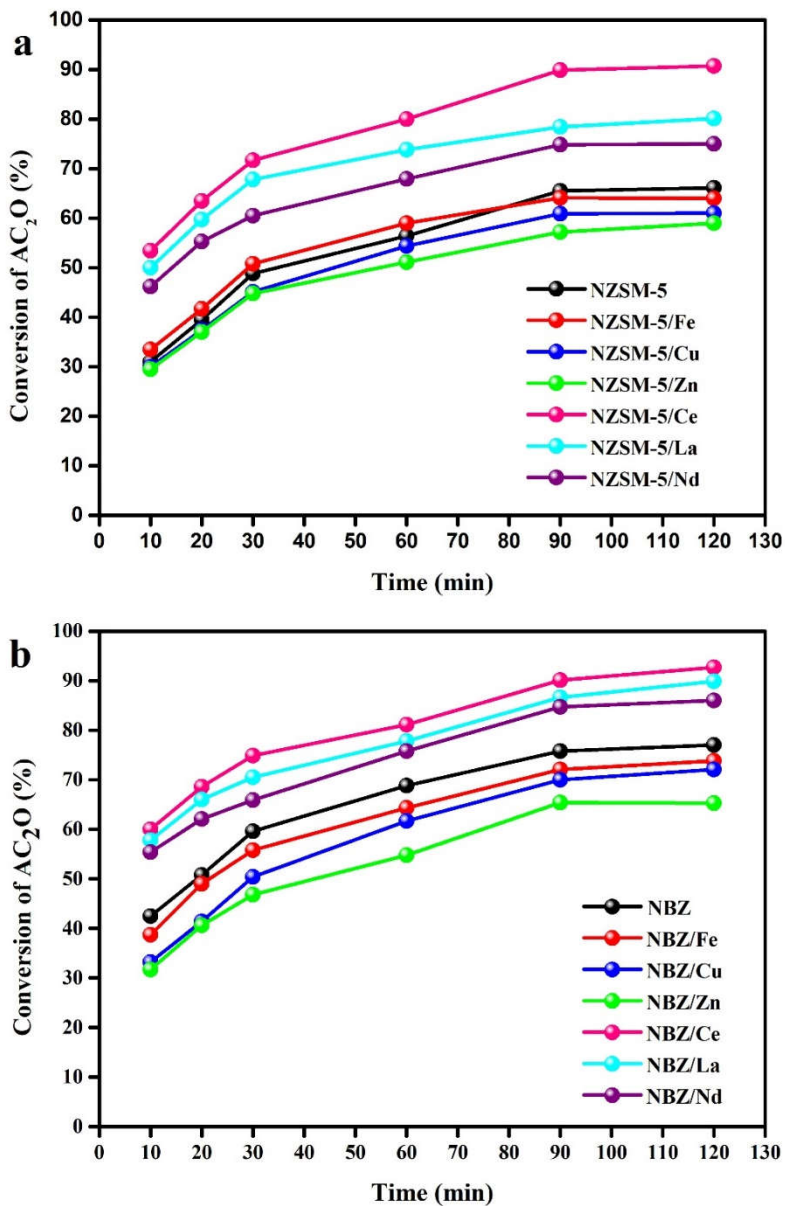


Figure 3C.4. Conversion of AC_2O against time on different zeolite samples a) NZSM-5/M and b) NBZ/M at optimized conditions.

Table 3C.4 Effect of metal modification of NZSM-5 on the conversion of AC₂O

Time (min)	Conversion of AC ₂ O (%)						
	NZSM-5	NZSM-5/Fe	NZSM-5/Cu	NZSM-5/Zn	NZSM-/La	NZSM-5/Ce	NZSM-/Nd
10	31.0	33.5	30.0	29.5	50.0	53.4	46.2
20	39.5	41.7	37.4	37.0	59.7	63.5	55.3
30	48.8	50.8	45.1	44.8	67.8	71.7	60.5
60	56.4	59.0	54.4	51.1	73.8	80.0	67.9
90	65.5	64.1	60.9	57.2	78.4	89.9	74.8
120	66.1	64.0	61.0	59.0	80.1	90.7	75.0

Table 3C.5. Effect of metal modification of NBZ on the conversion of AC₂O

Time (min)	Conversion of AC ₂ O (%)						
	NBZ	NBZ/Fe	NBZ/Cu	NBZ/Zn	NBZ/La	NBZ/Ce	NBZ/Nd
10	42.5	38.7	33.2	31.7	57.8	60.0	55.4
20	50.8	49.0	41.4	40.6	66.0	68.6	62.1
30	59.6	55.8	50.4	46.8	70.5	74.9	65.9
60	68.8	64.3	61.7	54.8	77.8	81.1	75.8
90	75.8	72.1	70.0	65.4	86.6	90.1	84.7
120	77.0	73.8	72.1	65.3	89.9	92.7	86.0

In the case of NBZ, a conversion rate of 77% was achieved. Similarly, NZSM-5 shows a conversion of 66%. Interestingly, the metal-modified NBZ samples and NZSM-5 exhibited higher percentage of conversion. Specifically, NBZ/Nd, NBZ/La, and NBZ/Ce demonstrated high AC₂O conversions in the range of 86.0 to 92.7%, maintaining 100% selectivity. Even though NBZ and

NZSM-5 zeolites possess considerable strength for their acid sites, they do not achieve the highest conversion of AC_2O . Other contributing factors, such as crystallite size and pore characteristics have lesser contribution towards activity when compared to metal-modified zeolites.

While comparing the catalytic performances of various samples, transition elements doped catalysts exhibited slightly lower conversion of AC_2O than unmodified catalysts. At the same time, those modified with rare earth elements exhibited increased conversion of AC_2O than the undoped ones.

Zeolites containing Fe, Cu, and Zn appeared to have a negative effect on the acid-catalyzed reactions, which agrees with previous observations from the literature.(91,92) This adverse impact on catalysis is likely attributed to metal nanoparticles getting deposited on the external surface of zeolite potentially obstructing the pore accessibility. The existence of oxide nanoparticles in zeolites has been confirmed through various analyses (Sections A and B).

In the case of iron-based catalysts, a decrease in conversion of AC_2O was observed, dropping from 66.1% to 64% for NZSM-5/Fe and from 77% to 73.8% for NBZ/Fe. Similarly, copper-based catalysts exhibited a significant decrease in conversion of AC_2O , declining from 66.1% to 61% for NZSM-5/Cu and from 77% to 72.1% for NBZ/Cu. Zinc-based catalysts also showed a substantial decrease in conversion of AC_2O , decreasing from 66.1% to 59% for NZSM-5/Zn and from 77% to 65.3% for NBZ/Zn. The negative effect of zinc species on Friedel-Crafts acid catalysis is more pronounced than

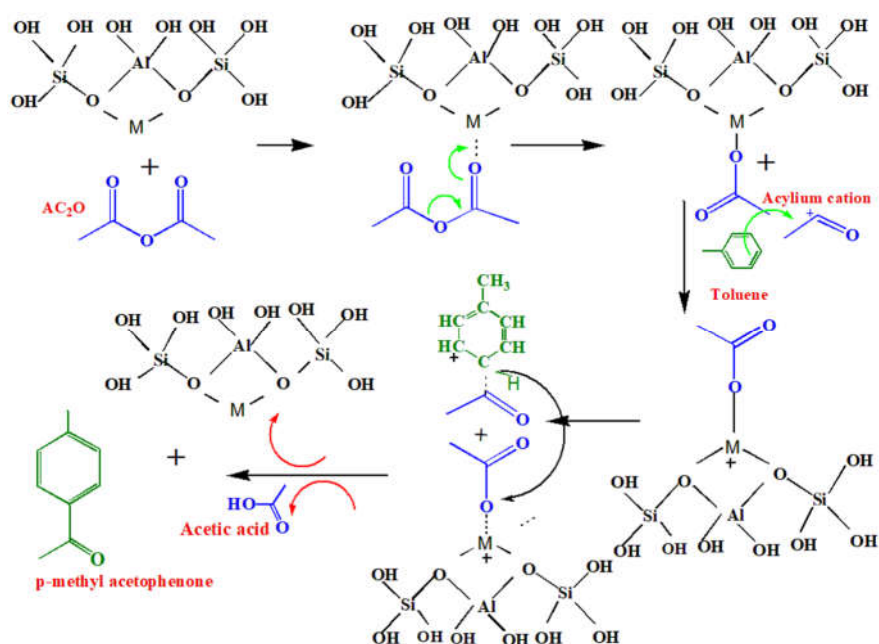
iron and copper species. In terms of selectivity, the introduction of different metal species does not result in the production of other acylated products. The activity sequence of different metal-exchanged zeolite beta is as follows: NBZ/Ce > NBZ/La > NBZ/Nd > NBZ > NBZ/Fe > NBZ/Cu > NBZ/Zn. Similarly, the order of activity for various metal-exchanged ZSM-5 zeolites is NZSM-5/Ce > NZSM-5/La > NZSM-5/Nd > NZSM-5 > NZSM-5/Fe > NZSM-5/Cu > NZSM-5/Zn. Hence, the variation in catalytic activity for acetylation of toluene cannot be ascribed solely to the nature of metal and its metal content in the zeolite. Factors such as location of the cation, crystallinity, acidity, pore size distribution, and crystallite size of the zeolite samples also significantly influence the catalytic activity.

Table 3C.6 Properties of metal-modified zeolite samples

Sample	Crystallite size (nm)	Acidity (mmol/g of ammonia)	Pore volume (cm ³ /g)
NZSM-5	37.55	0.17	0.20
NZSM-5/Fe	13.75	0.28	0.17
NZSM-5/Cu	13.43	0.27	0.17
NZSM-5/Zn	14.50	0.28	0.18
NZSM-5/La	13.10	0.32	0.19
NZSM-5/Ce	11.72	0.26	0.17
NZSM-5/Nd	12.53	0.49	0.19
NBZ	17.20	0.89	0.31
NBZ/Fe	16.35	1.54	0.20
NBZ/Cu	24.77	0.95	0.20
NBZ/Zn	13.77	2.10	0.19
NBZ/La	21.75	1.93	0.19
NBZ/Ce	10.57	2.44	0.17
NBZ/Nd	13.76	2.14	0.18

From the data given in Table 3C.6, it is clear that neither the increased acidity nor the pore characteristics in the samples result in a substantial improvement in catalytic activity for the acetylation of toluene with AC_2O . The higher total acidity in NZSM-5/Nd compared to the other NZSM-5 samples (as indicated in Table 3C.6) did not result in higher conversion rates.

In addition to the Bronsted acid-catalyzed mechanism as depicted in Scheme 3C.1, the acetylation reaction of toluene is predominantly driven by Lewis acid sites as seen in Scheme 3C.2.



Scheme 3C.2. Mechanism of the catalysis of acetylation at the Lewis acid sites of zeolites

Acetylation entails introducing an acetyl group (CH_3CO-) into a molecule. AC_2O interacts with the Lewis acid site on the zeolite

surface and gets activated by accepting electron density as indicated in Scheme 3C.2. This activation enhances the electrophilicity and reactivity of AC_2O , forming an acylium ion. This highly reactive species act as the electrophile in the acetylation reaction with toluene. The Lewis acid sites of zeolite can repeatedly activate AC_2O , facilitating the acetylation of multiple substrate molecules.

In this study, the modification of zeolite beta and ZSM-5 by metal, alters the surface acidity. The driving force for acetylation of toluene not only depends on the higher number of acid sites but also on the type and intensity of these acid sites. Among ZSM-5 samples, the highest activity is exhibited by NZSM-5/Ce despite having lower acid strength than other modified samples. Conversely, NBZ/Ce showed the most increased activity among zeolite beta samples which can be attributed to the higher acid strength compared to the other metal-modified samples.

Diffusion plays a pivotal role in acetylation reactions particularly when it is done in the liquid phase. The zeolite crystallite size is a significant factor influencing conversion and selectivity. Among the various samples, NZSM-5/Ce stands out with the maximum conversion of AC_2O showcasing the combined effect of smaller crystallite size and a broader pore size distribution. This emphasizes the importance of zeolite crystallite size in determining the effectiveness of the acetylation process.

The crystallite sizes of NZSM-5/Ce and NBZ/Ce are smaller than those of other NZSM-5 and NBZ samples. Unlike the acid sites inside zeolite micropores, the crystallite size reduction has a beneficial effect on the quantity of external acid sites, which are unrestricted by steric constraints. Moreover, the square of the crystallite size has an inverse relationship with the total diffusion rate via micropores.⁽⁹³⁾ Consequently, a notably higher intercrystalline diffusion rate is anticipated for the cerium-modified samples than the other zeolite samples. The excellent catalytic activity displayed by these cerium-modified nanocrystalline zeolite samples and their high conversion rates can be explained by the combined impact of these variables, which lead to improved accessibility of substrate molecules to active sites of zeolites.

Table 3C.7 presents a comparative analysis of the catalytic efficiency of zeolitic samples in this work alongside other heterogeneous catalysts employed in the acetylation of toluene. Compared to earlier published works, the conversion rates of the catalyst samples in this study are notably higher with 100% selectivity attributed to the specific characteristics of the synthesized samples. Notably, this study stands out as it is done at lower temperatures and with lesser amounts of catalyst compared to other reported reaction conditions.

Table 3C.7. Comparative analysis of various zeolite samples used in acetylation of toluene

Type of Catalyst	Experimental condition		Acylation agent	Selectivity to para methyl acetophenone (%)	Conversion of AC ₂ O (%)	References
	Temperature (°C)	Quantity of catalyst (g)				
HZSM-5	250	1.75	Acetic acid	43.7	55	(84)
HBEA	120	5.6	AC ₂ O and acetic acid	96	77.8	(94)
BEA	150	0.5	AC ₂ O	98	58	(95)
Nano-BEA	150	0.5	AC ₂ O	98	83	(95)
La-BEA	135	0.25	AC ₂ O	100	66	(88)
H-BEA	150	1.0	AC ₂ O	100	83	(86)
Fe/SBA	150	0.1	AC ₂ O	85.6	Not measured	(96)
Nano-HBEA	130	0.1	AC ₂ O	98	93	(89)
Hierarchical BEA	120	0.5	AC ₂ O	97	76.8	(90)
H-USY	180	0.4	AC ₂ O	85	100	(87)
Ce Nano ZSM-5	80	0.15	AC ₂ O	99	93	(42)
NZSM-5/Ce	60	0.1	AC ₂ O	100	90.7	Present study
NBZ/Ce	60	0.1	AC ₂ O	100	92.7	Present study

3C.3 Conclusions

The catalytic conversion of AC_2O for acetylation of toluene across different metal-exchanged zeolite samples was explored by optimizing experimental conditions to a minimum. The study explicitly focuses on lower temperatures and reduced amount of catalysts, which enhanced the conversion in this investigation. The zeolite ZSM-5 and beta samples modified with Ce exhibited superior catalytic conversion among the various modified samples. The acidity, crystallite size, and pore characteristics were found to play key roles in the enhanced activity of these samples. Smaller crystallite sizes, allowing the exposure of more external acid sites, and higher diffusion rates through micropores played pivotal roles in the high rate of conversion of cerium-modified nanocrystalline zeolite samples.

References

1. Hagen. J. Industrial catalysis: a practical approach. Vol. 21, WILEY-VCH, Germany. 2007. 520 p.
2. Othman I, Mohamed RM, Ibrahim IA, Mokhtar M. Synthesis and modification of ZSM-5 with manganese and lanthanum and their effects on decolorization of indigo carmine dye. *Appl Catal A Gen.* 2006;299:95-102. Available from: <https://doi.org/10.1016/j.apcata.2005.10.016>
3. Liao J, Bao W, Chen Y, Zhang Y, Chang L. The adsorptive removal of thiophene from benzene over ZSM-5 zeolite. *Energy Sources, Part A Recover Util Environ Eff.* 2012;34(7):618–25. Available from: <https://doi.org/10.1080/15567036.2010.549916>
4. Yadav MK, Patil M V, Jasra R V. Acetoxylation and hydration of limonene and α -pinene using cation-exchanged zeolite beta. *J Mol Catal A Chem.*2009;297:101–9. Available from: <https://doi.org/10.1016/j.molcata.2008.09.017>
5. Du X, Gao X, Zhang H, Li X, Liu P. Effect of cation location on the hydrothermal stability of rare earth-exchanged Y zeolites. *CATCOM [Internet].* 2013;35:17–22. Available from: <http://dx.doi.org/10.1016/j.catcom.2013.02.010>.
6. Yuan EH, Han W, Zhang G, Zhao K, Mo Z, Lu G, et al. Structural and Textural Characteristics of Zn-Containing ZSM-5 Zeolites and Application for the Selective Catalytic Reduction of NO_x with NH₃ at High Temperatures. *Catal Surv from Asia.* 2016;20(1):41–52.
7. Xiaoning W, Zhen Z, Chunming X, Aijun D, Li Z, Guiyuan J. Effects of Light Rare Earth on Acidity and Catalytic Performance of HZSM-5 Zeolite for Catalytic Cracking of Butane to Light Olefins. *J Rare Earths.* 2007;25(3):321–8. Available from: [https://doi.org/10.1016/S1002-0721\(07\)60430-X](https://doi.org/10.1016/S1002-0721(07)60430-X).
8. Saito H, Inagaki S, Kojima K, Han Q, Yabe T, Ogo S, et al. Preferential dealumination of Zn/H-ZSM-5 and its high and stable activity for ethane dehydroaromatization. *Appl Catal A Gen [Internet].* 2018;549(June 20):1776–81. Available from: <http://dx.doi.org/10.1016/j.apcata.2017.09.024>.

-
9. Lai S, Meng D, Zhan W, Guo Y, Guo Y, Zhang Z, et al. The promotional role of Ce in Cu/ZSM-5 and in situ surface reaction for selective catalytic reduction of NO_x with NH₃. *RSC Adv.* 2015;5(110). Available from: <https://doi.org/10.1039/C5RA12505G>
 10. Martins L, Peguin RPS, Urquieta-González EA. Cu and Co exchanged ZSM-5 zeolites: activity towards NO reduction and hydrocarbon oxidation. *Quim Nov.* 2006;29(2):223–9. Available from: <http://dx.doi.org/10.1590/S0100-40422006000200009>
 11. Zhang W, Xie J, Hou W, Liu Y, Zhou Y, Wang J. One-pot template-free synthesis of Cu-MOR zeolite toward efficient catalyst support for aerobic oxidation of 5-Hydroxymethylfurfural under ambient pressure. *ACS Appl Mater Interfaces.* 2016;8(35):23122–32. Available from: <https://doi.org/10.1021/acsami.6b07675>
 12. Smeets PJ, Groothaert MH, Schoonheydt RA. Cu based zeolites: A UV-vis study of the active site in the selective methane oxidation at low temperatures. *Catal Today.* 2005;110(3–4):303–9. Available from: <https://doi.org/10.1016/j.cattod.2005.09.028>
 13. Alayon EMC, Nachtegaal M, Bodi A, Ranocchiari M, Van Bokhoven JA. Bis(μ -oxo) versus mono(μ -oxo)dicopper cores in a zeolite for converting methane to methanol: An in situ XAS and DFT investigation. *Phys Chem Chem Phys* [Internet]. 2015;17(12):7681–93. Available from: <http://dx.doi.org/10.1039/C4CP03226H>
 14. Groothaert MH, Van Bokhoven JA, Battiston AA, Weckhuysen BM, Schoonheydt RA. Bis(μ -oxo)dicopper in Cu-ZSM-5 and its role in the decomposition of NO: A combined in situ XAFS, UV-vis-near-IR, and kinetic study. *J Am Chem Soc.* 2003;125(25):7629–40. Available from: <https://doi.org/10.1021/ja029684w>
 15. Kharchenko A, Zholobenko V, Vicente A, Fernandez C, Vezin H, De Waele V, et al. Formation of copper nanoparticles in LTL nanosized zeolite: Spectroscopic characterization. *Phys Chem Chem Phys.* 2018;20(4):2880–9. Available from: <https://doi.org/10.1039/C7CP07650A>
-

-
16. Giordanino F, Vennestrøm PNR, Lundegaard LF, Stappen FN, Mossin S, Beato P, et al. Characterization of Cu-exchanged SSZ-13: A comparative FTIR, UV-Vis, and EPR study with Cu-ZSM-5 and Cu- β with similar Si/Al and Cu/Al ratios. *Dalt Trans.* 2013;42(35):12741–61. Available from: <https://doi.org/10.1039/C3DT50732G>
 17. Jodłowski PJ. DeNO_x Abatement over Sonically Prepared Iron-Substituted Y, USY and MFI Zeolite Catalysts in Lean Exhaust Gas Conditions. *Nanomaterials.* 2018;8(21). Available from: <https://doi.org/10.3390/nano8010021>
 18. Divakar D, Aranzabal A. Catalytic oxidation of trichloroethylene over Fe-ZSM-5 : Influence of the preparation method on the iron species and the catalytic behavior. *Applied Catal B, Environ* [Internet]. 2016;180:210–8. Available from: <http://dx.doi.org/10.1016/j.apcatb.2015.06.027>
 19. Kalita B, Talukdar AK. Synthesis and characterization of Ce doped MFI zeolite. *Mater Chem Phys* [Internet]. 2012;133(2–3):713–7. Available from: <http://dx.doi.org/10.1016/j.matchemphys.2012.01.067>
 20. Krishna Reddy J, Suresh G, Hymavathi CH, Durga Kumari V, Subrahmanyam M. Ce (III) species supported zeolites as novel photocatalysts for hydrogen production from water. *Catal Today.* 2009;141(1–2):89–93. Available from: <https://doi.org/10.1016/j.cattod.2008.05.012>
 21. Zhang Y, Xue M, Zhou Y, Zhang H, Wang W, Wang Q, et al. Propane dehydrogenation over Ce-containing ZSM-5 supported platinum–tin catalysts: Ce concentration effect and reaction performance analysis†. *RSC Adv.* 2016;6(35):29410–22. Available from: <https://doi.org/10.1039/C6RA04173F>
 22. Neumann GT, Hicks JC. Novel hierarchical cerium-incorporated MFI zeolite catalysts for the catalytic fast pyrolysis of lignocellulosic biomass. *ACS Catal.* 2012;2(4):642–6. Available from: <https://doi.org/10.1021/cs200648q>
 23. Zhan W, Guo Y, Wang Y, Liu X, Guo Y, Wang Y, et al. Synthesis of Lanthanum-doped MCM-48 molecular sieves and its catalytic performance for the oxidation of styrene. *J Phys Chem B.*
-

-
- 2007;111(42):12103–10. Available from: <https://doi.org/10.1021/jp0745211>
24. Zamratul MIM, Zaidan AW, Khamirul AM, Nurzilla M, Halim SA. Formation, structural and optical characterization of neodymium doped-zinc soda lime silica based glass. *Results Phys* [Internet]. 2016;6:295–8. Available from: <http://dx.doi.org/10.1016/j.rinp.2016.05.014>
 25. Sharma SK, Behm T, Köhler T, Beyer J, Gloaguen R, Heitmann J. Library of UV-Visible Absorption Spectra of Rare Earth Orthophosphates, LnPO₄ (Ln = La-Lu, except Pm). *Crystl.*2020;4. Available from: <https://doi.org/10.3390/cryst10070593>
 26. Khamirul, Mimzwazam, Halim SA. Novel eco-friendly synthesis of neodymium doped zinc silicate phosphor based waste glass ceramic: structural, thermal and luminescence properties. *J Mater Sci Mater Electron*. 2017;28: 9395–9402. Available from: <https://doi.org/10.1007/s10854-017-6680-5>
 27. Chimalawong P, Kaewkhao J, Kaewkhao C, Limsuwan P. Optical and electronic polarizability investigation of Nd³⁺-doped soda-lime silicate glasses. *J Phys Chem Solids* [Internet]. 2010;71(7):965–70. Available from: <http://dx.doi.org/10.1016/j.jpcs.2010.03.044>
 28. Narayanan S, Judith Vijaya J, Sivasanker S, John Kennedy L, Ariharan A. Enhanced selectivity to benzaldehyde in the liquid phase oxidation of benzyl alcohol using nanocrystalline ZSM-5 zeolite catalyst. *J Porous Mater*. 2014;21(5):633–41. Available from: <https://doi.org/10.1007/s10934-014-9809-4>
 29. Hsu HL, Roselin LS, Selvin R, Bououdina M. Enhanced activity of hierarchical zeolitic material with ZSM-5 structure for the tert-butylation of phenol. *J Exp Nanosci*. 2011;6(6):612–21. Available from: <https://doi.org/10.1080/17458080.2010.513717>
 30. Srivastava R, Iwasa N, Fujita S ichiro, Arai M. Synthesis of Nanocrystalline MFI-Zeolites with Intracrystal Mesopores and Their Application in Fine Chemical Synthesis Involving Large Molecules. *Chem Euro J*. 2008;14(31):9507–11. Available from: <http://dx.doi.org/10.1002/chem.200801113>
 31. Zhu H, Liu Z, Kong D, Wang Y, Yuan X, Xie Z. Synthesis of
-

- ZSM-5 with intracrystal or intercrystal mesopores by polyvinyl butyral templating method. *J Colloid Interface Sci* [Internet]. 2009;331(2):432–8. Available from: <http://dx.doi.org/10.1016/j.jcis.2008.11.071>
32. Kore R, Srivastava R, Satpati B. ZSM-5 Zeolite Nanosheets with Improved Catalytic Activity Synthesized Using a New Class of Structure-Directing Agents. *Chem Eur J*. 2014;20:1–12. Available from: <http://dx.doi.org/10.1002/chem.201402665>
 33. Valchev LT and VP. Nanozeolites: Synthesis, Crystallization Mechanism, and Applications. *Chem Mater*. 2005;17:2494–513. Available from: <http://dx.doi.org/10.1021/cm 047908z>
 34. Persson H, Duman I, Wang S, Pettersson LJ, Yang W. Catalytic pyrolysis over transition metal-modified zeolites: A comparative study between catalyst activity and deactivation. *J Anal Appl Pyrolysis* [Internet]. 2019;138:54–61. Available from: <https://doi.org/10.1016/j.jaap.2018.12.005>
 35. Galarneau A, Desmurs L, Vaultot C, Nouali H, Lebeau B, Daou TJ, et al. Hierarchical MFI Zeolite Catalysts: How to Determine Their Textural Properties?-A Comparative Study. *Catal Res*. 2022;2(2):1–1. Available from: <http://dx.doi.org/10.21926/cr.2202009>
 36. Kapustin GI, Brueva TR, Klyachko AL, Beran S, Wichterlova B. Determination of the number and acid strength of acid sites in zeolites by ammonia adsorption: Comparison of calorimetry and temperature-programmed desorption of ammonia. *Appl Catal*. 1988;42(2):239–46. Available from: [https://doi.org/10.1016/0166-9834\(88\)80005-8](https://doi.org/10.1016/0166-9834(88)80005-8)
 37. Katada N, Igi H, Kim J ho, Niwa M. Determination of the Acidic Properties of Zeolite by Theoretical Analysis of Temperature-Programmed Desorption of Ammonia Based on Adsorption Equilibrium. *J Phys Chem B*. 1997;101(31):5969–77. Available from: <https://doi.org/10.1021/jp9639152>
 38. Ruiz MG, Casados DS, Pliego JA, Álvarez CM, Andrés ES, Tartalo DS, et al. ZSM-5 zeolites modified with Zn and their effect on the crystal size in the conversion of methanol to light aromatics (MTA). *React Kinet Mech Catal*. 2020;129:471–490. Available

from: <https://doi.org/10.1007/s11144-019-01716-4>

39. Ozhukka Parambil F, Kumari P, Padmanabhan A. Effect of copper on textural and acidic properties of hierarchical nanocrystalline ZSM-5. *Asia-Pacific J Chem Eng.* 2020;15(5):1–14. Available from: <https://doi.org/10.1002/apj.2547>
40. Begum SH, Hung C Te, Chen YT, Huang SJ, Wu PH, Han X, et al. Acidity-activity correlation over bimetallic iron-based ZSM-5 catalysts during selective catalytic reduction of NO by NH₃. *J Mol Catal A Chem [Internet].* 2016;423(November 2017):423–32. Available from: <http://dx.doi.org/10.1016/j.molcata.2016.07.036>
41. Zhang L, Gao J, Hu J, Li W, Wang J. Lanthanum Oxides-Improved Catalytic Performance of ZSM-5 in Toluene Alkylation with Methanol. 2009;130:355–61. Available from: <https://doi.org/10.1007/s10562-009-9965-3>
42. Ozhukka Parambil F, Kumari P, Padmanabhan A. Cerium Incorporated Nanocrystalline ZSM-5: An Efficient Catalyst for Friedel Crafts Acylation of Toluene. *J Nanosci Nanotechnol.* 2020;20(9):5823–32. Available from: <http://dx.doi.org/10.1166/jnn.2020.17811>
43. Kessouri A, Boukoussa B, Bengueddach A, Hamacha R. Synthesis of iron-MFI zeolite and its photocatalytic application for hydroxylation of phenol. *Res Chem Intermed [Internet].* 2018;44(4):2475–87. Available from: <https://doi.org/10.1007/s11164-017-3241-8>
44. Figueiredo AL, Araujo AS, Linares M, Peral Á, García RA, Serrano DP, et al. Catalytic cracking of LDPE over nanocrystalline HZSM-5 zeolite prepared by seed-assisted synthesis from an organic-template-free system. *J Anal Appl Pyrolysis.* 2015;117:132–40. Available from: <http://dx.doi.org/10.1016/j.jaap.2015.12.005>
45. Larsen SC. Nanocrystalline zeolites and zeolite structures: Synthesis, characterization, and applications. *J Phys Chem C.* 2007;111(50):18464–74. Available from: <https://doi.org/10.1021/jp074980m>.
46. Rahmani F, Haghghi M. One-pot hydrothermal synthesis of ZSM-5-CeO₂ composite as a support for Cr-based nanocatalysts:

-
- Influence of ceria loading and process conditions on CO₂-enhanced dehydrogenation of ethane. *RSC Adv.* 2016;6(92):89551–63. Available from: <http://dx.doi.org/10.1039/C6RA15787D>
47. Wang K, Dong M, Niu X, Li J, Qin Z, Fan W, et al. Highly active and stable Zn/ZSM-5 zeolite catalyst for the conversion of methanol to aromatics: Effect of support morphology. *Catal Sci Technol.* 2018;8(21):5646–56. Available from: <https://doi.org/10.1039/C8CY01734D>
48. Broeke P Van Den. Removal of SO_x and NO_x Gases From Stationary Sources Using Copper Zeolite Based Catalysts. Qatar University College of Engineering Environmental. 2014
49. Cheng Y, He L. Synthesis and characterization of Nd-doped ZSM-5 zeolite from diatom mud. *Key Eng Mater.* 2017;727:422–6. Available from: <https://doi.org/10.4028/www.scientific.net/KEM.727.422>.
50. Zhang GQ, Bai T, Chen TF, Fan WT, Zhang X. Conversion of methanol to light aromatics on Zn-modified nano-HZSM-5 zeolite catalysts. *Ind Eng Chem Res.* 2014;53(39):14932–40. Available from: <https://doi.org/10.1021/ie5021156>
51. Dolabella S, Borzi A, Dommann A, Neels A. Lattice Strain and Defects Analysis in Nanostructured Semiconductor Materials and Devices by High-Resolution X-Ray Diffraction: Theoretical and Practical Aspects. *Small Methods.* 2022;6(2). Available from: <https://doi.org/10.1002/smt.202100932>
52. Szyrkowska I, El M. Oxidation of odorous nitrogen-containing compounds: ammonia and trimethylamine over Cu/zeolite catalysts. *Reac Kinet Mech Cat.* 2014;111(2):763–73. Available from: <http://dx.doi.org/10.1007/s11144-013-0666-y>
53. Ruggeri MP, Nova I, Tronconi E, Collier JE, York APE. Structure–Activity Relationship of Different Cu–Zeolite Catalysts for NH₃–SCR. *Top Catal.* 2016;59(10–12):875–81. Available from: <https://doi.org/10.1007/s11244-016-0562-6>
54. Delahay G, Mauvezin M, Coq B, Kieger S. Effect of the reductant nature on the catalytic removal of N₂O on a Fe-zeolite-beta catalyst. *Catal Com.* 2001;3(8):385–9. Available from:
-

[https://doi.org/10.1016/S1566-7367\(02\)00157-7](https://doi.org/10.1016/S1566-7367(02)00157-7)

55. Wu M, Wang H, Zhong L, Zhang X, Hao Z, Shen Q. Effects of acid pretreatment on Fe - ZSM - 5 and Fe - beta catalysts for N₂O decomposition. *Chin J Catal* .2016;37(6):898–907. Available from: [https://doi.org/10.1016/S1872-2067\(15\)61052-X](https://doi.org/10.1016/S1872-2067(15)61052-X)
56. Gao F, Szanyi J, Wang Y, Schwenzler B, Kollár M, Peden CHF. Hydrothermal Aging Effects on Fe/SSZ-13 and Fe/Beta NH₃-SCR Catalysts. *Top Catal*. 2016;59(10–12):882–6. Available from: <https://doi.org/10.1007/s11244-016-0563-5>
57. Delahay G, Mauvezin M, Coq B, Kieger S. Selective catalytic reduction of nitrous oxide by ammonia on iron zeolite beta catalysts in an oxygen rich atmosphere: Effect of iron contents. *J Catal*. 2001;202(1):156–62. Available from: <https://doi.org/10.1006/jcat.2001.3279>.
58. Mehdad A, Lobo RF. Ethane and ethylene aromatization on zinc-containing zeolites. *Catal Sci Technol* [Internet]. 2017;7(16):3562–72. Available from: <http://dx.doi.org/10.1039/C7CY00890B>
59. Zhang B, Zhu X, Gao J, Zhu Y, Ma W. Zn modification of Beta zeolite: Effect on acid sites and propylene oxide rearrangement. *Chem Phys* [Internet]. 2020;539:110983. Available from: <https://doi.org/10.1016/j.chemphys.2020.110983>
60. Qi L, Zhang Y, Conrad MA, Russell CK, Miller J, Bell AT. Ethanol Conversion to Butadiene over Isolated Zinc and Yttrium Sites Grafted onto Dealuminated Beta Zeolite. *J Am Chem Soc*. 2020;142(34):14674–87. Available from: <https://doi.org/10.1021/jacs.0c06906>
61. Jia C, Massiani P, Beaunier P, Barthomeuf D. Solid-state exchange of lanthanum in beta zeolite. *Appl Catal A, Gen*. 1993;106(2): L185-L191. Available from: [https://doi.org/10.1016/0926-860X\(93\)80176-Q](https://doi.org/10.1016/0926-860X(93)80176-Q)
62. Dalla Costa BO, Peralta MA, Querini CA. Gas phase dehydration of glycerol over, lanthanum-modified beta-zeolite. *Appl Catal A Gen* [Internet]. 2014;472:53–63. Available from: <http://dx.doi.org/10.1016/j.apcata.2013.12.011>

-
63. Wang H, Zou Y. Modified beta zeolite as catalyst for Fries rearrangement reaction. *Catal Letters*. 2003;86(4):163–7. Available from: <https://doi.org/10.1023/A:1022642231296>
 64. Gołabek K, Palomares AE, Martínez-Triguero J, Tarach KA, Kruczała K, Girman V, et al. Ce-modified zeolite BEA catalysts for the trichloroethylene oxidation. The role of the different and necessary active sites. *Appl Catal B Environ*. 2019;259: 118022. Available from: <https://doi.org/10.1016/j.apcatb.2019.118022>
 65. Jiang L, Cai Y, Jin M, Zhu Z, Wang Y. The Influence of Ce or Mn Doping on Cu-Based Catalysts for De-NO_x with NH₃-SCR. *J Chem*.2020;1-8. Available from: <http://dx.doi.org/10.1155/2020/1462801>
 66. Lopes JH, Nogueira FGE, Gonçalves M, Oliveira LC. Modified zeolite with transition metals Cu and Fe for removal of methylene blue from aqueous medium: Mass spectrometry study. *Bull Chem React Eng Catal*. 2015;10(3):237–48. Available from: <http://dx.doi.org/10.9767/brec.10.3.8624.237-248>
 67. Santos RC, Freire Almeida D, de Aguiar Pontes D, Lau LY, Magalhães Pontes LA. Thiophene cracking on zinc modified beta zeolite. *Mol Catal [Internet]*. 2019;470:112–9. Available from: <https://doi.org/10.1016/j.mcat.2019.04.001>
 68. Haga Y, Pusparatu, Aoyama K, Komura K, Nishimura Y, Sugi Y, et al. Beta Zeolites Modified with Lanthanum and Cerium Oxides for the Isomerization of Hexane. *Mater Sci Forum*. 2007;539–543:2323–8. Available from: <http://dx.doi.org/10.4028/www.scientific.net/MSF.539-543.2323>
 69. Radhika NP, Selvin R, Kakkar R, Roselin LS, Hsu HL. Tertiary Butylation of Aniline Over Nanosized Zeolite Beta Catalyst. *J Nanosci Nanotechnol*. 2018;18(11):7960–8. Available from: <https://doi.org/10.1166/jnn.2018.15538>
 70. Li J, Liu H, An T, Yue Y, Bao X. Carboxylic acids to butyl esters over dealuminated-realuminated beta zeolites for removing organic acids from bio-oils. *RSC Adv [Internet]*. 2017;7(54):33714–25. Available from: <http://dx.doi.org/10.1039/C7RA05298G>
 71. Sakha MR, Halimitabrizi P, Soltanali S, Ektefa F, Hajjar Z, Salari
-

- D. Sustainable product-based approach in the production of olefins using a dual functional ZSM-5 catalyst. *RSC Adv.* 2023;13(11):7514–23. Available from: <https://doi.org/10.1039/D3RA00037K>
72. Alswat AA, Ahmad M Bin, Hussein MZ, Ibrahim NA, Saleh TA. Copper oxide nanoparticles-loaded zeolite and its characteristics and antibacterial activities. *J Mater Sci Technol [Internet]*. 2017;33(8):889–96. Available from: <http://dx.doi.org/10.1016/j.jmst.2017.03.015>
73. Li X, Li B, Xu J, Wang Q, Pang X, Gao X, et al. Synthesis and characterization of Ln-ZSM-5/MCM-41 (Ln = La, Ce) by using kaolin as raw material. *Appl Clay Sci [Internet]*. 2010;50(1):81–6. Available from: <http://dx.doi.org/10.1016/j.clay.2010.07.006>
74. Miri A, Darroudi M, Sarani M. Biosynthesis of cerium oxide nanoparticles and its cytotoxicity survey against colon cancer cell line. *Appl Organomet Chem.* 2020;34(1):1–7. Available from: <https://doi.org/10.1002/aoc.5308>
75. Cychosz KA, Thommes M. Progress in the Physisorption Characterization of Nanoporous Gas Storage Materials. *Engineering [Internet]*. 2018;4(4):559–66. Available from: <https://doi.org/10.1016/j.eng.2018.06.001>
76. Komurcu M. Ethene oligomerization on nickel containing beta zeolite catalyst. Norway: Department of Chemistry, Faculty of Mathematics and Natural Sciences, University of Oslo 2016. https://www.duo.uio.no/bitstream/handle/10852/51682/edit_final.pdf?sequence=6
77. Pereda-Ayo B, De La Torre U, Illán-Gómez MJ, Bueno-López A, González-Velasco JR. Role of the different copper species on the activity of Cu/zeolite catalysts for SCR of NO_x with NH₃. *Appl Catal B Environ [Internet]*. 2014;147:420–8. Available from: <http://dx.doi.org/10.1016/j.apcatb.2013.09.010>
78. Chiche B, Finiels Annie, Gauthier C, Geneste P. Acylation over cation-exchanged Montmorillonite. *J Mol Catal.* 1987;42(2):229–35. Available from: [https://doi.org/10.1016/0304-5102\(87\)85029-0](https://doi.org/10.1016/0304-5102(87)85029-0)
79. Kaur J, Kozhevnikov I V. Efficient acylation of toluene and

- anisole with aliphatic carboxylic acids catalysed by heteropoly salt $\text{Cs}_{2.5}\text{H}_{0.5}\text{PW}_{12}\text{O}_{40}$. *Chem Commun.* 2002;(21):2508–9. Available from: <https://doi.org/10.1039/B207915C>
80. De Castro C, Primo J, Corma A. Heteropolyacids and large-pore zeolites as catalysts in acylation reactions using α , β -unsaturated organic acids as acylating agents. *J Mol Catal A Chem.* 1998;134(1–3):215–22. Available from: [https://doi.org/10.1016/S1381-1169\(98\)00038-7](https://doi.org/10.1016/S1381-1169(98)00038-7)
 81. Su K, Li Z, Cheng B, Zhang L, Zhang M, Ming J. The studies on the Friedel-Crafts acylation of toluene with acetic anhydride over HPW/TiO₂. *Fuel Process Technol* [Internet]. 2011;92(10):2011–5. Available from: <http://dx.doi.org/10.1016/j.fuproc.2011.05.026>
 82. Zhang L, Su K, Ming J, Li Z, Cheng B. Support effects of PW/SiO₂ on friedel-crafts acylation of toluene with acetic anhydride. *Adv Mater Res.* 2011;233–235:58–61. Available from: <https://doi.org/10.4028/www.scientific.net/AMR.233-235.58>
 83. El-Sharkawy EA, Al-Shihry SS. Friedel-Crafts acylation of toluene using superacid catalysts in a solvent-free medium. *Monatshefte fur Chemie.* 2010;141(3):259–67. Available from: <https://doi.org/10.1007/s00706-010-0250-3>.
 84. Pandey AK, Singh AP. A novel catalytic method for the acylation of aromatics to the corresponding ketones over zeolite catalysts. *Catal Letters.* 1997;44(1–2):129–33. Available from: <https://doi.org/10.1023/A:1018964722746>
 85. Chiche B, Finiels Annie, Gauthier C, Geneste P. Friedel-Crafts Acylation of Toluene and p -Xylene with Carboxylic Acids Catalyzed by Zeolites. *J Org Chem.* 1986;51(11):2128–30. Available from: <https://doi.org/10.1021/jo00361a039>
 86. Botella P, Corma A, López-Nieto JM, Valencia S, Jacquot R. Acylation of Toluene with Acetic Anhydride over Beta Zeolites: Influence of Reaction Conditions and Physicochemical Properties of the Catalyst. *J Catal.* 2000;195(1):161–8. Available from: <https://doi.org/10.1006/jcat.2000.2971>
 87. Dejaegere EA, Thybaut JW, Marin GB, Baron G V, Denayer JFM. Modeling of toluene acetylation with acetic anhydride on H-USY

- zeolite. *Ind Eng Chem Res.* 2011;50(21):11822–32. Available from: <https://doi.org/10.1021/ie2007906>
88. Sheemol VN, Tyagi B, Jasra R V. Acylation of toluene using rare earth cation exchanged zeolite β as solid acid catalyst. *J Mol Catal A Chem.* 2004;215(1–2):201–8. Available from: <https://doi.org/10.1016/j.molcata.2004.02.002>
89. Ji X, Qin Z, Dong M, Wang G, Dou T, Wang J. Friedel-Crafts acylation of anisole and toluene with acetic anhydride over nano-sized Beta zeolites. *Catal Letters.* 2007;117(3–4):171–6. Available from: <https://doi.org/10.1007/s10562-007-9131-8>
90. Selvin R, Roselin LS, Khayyat SA, Umar A. Hierarchical zeolite Beta: An efficient and eco-friendly nanocatalyst for the Friedel-Crafts acylation of toluene. *J Nanosci Nanotechnol.* 2013;13(6):4415–20. Available from: <http://dx.doi.org/10.1166/jnn.2013.7153>
91. Cruz-Cabeza AJ, Esquivel D, Jiménez-Sanchidrián C, Romero-Salguero FJ. Metal-Exchanged β Zeolites as Catalysts for the Conversion of Acetone to Hydrocarbons. *Materials (Basel).* 2012;5(1):121–34. Available from: <https://doi.org/10.3390/ma5010121>
92. Bernardon C, Ben Osman M, Laugel G, Louis B, Pale P. Acidity versus metal-induced Lewis acidity in zeolites for Friedel–Crafts acylation. *Comptes Rendus Chim [Internet].* 2017;20(1):20–9. Available from: <http://dx.doi.org/10.1016/j.crci.2016.03.008>
93. Serrano DP, van Grieken R, Melero JA, García A, Vargas C. Nanocrystalline ZSM-5: A catalyst with high activity and selectivity for epoxide rearrangement reactions. *J Mol Catal A Chem.* 2010;318(1–2):68–74. Available from: <https://doi.org/10.1016/j.molcata.2009.11.009>
94. Chen Z, Chen W, Tong T, Zeng A. Continuous liquid phase acylation of toluene over HBEA zeolite: Solvent effects and origin of the deactivation. *J Mol Catal A Chem [Internet].* 2015;396:231–8. Available from: <http://dx.doi.org/10.1016/j.molcata.2014.09.038>
95. Derouane EG, Crehan G, Dillon CJ, Bethell D, He H, Derouane-Abd Hamid SB. Zeolite catalysts as solid solvents in fine

chemicals synthesis: 2. Competitive adsorption of the reactants and products in the Friedel-Crafts acylations of anisole and toluene. *J Catal.* 2000;194(2):410–23. Available from: <https://doi.org/10.1006/jcat.2000.2933>

96. Vinu A, Krithiga T, Gokulakrishnan N, Srinivasu P, Anandan S, Ariga K, et al. Halogen-free acylation of toluene over FeSBA-1 molecular sieves. *Microporous Mesoporous Mater.* 2007;100(1–3):87–94. Available from: <https://doi.org/10.1016/j.micromeso.2006.10.014>

Chapter 4

Development of Nanocrystalline Hierarchical ZSM-5 and Zeolite Beta: Investigating Structural Properties and Catalytic Activity

Abstract

This chapter showcases innovative strategies for enhancing the catalytic activity through developing hierarchical porosity in nanocrystalline ZSM-5 and zeolite beta. Adding PMMA during nucleation minimizes internal defective silanols and successfully creates hierarchically porous ZSM-5 zeolite. However, the zeolite beta synthesized with addition of PMMA has narrow distribution of mesopores and micropores. This chapter also evaluates the catalytic properties of hierarchical ZSM-5 and zeolite beta in the acetylation of 2-methoxynaphthalene (2-MON) using acetic anhydride. Improved homogeneity of mesopores and environment of active sites enhance selective catalytic behaviour, highlighting the significance of heteroporous structures in zeolite catalysis.

Section A

Tailoring of Hierarchical Porosity in Nanocrystalline ZSM-5 and Curing of Silanol Defects

4A.1 Introduction

Introducing hierarchical pore structure into the zeolitic matrix is highly beneficial, as it modifies the acidic properties, enhances stability, and reduces coke formation. This, in turn, elevates turnover number, turnover frequency, and catalyst efficiency. The improvement in properties is achieved by introducing mesopores that serve as a pathway from external to internal micropores, ultimately augmenting reactant permittivity. The growing need for hierarchically porous zeolites across diverse fields has prompted the exploration of various techniques to customize hetero porosity.(1-3)

Techniques involved in the synthesis of zeolites can alter the crystallinity. The perturbation in the crystalline arrangement breaks the perfect symmetry when the Si-O-Si or Si-O-Al bonds are fractured to yield Si-OH groups which are considered as defects. The bulk of these materials and their outer physical surfaces have the largest concentration of silanol hydroxyl groups. The number of Si-OH groups in the defective zeolites appears to be 10^3 times greater than the number of silanol groups required to terminate the exterior crystal surface.(4) Heat treatment, fluoride-mediated approach, hydroxyl radical-assisted approach, addition of silane-based molecules, and incorporation of heteroatoms into the framework are some of the techniques available for healing silanol defects

generated in zeolites. The fluoride-assisted synthesis results in decreased Si-OH moieties, forming crystals with fewer defects. However, fluoride ions should be avoided for environment-friendly production of zeolite due to their poisonous and corrosive nature.(5,6)

Templates used in the synthesis can change the texture of zeolite precursor gel and encourage the synthesis of oligomer units in solution. They control the condensation of these units into a specific framework through electrostatic and dispersive interactions within the micropores in which they are imprisoned.(7) In recent decades, a significant amount of research has been done in templating techniques for selecting and modifying specific zeolite structures.(8) Tetra propylammonium hydroxide (TPAOH) is widely used as a template in the synthesis of ZSM-5. It offers excellent selectivity and crystallinity to the zeolite structure and requires moderate reaction conditions. It also synthesizes mesoporous molecular sieves, imparting high acidity to zeolite secondary building units.(9) Nevertheless, using only TPAOH in the synthesis results in certain imperfections within the zeolite framework. The post-synthesis alkali treatment of the zeolite structure obtained using the TPAOH templating method preferentially removes the defective Si-sites internally by desilication, leading to a hollow structure rather than a uniform mesoporous structure. Thus, ZSM-5 synthesized using TPAOH as template has a defective Si-rich interior and an Al-rich exterior with a hollow structure that micropore channels can only

access.(10) Since defects severely affect the essential qualities of zeolite, research efforts are concentrated on healing defects without further distorting the zeolite framework.

During the synthesis of hierarchical zeolites, the zeolite precursors are mixed with micropore structure directing agents and meso-macropore directing templates. Surfactant-based templates and cationic polymers are good candidates for the role of dual-function templates in the synthesis of hierarchical zeolites.(11–17) Surfactant-based templates help to crystallize zeolite, and they self-assemble into organized mesostructures. Consequently, the synthesized zeolites have intercrystalline mesopore-containing two-dimensional nanosheets or small crystallites.(18) Using cationic polymers as templates initiates the formation of an ordered mesoporous structure, giving rise to hierarchical zeolites with 3D continuous zeolitic frameworks and densely interconnected intercrystalline mesopores.(19)

Non-surfactant and non-ionic polymers are also attractive exotemplates because of their low cost and easy availability. They interact highly with Si- and Al- precursor species via hydrogen bonds and covalent and Coulomb forces.(16,20–23) Among the different templates used in the hydrothermal synthesis of hierarchical zeolites, PMMA is an excellent exotemplate because, during crystallization, the silanol groups condense by their interaction with PMMA, forming hierarchically ordered materials.(24)

The sequence and the mode of PMMA addition in the synthesis process are crucial for influencing the arrangement of pores within the matrix.(24–26)

The primary objective of this work is to establish a straightforward approach for producing nanocrystalline hierarchical zeolite ZSM-5 with reduced defects. To maintain precise control over the crystallinity, shape, and microporosity of ZSM-5, a novel method is employed in this study, involving the addition of PMMA powder during the crystallization process. PMMA becomes encapsulated into zeolite particles during hydrothermal synthesis due to its affinity for the partially crystallized precursor solution. A thorough analysis of the results obtained through various characterization techniques enables a comprehensive understanding of the characteristics of the synthesized zeolites. The investigation delves extensively into the impact of polymer incorporation on producing hetero porosity and it elucidates the mechanism involved in defect healing.

4A.2 Results and Discussion

The synthesis of NZ and the procedure for synthesizing nanocrystalline hierarchical ZSM-5 (NZ xP) is explained in detail in Sections 2.6 of Chapter 2.

Figure 4A.1 shows the XRD patterns of the hydrothermally synthesized nanocrystalline ZSM-5(NZ) and hierarchically porous ZSM-5 synthesized using PMMA (NZ xP; x=0.5, 1.0, 1.5 and 2.0 g of PMMA). The characteristic diffraction peaks indicate the ZSM-5

structure of MFI topology, which matches with the XRD of IZA data. The sharp peaks in XRD patterns of NZ and NZ xP represent the characteristic peaks associated with the MFI structure. There is no evidence of other crystalline phases, suggesting the formation of ZSM-5 zeolite with high phase purity. It is found that the total percentage crystallinity calculated using equation (2.2) of NZ decreased upon treatment with PMMA, as depicted in Table 4A.1. The decrease in intensity of the peaks of NZ xP indicates the reduced number of planes oriented in a particular direction, thereby suggesting a reduction in their crystalline nature. The absence of PMMA in the calcined zeolitic matrix is proven by comparing the XRD patterns obtained with the XRD of virgin PMMA with peaks at 2θ values of 12° , 30° and 32° .⁽²⁷⁾ The absence of such peaks in Figure 4A.1 indicates that PMMA and TPAOH have been completely burnt off during calcination.

Table 4A.1. Crystallinity of NZ and NZ xP

Zeolite sample	Crystallinity (%)
NZ	89.23
NZ 0.5P	87.05
NZ 1.0P	72.51
NZ 1.5P	65.62
NZ 2.0P	61.33

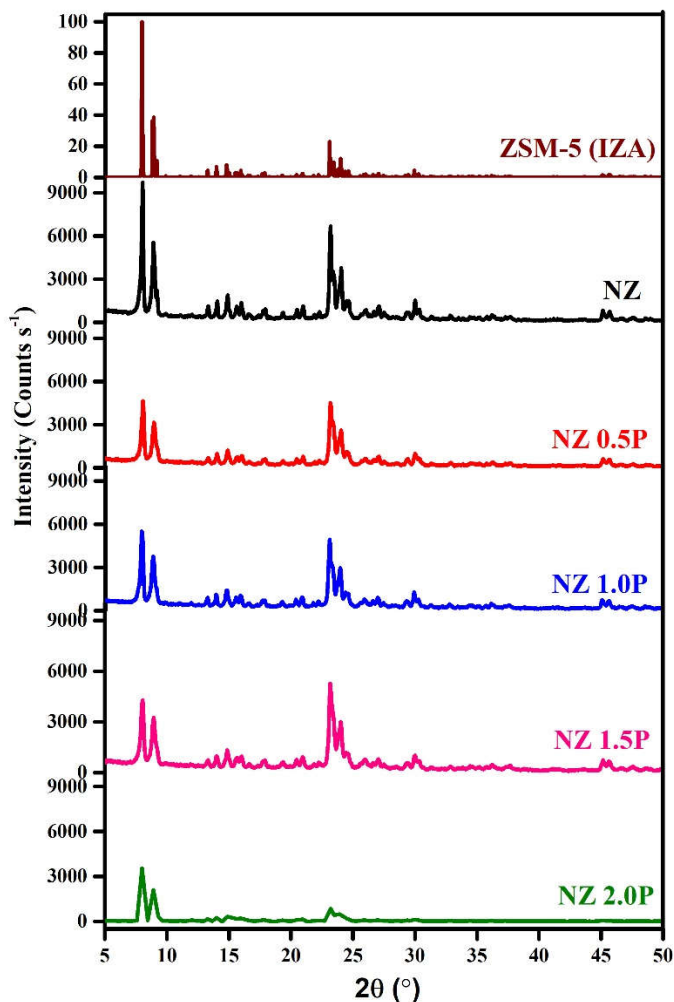


Figure 4A.1. XRD patterns of NZ and NZ xP with simulated IZA pattern

Figure 4A.2 shows the FT-IR spectra of NZ and NZ xP. The presence of the infrared band at 550 cm^{-1} indicates the five-membered ring of the pentasil zeolite structure. The band at 1225 cm^{-1} has been attributed to the external asymmetric stretching

vibration of the Si–O–Si groups, which is the structure-sensitive infrared band of ZSM-5 and so it is an evidence of nanosized ZSM-5. The bands at 796 cm^{-1} and $1056\text{--}1100\text{ cm}^{-1}$ are due to the external symmetric stretching and internal asymmetric stretching of Si–O–Si groups, respectively.(28,29) The IR bands of NZ xP do not have similarities to the FTIR features of PMMA (Figure 4A.3).(30) In contrast, it resembles the FTIR spectrum of NZ, which indicates the complete removal of PMMA by calcination and ascertains the formation of the NZ structure.

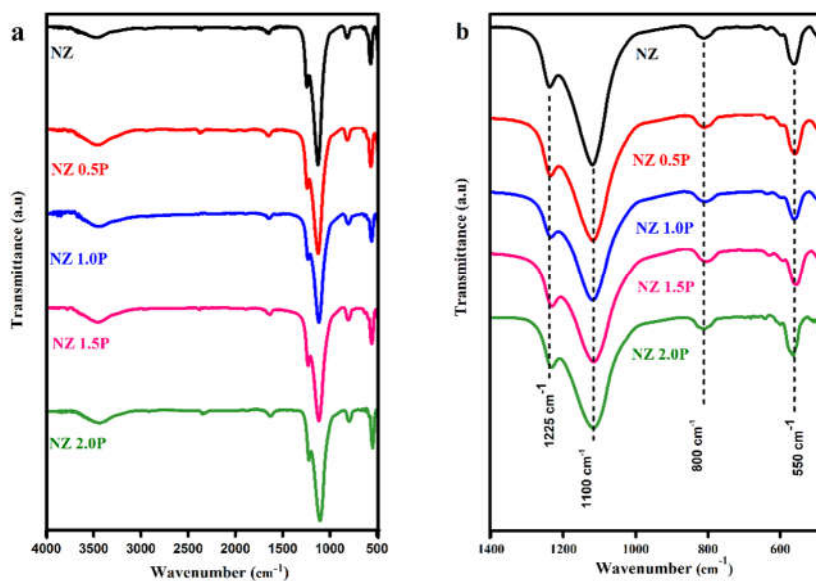


Figure 4A.2. FTIR spectra of NZ and NZ xP samples a) 4000-500 cm^{-1} b) 1400-500 cm^{-1}

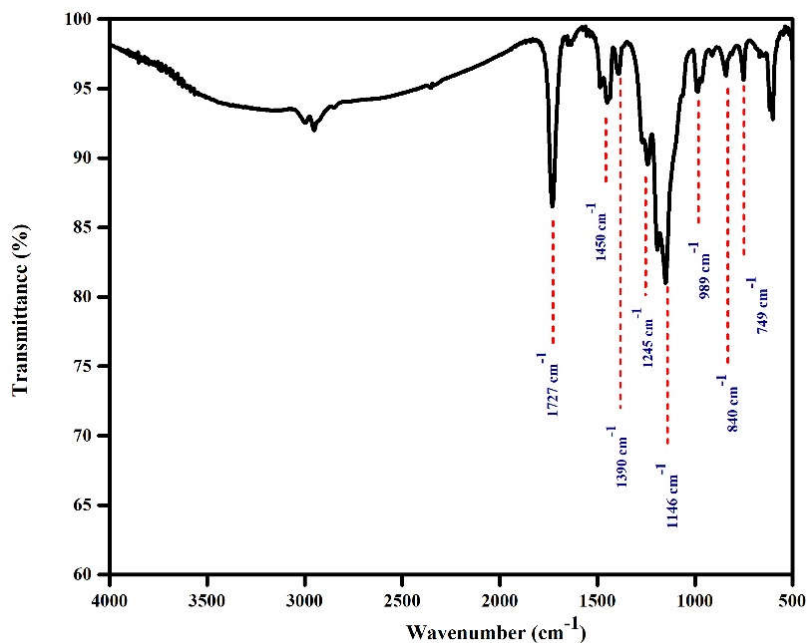


Figure 4A.3. FTIR spectra of prepared PMMA

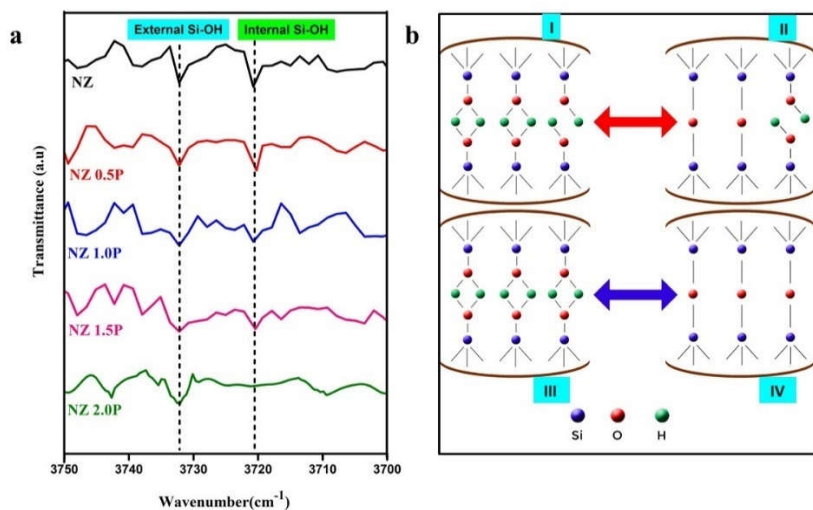
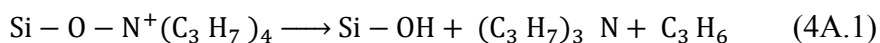


Figure 4A.4. (a) FTIR spectra of NZ and NZ xP samples from 3750 cm^{-1} to 3700 cm^{-1} (b) Schematic representation of the formation of internal silanols in NZ (I) & (II) and disappearance of internal silanols in NZ xP by PMMA (III) & (IV)

The silanol groups (3750 cm^{-1} to 3700 cm^{-1}) in NZ and NZ xP samples are identified by FTIR (Figure 4A.4a). The external and internal silanol groups can be differentiated because the external silanols are free, but internal silanols undergo hydrogen bonding. Peaks corresponding to external free silanols appear around 3732 cm^{-1} , and that corresponding to internal silanols appear at a lower frequency of 3720 cm^{-1} due to hydrogen bonding. The internal silanol groups in the case of NZ are generated by the breakdown of TPA^+ cations as illustrated in the following equation 4A.1.



Due to the excellent templating property of TPAOH, the intersection of zeolite channels is formed at the position of TPA^+ , the straight and sinusoidal channels are directed by its four propyl chains. The generated silanols pointed out in Equation 4A.1 are located close to methyl groups of TPA^+ . Since there are more internal silanols in NZ, the intensity of IR bands corresponding to silanols is substantially higher than that for NZ xP, as indicated in Figure 4A.4 (a). This is caused by the extensive usage of highly basic TPA^+ template, which prevents sufficient condensation of silicate species during the synthesis.(31–34) The water molecule and TPA^+ cations were removed during the high-temperature calcination process, which caused the production of Si-O-Si groups. In contrast, the defective internal silanol group remains unaltered, as seen in (I) and (II) in Figure 4A.4 (b). In the case of NZ xP, there are a relatively small number of silanol groups compared to NZ, which is evidenced by

the decrease in intensity of the bands corresponding to internal silanols. These internal silanols are referred to as defects. Here, PMMA is also used as a structure-directing agent in addition to TPAOH, and the presence of PMMA controls the defects, as schematically represented in (III) and (IV) of Figure 4A.4.

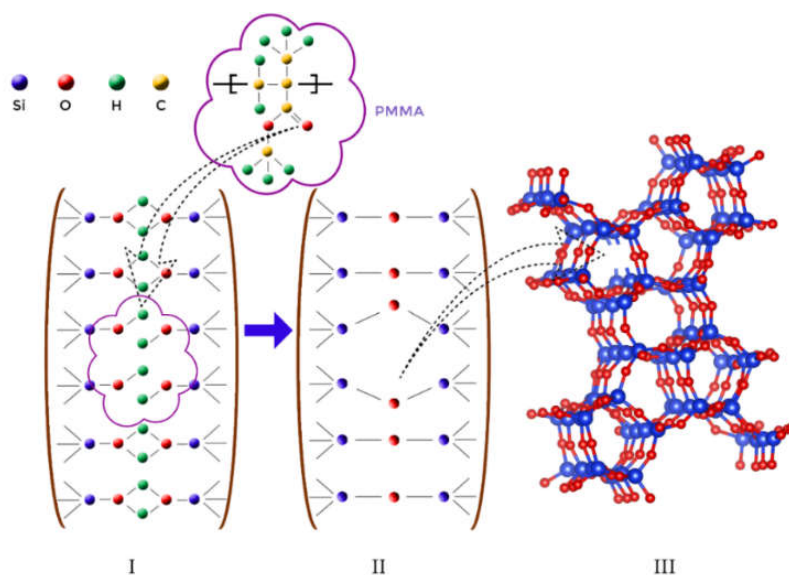


Figure 4A.5. Suggested mechanism for the creation of mesoporosity and the removal of silanol defects in zeolites using PMMA

Figure 4A.5 depicts a schematic picture of how PMMA can help to reduce the number of defective silanols in NZ xP. As shown in (I) of Figure 4A.5, TPA⁺ cations create the internal silanol groups. The reduction of defective silanols in NZ xP is caused by the efficient hydrogen bonding interaction between the C=O of the PMMA and silanol groups, which subsequently leads to the condensation of silicate species. The incorporation of PMMA led to specific

condensation and recrystallization mechanisms, which led to the formation of Si-O-Si groups. These siloxane groups obtained after the calcination step are responsible for producing mesoporous crystals with fewer defects, as shown in (II) of Figure 4A.5.

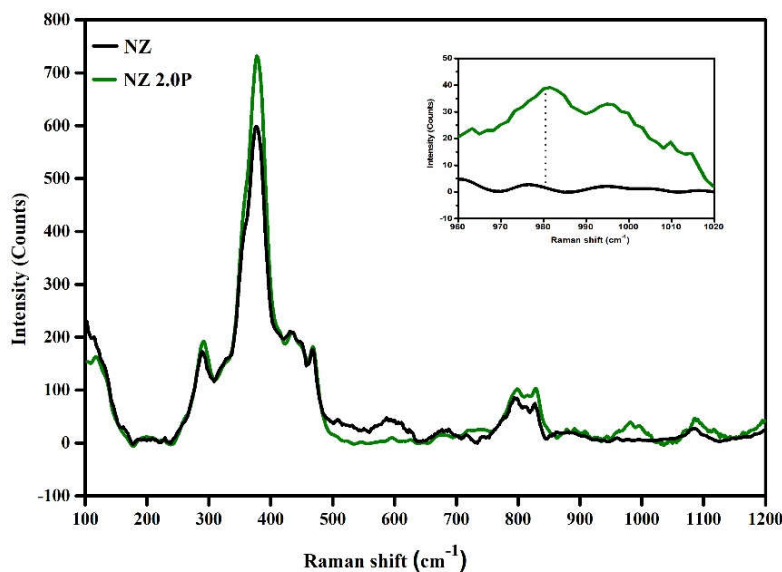


Figure 4A.6. Raman spectra of NZ and NZ 2.0P; the inset highlights the spectral region between 960-1020 cm⁻¹

Figure 4A.6 depicts the 2-D Raman spectra of the zeolites NZ and NZ 2.0P samples in the range 250-1200 cm⁻¹. The first noticeable difference in the Raman spectra of the two zeolite samples is the change in spectral intensity. The most prominent band in the spectra of both NZ and NZ 2.0P is attributable to the vibration of the O atom within the Si-O-Si bond plane at 380 cm⁻¹, confirming the presence of five-membered rings in the ZSM-5 zeolite. This effect is believed to arise from the symmetrical stretching of Si-O-Si vibrations within

the 5-membered rings of the MFI framework. This spectral characteristic proved the presence of the ZSM-5 phase, indicating the formation of the ZSM-5 structure in both samples.(35–37) Furthermore, the peak at 380 cm^{-1} is indicative of crystallinity. The slight decrease in intensity of this band of NZ 2.0P complies with the XRD studies.(38) All of the other notable bands at 438 cm^{-1} , 454 cm^{-1} , and 470 cm^{-1} , corresponding to stretching of oxygen atom in a plane perpendicular to Si-O-Si, bending of O-Si-O(Al), and bending of Si-O respectively, have decreased in their intensities for NZ 2.0P when compared to NZ. The spectral intensity of the Raman band at 800 cm^{-1} is attributed to the symmetric stretching of bridging oxygen of Si-O-Si linkage, and the intensity is similar for both samples.(39,40) The most striking change in the spectra of ZSM-5 due to PMMA addition is evident in the $960\text{--}1050\text{ cm}^{-1}$ range (inset of Figure 4A.6). The spectra revealed the presence of silanols in NZ, as evidenced by the band at 980 cm^{-1} , which is attributed to Si-O stretching vibrations caused by the existence of terminal silanol species or a defective Si-OH group.(41–44) However, signal intensity is very low at 980 cm^{-1} for the NZ 2.0P sample, which complements and confirms the low concentration of silanols observed in FTIR spectra.

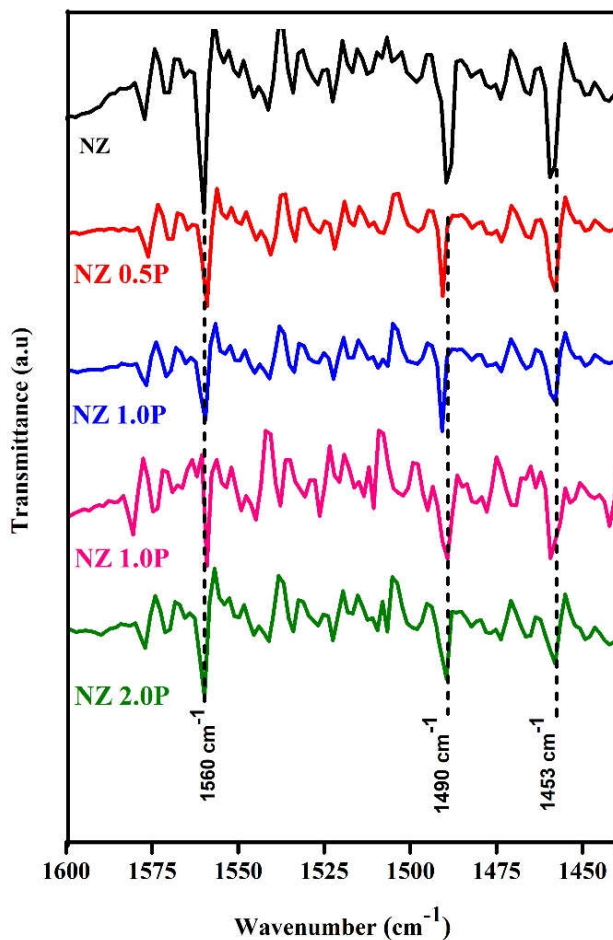


Figure 4A.7. FTIR of pyridine sorbed NZ and NZ xP samples

The acidity profile of pyridine sorbed NZ and NZ xP samples are shown in Figure 4A.7. The vibration of pyridinium ions (Brønsted acid sites) gives rise to a peak seen around 1560 cm^{-1} , and interaction of pyridine with Lewis acid sites generates a peak at 1453 cm^{-1} . Both the zeolite samples exhibit Brønsted and Lewis acidity with slight changes in intensity. The peak corresponding to total acid sites in the

NZ sample at 1490 cm^{-1} is more intense than that of NZ xP samples. The slight decrease in intensity of peaks corresponding to acid sites exhibited by NZ xP is attributed to the generation of mesopores in the structure, which thereby affects the microstructure.(45)

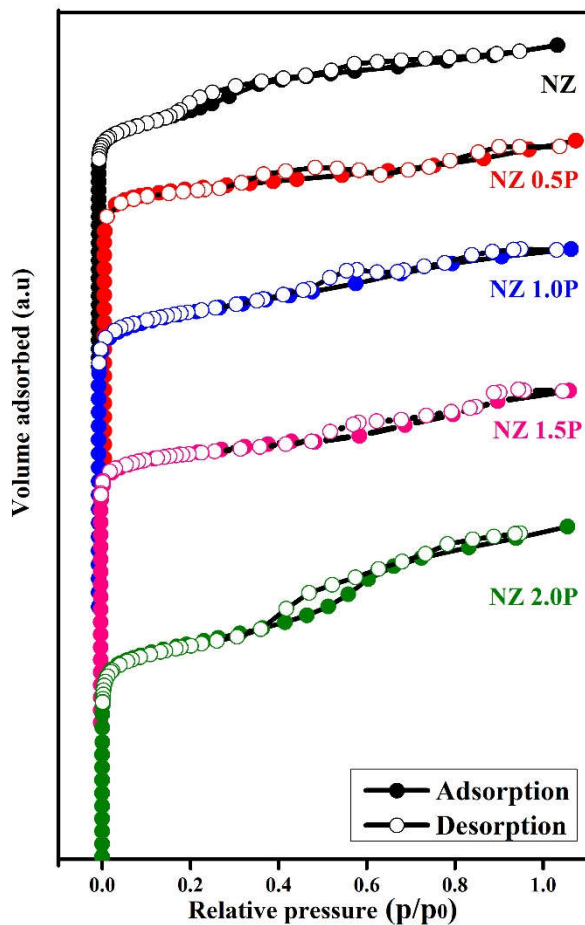


Figure 4A.8. Nitrogen adsorption-desorption isotherm of NZ and NZ xP samples

The nitrogen sorption isotherms of NZ and NZ xP in Figure 4A.8. are a combination of IUPAC Type I and Type IV, typical for microporous and mesoporous materials, respectively. Adsorption of nitrogen proceeds through two steps in MFI structure; the first is the preferential adsorption on strong sites, and the second step is the clustering around the adsorbed molecules.(46) The clustering occurs slowly only after the completion of the adsorption on strong sites. This results in a low-pressure hysteresis loop in MFI at $p/p_0 = 0.2$, caused by precise adsorbent–adsorbate interactions.(47,48) Due to the strong interactions of silanols with nitrogen molecules, a significant amount of nitrogen is adsorbed at low pressures. Low-pressure hysteresis is exhibited by NZ due to the high nitrogen adsorption on silanols. The proposed interpretation agrees with the FTIR (Figure 4A.4 a) since a higher amount of silanols is observed for the NZ than NZ xP, indicating the presence of additional adsorption sites for nitrogen adsorbate by fundamental adsorption interactions.(49) The disappearance of the low-pressure hysteresis loop in NZ xP is caused by the lower number of defective silanols in it. As a result, it proves that the PMMA-assisted synthesis method did not result in any defect sites like those seen in NZ. In addition to this, isotherms of NZ and NZ xP exhibit a hysteresis loop from $0.4 < p/p_0 > 1$, which is due to the existence of mesopores. It is found that the hysteresis in the nitrogen adsorption-desorption isotherms of NZ xP is shifted to higher p/p_0 , reflecting the correspondingly larger mesopore sizes in the respective NZ. The mesoporosity in NZ can be attributed to the intercrystalline voids. However, the isotherms of

NZ xP exhibit a more significant H4 hysteresis loop, suggesting a typical mesoporous structure generated by PMMA-assisted synthesis in addition to inherent micropores.

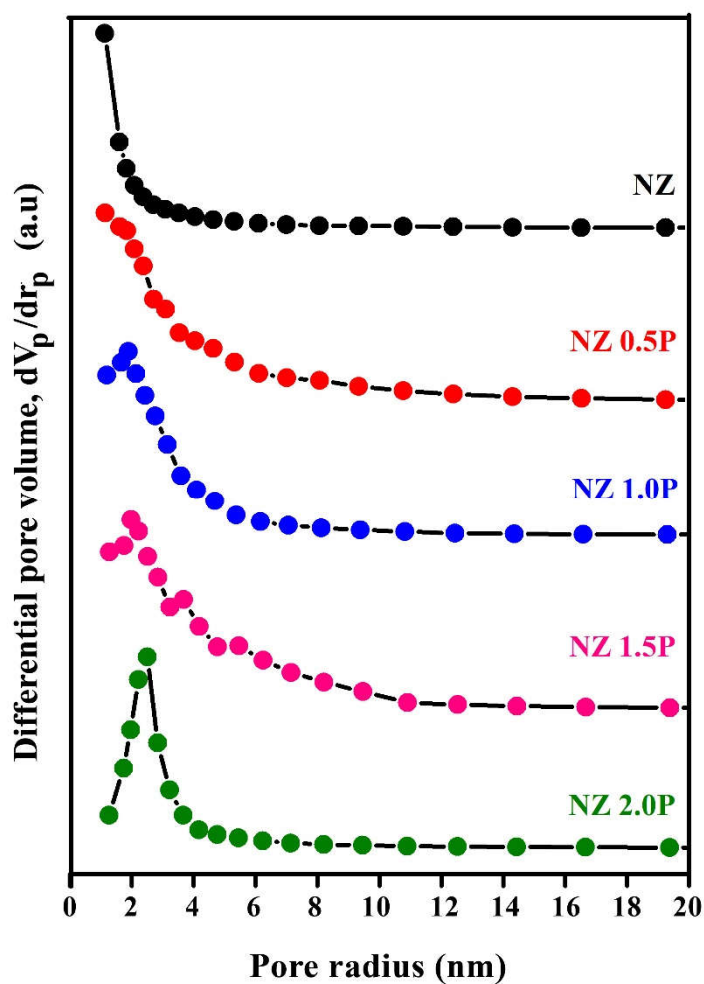


Figure 4A.9. Pore size distribution of NZ and NZ xP samples

Figure 4A.9 shows the mesoporous size distribution of NZ and NZ xP samples acquired by the BJH method using the adsorption branch.

It can be seen that the NZ 2.0P sample has mesopores of 2 to 4 nm radius, with a distribution peak at 2.5 nm. The result matches well with the N₂ adsorption-desorption isotherms. The introduction of PMMA into the zeolite structure of NZ xP induces an internal pore strain, ultimately leading to an expansion in pore diameters, thereby giving rise to mesopores. The templates TPAOH and PMMA burn simultaneously during calcination, which causes a localized rise in temperature and increased pressure. This increase in pressure partially breaks the zeolite structure. This phenomenon elucidates the observed reduction in surface area and pore volume of NZ xP.(50,51) This can be observed in Table 4A.2.

Table 4A.2: Textural properties of NZ and NZ xP

Zeolite samples	Total Surface area ^a	Total pore volume _a	Meso pore-specific surface area ^b	Mesopore volume ^b	Pore distribution peak ^c
	[m ² g ⁻¹]	[cm ³ g ⁻¹]	[m ² g ⁻¹]	[cm ³ g ⁻¹]	[nm]
NZ	394.52	0.20	20.23	0.03	1.26
NZ 0.5P	331.82	0.15	11.494	0.02	1.79
NZ 1.0P	334.15	0.16	21.70	0.03	1.92
NZ 1.5P	337.26	0.16	27.39	0.04	1.96
NZ 2.0P	366.70	0.18	40.53	0.06	2.50

^aBET; ^b CI(Cranston and Inkley) method; ^c BJH method ;

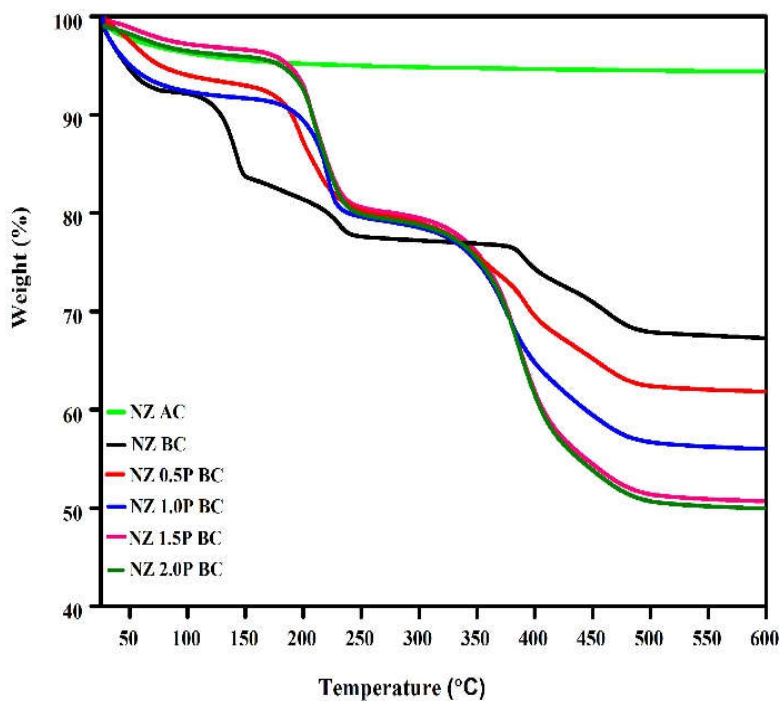


Figure 4A.10. TGA curves of NZ and NZ xP samples; AC and BC indicate after and before calcination, respectively

Table 4A.3 Summary of TGA results of NZ and NZ xP

Sample	Weight loss Region 1		Weight loss (%) Region 2 (200-400 °C)	Weight loss (%) Region 3 (above 400 °C)	Total weight loss (%)
	Temperature (°C)	Weight loss (%)			
NZ BC	130	7.80	15.32	8.97	32.09
NZ 0.5P BC	184	6.90	14.56	16.66	38.12
NZ 1.0P BC	201	8.57	13.19	22.12	43.88
NZ 1.5P BC	190	3.45	16.65	27.83	47.93
NZ 2.0 P BC	191	5.55	18.69	28.16	52.40

To confirm the presence of silanol groups and subsequent removal of internal silanols by introducing PMMA, thermogravimetric analysis (TGA) is conducted before the calcination phase in a nitrogen atmosphere. The TGA curves of uncalcined NZ (NZ BC), uncalcined NZ xP (NZ xP BC), and calcined NZ (NZ AC) composites in the temperature range from 50 °C to 600 °C were compared in Figure 4A.10 and corresponding weight loss % is tabulated in Table 4A.3. The only change in the thermogram of NZ AC is that it exhibited a weight loss of 5.3 %, which corresponds to removal of water trapped in it. Three weight losses were observed mainly for the samples except for NZ AC. The first weight loss above 200 °C is attributed to the removal of CO₂ and freely bounded physisorbed water molecules. This temperature is shifted to a higher value for the PMMA-incorporated samples than NZ. PMMA degradation proceeds in three primary weight loss stages. Generally, PMMA degrades through end-chain scission at approximately 360 °C and random scission at around 400 °C. The concluding phase is associated with char oxidation at around 410 °C and 460 °C.⁽⁵²⁾ In NZ xP the primary thermal breakdown of PMMA initiates around 250 °C and persists up to 500 °C. The weight loss in the 200-400 °C range confirms the amount of PMMA added to each sample. The breakdown and pyrolysis of TPAOH that is obstructed in the channels and cages is responsible for the weight loss beyond 400 °C.

For investigating more about defects and their healing, the weight loss regions in connection with the phase changes of water, hydroxyl

groups, and condensation have to be closely monitored. The initial weight loss region (below 200 °C) is assigned to the interlayer and physisorbed water molecules, which exhibit mobility and unrestricted binding. The second weight loss region (200-400 °C) is typically linked to tightly bound water molecules found in the first coordination sphere of interlayer ions or the lattice structure of zeolite. The third weight-loss region indicates structural hydroxyl groups that undergo condensation and dehydration at higher temperatures.(53,54)

Above 200°C, the reduction in silanol content becomes noticeable due to condensation facilitated by PMMA. This pattern is evident in Table 4A.3. In the case of NZ xP BC, it is evident that hydroxyl groups present as silanol groups undergo condensation to yield siloxane groups between 200 - 400 °C. In contrast, isolated internal silanols are gradually removed at higher temperatures.(55) In the case of the NZ BC sample, the weight loss between 200 - 400 °C is comparable to that of other zeolite samples, whereas weight loss at temperatures above 400 °C is notably lower for NZ BC. This lower weight loss is solely attributed to the decomposition and pyrolysis of TPAOH. In contrast, there is a marginal increase in the weight loss percentage of NZ xP BC at the higher temperature region, indicating that PMMA facilitates the condensation and dehydroxylation of silanol groups within the samples.

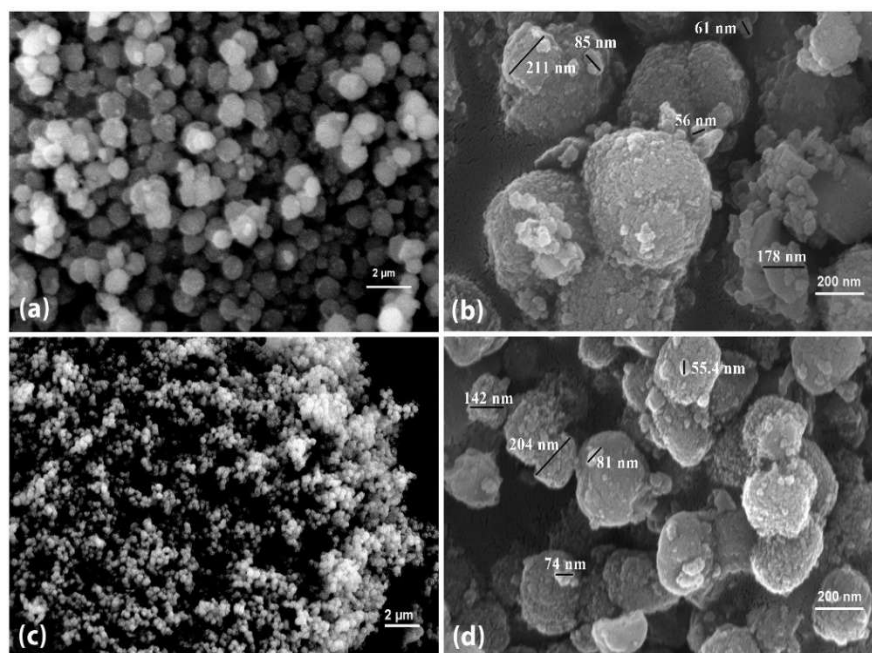


Figure 4A.11. Low and High magnification SEM images of NZ (a) and (b); NZ 2.0 P (c) and (d)

The SEM images given in Figures 4A.11 (a) and 4A.11 (c) are proof of the continuous and interconnected porous texture of nanocrystalline zeolites that extends over the entire sample of NZ and NZ 2.0P. The size of the spherical agglomerates of NZ and NZ 2.0P ranges from 50 nm to 250 nm (Figure 4A.11 b and 4A.11 d). The NZ xP samples have a smaller aggregate size when compared to NZ, which implies that the PMMA is responsible for the decrease in the particle size and imparting hierarchical porosity to NZ 2.0P. This observation can be traced back to the synthesis procedure of NZ 2.0P, the PMMA powder added to the aged precursor solution, in which nucleation of nanocrystals has already begun leading to the

initiation of mesopores formation.(56) The simultaneous removal of PMMA and TPAOH by calcination produces intracrystal mesopores. The PMMA powder keeps the preformed nanocrystals from adhering to each other and gives a hierarchical porous structure in NZ 2.0P.

Figure 4A.12. (a-d) illustrates TEM images corresponding to the NZ and NZ 2.0P with different magnification levels. Here, zeolite samples are found as agglomerates of smaller crystals of about 50 nm. The TEM images in Figure 4A.12 (a) and (b) show the crystal aggregates. The voids created within crystallites aggregate to form additional mesoscale porosity. The interparticle mesopore does not have a well-defined shape and orientation. The TEM images of NZ and NZ 2.0P given in Figure 4A.12 (c) and (d) depicted orderly intergrown ZSM-5 crystals with distinct lattice fringes and sharp edges throughout the sample, composed of numerous crystals. This demonstrated that zeolite crystals continuously grew in specific directions during the crystallization.(57) The neighboring nanocrystals in an aggregate display the same crystalline orientations, proposing a similar degree of intergrowth. An additional porosity in the NZ 2.0P is observable as bright areas, which could be identified as mesopores. These are created by the voids between the nanocrystals resulting from removing the exopolymer template.(58).

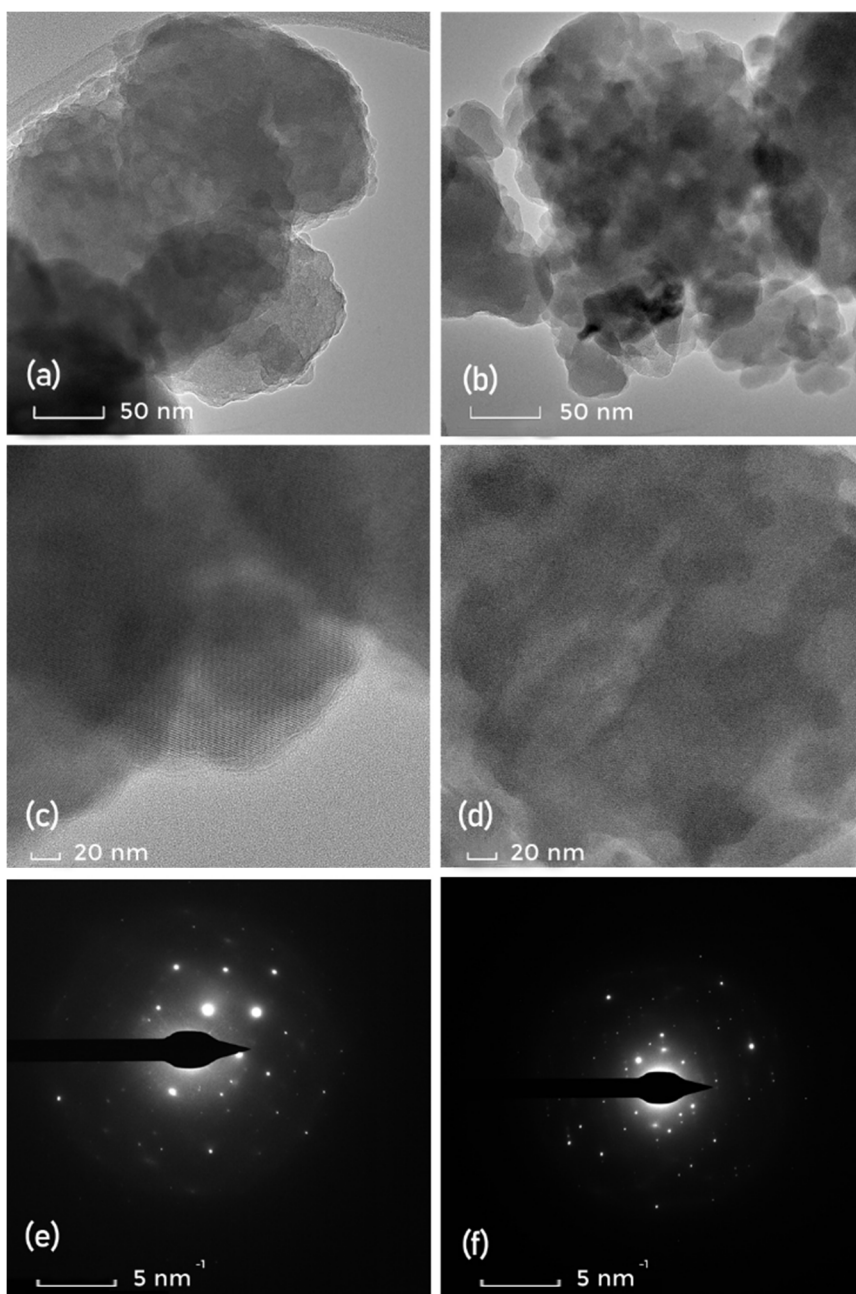


Figure 4A.12. Typical TEM images and SAED pattern of NZ(a,c,e) and NZ 2.0P (b,d,f)

SAED of the ZSM-5 samples (Figure 4A.12 e and f) reveal polycrystalline diffraction patterns. As shown in Figure 4A.12 f, the polycrystalline pattern in the NZ 2.0P indicates the presence of highly crystalline material obtained by transforming zeolite precursor solution and polymer, both having an amorphous character. Figure 4A.12 e and f exhibit multiple little spots from Bragg reflections, resulting in a diffused ring indicating crystallinity of NZ and NZ 2.0P. The diffused ring image obtained in the SAED pattern of NZ 2.0P results due to the hierarchical porous structure imparted from the mild amorphization of NZ.(51,59,60) TEM images complement the findings of XRD, SEM, and BJH analysis, supporting the formation of nanosized stacking crystals with highly crystalline hierarchical zeolite.

4A.3 Conclusions

This section discusses defects in zeolitic structures and the curing of them using PMMA. Defects creep in, leading to structural instability due to the formation of silanol groups instead of specific silicon-oxygen linkages in the zeolite framework. The healing of the defects is done by selective condensation by using PMMA alongside TPAOH as a sacrificial template. Electrostatic attraction and hydrogen bonding occur between silanol groups (Si-OH) on the zeolite surface and PMMA molecules, thus PMMA facilitates Si-O-Si linkages instead of silanol groups thereby leading to defect-free structure of zeolites, thus enhancing stability and economic feasibility. The research addresses structural defects in zeolites and

proposes a straightforward approach to establish hierarchical porosity within the structure, minimizing defect occurrences.

The innovative synthesis approach involves adding PMMA powder to an aging precursor solution where nucleation of nanocrystal has already begun, thereby reducing the occurrence of internal defective silanols. Infrared and Raman spectroscopic analyses provide evidence supporting this observation based on framework vibrations and silanol group vibrations. Results from nitrogen sorption, SEM, and TEM confirm the development of a porous structure without compromising on crystallinity of the matrix. This successful creation of hierarchical porosity in ZSM-5 zeolite could offer valuable insights for the improvisation of the structure of other zeolites. The hierarchical porosity introduced by PMMA facilitates the easy diffusion of reactants and reduces internal coke formation and percolation effects. In summary, the study illustrates that tiny crystals of hierarchically porous ZSM-5, synthesized using PMMA, contain minimum internal structural defects.

Section B

Designing and Structural Assessment of Nanocrystalline Hierarchical Zeolite Beta

4B.1 Introduction

Numerous approaches have been developed to introduce heterogeneous porosity as the demand for hierarchical zeolites remains high across various fields. These approaches can be broadly categorized into two types: destructive and constructive. The destructive method, commonly known as a top-down approach, involves leaching silicon and aluminium atoms from the framework. The most sought-after constructive method is employing templates to induce the formation of secondary porous structures. Templating entails the usage of substances that generate macropores or mesopores to guide the development of additional porosity. During the crystallization of zeolites, these substances are blended with micropore-directing templates and silica-alumina precursors. Polymers present an intriguing option as templates for generating hierarchical porosity due to their cost-effectiveness and easy availability. Polymers can interact with Si- and Al- precursor zeolite species through Coulomb forces.(20) Polymers exhibit superior control over the creation of mesopores compared to alternative templates. Many polymers, including polystyrene beads, natural rubber latex, styrene-butadiene rubber, and PMMA have already been employed as templates. (16,21-25,61)

Compared to other templates, PMMA is a non-toxic and ecologically acceptable template that offers control over the size, shape, and morphology of the nanostructures. It enables the formation of a continuous zeolitic layer by facilitating the heterogeneous nucleation and development of mesoporous zeolites on preexisting sites. This section focuses on synthesizing and characterizing nanocrystalline hierarchical zeolite beta utilizing PMMA.

4B.2 Results and Discussion

The synthesis of NBZ and the procedure for synthesizing nanocrystalline hierarchical zeolite beta (NBZ xP) is explained in detail in Sections 2.6 of Chapter 2. XRD patterns of the nanocrystalline zeolite beta samples are shown in Figure 4B.1. The diffractograms demonstrate good crystallinity, with characteristic peaks at $2\theta = 6.98\text{--}8.31$ and $22.46\text{--}23.86$, typical of the zeolite beta of the BEA framework. The simulated XRD pattern from IZA BEA confirms this. The broad peak in the low-angle region ($6.98\text{--}8.31$) arises from the overlap of peaks at $2\theta = 6.98$ (100), 7.74 (101), 7.34 (110), and 8.31 (111), while the peak at $22.46\text{--}23.86$ corresponds to peaks at $2\theta = 22.46$ (311), 22.64 (422), 22.65 (240), 23.03 (222), and 23.86 (113). These observations rationalize that the crystals obtained are polymorphs A and B.(62)

The treatment with PMMA decreased the percentage crystallinity of zeolite samples. Increased quantities of added polymer may lead to a decrease in zeolite crystallinity. While examining XRD patterns, a

reduction in intensity of X-ray is noted with an increasing amount of polymer content. Due to its polymorphic nature, the diffractograms of zeolite beta exhibit less distinctiveness compared to other highly crystalline zeolites.(63) Increasing polymer content in the synthesis mixture leads to peak broadening and a crystal size reduction, as illustrated in Table 4B.1.

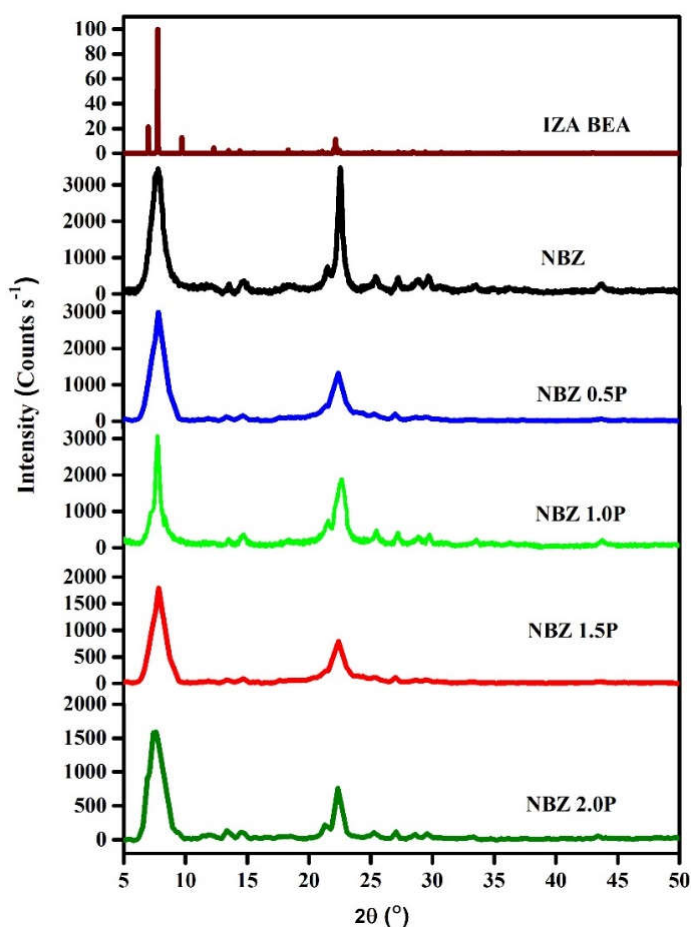


Figure 4B.1. XRD patterns of NBZ and NBZ xP samples with simulated IZA pattern

Table 4B.1. Crystallinity and crystallite size of NBZ and NBZ xP

Sample	Crystallinity (%)	Crystallite Size (nm)
NBZ	79.86	23.21
NBZ 0.5 P	77.79	15.55
NBZ 1.0 P	72.51	14.50
NBZ 1.5 P	72.51	11.97
NBZ 2.0 P	69.59	6.05

Figure 4B.2 depicts the FTIR spectra of NBZ samples. The absorption peaks at 796 cm^{-1} and 1230 cm^{-1} are associated with the external symmetric and asymmetric stretching of Si–O–Al linkages stretching. Notably, the double six-ring (D6R) and double four-ring (D4R) lattice vibrations of zeolite beta manifest as bands at 524 cm^{-1} and 573 cm^{-1} , respectively. These bands verify the existence of the zeolite beta structure. The 1097 cm^{-1} absorption peak in zeolite beta corresponds to the internal asymmetric stretching vibration of the O–Si–O bonds or O–Al–O bonds. (64,65) NBZ xP samples resemble the FTIR spectrum of NBZ, which indicates the complete removal of PMMA by calcination and ascertains the formation of NBZ structure.

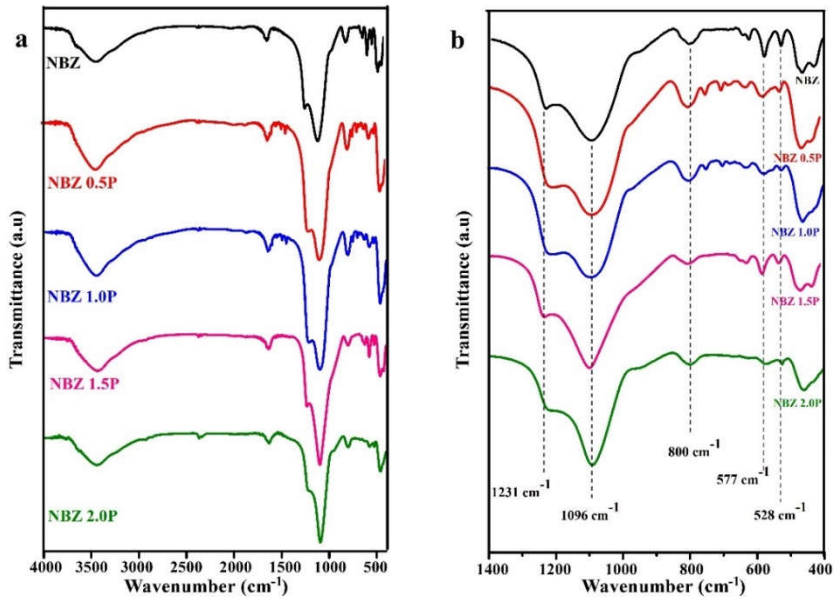


Figure 4B.2. FTIR spectra of NBZ and NBZ xP samples a) 4000-500 cm⁻¹ b) 1400-500 cm⁻¹

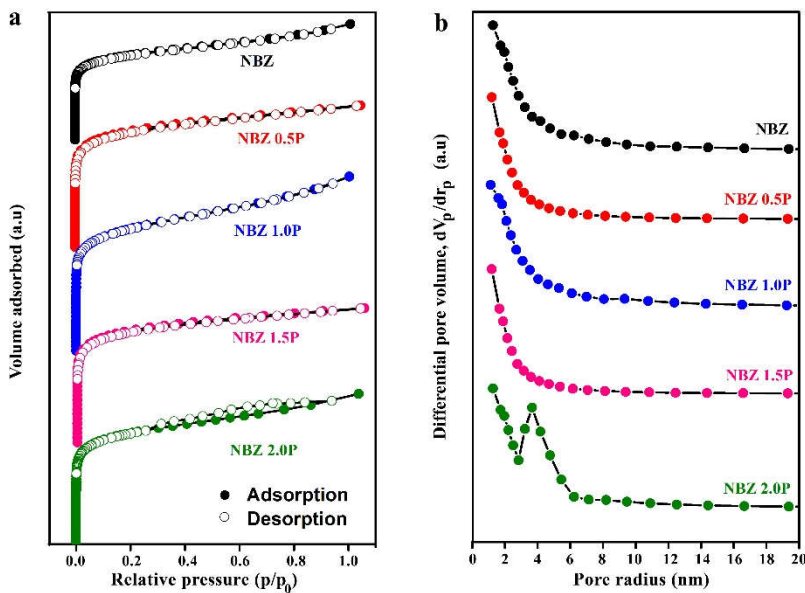


Figure 4B.3. a) Nitrogen adsorption-desorption isotherm and b) Pore size distribution (right) of NBZ and NBZ xP samples

Table 4B.2. Textural properties of NBZ and NBZ xP

Zeolite samples	Total Surface area ^a	Total pore volume ^a	Meso pore-specific surface area ^b	Mesopore volume ^c	Pore distribution peak ^c
	[m ² g ⁻¹]	[cm ³ g ⁻¹]	[m ² g ⁻¹]	[cm ³ g ⁻¹]	[nm]
NBZ	541.23	0.31	20.53	0.05	1.26
NBZ 0.5P	446.08	0.22	26.43	0.06	1.66
NBZ 1.0P	363.12	0.22	39.80	0.09	1.99
NBZ 1.5P	354.58	0.18	38.55	0.05	1.99
NBZ 2.0P	482.42	0.27	44.12	0.10	3.75

^aBET; ^b CI(Cranston and Inkley) method; ^c BJH method

Figure 4B.3a depicts the nitrogen adsorption isotherms at 77K for zeolite samples, while Table 4B.2 summarizes their textural properties. Nitrogen sorption isotherm plots of all samples display a distinct rise occurring below 0.1 relative pressure (p/p_0), indicative of an IUPAC Type-I isotherm pattern commonly associated with microporous substances exhibiting monolayer adsorption. The isotherms of NBZ, NBZ 0.5P, NBZ 1.0P, and NBZ 1.5P show a distinct uptake at low pressures followed by a plateau region with significant adsorptive volume ranging from $p/p_0 = 0.2$ to $p/p_0 = 1$. There is a slight difference between the amount of adsorbed gas during adsorption and desorption at the same pressure. There is a slight lag in pressure compared to its adsorption curve, indicating the presence of slight mesoporosity development, possibly attributed to intercrystalline voids, the compact arrangement of nanocrystals, or

void spaces between nanosized crystal domains within the zeolite particles formed post-calcination.

The isotherm plot of NBZ 2.0P exhibits a combination of characteristics found in both type IV (common in mesoporous materials) and type I isotherms. Notably, it displays an H4-type hysteresis loop ranging from $p/p_0 = 0.3$ to $p/p_0 = 0.8$, attributed to a narrow-slit structure. It is noted that, increasing the amount of PMMA incorporated gradually enlarges the hysteresis loop, thereby confirming the formation of intercrystalline mesoporosity.

The mesoporous pore size distributions are determined using the Barrett–Joyner–Halenda (BJH) method, illustrated in Figure 4B.3b. A distinct narrow peak is observed between 2 and 6 nm pore radii for the NBZ 2.0P sample, indicating a wider pore size distribution than other samples. This suggests that most mesopores fall within the 2 to 6 nm diameter range. These findings are consistent with the N_2 adsorption-desorption isotherms, indicating the presence of additional mesoporosity upon PMMA removal. Consequently, the N_2 adsorption and pore size distribution results confirm the formation of hierarchical zeolite beta during hydrothermal synthesis involving the introduction and removal of PMMA. This underscores that NBZ 2.0P zeolite exhibits both micro-porous framework and mesoporous characteristics, which are pivotal for catalytic performance. The mesoporous volumes and mesopore-specific surface areas of NBZ xP samples are slightly higher than NBZ, indicating the presence of higher mesoporosity.

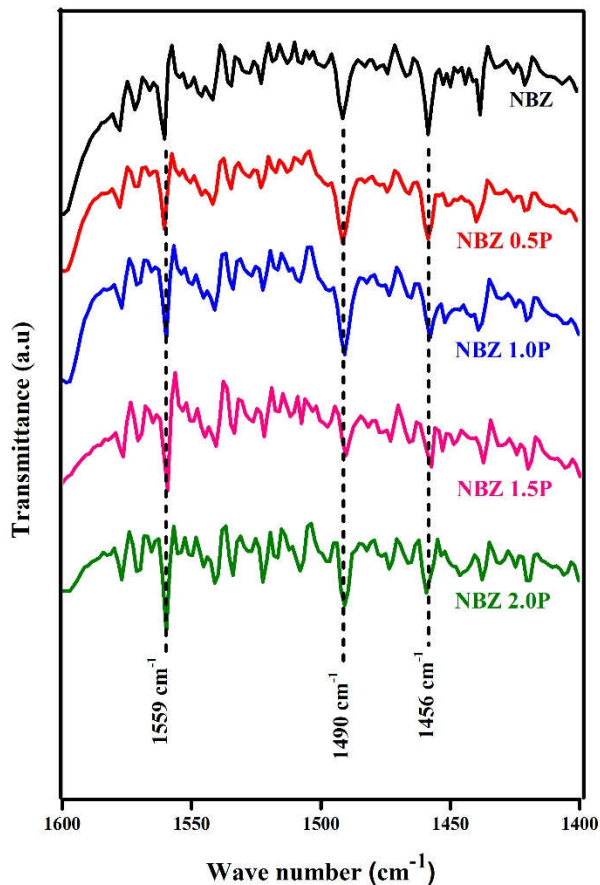


Figure 4B.4. FTIR of pyridine sorbed NBZ and NBZ xP

Figure 4B.4 displays FTIR spectra obtained after pyridine adsorption and evacuation at 80 °C. Bands indicative of Bronsted acid sites at 1559 cm⁻¹ and Lewis acid sites at 1456 cm⁻¹ were consistently identified across all samples. A band observed at 1440 cm⁻¹ corresponds to the hydrogen bonds between the OH groups of zeolites and the nitrogen atom of pyridine. Pyridine interacts with all the different types of acid sites resulting in the band at 1490 cm⁻¹.

The spectra reveal that the formation of mesopores led to a decrease in the intensity of Lewis and Bronsted sites.(66) Expanding the mesoporous surface area increased the concentration of Bronsted acid sites on the external surface.(67) This higher abundance of Bronsted acid sites on the mesopore surface of hierarchical zeolites can significantly enhance the catalytic activity.

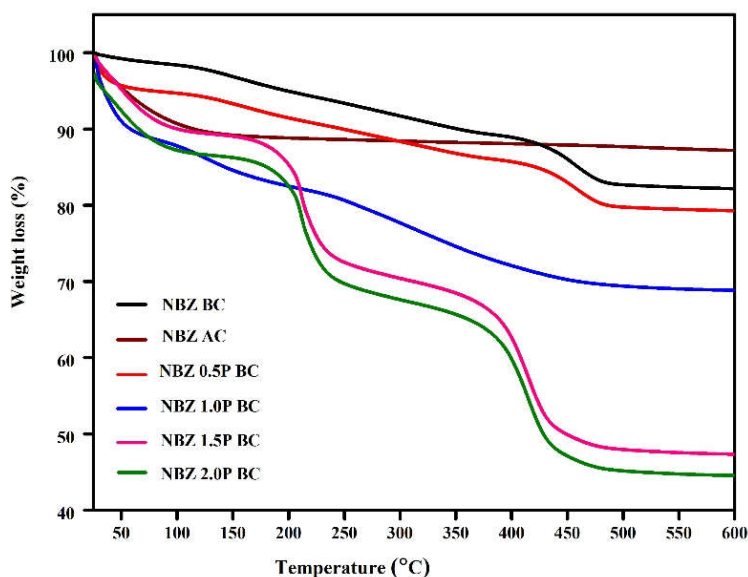


Figure 4B.5. TGA profile of NBZ and NBZ xP; BC and AC indicate before and after calcination, respectively

An idea about the formation of a hierarchical porous structure can be obtained by analyzing the thermogravimetric analysis. The weight loss % in the temperature range from 50 °C to 600 °C was tabulated in Table 4B.3. A weight loss of 12.54% observed in NBZ AC corresponds to the elimination of water trapped. The TGA curves show a pattern of three weight loss phases except for NBZ AC. Generally, the weight loss at 200 °C results from the expulsion of

physically adsorbed water and CO₂. The weight loss seen between 200 and 400 °C corresponds to the decomposition of TEAOH species contained within the zeolite structure, while above 400 °C, the pyrolysis of TEA⁺ species occurs. Weight loss beyond 400 °C signifies the breakdown of organic species serving as charge-compensating cations, chemically bonding with Si-O-Al or Si-O-Si within the zeolite framework.(68)

First phase of decomposition of PMMA also falls in the 50-250 °C range as observed in NBZ xP samples. The second phase of PMMA decomposition ranges from 250 to 400 °C which is also the range when TEAOH decomposition. It is seen that the TGA curve of the NBZ 1.5P and NBZ 2.0P samples are different from the curves of the other three samples, which suggests that the higher amount of PMMA in the samples influences the decomposition and pyrolysis of TEAOH.

Table 4B.3. Summary of TGA results of NBZ and NBZ xP

Sample	Weight loss % (below 200 °C)	Weight loss % (200-400 °C)	Weight loss % (above 400 °C)	Total weight loss (%)
NBZ BC	1.46	8.89	7.21	17.56
NBZ 0.5P BC	4.82	8.97	6.63	20.42
NBZ 1.0P BC	11.64	6.81	12.21	30.66
NBZ 1.5P BC	10.38	18.68	22.96	52.02
NBZ 2.0 P BC	13.43	19.91	22.07	55.41

In NBZ 0.5P BC and NBZ 1.0P BC, where the PMMA content is lower, the resulting thermogram closely resembles that of NBZ BC.

This suggests that PMMA does not persist within the zeolite framework, thus not aiding in the formation of mesopores. Conversely, in NBZ 1.5P BC and NBZ 2.0P BC with higher PMMA content, the thermogram exhibits distinct stages of weight loss, indicating that notable amount of PMMA is incorporated in the matrix.

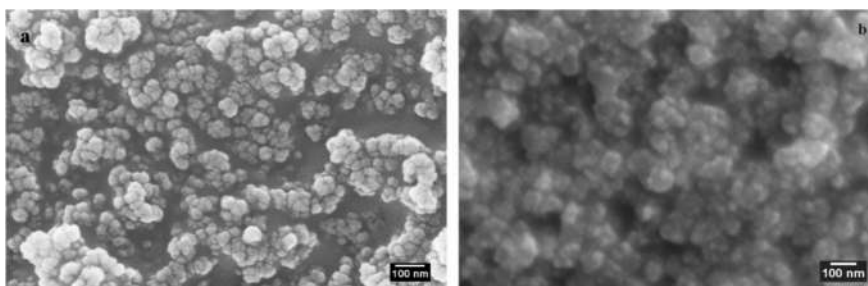


Figure 4B.6. SEM images of a) NBZ and b) NBZ 2.0P

SEM images of the nanocrystalline zeolite and the synthesized hierarchical zeolite are shown in Figure 4B.6. The NBZ zeolite exhibits typical spherical-shaped crystal structures built with an assembly of tiny crystallites. The sample appears very crystalline and shows a structure with interconnecting textural pores. The particles in the SEM picture are tiny aggregates measuring about 100 nm. Small nanoparticles fill the interparticle spaces between these large assemblies. The addition of PMMA and its subsequent removal promotes aggregation into slightly bigger agglomerates in NBZ 2.0P (Figure 4B.6 b). The increase in mesopore distribution, as per BJH analysis is at par with the findings of SEM studies of NBZ 2.0P samples. The incorporation of PMMA causes condensation into larger zeolite agglomerates of about 100-150 nm. The hierarchical zeolite samples are supposed to be constructed by nano zeolite

crystals, which can be easily detected from the SEM images. Moreover, it is hard to find larger crystallite in the SEM images of both NBZ and NBZ 2.0P, confirming that the hierarchical zeolite framework consists of tiny nano-sized crystals. Most of the pores are notably well-interlaced and show good connectivity, which leads to convenient paths for the diffusion of large molecules into the internal surface of the zeolite.

Figure 4B.7 displays the TEM images of zeolite structures with different magnifications. The NBZ and NBZ 2.0P exhibit the presence of highly crystalline aggregated particles. In the case of NBZ 2.0P, the images reveal similarly sized aggregated nanoparticles with brighter areas interspersed between the aggregates, indicating the existence of mesopores. While the crystal structure remains intact, the pore structure appears blurred in NBZ 2.0P. This observation is due to the addition of PMMA to the partially crystallized medium, leading to a slight disorientation. The NBZ and NBZ 2.0P particles consist of aggregates smaller than 200 nm, displaying a polycrystalline nature indicating that the nanostructured crystals form the aggregates. Figures 4B.7 e and f offer evidence supporting the crystallite size furnished in Table 4B.1, determined by applying the Scherrer formula to XRD data.

The crystallite size of NBZ 2.0P measures below 10 nm, as depicted in Figure 4B.7f. The reduced size of nanostructured crystals in NBZ 2.0P indicates an increased presence of voids within its structure. As a result, NBZ 2.0P exhibits superior textural properties compared to NBZ.

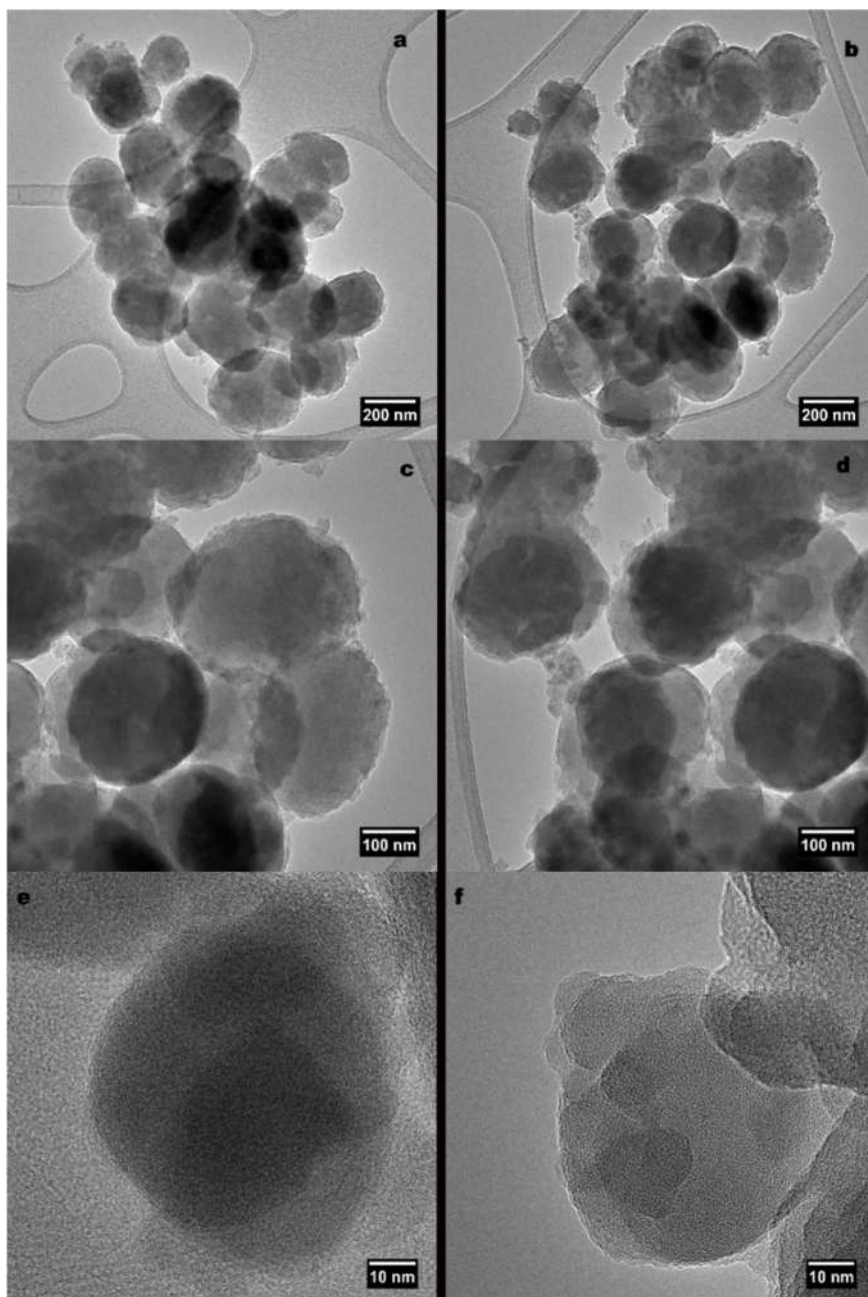


Figure 4B.7. TEM images of NBZ (a, c, e) and NBZ 2.0P (b, d, f)

4B.3 Conclusions

Hierarchical zeolite beta was synthesized through a direct hydrothermal method, employing PMMA as a secondary structure-directing agent and TEAOH as the micropore structure-directing agent. The resulting zeolite beta exhibits XRD patterns and FTIR spectra similar to those of zeolite beta prepared using TEAOH as structure-directing agent. However, the zeolite beta synthesized with PMMA features narrowly distributed mesopores alongside its microporous structure. The samples with minimal polymer addition exhibit a sharp isotherm. The mesoporous nature is evidenced by the hysteresis loop and it shifts towards lower partial pressures; an expansion of the loop is visible in the sample with higher polymer content, indicating a rise in mesopore volume. The zeolite beta with 2.0 g of added PMMA (NBZ 2.0P), exhibits a bimodal pore system and it is expected to benefit catalytic reactions and adsorption applications.

Section C

Evaluation of Catalytic Activity of Nanocrystalline Hierarchical ZSM-5 and Zeolite Beta

4C.1 Introduction

Conventional Friedel-Crafts acylation methods utilizing Lewis acids suffer from a lack of regioselectivity, resulting in the formation of undesired by-products, necessitating their elimination. Moreover, this method generates significant waste and often necessitates excess catalysts. The presence of undesirable reagents further complicates the procedure. Consequently, heterogeneous solid acids like zeolites are employed in the synthesis process to enhance sustainability.

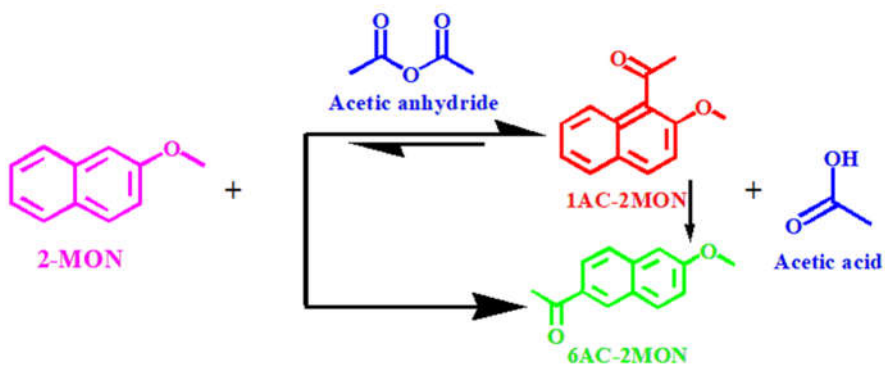
The lower reaction rate is one major issue when using zeolites as a catalyst in synthesizing chemicals. This occurs due to the accumulation of heavy byproducts in the pores or on the surface thereby inhibiting the reaction. However, the reasons for the gradual decrease in zeolite activity during the process remain uncertain, as the rate of change can vary depending on the reaction conditions.

Owing to the remarkable versatility of 2-methoxynaphthalene (2-MON), investigation into its acetylation employing zeolite as a catalyst is undertaken. This reaction can potentially yield 1AC-2MON, which is a compelling intermediate, particularly in phenylation reactions.^(69,70) Conversely, the formation of 6AC-2MON is also significant, as it acts as an intermediate in the synthesis of the anti-inflammatory compound naproxen.^(71,72)

The two most likely locations for electrophilic attacks are positions 1 and 6. If the reaction is kinetically favored the product 1AC-2MON is formed and if it is thermodynamically favored 6AC-2MON is formed, as depicted in scheme 4C.1. Acetic acid and a carbocation are produced during the acylation process by chemisorbed AC_2O . Subsequently, in the pore space, the carbocation combines with 2-MON from the liquid phase to generate 1AC-2MON. These pore diameters play a crucial role in determining the product, as the pore diameter becomes smaller it significantly hinders the access of the reactant 2-MON to the catalytic sites due to intraparticle resistance.⁽⁷³⁾ The adsorbed AC_2O reacts with 2-MON, but 2-MON is also competitively adsorbed on the active sites, functioning as a poison to the acid sites.⁽⁷⁴⁾ Zeolites with higher concentrations of extra-framework aluminium species or Lewis acid sites exhibit lower activity in the acylation of 2-MON.⁽⁷⁵⁾ As the crystal size of zeolite increases, the relative number of external acid sites decreases, resulting in a preference for the core of the crystals for the shape-selective acylation at the 6-position.⁽⁷⁶⁾ Studies revealed that the kind of zeolite structure had less impact on the final product selectivity of 2-MON acylation where as the nature of the acylating agents and the reaction temperature plays a more crucial role. An increase in reaction temperature favored the migration of the acyl group from the 1-position to the 6-position.⁽⁷⁷⁾ Polar and non-polar solvents considerably alter the acylation rate. Non-polar solvents inhibit the reaction by producing various acylated products and acetic acid. In contrast, polar solvents compete with reactant

molecules to penetrate the micropores and adsorb on the acidic sites.(71) However, activity and selectivity decreased when acylation was carried out without a solvent.(78)

This section deals with the suitability of ZSM-5 and beta for the selective acetylation of 2-MON by AC_2O . The acetylation of 2-MON with AC_2O using hierarchical zeolite as a catalyst without any solvent has never been reported earlier.

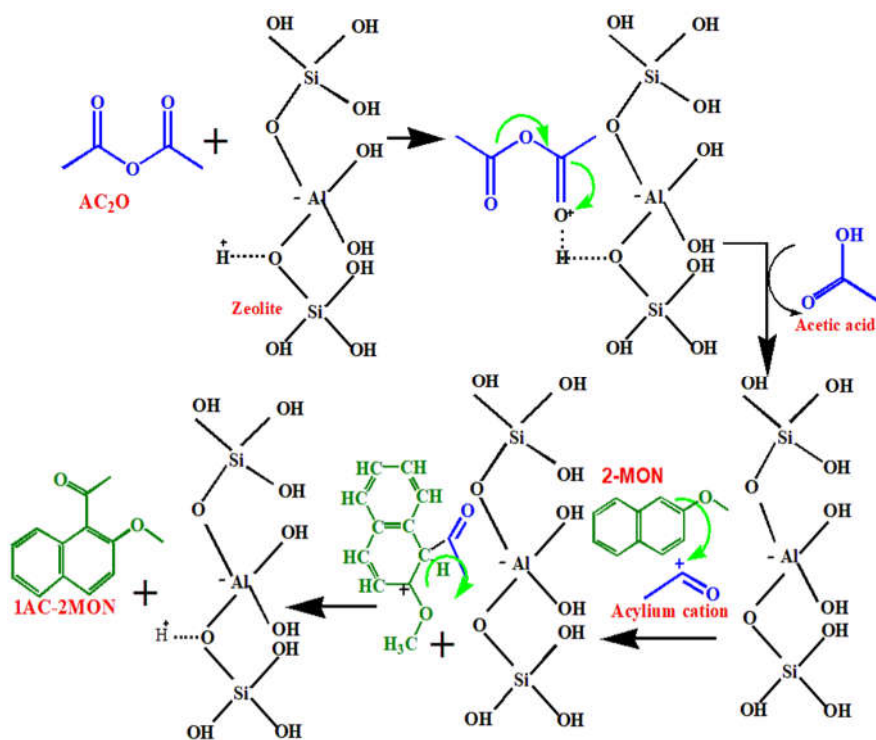


Scheme 4C.1. Acetylation of 2-MON

4C.2 Results and Discussion

The catalytic efficiency of zeolite samples is evaluated by the liquid phase acetylation of 2-MON using AC_2O as the acylating agent. Section 2.7 delves into the specifics of the reaction. The usage of solvents induces competitive adsorption between solvents and reactants. Consequently, the catalytic activity is lowered. (79) By avoiding solvents, the acetylation is made entirely green. Therefore, this work provides an additional advantage over the existing results.

The catalytic activities are evaluated by measuring the percentage conversion of acetylating agents. Excellent selectivity is exhibited during the reaction; the only product formed is 1AC-2MON. The highly permeable internal structure of ZSM-5 and zeolite beta with mesoporosity encourages electrophilic attack at the most active 1-position to the extent that no other product is generated. Scheme 4C.2 represents the mechanism of formation of 1AC-2MON.



Scheme 4C.2. Mechanism of acetylation of 2-MON on zeolite

Initially, the zeolite samples were used to investigate how TOS affected the conversion. The acetylation of 2-MON proceeds through the activation of a Bronsted acid site, which initiates the generation of an acylium cation. The Bronsted acid site in zeolite catalyzes the proton attack on the nucleophilic carbonyl group of AC₂O, forming an acylium ion and acetic acid. Subsequently, the acylium ion reacts with 2-MON to produce an arenium ion. The final step involves the restoration of ring aromaticity, accompanied by proton release, leading to the formation of 1AC-2MON and the regeneration of the zeolitic acid site. Thus, the extent of AC₂O conversion significantly influences the efficiency of the acetylation reaction, reflecting the degree to which AC₂O has reacted to produce the desired product. Monitoring AC₂O conversion enables the optimization of reaction conditions, control of reaction progress, and ensures maximum yield of the desired product while maintaining selectivity.

It was found that after 210 minutes, the conversion of AC₂O nearly stays constant after initially increasing with increasing TOS. Therefore, 210 minutes was fixed as TOS for doing all the following acetylation reaction. The reaction parameters, such as temperature, 2-MON/AC₂O molar ratio, and catalyst quantity, were optimized using NBZ and NZ. The catalytic activity of nanocrystalline ZSM-5 and beta and its hierarchical zeolite samples were compared under these optimized reaction conditions.

4C.2.1 Effect of Molar Ratio of Reactants on Acetylation of 2-MON

The different molar ratios of 2-MON: AC₂O were taken as 1:1, 1:5, and 1:10, and the results are tabulated in Table 4C.1. It can be observed that only 26.1% and 57% AC₂O conversion over NZ and NBZ is attained for the 1:1 ratio of AC₂O to 2-MON (Figure 4C.1). While increasing the molar ratio of 2-MON and AC₂O up to 1:5, the conversion reaches 53.2% and 80.9 % over NZ and NBZ respectively with 100 % selectivity. The excess amount of AC₂O enhances the conversion. Further increasing the amount of AC₂O leads to a slight increase in the conversion with NZ as a catalyst and a decrease in the case of NBZ. This indicates that excessive AC₂O might also lead to a minor increase in deacylation into 2-MON and acetyl migration into 6AC-2MON.(80) Considering the results above, the favorable molar ratio of 2-MON:AC₂O is 1:5 for the selective formation of 1AC-2MON.

Table 4C.1. Comparative study of acetylation of 2-MON over NZ and NBZ at different ratios of 2-MON:AC₂O.

Time (min)	Conversion of AC ₂ O (%)					
	1:1		1:5		1:10	
	NZ	NBZ	NZ	NBZ	NZ	NBZ
15	4.9	27.8	7.7	43.5	9.5	44.9
30	6.0	36.9	12.0	55.8	13.5	56.9
90	9.8	43.0	21.0	63.7	24.0	65.0
120	13.9	49.9	30.1	74.6	33.0	75.9
150	20.0	56.6	43.2	80.7	44.7	80.5
180	25.3	56.8	53.0	81.0	56.3	80.6
210	26.1	57.0	53.2	80.9	56.8	80.6

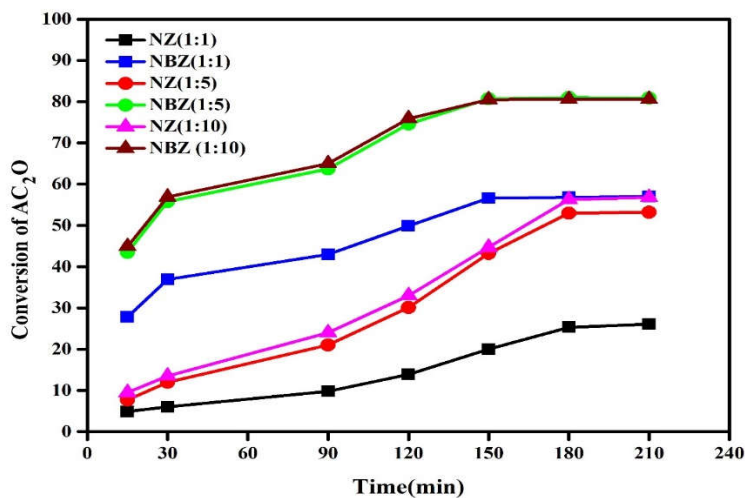


Figure 4C.1. Variation of conversion of AC₂O in the acetylation of 2-MON at different molar ratios of 2-MON: AC₂O

4C.2.2 Effect of Temperature on Acetylation of 2-MON

The acetylation reaction was carried out at three different temperatures, 30 °C, 40 °C, and 50 °C, and results are depicted in Figure 4C.2. The results are tabulated in Table 4C.2.

Table 4C.2. Comparative study of acetylation of 2-MON over NZ and NBZ at different temperatures

Time (min)	Conversion of AC ₂ O (%)					
	30 °C		40 °C		50 °C	
	NZ	NBZ	NZ	NBZ	NZ	NBZ
15	5.0	29.7	7.7	43.5	9.6	52.0
30	6.6	39.9	12.0	55.8	17.2	64.8
90	15.1	48.0	21.0	63.7	28.2	70.4
120	19.4	55.9	30.1	74.6	39.0	77.8
150	25.1	64.3	43.2	80.7	47.4	83.1
180	27.7	66.0	53.0	81.0	55.9	84.1
210	30.0	67.1	53.2	80.9	56.0	83.9

The conversion reached 53.2 % and 80.9 % at around 210 min of TOS at 40 °C. A higher reaction temperature does, however, only speed up the deacylation step rather than significantly increasing conversion. At higher reaction temperatures, this decrease in conversion by deacylation was more apparent. Moreover, the previous works on the acetylation of 2- MON with a higher reaction time led to isomerization.(81)

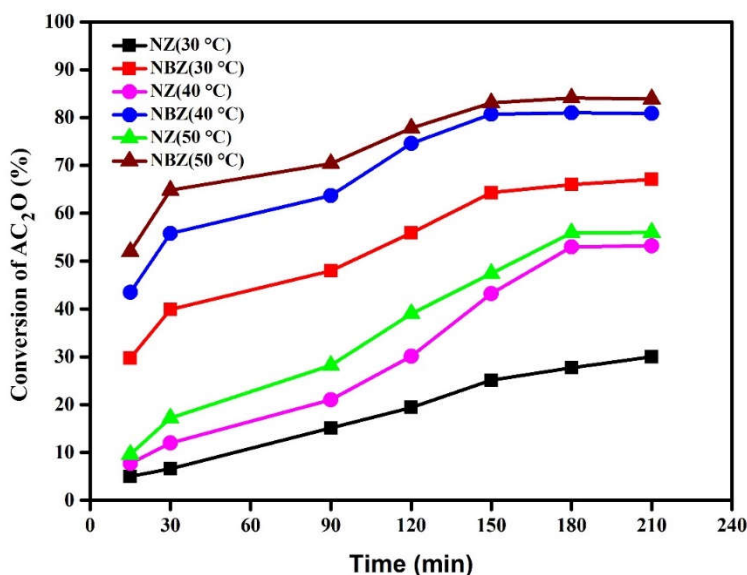


Figure 4C.2. Variation of conversion of AC₂O in the acetylation of 2-MON at different temperatures

4C.2.3. Effect of Quantity of Catalyst on Acetylation of 2-MON

The reaction was carried out by varying the amount of catalyst aiming to optimize the amount of catalyst, and the results are tabulated in Table 4C.3. Different amounts of catalyst were applied at a mole ratio of 2-MON: AC₂O equal to 1:5 at 40 °C. An increase

in the conversion of AC₂O was observed in Figure 4C.3, with the catalyst amount rising from 0.1 to 0.2 g. No significant increase in the conversion is observed with a further increase in the amount of catalyst. In general, the higher the catalyst amount applied, the higher the conversion of 2- MON. It is well known that a high catalyst amount accelerates deacylation and rearrangement reactions. Furthermore, too much catalyst accelerates the occurrence of side reactions and significantly increases the cost of the reaction. So, the dosage of NBZ and NZ was optimized at 0.2 g.

Table 4C.3. Comparative study of acetylation of 2-MON over NZ and NBZ for different amounts of catalyst samples

Time (min)	Conversion of AC ₂ O (%)					
	0.1 g		0.2 g		0.3 g	
	NZ	NBZ	NZ	NBZ	NZ	NBZ
15	3.5	31.8	7.7	43.5	9.3	52.7
30	9.7	40.0	12.0	55.8	15.0	60.8
90	15.0	49.4	21.0	63.7	26.1	66.0
120	17.8	57.0	30.1	74.6	35.1	78.8
150	20.8	64.8	43.2	80.7	46.8	84.4
180	27.5	65.9	53.0	81.0	52.7	84.3
210	29.1	65.9	53.2	80.9	55.5	84.6

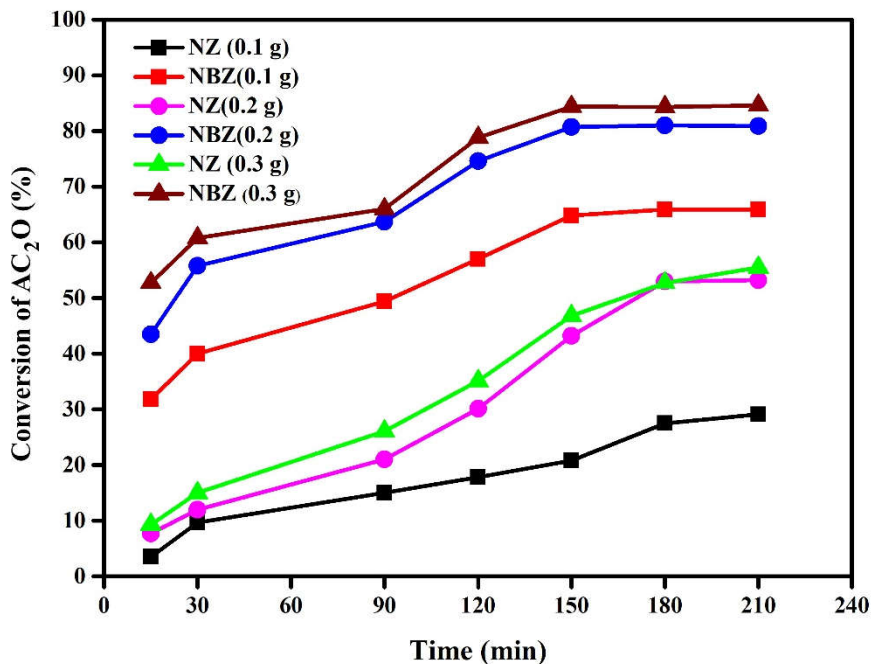


Figure 4C.3. Variation of conversion of AC₂O in the acetylation of 2-MON over different amounts of catalyst samples

4C.2.4. Effect of Hierarchical Porosity on Acetylation

A comparative analysis assessed the performance of NZ, NZ 2.0 P, NBZ, and NBZ 2.0 P. The results (Table 4C.4) showed that NZ and NBZ achieved only 66% and 80.9% conversion of AC₂O, respectively. In contrast, NZSM-5 2.0P and NBZ 2.0 P demonstrated significantly higher conversions, reaching 88.8% and 89%, respectively, as depicted in Figure 4C.4. This underscores the impact of the hierarchical pore structure of NZ 2.0 P and NBZ 2.0 P; unlike NZ and NBZ, which predominantly feature micropores with limited mesopore content, NZ 2.0 P and NBZ 2.0 P exhibit an enriched abundance of mesopores, along with increased mesopore volume and specific surface area. This enhancement facilitates greater

diffusion of reactants into the catalytic site, thereby substantially elevating their catalytic activity.

Table 4C.4. Comparative study of acetylation of 2-MON over different zeolite samples

Time (min)	Conversion of AC_2O (%)			
	NZ	NZ 2.0P	NBZ	NBZ 2.0P
15	7.7	48.4	43.5	49.0
30	12.0	56.6	55.8	59.7
90	21.0	64.1	63.7	69.0
120	30.1	73.8	74.6	79.9
150	43.2	86.6	80.7	88.3
180	53.0	88.0	81.0	88.5
210	53.2	88.8	80.9	89.0

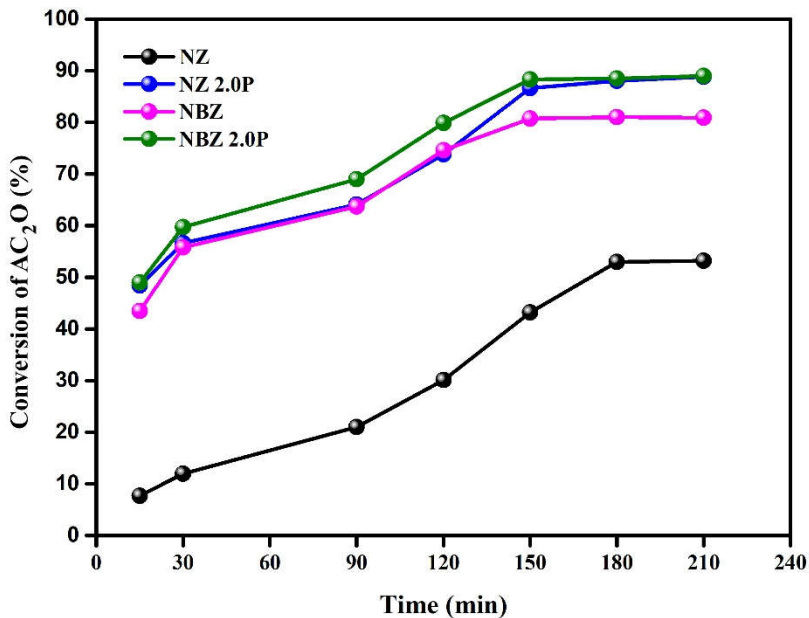


Figure 4C.4. Variation of conversion of AC_2O in the acetylation of 2-MON over different zeolite samples

Table 4C.5 demonstrates the catalytic activity of various catalysts reported in the literature.

In all experiments, the desired product remains consistently as 1AC-2MON. Various catalysts mentioned in Table 4C.5 also yield 1AC-2MON initially. However, with extended reaction times, there is a possibility of its conversion to the slimmer 6AC-2MON. Notably, only a negligible portion of 1AC-2MON is isomerized to 6AC-2MON, especially at elevated temperatures. The experiments conducted within a 25 to 50 °C temperature range and reaction times up to 210 minutes support these findings. Throughout these experiments, the production of 1AC-2MON was consistently observed alongside a higher conversion of AC₂O.

The formation of the bulky 1AC-2MON, the kinetic product, predominantly occurs on the external surface rather than within the pore channels of zeolite due to diffusion limitations posed by its microporous structure. This work focuses on hierarchical zeolite, which addresses these limitations by increasing pore width to the mesoporous range and external surface area, thereby enhancing activity. The enlarged mesopore width directly enhances the conversion of AC₂O with 100% selectivity over NBZ 2.0P. Additionally, the improved porosity resulting from the defect-free catalyst matrix is responsible for the improved catalytic activity of NZ 2.0P in selective acetylation.

Zeolite samples with consistently sized mesopores exhibited the highest activity and selectivity towards 1AC-2MON. This outcome was attributed to more uniform mesopores with a narrow pore size distribution below 5 nm in NBZ 2.0P and NZ 2.0P. These regular mesopores facilitate the interaction between reactant molecules and active sites distributed throughout the mesoporous structure.

Table 4C.5. Comparative analysis of different zeolite samples from literature for acetylation of 2-MON

Si No	Catalyst	Conditions (Temperature, Time, and solvent)	Acylating agent	Selectivity towards 1AC, 2-MON	References
1.	BEA	100 °C, 1hr and Nitrobenzene	AC ₂ O	74.1%	(81)
2	HBEA	80 °C, 4 hr and Chlorobenzene	AC ₂ O	>50%	(79)
3	HBEA	155 °C, 8hr and Nitrobenzene	AC ₂ O	50%	(82)
4	Dealuminated HBEA	120 °C, 1.17 hr Nitrobenzene	AC ₂ O	72.9%	(75)
5	HBeta	100 °C, 6hr Sulfolane	Acetyl chloride	30 %	(77)
6	HY	100 °C, 6hr Sulfolane	Acetyl chloride	60 %	(77)
7	H-Mordenite	100 °C, 6hr Sulfolane	Acetyl chloride	59%	(77)
8	Al-HMS	100°C, 8hr, Chlorobenzene	AC ₂ O	89.6 %	(83)
9	Amberlyst-15	50 °C, 5hr Dichloroethane	AC ₂ O	100%	(73)
10	Nafion /silica 80	140 °C, 4 hr Sulfolane	AC ₂ O	>70%	(71)
11	BEA	100 °C, 24 hr Dichloroethane	AC ₂ O	40-60%	(76)
12	H ₃ PW ₁₂ O ₄₀	<ul style="list-style-type: none"> ➤ 100 °C, 1 hr Chlorobenzene ➤ 100 °C, 1 hr [BPy]BF₄ ionic liquid 	AC ₂ O	<ul style="list-style-type: none"> ➤ 93.2% ➤ 96.4 % 	(80)
13	HY	80 °C, 1 hr Chlorobenzene	AC ₂ O	95%	(74)

Regarding the nanocrystalline zeolites discussed in this work, an acylium ion is initially produced and bonded to the 1-position of the 2-MON and no bonding of the acylium ion takes place to the 6-position of 2-MON. All the zeolite catalysts lead to 100% selective 1AC-2MON, the hierarchical pore characteristics can vary the conversion percentage. Under the optimal experimental conditions, when the reaction is conducted for the second and third runs, the conversion rates are nearly identical to those of the first run. So, it is summarized that the catalyst used can survive multiple usages, indicating higher TON and TOF.

4C.3 Conclusions

The impact of hetero porosity on the catalytic properties of nanocrystalline hierarchical ZSM-5 and zeolite beta was evaluated through the acetylation of 2-MON. Materials with uniform mesopores exhibited superior activity and selectivity toward 1AC-2MON. Hierarchical ZSM-5 and zeolite beta showed high conversions of AC₂O and 100% selectivity toward the kinetic product 1AC-2MON isomer. This outcome was attributed to a more regular mesopore surface, facilitating interactions between reactant molecules and active sites distributed throughout the mesopores rather than the external surface. These effects stem from the improved homogeneity of mesopore features (size, geometry, and surface) and the environment surrounding active sites, thereby enhancing catalytic behavior.

References

1. Bai R, Song Y, Li Y, Yu J. Creating Hierarchical Pores in Zeolite Catalysts. *Trends Chem.* 2019;1(6):601–11. Available from: <https://doi.org/10.1016/j.trechm.2019.05.010>.
2. Jia X, Khan W, Wu Z, Choi J, Yip ACK. Modern synthesis strategies for hierarchical zeolites: Bottom-up versus top-down strategies. *Adv Powder Technol* [Internet]. 2019;30(3):467–84. Available from: <https://doi.org/10.1016/j.appt.2018.12.014>.
3. Ozhukka Parambil F, Kumari P, Padmanabhan A. Curing of Silanol Defects and Tailoring Hierarchical Porosity in ZSM-5 Using PMMA. *Iran J Sci* [Internet]. 2023;47(5–6):1541–51. Available from: <https://doi.org/10.1007/s40995-023-01548-x>
4. Freude D, Hunger M, Pfeifer H, Schwieger W. ¹H MAS NMR studies on the acidity of zeolites. *Chem Phys Lett.* 1986;128(1):62–6. Available from: [https://doi.org/10.1016/0009-2614\(86\)80146-4](https://doi.org/10.1016/0009-2614(86)80146-4).
5. Qin Z, Hafiz L, Shen Y, Daele S Van, Boullay P, Ruaux V, et al. Defect-engineered zeolite porosity and accessibility. *J Mater Chem A.* 2020;8(7):3621–31. Available from: <https://doi.org/10.1039/C9TA11465C>.
6. Izabel C. Medeiros-Costa, Eddy Dib, Nikolai Nesterenko, Jean-Pierre Dath, Jean-Pierre Gilson SM. Silanol defects engineering and healing in zeolites: Opportunities to fine-tune their properties and performances. *AIChE Annu Meet Conf Proc.* 2019. Available from: <https://doi.org/10.1039/D1CS00395J>.
7. Fouad OA, Mohamed RM, Hassan MS, Ibrahim IA. Effect of template type and template / silica mole ratio on the crystallinity of synthesized nanosized ZSM-5. *Catal Today.* 2006;116:82–7. Available from: <https://doi.org/10.1016/j.cattod.2006.03.004>.
8. Dib E, Grand J, Gedeon A, Mintova S, Fernandez C. Control the position of framework defects in zeolites by changing the symmetry of organic structure directing agents. *Microporous Mesoporous Mater.* 2021;315. Available from: <https://dx.doi.org/10.1016/j.micromeso.2021.110899>.
9. Sakthivel A, Huang SJ, Chen WH, Lan ZH, Chen KH, Lin HP, et al.

- Direct synthesis of highly stable mesoporous molecular sieves containing zeolite building units. *Adv Funct Mater.* 2005;15(2):253–8. Available from: <https://doi.org/10.1002/adfm.200400038>.
10. Sun Y, Ma T, Cao S, Wang J, Meng X, Gong Y, et al. Defective sites in ZSM-5 zeolite synthesized by n-butylamine template facilitating uniform meso-microporosity by alkali-treatment. *Microporous Mesoporous Mater.* 2021;326. Available from: <http://dx.doi.org/10.1016/j.micromeso.2021.111360>.
 11. Choi M, Na K, Kim J, Sakamoto Y, Terasaki O, Ryoo R. Stable single-unit-cell nanosheets of zeolite MFI as active and long-lived catalysts. *Nature* [Internet]. 2009;461(7261):246–9. Available from: <http://dx.doi.org/10.1038/nature08288>.
 12. Na K, Chol M, Park W, Sakamoto Y, Terasaki O, Ryoo R. Pillared MFI zeolite nanosheets of a single-unit-cell thickness. *J Am Chem Soc* [Internet]. 2010 Mar 31 [cited 2022 Oct 17];132(12):4169–77. Available from: <https://pubs.acs.org/doi/abs/10.1021/ja908382n>.
 13. Kim W, Kim JC, Kim J, Seo Y, Ryoo R. External surface catalytic sites of surfactant-tailored nanomorphous zeolites for benzene isopropylation to cumene. *ACS Catal* [Internet]. 2013 Feb 1 [cited 2022 Oct 17];3(2):192–5. Available from: <https://pubs.acs.org/doi/abs/10.1021/cs300678n>.
 14. Seo Y, Lee S, Jo C, Ryoo R. Microporous aluminophosphate nanosheets and their nanomorphous zeolite analogues tailored by hierarchical structure-directing amines. *J Am Chem Soc* [Internet]. 2013 Jun 19 [cited 2022 Oct 17];135(24):8806–9. Available from: <https://pubs.acs.org/doi/abs/10.1021/ja403580j>.
 15. Singh BK, Xu D, Han L, Ding J, Wang Y, Che S. Synthesis of single-crystalline mesoporous ZSM-5 with three-dimensional pores via the self-assembly of a designed triply branched cationic surfactant. *Chem Mater* [Internet]. 2014 Dec 23 [cited 2022 Oct 17];26(24):7183–8. Available from: <https://pubs.acs.org/doi/abs/10.1021/cm503919h>.
 16. Xu L, Wu S, Guan J, Wang H, Ma Y, Song K, et al. Synthesis, characterization of hierarchical ZSM-5 zeolite catalyst and its catalytic performance for phenol tert-butylation reaction. *Catal*

-
- Commun. 2008;9:1272–6. Available from: <http://dx.doi.org/10.1016%2Fj.catcom.2007.11.018>.
17. Peng M, Wang ZQ, Huang J, Shen M, Jiang J, Xu H, et al. Two Coexisting Forms of Simple Molecules for Directing Sesqui-Unit-Cell Zeolite Nanosheets. *Chem Mater* [Internet]. 2021 Sep 14 [cited 2022 Oct 17];33(17):6934–41. Available from: <https://pubs.acs.org/doi/abs/10.1021/acs.chemmater.1c01876>.
 18. Roth WJ, Nachtigall P, Morris RE, Jir C. Two-Dimensional Zeolites: Current Status and Perspectives. *Chem Rev*. 2014;114:4807–37. Available from: <https://doi.org/10.1021/cr400600f>.
 19. Tian Q, Liu Z, Zhu Y, Dong X, Saih Y, Basset JM, et al. Beyond Creation of Mesoporosity: The Advantages of Polymer-Based Dual-Function Templates for Fabricating Hierarchical Zeolites. *Adv Funct Mater*. 2016;26(12):1881–91. Available from: <http://dx.doi.org/10.1002/adfm.201504888>.
 20. Peng P, Gao XH, Yan ZF, Mintova S. Diffusion and catalyst efficiency in hierarchical zeolite catalysts. *Natl Sci Rev*. 2020;7(11):1726–42. Available from: <https://doi.org/10.1093/nsr/nwaal84>.
 21. Holland BT, Abrams L, Stein A. Dual Templating of Macroporous Silicates with Zeolitic Microporous Frameworks. *J Am Chem Soc*. 1999;121(13):4308–9. Available from: <https://doi.org/10.1021/ja990425p>.
 22. Hsu HL, Roselin LS, Selvin R, Bououdina M. Enhanced activity of hierarchical zeolitic material with ZSM-5 structure for the tert-butylation of phenol. *J Exp Nanosci*. 2011;6(6):612–21. Available from: <http://dx.doi.org/10.1080/17458080.2010.513717>.
 23. Padmanabhan A, Selvin R, Hsu HL, Xiao LW. Efficient Acylation of Anisole over Hierarchical Porous ZSM-5 Structure. *Chem Eng Technol*. 2010;33(6):998–1002. Available from: <http://dx.doi.org/10.1002/ceat.200900542>.
 24. Roselin LS, Selvin R. Selective Monoacylation of Mesitylene Using Hierarchical Nanocrystalline ZSM-5 Catalyst. *J Nanosci Nanotechnol*. 2019;20(2):1315–9. Available from: doi: 10.1166/jnn.2020.16979.
-

-
25. Naik SP, Chiang AST, Sasakura H, Yamaguchi Y, Okubo T. Fabrication of hierarchical zeolitic material from zeolite nanoprecursors and macromolecular template. *Chem Lett.* 2005;34(7):982–3. Available from: <http://dx.doi.org/10.1246/cl.2005.982>.
 26. Zhao J, Zhou J, Chen Y, He Q, Ruan M, Guo L, et al. Fabrication of mesoporous zeolite microspheres by a one-pot dual-functional templating approach. *J Mater Chem.* 2009;19(41):7614–6. Available from: <https://doi.org/10.1039/B916862A>.
 27. Ahmad S, Ahmad S, Agnihotry SA. Synthesis and characterization of in situ prepared poly (methyl methacrylate) nanocomposites. *Bull Mater Sci.* 2007;30(1):31–5. Available from: <https://doi.org/10.1007/s12034-007-0006-9>.
 28. Hsu C ye, Chiang AST, Selvin R, Thompson RW. Rapid Synthesis of MFI Zeolite Nanocrystals. *J Phys Chem.* 2005;18804–14. Available from: <http://dx.doi.org/10.1021/jp0526391>.
 29. Radhika NP, Selvin R, Kakkar R, Hsu H ling. Nanocrystals of Zeolite ZSM-5 as Catalysts for the Liquid Phase Benzylolation of Anisole with Benzyl Alcohol. *J Nanosci Nanotechnol.* 2017;17(2):1329–37. Available from: <https://doi.org/10.1166/jnn.2017.12726>.
 30. Tahrin RAA, Azma NS, Kassim S, Harun NA. Preparation and properties of PMMA nanoparticles as 3 dimensional photonic crystals and its thin film via Surfactant-free emulsion polymerization. In: *AIP Conference Proceedings.* 2017
 31. Hunger M, Kärger J, Pfeifer H, Caro J, Zibrowius B, Bülow M, et al. Investigation of internal silanol groups as structural defects in ZSM-5-type zeolites. *J Chem Soc Faraday Trans 1 Phys Chem Condens Phases.* 1987;83(11):3459–68. Available from: <https://doi.org/10.1039/F19878303459>.
 32. Palčić A, Moldovan S, El Siblani H, Vicente A, Valtchev V. Defect Sites in Zeolites: Origin and Healing. *Adv Sci.* 2022;9(4):1–11. Available from: <https://doi.org/10.1002/advs.202104414>.
 33. Sano T, Ikeya H, Kasuno T, Wang ZB, Kawakami Y, Soga K. Influence of crystallinity of HZSM-5 zeolite on its dealumination rate. *Zeolites.* 1997;19(1):80–6. Available from: <https://doi.org/>
-

- 10.1016/S0144-2449(97)00052-3.
34. Dib E, Grand J, Mintova S, Fernandez C. Structure-Directing Agent Governs the Location of Silanol Defects in Zeolites. *Chem Mater.* 2015;27(22):7577–9. Available from: <https://doi.org/10.1021/acs.chemmater.5b03668>.
 35. Milne K. Influence of the synthesis of Fe-MFI for partial methane oxidation. Cardiff University; 2020. Available from: <https://orca.cardiff.ac.uk/id/eprint/138287>.
 36. Dutta PK, Puri M. Synthesis and Structure of Zeolite ZSM-5: A Raman Spectroscopic Study. *J Phys Chem.* 1987;(18):4329–33. Available from: <https://doi.org/10.1021/j100300a025>.
 37. Kadja GTM, Fabiani VA, Aziz MH, Fajar ATN, Prasetyo A, Suendo V, et al. The effect of structural properties of natural silica precursors in the mesopore-free synthesis of hierarchical ZSM-5 below 100 °C. *Adv Powder Technol [Internet].* 2017;28(2):443–52. Available from: <http://dx.doi.org/10.1016/j.appt.2016.10.017>.
 38. S. Mintova, B. Mihailova VV and LK. The Degree of Crystallinity of ZSM-5 determined by Raman Spectroscopy. *J. Chem. Soc., Chem. Commun.* 1994;46:1791–2. Available from: <https://doi.org/10.1039/C39940001791>.
 39. Hongshen Liu, Huseyin Kaya, Yen-Ting Lin, Andrew Ogrinc SHK. Vibrational Spectroscopy Analysis of Silica and Silicate Glass Networks. *J Am Ceram Soc.* 2022;(105):2355–2384. Available from: <https://doi.org/10.1111/jace.18206>.
 40. Attila Ö, King HE, Meirer F, Weckhuysen BM. 3D Raman Spectroscopy of Large Zeolite ZSM-5 Crystals. *Chem - A Eur J.* 2019;25(29):7158–67. Available from: <https://doi.org/10.1002/chem.201805664>.
 41. Dubray F, Dib E, Medeiros-Costa I, Aquino C, Minoux D, van Daele S, et al. The challenge of silanol species characterization in zeolites†. *Inorg Chem Front.* 2022;9(6):1125–33. Available from: <https://doi.org/10.1039/D1QI01483H>.
 42. Martinelli A, Creci S, Vavra S, Carlsson PA, Skoglundh M. Local anisotropy in single crystals of zeotypes with the MFI framework structure evidenced by polarised Raman spectroscopy. *Phys Chem*

-
- Chem Phys. 2020;22(3):1640–54. Available from: <https://doi.org/10.1039/C9CP06199A>.
43. Shih PTK, Koenig JL, Lagally P. Raman and Infrared Spectroscopic Studies of the Reactions of Silica and Glass Surfaces. *Mater Sci Eng.* 1975;20:127–35. Available from: [https://doi.org/10.1016/0025-5416\(75\)90141-X](https://doi.org/10.1016/0025-5416(75)90141-X)
 44. Morrow BA, McFarlan AJ. Surface vibrational modes of silanol groups on silica. *J Phys Chem.* 1992;96(3):1395–400. Available from: <https://doi.org/10.1021/j100182a068>.
 45. Silva DSA, Castelblanco WN, Piva DH, de Macedo V, Carvalho KTG, Urquieta-González EA. Tuning the Brønsted and Lewis acid nature in HZSM-5 zeolites by the generation of intracrystalline mesoporosity—Catalytic behavior for the acylation of anisole. *Mol Catal [Internet].* 2020;492:111026. Available from: <https://doi.org/10.1016/j.mcat.2020.111026>.
 46. Kyriakou G, Theocharis CR. The anomalous sorptive behaviour of ZSM-5 and silicalite-I: Observation of low-pressure hysteresis in nitrogen adsorption. *Stud Surf Sci Catal.* 2002;144:709–16. Available from: [http://dx.doi.org/10.1016/S0167-2991\(02\)80200-2](http://dx.doi.org/10.1016/S0167-2991(02)80200-2).
 47. Cychosz KA, Guillet-Nicolas R, García-Martínez J, Thommes M. Recent advances in the textural characterization of hierarchically structured nanoporous materials. *Chem Soc Rev.* 2017;46(2):389–414. Available from: <https://doi.org/10.1039/C6CS00391E>.
 48. Nakai K, Sonoda J, Yoshida M, Hakuman M, Naono H. High resolution adsorption isotherms of N₂ and Ar for nonporous silicas and MFI zeolites. *Adsorption.* 2007;13(3–4):351–6. Available from: <http://dx.doi.org/10.1007/s10450-007-9071-z>.
 49. Jaroniec CP, Kruk M, Jaroniec M, Sayari A. Tailoring surface and structural properties of MCM-41 silicas by bonding organosilanes. *J Phys Chem B.* 1998;102(28):5503–10. Available from: <https://doi.org/10.1021/jp981304z>.
 50. De Ó, Luis J sanchez, Coronas J. Hierarchical silicalite-1 structures based on pyrolyzed materials. *Mater Lett [Internet].* 2011;65(19–20):3124–7. Available from: <http://dx.doi.org/10.1016/j.matlet.2011.06.080>.
-

-
51. Zheng J, Zeng Q, Yi Y, Wang Y, Ma J, Qin B, et al. The hierarchical effects of zeolite composites in catalysis. *Catal Today* [Internet]. 2011;168(1):124–32. Available from: <http://dx.doi.org/10.1016/j.cattod.2011.01.006>.
 52. Ferriol M, Gentilhomme A, Cochez M, Oget N, Mieloszynski JL. Thermal degradation of poly(methyl methacrylate) (PMMA): Modelling of DTG and TG curves. *Polym Degrad Stab*. 2003;79(2):271–81. Available from [https://doi.org/10.1016/S0141-3910\(02\)00291-4](https://doi.org/10.1016/S0141-3910(02)00291-4).
 53. Soltanali S, Halladj R, Rashidi A, Hajjar Z, Shafeghat A. The effect of copper loading method on the performance of Cu / HZSM-5 nanocatalysts in methanol to gasoline conversion. *Energy Sources, Part A Recover Util Environ Eff* [Internet]. 2017;44(4):1–7. Available from: <http://dx.doi.org/10.1080/15567036.2016.1236301>.
 54. Ayodele OB. Influence of oxalate ligand functionalization on Co/ZSM-5 activity in Fischer Tropsch synthesis and hydrodeoxygenation of oleic acid into hydrocarbon fuels. *Sci Rep* [Internet]. 2017;7(1):1–14. Available from: <http://dx.doi.org/10.1038/s41598-017-09706-z>
 55. Ek S, Root A, Peussa M, Niinistö L. Determination of the hydroxyl group content in silica by thermogravimetry and a comparison with ¹H MAS NMR results. *Thermochim Acta*. 2001;379(1–2):201–12. Available from: [http://dx.doi.org/10.1016/S0040-6031\(01\)00618-9](http://dx.doi.org/10.1016/S0040-6031(01)00618-9).
 56. Selvin R, Roselin LS, Khayyat SA, Umar A. Hierarchical zeolite Beta: An efficient and eco-friendly nanocatalyst for the Friedel-Crafts acylation of toluene. *J Nanosci Nanotechnol*. 2013;13(6):4415–20. Available from: <http://dx.doi.org/10.1166/jnn.2013.7153>.
 57. Zhang C, Li S, Bao S. Sustainable Synthesis of ZSM-5 Zeolite from Rice Husk Ash Without Addition of Solvents. *Waste and Biomass Valorization* [Internet]. 2019;10(10):2825–35. Available from: <http://dx.doi.org/10.1007/s12649-018-0356-0>.
 58. Narayanan S, Judith Vijaya J, Sivasanker S, John Kennedy L, Ariharan A. Enhanced selectivity to benzaldehyde in the liquid phase oxidation of benzyl alcohol using nanocrystalline ZSM-5 zeolite catalyst. *J Porous Mater*. 2014;21(5):633–41. Available from
-

<http://dx.doi.org/10.1007/s10934-014-9809-4>.

59. Serrano DP, Aguado J, Escola M, Rodriguez M, Peral A. Hierarchical Zeolites with Enhanced Textural and Catalytic Properties Synthesized from Organofunctionalized Seeds. *Chem Mater*. 2006;18(10):2462–4. Available from: <http://dx.doi.org/10.1021/cm060080r>.
60. Zhu H, Liu Z, Kong D, Wang Y, Yuan X, Xie Z. Synthesis of ZSM-5 with intracrystal or intercrystal mesopores by polyvinyl butyral templating method. *J Colloid Interface Sci* [Internet]. 2009;331(2):432–8. Available from: <http://dx.doi.org/10.1016/j.jcis.2008.11.071>.
61. Parkhomchuk E V, Semeykina VS, Sashkina KA, Okunev AG, Lysikov AI, Parmon VN. Synthesis of Polystyrene Beads for Hard-Templating of Three-Dimensionally Ordered Macroporosity and Hierarchical Texture of Adsorbents and Catalysts. *Top Catal*. 2016;60(1–2):178–89. Available from <http://dx.doi.org/10.1007/s11244-016-0719-3>.
62. Radhika NP, Selvin R, Kakkar R, Roselin LS, Hsu HL. Tertiary Butylation of Aniline Over Nanosized Zeolite Beta Catalyst. *J Nanosci Nanotechnol*. 2018;18(11):7960–8. Available from: <https://doi.org/10.1166/jnn.2018.15538>
63. Karin M, Yilmaz B, Ulrich M, Bein T. Hierarchical Zeolite Beta via Nanoparticle Assembly with a Cationic Polymer. *Chem Mater*. 2011;23(19):4301–10. Available from: <https://doi.org/10.1021/cm103533e>.
64. Thakur R, Barman S, Kumar Gupta R. Synthesis of cumene by transalkylation over modified beta zeolite: A kinetic study. *Brazilian J Chem Eng*. 2016;33(4):957–67. Available from: <https://doi.org/10.1590/0104-6632.20160334s20150333>.
65. Wei Q, Zhang J, Liu X, Zhang P, Wang S, Wang Y, et al. Citric Acid-Treated Zeolite Y (CY)/Zeolite Beta Composites as Supports for Vacuum Gas Oil Hydrocracking Catalysts: High Yield Production of Highly-Aromatic Heavy Naphtha and Low-BMCI Value Tail Oil. *Front Chem*. 2019;7:705. Available from: <https://doi.org/10.3389/fchem.2019.00705>.
66. Rac V, Rakić V, Stošić D, Otman O, Auroux A. Hierarchical ZSM-

-
- 5, Beta and USY zeolites: Acidity assessment by gas and aqueous phase calorimetry and catalytic activity in fructose dehydration reaction. *Microporous Mesoporous Mater.* 2014;194:126–34. Available from: <https://doi.org/10.1016/j.micromeso.2014.04.003>.
67. Khan W, Jia X, Wu Z, Choi J, Yip ACK. Incorporating hierarchy into conventional zeolites for catalytic biomass conversions: A review. *Catalysts.* 2019;9(2):127. Available from: <https://doi.org/10.3390/catal9020127>
68. Sahu P, Sakthivel A. Zeolite- β based molecular sieves: A potential catalyst for esterification of biomass derived model compound levulinic acid. *Mater Sci Energy Technol [Internet].* 2021;4:307–16. Available from: <https://doi.org/10.1016/j.mset.2021.08.007>.
69. Kakiuchi F, Usui M, Ueno S, Chatani N, Murai S. Ruthenium-Catalyzed Functionalization of Aryl Carbon-Oxygen Bonds in Aromatic Ethers with Organoboron Compounds. *J Am Chem Soc.* 2004;126(9):2706–7. Available from: <https://doi.org/10.1021/ja0393170>.
70. Pârvulescu AN, Gagea BC, Pârvulescu VI, De Vos D, Jacobs PA. Acylation of 2-methoxynaphthalene with acetic anhydride over silica-embedded triflate catalysts. *Appl Catal A Gen.* 2006;306(2):159–64. Available from: [https://doi.org/10.1016/S1381-1169\(00\)00225-9](https://doi.org/10.1016/S1381-1169(00)00225-9)
71. Schuster H, Hölderich WF. The acylation of 2-methoxynaphthalene with acetic anhydride over Nafion/silica composites and BEA zeolites containing Lewis acid sites. *Appl Catal A Gen.* 2008;350(1):1–5. Available from: <https://doi.org/10.1016/j.apcata.2008.07.026>.
72. Yadav GD, Krishnan MS. Solid acid catalysed acylation of 2-methoxy-naphthalene: role of intraparticle diffusional resistance. *Chem Eng Sci.* 1999;54(19):4189–97. Available from: [https://dx.doi.org/10.1016/S0009-2509\(99\)00092-5](https://dx.doi.org/10.1016/S0009-2509(99)00092-5).
73. Méric P, Finiels A, Moreau P. Kinetics of 2-methoxynaphthalene acetylation with acetic anhydride over dealuminated HY zeolites. *J Mol Catal A Chem.* 2002;189(2):251–62. Available from: [https://dx.doi.org/10.1016/S1381-1169\(02\)00348-5](https://dx.doi.org/10.1016/S1381-1169(02)00348-5).
74. Muller M, Harvey G, Prins R. Comparison of the dealumination of
-

- zeolites beta, mordenite, ZSM-5 and ferrierite by thermal treatment, leaching with oxalic acid and treatment with SiCl₄ by ¹H, ²⁹Si and ²⁷Al MAS NMR. *Microporous Mesoporous Mater.* 2000;34(2):135–47. Available from: [https://doi.org/10.1016/S1387-1811\(99\)00167-5](https://doi.org/10.1016/S1387-1811(99)00167-5).
75. Berreghis A, Ayrault P, Fromentin E, Guisnet M. Acetylation of 2-methoxynaphthalene with acetic anhydride over a series of dealuminated HBEA zeolites. *Catal Letters.* 2000; 68, 121–127. Available from: <https://doi.org/10.1023/A:1019083420175>
76. Andy P, Garcia-Martinez J, Lee G, Gonzalez H, Jones CW, Davis ME. Acylation of 2-methoxynaphthalene and isobutylbenzene over zeolite beta. *J Catal.* 2000;192(1):215–23. Available from: <https://doi.org/10.1006/jcat.2000.2855>.
77. Das D, Cheng S. Friedel-Crafts acylation of 2-methoxynaphthalene over zeolite catalysts. *Appl Catal A Gen.* 2000;201(2):159–68. Available from: [http://dx.doi.org/10.1016/S0926-860X\(00\)00438-5](http://dx.doi.org/10.1016/S0926-860X(00)00438-5).
78. Cahyono EDY, Priatmoko S, Haryani SRI. Acetylation of 2-Methoxynaphthalene with Acetic anhydride over Zr 4+ -Zeolite beta. *Orient J Chem.* 2015;31(1):79–83. Available from: <http://dx.doi.org/10.13005/ojc/31.Special-Issue1.09>.
79. Moreau P, Finiels A, Meric P, Fajula F. Acetylation of 2-methoxynaphthalene in the presence of beta zeolites: Influence of reaction conditions and textural properties of the catalysts. *Catal Letters.* 2003;85(3–4):199–203. Available from: <https://doi.org/10.1023/A:1022145814145>
80. Guo Y, Sun J, Guo F, He Y, Chen P. Friedel-Crafts acylation of 2-methoxynaphthalene with acetic anhydride catalyzed by phosphotungstic acid in ionic liquid. *Bulg Chem Commun.* 2019;51(2):289–94. Available from: <http://dx.doi.org/10.34049/bcc.51.2.4449>.
81. Guidotti M, Canaff C, Coustard JM, Magnoux P, Guisnet M. Acetylation of aromatic compounds over H-BEA zeolite: The influence of the substituents on the reactivity and on the catalyst stability. *J of Catalysis.* 2005;230(2):375–83. Available from: <http://dx.doi.org/10.1016/j.jcat.2004.12.021>.

82. Fromentin E, Coustard JM, Guisnet M. Mechanism of 1-Acetyl-2-methoxynaphthalene Isomerisation over a HBEA Zeolite. *J Catal.* 2000;190(2):433–8. Available from: <https://doi.org/10.1006/jcat.1999.2762>.
83. Chen P, Wang W, Zhai Y. Friedel – Crafts acylation of 2-methoxynaphthalene with acetic anhydride over Al-HMS. *J Porous Mater.* 2014;21:441-8. Available from: <https://doi.org/10.1007/s10934-014-9790-y>.

Chapter 5

Exploring the Dielectric and Electrical Properties of Cerium-Doped Zeolite Beta: Temperature-Dependent Analysis

Abstract

This chapter delves into the dielectric characteristics of cerium-doped zeolite beta employing broadband spectroscopic methods. The introduction of cerium induces significant variations in zeolitic matrix leading to remarkably high dielectric constants compared to unmodified zeolite beta. Insights gained from impedance and modulus analyses contribute to the progression of zeolite-based charge storage and optoelectronic device technologies.

5.1 Introduction

The idea of zeolite as a dielectric material has been conceived by the fact that it has exchangeable extra framework cations. Recent years have witnessed various techniques that involve low-frequency and high-frequency impedance spectroscopies by varying the temperature to examine the electrical properties of zeolites. Comprehensive investigations, which integrate experimental and theoretical approaches, have been conducted to elucidate the impact of cation types instead of proton motion within zeolites.(1) Furthermore, dielectric spectroscopy yields significant understanding regarding localized charges and dipolar species.(2) The mobility of encapsulated extra framework metal ions enhances the dielectric response. However, in certain cases, the presence of water molecules within the cavities impedes the movement of ions, resulting in a diminished dielectric response.(3) Dielectric response varies significantly with the nature of cations, size, and crystal structure.(4) Researchers have utilized impedance data to study the arrangements of cations across different sites within zeolite.(5) They have discovered numerous beneficial applications for zeolites, yet their understanding of the dielectric properties of zeolite beta and its metal analogs at various temperatures remains incomplete. There hasn't been any systematic investigation into the electric modulus analysis of cerium-doped nanocrystalline zeolite beta. In this context, this chapter investigates the dielectric properties of

nanocrystalline zeolite beta and cerium-modified nanocrystalline zeolite beta.

5.2 Experimental

Nanocrystalline zeolite beta (NBZ) and cerium-modified nanocrystalline zeolite beta (NBZ/Ce) are prepared, as explained in Chapter 2. The samples were characterized using different methods. The results obtained from various characterization techniques are discussed in section B of Chapter 3. The powdered samples were pelletized for dielectric analysis using a pelletizer, and pellets were analyzed using Broadband Dielectric Spectroscopy. These pellets were sandwiched between two conducting plates, and then a reference voltage of 0.5 V_{rms} was applied across the pellet. The range of frequencies applied is from 1 Hz to 10⁸ Hz. The resulting data were analyzed to study the behavior of the samples for different frequencies from 25 °C to 250 °C.

5.3 Results and Discussion

5.3.1 Analysis of dielectric parameters

Dielectric constant ϵ_r^* is a complex quantity comprising of the real form ϵ_r' and an imaginary form ϵ_r'' and can be mathematically represented as equation 5.1:

$$\epsilon_r^* = \epsilon_r' - j \times \epsilon_r'' \quad (5.1)$$

The real part is real permittivity or real dielectric constant and the imaginary part corresponds to the energy loss. Figure 5.1 depicts the change in dielectric constants as a function of frequency at various temperatures for NBZ and NBZ/Ce. The frequency dependence of the dielectric constant can be separated into two regions: low-frequency (1 Hz to 10^3 Hz) and high-frequency (10^3 Hz to 10^7 Hz). A high-frequency area exceeding 10^3 Hz exhibits a very low dielectric constant subsequently resulting in a plateau zone.

To explain the variation of dielectric properties, it is a must to have an understanding of the different factors contributing to it. Space charge and dipolar polarizations are the major contributing factors at low frequencies and ionic and electronic polarizations play a predominant role at high frequencies.(6)

The application of an electric field to the material containing ions exerts a force that force can cause the ions to move, leading to a stretching of the bond. As a result of this stretching, a dipole moment is created. The electrostatic attraction is overcome by the cations, allowing localized movement inside the zeolite structure. This aspect most likely contributes to the accumulation of interfacial polarization due to the charges that build up inside the zeolite structure.(7) Additionally, as zeolite consists of polycrystalline material, each crystal exhibits its unique preferential atomic structure. In this context, a grain boundary delineates a finite two-dimensional plane that separates two or more crystals with differing lattice orientations. When subjected to an AC field, a charge buildup

occurs at the grain boundary, leading to an increase in dielectric constant at lower frequencies. Thus interfacial polarization becomes responsible for increase in dielectric constant at frequencies below 10 Hz.

The sudden drop of dielectric constant observed above 10^3 Hz results from the fact that the field reversals are quick at higher frequencies, and ion displacements cannot keep up with the field changes resulting in a decreased ionic polarization.(8) The ionic displacements are further decreased because at higher frequencies the ions tend to displace into the narrow interfacial grain boundary region. As a result, both NBZ and NBZ/Ce exhibit a sudden lowering of the dielectric constant with increasing frequency.(9)

The polarization found in NBZ/Ce is due to the presence of Ce^{3+} , Ce^{4+} and H^+ ions where as in case of NBZ, the polarization is due to H^+ ions.(6) The dielectric constants of NBZ/Ce are greater than those of NBZ. This finding can be explained by the fact that cerium ions have significant charge density when compared to H^+ ions.

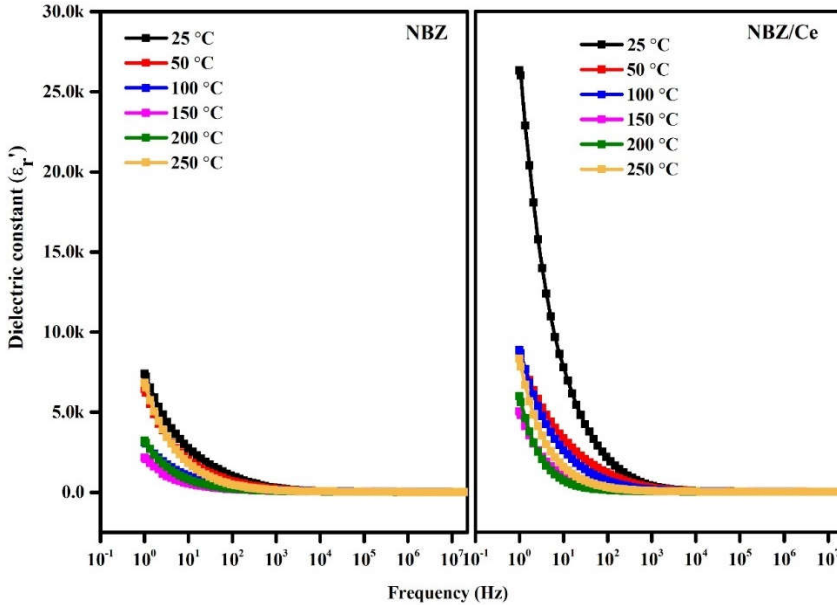


Figure 5.1. Variation of the dielectric constant of NBZ and NBZ/Ce with frequency at different temperatures

The variation of dielectric constants of zeolite samples at different temperatures is also depicted in Figure 5.1. At room temperature, the dielectric constant of NBZ/Ce is initially high but diminishes rapidly as the temperature increases. This occurs because elevated temperatures induce more pronounced molecular vibrations and can lead to heightened random thermal motion. As a result, the alignment of the molecules is disturbed and they randomly align themselves less closely with each other and with the applied electric field. These changes lead to a decrease in the net orientation polarizability and, consequently, a reduction in the dielectric constant is observed.⁽¹⁰⁾ So it can be surmised that both the samples exhibit a negative temperature coefficient.

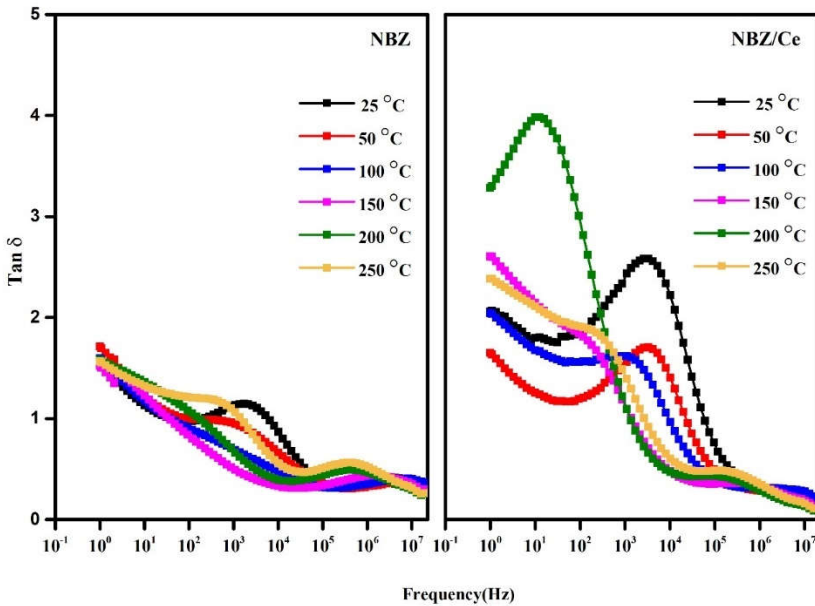


Figure 5.2. Variation of dielectric Loss factor ($\tan \delta$) of NBZ and NBZ/Ce with frequency at different temperatures

The ratio of the imaginary part and the real part of the dielectric constant is the dissipation factor (Equation 1.4). Figure 5.2 shows the variation of dielectric loss tangent ($\tan \delta$) or dissipation factor of zeolite beta and cerium-doped zeolite beta. $\tan \delta$ of a material quantifies the electrical energy dissipated as heat through various physical processes including dielectric relaxation, electrical conduction, and dielectric resonance. At high frequencies the zeolite material approaches saturation point. The electric field oscillates too quickly for significant alignment or movement of charges which minimizes energy dissipation and hence reduces dielectric losses. Both samples exhibit the same trend of decreasing dissipation factor with increasing frequency. The peak maxima (dielectric relaxation

peaks) are detected in the curves of both samples which corresponds to the point when the electric field and molecular rotation frequencies are perfectly matched. This resonance results in the most significant power transfer to the dipoles of the system and, thus the results in maximum generation of heat. The heat dissipation is higher for NBZ/Ce as observed from Figure 5.2. Altogether, it can be surmised that the dielectric loss of NBZ and NBZ/Ce amounts to a very meager value of 1.14 and 2.64 respectively at 25 °C.

5.3.2 Analysis of AC Conductivity

Figure 5.3 shows the variation of AC conductivity with frequency for zeolite samples. The two samples follow the same pattern. In the low-frequency range, the samples exhibit no appreciable conductivity. This is followed by a sudden increase at around 10^5 Hz in both samples. The universal power law governs the high-frequency region, where the value of AC conductivity increases linearly with frequency. Ion (charge carrier) hopping is the cause of the increase in conductivity.(8) This type of hopping is more typical in zeolite materials. The NBZ shows slightly higher conductivity than NBZ/Ce and this increase is attributed to the hopping of protons between the four oxygen atoms surrounding the Al-center, in contrast to the much bigger metal cations like cerium as they are expected to be localized on their respective sites.(11)

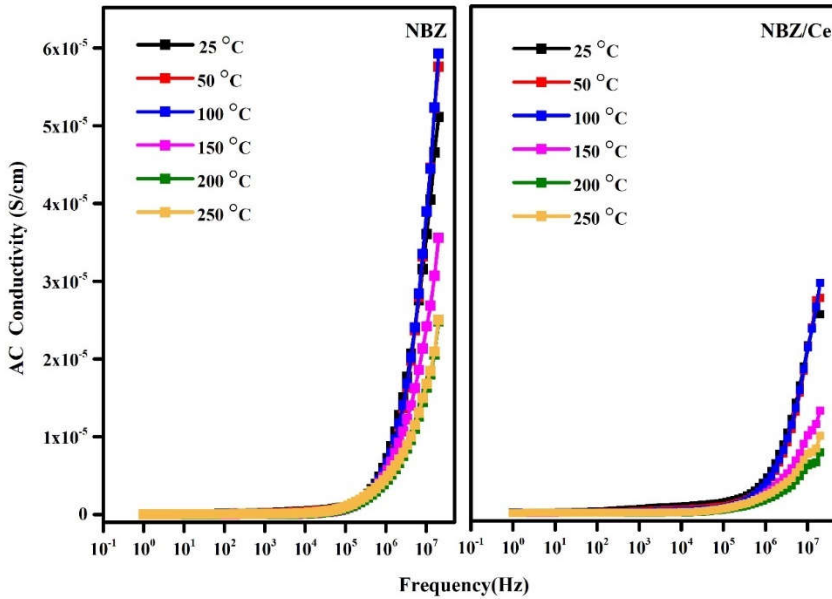


Figure 5.3. Variation of AC conductivity of NBZ and NBZ/Ce with frequency at different temperatures

During the modification process, there occurs a slight amount of dealumination, and the four oxygen atoms bound to it are converted to four hydroxyl groups, implying the development of silanol nests. The dealumination of the surface is proven by EDX studies in Chapter 3. It was concluded that the surface silanol groups present in the microchannels of the NBZ/Ce substantially contribute to the conductivity of zeolite samples.(12) Altogether, when compared to the reported works on zeolite beta, the two samples show very low ionic conductivity in the order of 10^{-5} S/cm and it can be attributed to the tightly bound ions because of the electrostatic force.(13) As the temperature rises, both samples exhibit a decrease of conductivity with temperature. When temperature increases the

vibrations of metal ions or the charge carriers also increase resulting in an increase in resistance.

5.3.3 Analysis of Impedance spectra

Impedance is the opposition that a dielectric material presents to the flow of electricity. The two contributing factors to impedance are resistance(Z') and reactance i.e. the slowing of current due to capacitive and inductive reactance(Z''). Impedance is typically represented by a complex number, denoted as $Z = Z' - jZ''$, with real(Z') and imaginary (Z'') components. By taking into consideration all these factors, The mathematical expression for impedance is given in equation 5.2:

$$Z = \sqrt{R^2 + (X_L - X_C)^2} \quad (5.2)$$

Where R is resistance, X_L , and X_C are inductive and capacitive reactance. Impedance measurements are conducted at varying temperatures and frequencies to characterize the electrical properties of the zeolites. Analyzing the impedance data, aids in understanding the kinetics of bound and mobile charges in both the bulk and interfacial regions and the relaxation mechanisms within the system.(14)

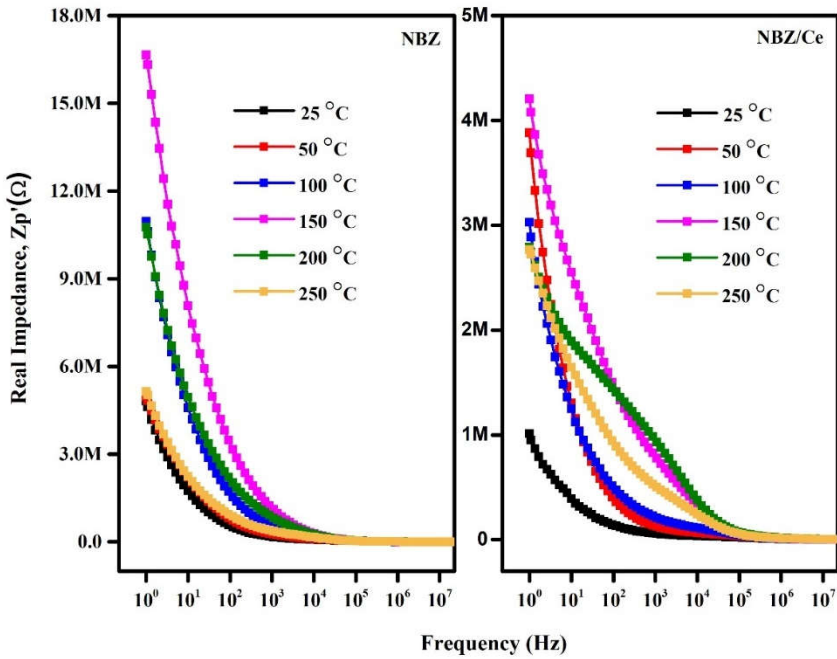


Figure 5.4. Variation of the real impedance of NBZ and NBZ/Ce with frequency at different temperatures

In Figure 5.4, both NBZ and NBZ/Ce exhibit a typical behavior where Z' decreases with increasing frequency, becoming negligible beyond 10^5 Hz. The NBZ demonstrates positive temperature coefficient of resistivity (PTCR) behavior, indicating that the resistance increases with rising temperature, particularly up to 150 °C. The increase in resistance observed is due to decreased mean free path of the conducting ions arising because of the increased collision frequency which in turn arises due to increased amplitude of vibration.⁽¹⁵⁾ It can be observed that as temperature increases to 200 °C, the impedance does not rise substantially but decreases in both NBZ and NBZ/Ce samples. This explanation for the decrease in resistance is based on the fact that the matrix is a zeolite with a high

dielectric constant. At temperatures above 200 °C the zeolite lattice undergoes expansion that creates new pathways for more number of ions.(16)

When comparing the resistance values of NBZ and NBZ/Ce, the higher values are recorded for the NBZ sample. The mobility of protons in the NBZ sample is restricted due to electrostatic interactions and hydrogen bonding with the surrounding framework. Whereas, in the case of NBZ/Ce, the multivalent cerium ions are larger and have different charge characteristics compared to protons. Ce ions encounter less resistance to movement as it is not bound to the zeolitic framework as in the case of protons in NBZ.(17)

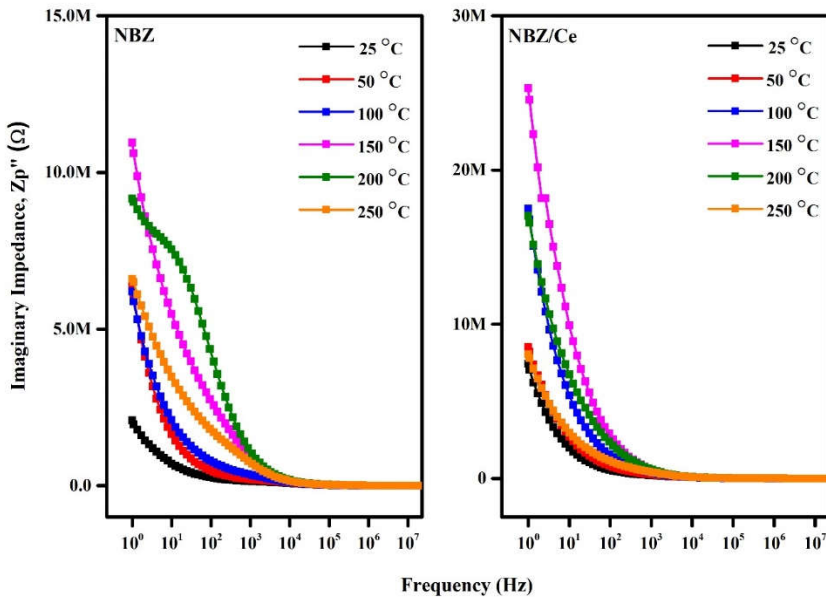


Figure 5.5. Variation of the imaginary impedance of NBZ and NBZ/Ce with frequency at different temperatures

The reactance part plays a very important role in determining the value of impedance as per equation 5.2. The inductive reactance is given by the equation 5.3:

$$X_L = 2\pi fL \quad (5.3)$$

Where f is the frequency and L is the inductance

The capacitive reactance is given by the equation 5.4:

$$X_C = \frac{1}{2\pi fC} \quad (5.4)$$

Where C is capacitance

The Figure 5.5 depicts the variation of imaginary impedance Z'' with frequency. It displays a consistent decreasing trend with increase in frequency up to a specific frequency limit (10^4 Hz). Beyond this limit, the plots converge and exhibit frequency-independent behavior across all temperatures within the experimental range. The large values of the imaginary impedance Z'' at low frequency indicate that this value is largely contributed by capacitive reactance as indicated by equation 5.5. Imaginary impedance, Z'' contributed by capacitive reactance is associated with the ability of the material to store and release electrical energy which is analogous to the concept of dielectric constant. It is observed that both NBZ and NBZ/Ce follow a similar type of variation as observed in the case of the variation of the dielectric constant.

Dielectric constant and capacitive reactance are inversely related through their effects on capacitance. An increase in dielectric constant leads to an increase in capacitance which in turn results in a decrease in capacitive reactance (Equation 5.4).(18) The observation that is already discussed is that the capacitance values of NBZ and NBZ/Ce exhibit a negative temperature coefficient. So, as the temperature rises, capacitive reactance increases because capacitance decreases.

As the temperature reaches 250 °C, the imaginary impedance Z'' reduces to levels comparable to room temperature. This observation can be attributed to the fact that the molecules gain high energy to overcome the opposition imparted by reasons for the reactance.

5.3.4 Analysis of Electric modulus spectra

A detailed study of the electrical modulus is conducted to understand the relaxation processes within the zeolite samples. The electrical modulus is a complex quantity. The real part is the storage component (M') and the imaginary part is the dissipation component (M''). The study of electrical modulus furnishes information about dipolar relaxation, ionic conduction, and other mechanisms contributing to the dielectric behavior of materials.

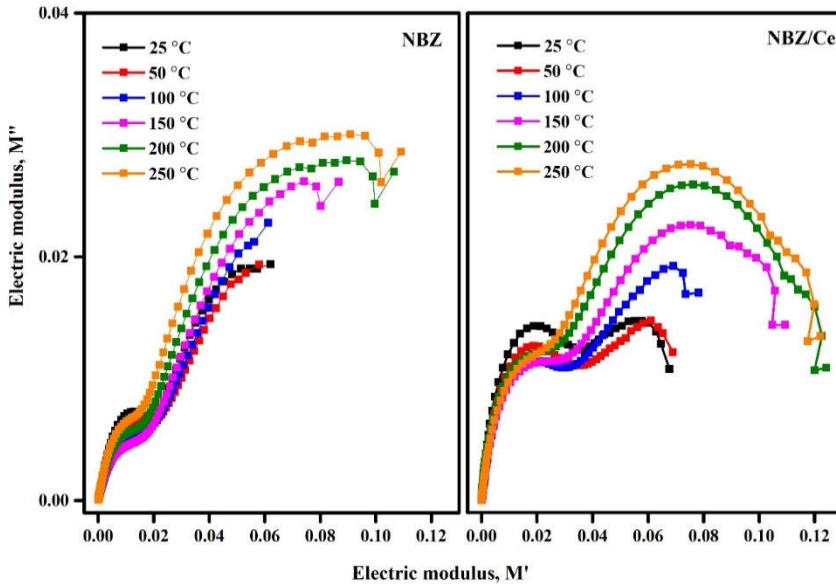


Figure 5.6. Cole-Cole plot of NBZ and NBZ/Ce at different temperatures

The electrical modulus plane plots of both samples, which illustrate the real M' vs imaginary M'' curves over the temperature range of 25 °C to 250 °C, are shown in Figure 5.6. Generally, the cole–cole plots exhibit three semicircles corresponding to conductivities attributed to grain boundaries, grain size, and electrode effects, respectively.(19) Observations from the cole–cole plots indicate the presence of two semicircular arcs for both NBZ and NBZ/Ce samples, reflecting conductivities arising from grain boundaries and grain size. The presence of two relaxation processes is shown by these arcs, which are visible in the modulus plane plot of both samples at low and high frequencies. The smaller semicircular arcs observed at low frequencies suggests weak grain boundary effects,

incontras with the dominant grain size effects. On the other hand, at higher frequencies, the bigger semicircular arcs indicate the bulk or grain response.(20) The expansion of the semicircular areas in the two samples indicates an increase of both the effects, while the upward shift of the semicircle towards higher M' values signifies a rise in capacitance. The third arc corresponding to the electrode polarization is not visible and this indicates the superior dielectric properties of the zeolite samples.(21)

5.4 Conclusions

Broadband dielectric spectroscopic techniques can yield novel and crucial insights into molecular reorientation and translational motion when applied to diverse crystalline systems. During cerium doping, notable fluctuations are evident in dielectric and impedance measurements. At room temperature, significant ultrahigh dielectric constants, 26k and 7k, are observed for cerium-doped beta and unmodified zeolite beta, respectively. This is caused by larger interactions between the zeolite structure and protons in NBZ samples than the interaction of cerium ions with zeolitic structure in NBZ/Ce samples. As a result, the cerium ions within the zeolites' structure are better able to be field-induced to move, which increases the dielectric response at lower frequencies. Analysis of dielectric properties of synthesized nanoparticles reveals a decreasing loss tangent with increasing frequency, with cerium-doped zeolite beta exhibiting comparatively higher values. The AC conductivity rises with increasing frequency, particularly notable for zeolite beta.

Metal cations in NBZ/Ce and protons and surface hydroxyls in NBZ contribute to the observed AC conductivity at high frequencies. Electric modulus analysis elucidates the variation of the storage component and dissipative component accompanying various relaxation process taking place in the sample. Grain size and grain boundary contributions are elucidated through Cole-Cole plots of electric modulus. These findings on electrical and dielectric properties hold potential applications in charge storage and optoelectronic devices.

References

1. Chen P, Schönebaum S, Simons T, Rauch D, Dietrich M, Moos R, et al. Correlating the Integral Sensing Properties of Zeolites with Molecular Processes by Combining Broadband Impedance and DRIFT Spectroscopy—A New Approach for Bridging the Scales. *Sensors*. 2015;15(11):28915–41. Available from: <https://doi.org/10.3390/s151128915>.
2. Izci E, Izci A. Dielectric behavior of the catalyst zeolite NaY. *Turkish J Chem*. 2007;31(5):523–30. Available from: <https://journals.tubitak.gov.tr/chem/vol31/iss5/13>.
3. Mahabole MP, Lakhane MA, Choudhari A, Khairnar R. Dielectric and ethanol sensing studies on synthesized nano-ZSM-5 zeolite. *Indian J Phys*. 2014;89(2):167–74. Available from: <https://doi.org/10.1007/s12648-014-0572-9>.
4. Zhou W, Zhao KS. Dielectric Response and Analysis of Structural Evolution of NaA Zeolite with High Pretreatment Temperature. *J Phys Chem C*. 2008;112(38):15015–21. Available from: <https://doi.org/10.1021/jp802106q>.
5. Simon U, Flesch U. Cation-cation interaction in dehydrated zeolites X and Y monitored by modulus spectroscopy. *J Porous Mater*. 1999;6(1):33–40. Available from: <https://doi.org/10.1023/A:1009637102831>.
6. Kumar LP and V. Structural, thermomagnetic, and dielectric properties of $Mn_{0.5}Zn_{0.5}GdxFe_{2-x}O_4$ ($x = 0, 0.025, 0.050, 0.075,$ and 0.1). *J Adv Ceram*. 2020;9(2):243–54. Available from: <https://doi.org/10.1007/s40145-020-0364-y>.
7. Lopes AC, Silva MP, Gonçalves R, Pereira MFR, Botelho G, Fonseca AM, et al. Enhancement of the dielectric constant and thermal properties of α -Poly(vinylidene fluoride)/zeolite nanocomposites. *J Phys Chem C*. 2010;114(34):14446–52. Available from: <https://doi.org/10.1021/jp1052997>.
8. Lakhane M, Bogle K, Khairnar R, Dahiwalé S, Sharma R, Mokale V, et al. Dielectric properties of zeolite based metal oxide nanocomposites. *Nano-Struct Nano-Objects* [Internet]. 2019;17(3):248–58. Available from: <https://doi.org/10.1016/>

j.nanoso.2019.01.008.

9. Lakhane M, Khairnar R, Mahabole M. Metal oxide blended ZSM-5 nanocomposites as ethanol sensors. *Bull Mater Sci*. 2016; 39(6):1483–92. Available from: <http://link.springer.com/10.1007/s12034-016-1286-8>
10. Jose J, Thomas V, John J, Mathew RM, Salam JA, Jose G, et al. Effect of temperature and frequency on the dielectric properties of cellulose nanofibers from cotton. *J Mater Sci Mater Electron* [Internet]. 2021;32(16):21213–24. Available from: <https://doi.org/10.1007/s10854-021-06624-9>.
11. Franke ME, Simon U. Characteristics of Proton Hopping in Zeolite H-ZSM5. *Phys Status Solidi B*. 2000;218(1):287–90. Available from: [https://doi.org/10.1002/\(SICI\)15213951\(200003\)218:1<287:AID-PSSB287>3.0.CO;2-8](https://doi.org/10.1002/(SICI)15213951(200003)218:1<287:AID-PSSB287>3.0.CO;2-8)
12. Hojo K, Takahashi T, Oshima K, Haji T, Terayama Y, Matsumoto H, et al. Enhancement of ionic conductivity of aqueous solution by silanol groups over zeolite surface. *Microporous Mesoporous Mater* [Internet]. 2021;312(3):110743. Available from: <https://doi.org/10.1016/j.micromeso.2020.110743>.
13. Mckeen JC, Yan YS, Davis ME, Funct GAA V. Proton Conductivity in Sulfonic Acid-Functionalized Zeolite Beta: Effect of Hydroxyl Group. *Chem Mater*. 2008;20(12):3791–3. Available from: <https://doi.org/10.1021/cm800762x>.
14. Purohit V, Padhee R, Choudhary RNP. Structural and electrical properties of Bi(Mg_{0.5}Ti_{0.5})O₃ ceramic. *J Mater Sci Mater Electron* [Internet]. 2018;29(6):5224–32. Available from: <http://dx.doi.org/10.1007/s10854-017-8487-9>.
15. Sinclair DC, West AR. Impedance and modulus spectroscopy of semiconducting BaTiO₃ showing positive temperature coefficient of resistance. *J Appl Phys*. 1989;66(8):3850–6. Available from: <https://doi.org/10.1063/1.344049>.
16. Ghojavand S, Dib E, Mintova S. Flexibility in zeolites: origin, limits, and evaluation. *Chem Sci*. 2023;14(44):12430–46. Available from: <https://doi.org/10.1039/D3SC03934J>

17. Franke ME, Simon U. Solvate-supported proton transport in zeolites. *ChemPhysChem*. 2004;5(4):465–72. Available from: <https://doi.org/10.1002/cphc.200301011>
18. Weik, M.H. (2000). capacitive reactance. In: *Computer Science and Communications Dictionary*. Springer, Boston, MA. https://doi.org/10.1007/1-4020-0613-6_2181
19. Pratibha S, Dhananjaya N, Manohara SR, Yadav LSR. Effect of Sm³⁺, Bi³⁺ ion doping on the photoluminescence and dielectric properties of phytosynthesized LaAlO₃ nanoparticles. *J Mater Sci Mater Electron* [Internet]. 2019;30(7):6745–59. Available from: <http://dx.doi.org/10.1007/s10854-019-00986-x>.
20. Abdulvakhidov B, Li Z, Abdulvakhidov K, Soldatov A, Nazarenko A, Kulbuzhev B, et al. Study of the structural - phase state and physical properties. *Appl Phys A* [Internet]. 2022;128(4). Available from: <https://doi.org/10.1007/s00339-022-05442-y>.
21. Gajula GR, Buddiga LR, Chidambara Kumar KN, Dasari M. Study on electric modulus, complex modulus and conductivity properties of Nb/Sm, Gd doped barium titanate-lithium ferrite ceramic composites. *Results Phys* [Internet]. 2020;17(3-4):103076. Available from: <https://doi.org/10.1016/j.rinp.2020.103076>.

Chapter 6

Conclusions

Abstract

This chapter presents the findings and inferences derived from the conducted research. This study has delved into augmenting the textural and acidic attributes while preserving the crystalline parameters of nanocrystalline zeolites intact. The outcomes showcase the selective catalytic acetylation of toluene and 2-MON and provide insights into the dielectric response of cerium-doped zeolite.

This thesis explores multiple investigations concerning nanocrystalline and hierarchical ZSM-5 and zeolite beta. It is structured into three main sections. The first part is the synthesis and characterization of metal-doped ZSM-5 and zeolite beta. The nanocrystalline ZSM-5 and zeolite beta were synthesized hydrothermally and modified with transition elements such as iron, copper, zinc, and rare earth elements such as lanthanum, cerium, and neodymium.

A comprehensive analysis has been done to investigate the acidity, textural properties, and structural parameters of Fe, Zn, Cu, Nd, Ce, and La-doped nanocrystalline ZSM-5. According to the morphological examination, all the ZSM-5 samples have spherical crystals with a crystallite size of less than 40 nm. Significant absorbance is seen in between 220 - 800 nm for metal-ion exchanged ZSM-5, suggesting the presence of several metal-oxide species in the samples. The total surface area and pore volume of nanocrystalline ZSM-5 exhibited a marginal decrease as a result of the metal ion impregnation, according to the nitrogen adsorption isotherm. The introduction of metal ions induces the dissolution of the zeolitic matrix into smaller nanoparticles, which subsequently redeposit onto larger ones. This process leads to the fusion of pores and the simultaneous generation of mesopores. The TPD studies show that metal-modified nanocrystalline ZSM-5 has a significantly higher acidity. XRD measurements confirmed that, the lattice stability and crystallinity are impacted by metal alteration. The

findings indicate that ZSM-5 can effectively host various ions, which enhances its acidic qualities and improves its porous nature while maintaining its crystalline structure and keeping the lattice strain at a minimum.

The study on the synthesis and characterization of nanocrystalline zeolite beta modified with Cu, Zn, Fe, La, Ce, and Nd provides a better understanding of the coordination environment and structural characteristics. According to XRD data, metal loading raises lattice strain but does not change the zeolite structure. The average crystallite size is less than 30 nm for both modified and unmodified nanocrystalline zeolite samples. The phenomena of Ostwald ripening is also witnessed in the synthesis of zeolite beta samples leading to the formation of mesopores. UV-visible spectra show that metal ions can be found in the form of metal oxides and cations. Skeletal vibration patterns in FTIR spectra are comparable to typical zeolite absorption peaks.

The examination of acetylation of toluene using various metal-exchanged zeolite beta and ZSM-5 as catalysts were investigated by optimizing experimental settings to the bare minimum, with a particular emphasis on lower temperatures and lower catalyst concentrations, which improved the conversion significantly. Among the many metal modified samples, the ZSM-5 and zeolite beta samples treated with Ce showed catalytic conversion of over 90%. The catalytic efficiency of metal modified zeolites are based on their crystallite sizes, external acid sites, and diffusion rates

through micropores. All these factors favour cerium-modified nanocrystalline zeolite samples leading to exhibition of excellent catalytic selectivity by improving substrate accessibility to active sites thereby increasing the conversion.

The second part of the thesis describes the synthesis, characterization, and catalytic evaluation of hierarchical zeolites. The development of hierarchical porosity in nanocrystalline ZSM-5 and beta is achieved by using PMMA powder in the aged precursor solution. This novel synthesis method of adding PMMA powder to an aging precursor solution where nanocrystal nucleation has already begun, lowers the occurrence of internal defective silanols in nanocrystalline ZSM-5. This observation is confirmed by infrared and Raman spectroscopic investigations based on framework and silanol group vibrations. SEM, TEM, XRD and nitrogen sorption results confirm the formation of a porous structure without sacrificing crystallinity. The thermogravimetric analysis also confirms the interaction of PMMA and TPAOH for providing hierarchical porosity via reducing internal defective silanols.

Hierarchical zeolite beta was synthesized via a direct hydrothermal approach, utilizing PMMA as an additional structure-directing agent alongside TEAOH as the primary micropore structure-directing agent. The resultant zeolite beta displays XRD patterns and FTIR spectra similar to those obtained from zeolite beta synthesized using only a single structure-directing agent. Nonetheless, the zeolite beta synthesized with the inclusion of PMMA showcases a distinctly

narrow distribution of mesopores in addition to its inherent microporous structure. Samples with minimal polymer incorporation exhibit a well-defined isotherm with observable hysteresis loops that shift towards lower partial pressures. This shift expands notably in samples with higher polymer content, indicating increased mesopore volume. The augmentation of the mesoporous surface area results in a heightened concentration of Bronsted acid sites on the external surface.

Using the acetylation of 2-methoxynaphthalene, the impact of heterogeneous porosity on the catalytic activity of nanocrystalline hierarchical ZSM-5 and zeolite beta was demonstrated.

Materials possessing uniform mesopores displayed enhanced activity and selectivity towards 1-acetyl-2-methoxynaphthalene. Hierarchical ZSM-5 and beta demonstrated significant conversions of acetic anhydride with exclusive selectivity towards the kinetic product 1-acetyl-2-methoxynaphthalene isomer. This observation was attributed to a more uniform mesopore surface, facilitating interactions between reactant molecules and active sites distributed throughout the mesopores rather than the external surface. These effects arise from the improved homogeneity of mesopore characteristics (size, geometry, and surface) and the environment surrounding active sites, consequently amplifying catalytic performance.

The third part describes the study of the dielectric response of metal-modified zeolite beta. The broadband dielectric spectroscopic technique provides a wealth of novel and critical insights into molecular reorientation and translational motion across a diverse array of crystalline systems. Metal doping of nanocrystalline zeolites leads to remarkable changes in dielectric and impedance measurements. At room temperature, synthesized cerium-doped zeolite beta and the unmodified one exhibit significant ultrahigh dielectric constants, measured at 26k and 7k, respectively. This phenomenon arises from stronger interactions between the zeolite and protons than between the zeolite and cerium ions. Consequently, the cerium ions within the structure are more readily induced to move by an electric field, leading to an enhanced dielectric response at lower frequencies. Both the Ce doped and undoped samples exhibit a low $\tan \delta$ value, out of which cerium-doped zeolite beta demonstrates relatively higher values. The AC conductivity escalates with frequency, particularly in zeolite beta. AC conductivity of cerium-doped zeolite beta is due to the mobility of metal cations and surface hydroxyls whereas in a zeolite beta it is due to mobility of protons.

Chapter 7

Recommendations

Abstract

The chapter discusses future possibilities based on the current study. It suggests that the research would lead to improvements in the methods used for fixing defects in zeolites and these bettered zeolites can be used in synthesizing specific industrially important organic compounds for the production of medicines. It also hints at potential use of zeolites as capacitors.

The results presented in this work contribute to a fundamental understanding of the stability and reactivity of transition and rare earth elements on nanocrystalline ZSM-5 and zeolite beta. This can provide useful insights into the synthesis of metal ions doped zeolites and in understanding the connection between the nanostructure and activity of zeolite samples. This investigation can provide constructive suggestions for the design of metal-exchanged high-silica zeolites for greener catalytic reactions. The generation of hierarchical porosity in the metal exchanged zeolite also opens up a new strategy not only for enhancing the inherent properties of zeolite but also improves its capability as an efficient catalyst in various reactions.

The development of hierarchical porosity by using PMMA gives special emphasis on healing the silanol defects in ZSM-5. The detailed study on the dependency of PMMA for the condensation of internal silanol defects offer valuable information towards future investigations on new bettered synthesis routes for hierarchical zeolites. The synthesis strategies for defect-free nanocrystalline hierarchical zeolites have been streamlined and it can be extended to other type of zeolites for imparting hierarchical porosity. The application of zeolites for greener acetylation with high selectivity and understanding of the structure-catalytic relationships in hierarchical zeolites promise to boost the rational design and industrial application of hierarchical zeolite catalysts with narrower pore size distribution.

Dielectric spectroscopy study proves that the high dielectric constant of the cerium-doped zeolite beta can be foreseen as an excellent material for the fabrication of a super capacitor. Manufacture of sensors based on the dielectric response of nanocrystalline zeolites can be thought of. Chemists, physicists, material scientists, and engineers have opportunities to develop nanocrystalline zeolite-based systems, which could be innovatively applied in creating a new kind of capacitors..

Curriculum Vitae

Farsana. O. P

Address:

Ozhukka Parambil (House),
Randathani (PO),
Malappuram(dt),
Kerala, India-676510

Education

- MSc in Chemistry, Pocker Sahib Memorial Orphanage College, Tirurangadi, Malappuram, Kerala, India (2011-2013)
- BSc in Polymer Chemistry, MESKVM College Valanchery, Malappuram, Kerala, India (2008-2011)
- Higher Secondary, MSMHSS Kallingalparamba, Malappuram, Kerala, India (2006-2008)
- High School, PKMMHSS Edarikode, Malappuram, Kerala, India 2006

Academic Achievements

- UGC JRF in chemical science secured 069 rank in June 2015
- NET in chemical science secured 048 rank in June 2014
- 7th Position in the MSc Chemistry, University of Calicut

Research Experience

Experienced in preparation, characterization and properties of nanocrystalline zeolites

Demonstrable expertise in operation and application ATR/FTIR, UV Visible spectroscopy, Sonicator and TGA

Project Work Co-guided

- Crafting Hierarchical Structures: Nanocrystalline ZSM-5 Zeolites via PMMA Templating (2024)
- Advanced Synthesis and Characterization of Hierarchical Nanocrystalline Beta Zeolite via PMMA Templating (2024)
- Lanthanum Modified Nanocrystalline Beta Zeolite: An Efficient Adsorbent for Removal of Phosphatic Pesticide from Water (2022)
- Synthesis and Characterization of Hierarchically Porous and Modified Nanocrystalline ZSM-5(2020)
- Fabrication and Characterisation of Hierarchically Porous Zeolite Beta (2020)
- Copper Modified Nanocrystalline ZSM-5: Synthesis, Characterization and Catalytic Evaluation by Friedel Crafts Acylation (2019)

List of Publications

1. **Farsana. O. P**, Prajitha Kumari, Aneesh P. (2023). Curing of Silanol Defects and Tailoring Hierarchical Porosity in ZSM-5 Using PMMA. *Iranian Journal of Science*, 47(5–6), 1541–1551. <https://doi.org/10.1007/s40995-023-01548-x>
2. **Farsana.O. P**, Prajitha Kumari. (2022). Hierarchical Assembly of Zeolites: A Present Scenario. *Engineered Science*. <https://doi.org/10.30919/es8d781>
3. **Farsana.O. P**, Prajitha Kumari, Aneesh P. (2020). Cerium Incorporated Nanocrystalline ZSM-5: An Efficient Catalyst for Friedel Crafts Acylation of Toluene. *Journal of Nanoscience and Nanotechnology*, 20(9), 5823–5832. <https://doi.org/10.1166/jnn.2020.17811>
4. **Farsana.O. P**, Prajitha Kumari, Aneesh P. (2020). Effect of copper on textural and acidic properties of hierarchical nanocrystalline ZSM-5. *Asia-Pacific Journal of Chemical Engineering*, 15(5), 1–14. <https://doi.org/10.1002/apj.2547>

List of Conference Presentations

1. **Farsana. O. P**, Prajitha Kumari, Aneesh P. “A COMPREHENSIVE ROOM TEMPERATURE DIELECTRIC ANALYSIS OF CERIUM DOPED ZEOLITE BETA” at 1st International Conference on Advancement in Energy on 18-20 December 2023 Organized by *Motilal Nehru National Institute of Technology, Allahabad, Prayagraj*.
2. **Farsana. O. P**, Prajitha Kumari, Aneesh P. “A DELINEATED ROOM TEMPERATURE DIELECTRIC STUDY ON CERIUM DOPED ZEOLITE BETA” at a Poster/oral competition on Recent Trends in Nano Materials Towards the Sustainable Developments in Energy and Environment-2022, on 25, 26 and 28 February 2022 organized by *Institute of Science, Mumbai* In collaboration

with *Savariammal Universal Research and Education (SURE) Foundation*.

3. **Farsana. O. P**, Prajitha Kumari, Aneesh P. “DUAL TEMPLATE MEDIATED SYNTHESIS OF HIERARCHICALLY POROUS ZSM-5 FOR GREENER ACYLATION” at 2nd International Conference(online) on 20-22 August 2021, organized by *Dr. B R Ambedkar National Institute Of Technology, Jalandhar, Punjab*.
4. **Farsana. O. P**, Prajitha Kumari, Aneesh P. “INFLUENCE OF METAL ENCAPSULATION AND DUAL TEMPLATE SYNTHESIS ON CATALYTIC ACTIVITY OF ZEOLITE BETA” at National E-Conference on 22-23 February 2021 organized by *Kamaraj College Thoothukudi, Tamilnadu*.
5. **Farsana. O. P**, Prajitha Kumari, Aneesh P. “ENHANCING THE TEXTURAL AND STRUCTURAL PROPERTIES OF NANOCRYSTALLINE ZSM-5 USING Fe, Zn AND La” at 6th International Conference (Virtual Conference) on 01 – 03 February 2021, organized by *SRM Institute of Science and Technology, Kattankulathur*.
6. **Farsana. O. P**, Prajitha Kumari, Aneesh P. “ENHANCING CATALYTIC POWER OF ZEOLITE BETA BY COPPER AND PMMA” at 26th International Conference (online) on 18-20 December 2020, organized by *Mahatma Gandhi University, Kottayam, Kerala, India*.
7. **Farsana. O. P**, Prajitha Kumari, Aneesh P. “BOOSTING THE ZEOLITIC PROPERTIES BY DOPING WITH RARE EARTH AND TRANSITION METAL IONS,” at International conference on 6-8 January 2020 organized by *VIT and Royal Society of Chemistry, UK*.
8. **Farsana. O. P**, Prajitha Kumari, Aneesh P. “LANTHANUM DOPING EFFECT ON SPECTRAL AND TEXTURAL PROPERTIES OF NANOCRYSTALLINE ZSM-5,” at International conference On 11-13 October 2019 organized by *Mahatma Gandhi University, Kottayam, Kerala, India*.

9. **Farsana. O. P**, Prajitha Kumari, Aneesh P. “EFFECT OF COPPER IONS IN TEXTURAL AND ACIDIC PROPERTIES OF HIERARCHICAL NANOCRYSTALLINE ZSM-5” at International conference on 9-11 September 2019 organized by the *National Institute of Technology, Trichy (Best oral presentation award)*.
10. **Farsana. O. P**, Prajitha Kumari, Aneesh P. “STUDIES ON CERIUM DOPED NANOCRYSTALLINE ZSM-5 “a National Seminar on 18 December 2018 organized by *Majlis Arts and Science college Valanchery, Kerala*.
11. **Farsana. O. P**, Prajitha Kumari, Aneesh P. “STRUCTURAL STUDY OF MODIFIED NANOCRYSTALLINE ZEOLITE,” at International conference on 6 December 2018 organized by *SANDIP University, Nashik*.